UNIVERSITÀ DEGLI STUDI DI CATANIA
Ph.D. Course in Materials Science and Nanotechnology
XXXVIII cycle

Rosaria Galvagno

DEVELOPMENT OF A LUMINESCENCE PROTOCOL FOR THE DATING OF HISTORICAL MORTARS

Ph.D. Thesis

Tutor: Prof. Riccardo Reitano
Tutor: Prof. Anna Maria Gueli

Academic year 2024/2025

Contents

Introduction

Luminescence emission, stimulated in many materials by different physical or chemical interactions, has gained increasing scientific interest since the 1960s due to its broad range of applications. Numerous physical models have been developed to describe luminescence in laboratory-grown materials intentionally doped with controlled impurities, allowing for theoretical predictions consistent with experimental observations. In contrast, luminescence phenomena in natural crystals remain difficult to model due to the uncontrolled and often unknown nature of their impurities and structural defects. Nonetheless, it is still possible to interpret experimental results using phenomenological models.

The luminescence stimulated process can be separated into two distinct phases. In the first phase, energy is absorbed by the luminescent material from an external source of ionising radiation, driving the system into a non-equilibrium state. During this stage, the free charge carriers generated (i.e., electrons and holes) may become trapped in metastable energy levels within the band gap. In the second phase, the system returns to equilibrium upon stimulation, which allows the trapped electrons to escape their metastable states and recombine radiatively with holes, giving rise to luminescence emission.

When stimulation is thermal, the resulting emission is referred to as Thermoluminescence (TL); when the sample is exposed to a light source, the signal is known as Optically Stimulated Luminescence (OSL). In both cases, the intensity of the emitted signal depends on the population of the trapping levels, which in turn is related to the total energy absorbed by the material. Consequently, TL and OSL intensity in natural crystals is directly linked to the *absorbed dose*, defined as the energy absorbed per unit mass.

One of the most significant applications of luminescence phenomena is *luminescence dating*, which allows the determination of the time elapsed since a specific *zeroing event* that reset any luminescent signal. This method is applied to a wide range of materials and contexts, including the last exposure of ceramics, bricks, sediments, and burnt stones to heat or sunlight, as well as the reconstruction of geological processes, archaeological occupation phases, and the chronology of historical buildings. The principle underlying these applications is the measurement of the absorbed dose, which accumulates progressively after the resetting event and thus provides a direct means to calculate the absolute time elapsed.

In luminescence dating, this absorbed dose corresponds to the radiation dose accumulated by the material since the zeroing event. It is evaluated from the intensity of the luminescence signal stored in the mineral phases, which act as natural dosimeters. Their stimulated emission provides the measurable signal used to reconstruct the sample's exposure history. The minerals involved,

such as quartz, feldspar, and calcite, are naturally present in the raw materials used in the manufacture of ceramics and construction materials, occurring in different proportions. They record the energy deposited by ionising radiation and are therefore regarded as natural dosimeters, as they store information about the radiation dose absorbed since the last resetting event. The accumulated energy is referred to as the *palaeodose* and originates mainly from the decay of naturally occurring radionuclides such as ^{235}U, ^{238}U, ^{232}Th, ^{40}K, and ^{87}Rb, in addition to the contribution from cosmic radiation. To determine the time elapsed since the resetting event, it is necessary to evaluate the rate at which this energy was absorbed, known as the *annual dose rate* ($\dot{D}_R$).

In the literature, the term *palaeodose* is often used interchangeably with *natural dose*, both referring to the dose accumulated since the last effective reset [1]. In practice, however, this quantity is not directly measured but reconstructed experimentally through laboratory procedures that yield the so-called *equivalent dose* (D_e). The equivalent dose corresponds to the amount of radiation required, under controlled conditions, to reproduce a luminescence signal equal to that observed in the natural state of the sample. In this thesis, the term *equivalent dose* will be used to denote the experimentally derived quantity employed in age calculation.

The present research is situated precisely within the framework of luminescence dating applied to historical buildings, with a specific focus on mortar dating. Initial applications of luminescence dating targeted fired materials such as bricks, whose high-temperature manufacture effectively resets the luminescence signal in quartz and feldspar [2, 3]. Once incorporated into masonry, the signal accumulates again, and the TL age reflects the time since firing. Although bricks are abundant and well suited for dating, their reuse and uncertainties related to heating or architectural modifications may compromise the reliability of TL chronologies [4, 5, 6].

To address these limitations, OSL has been increasingly applied to construction mortars. In lime-based mortars, the quartz grains contained in the sandy aggregates are exposed to sunlight during preparation, and the final daylight exposure before setting defines the zeroing event [7, 8, 9]. Once incorporated into the structure and shielded from light, the signal accumulates again under environmental radiation, and the OSL age corresponds directly to the construction phase. Unlike bricks, mortars cannot be reused once hardened, which ensures a direct association between the luminescence signal and the original building event, providing new opportunities for establishing the chronology of architectural phases where archaeological or documentary evidence is lacking.

Over time, OSL applied to mortars has gained recognition as a valuable tool for absolute dating. A major challenge, however, is incomplete bleaching, since not all quartz grains are fully reset during mortar preparation [10, 11]. Residual luminescence from earlier light exposures may lead to overestimation of the D_e and thus of the calculated age. This results in wide D_e distributions, which are difficult to resolve using conventional multigrain aliquots. The adoption of small aliquots or single-grain OSL (SG-OSL) allows the identification of the best-bleached grains and improves the reliability of age estimates [12, 7]. SG-OSL has been successfully applied to mortars, providing consistent

chronologies even in cases of low sensitivity and significant dose dispersion [13, 14]. Despite its advantages, no standardised protocol has yet been established for SG-OSL applied to mortars, due to persistent methodological limitations. These include the difficulty of selecting appropriate statistical models for D_e estimation when dose distributions deviate markedly from Gaussian behaviour, as well as the low luminescence sensitivity of some quartz fractions, which often requires large numbers of single-grain measurements and significantly increases analysis time [13]. Although SG-OSL is currently regarded as the reference technique for mortar dating, its limitations highlight the need to explore alternative luminescent components capable of recording the time of construction through different mechanisms.

In this context, particular attention has been directed to the carbonate fraction of the binder, primarily composed of calcium carbonate ($CaCO_3$), which forms during the setting and hardening of lime mortars via the carbonation process. Under ambient conditions, $CaCO_3$ crystallises mainly as calcite, the most stable polymorph, whose luminescent properties are at the core of the present study [15, 16, 17]. Unlike quartz, whose signal resetting depends on variable and often insufficient sunlight exposure during mortar preparation, the carbonate-related luminescence signal may be reset through thermal or chemical processes directly linked to mortar manufacture. Specifically, zeroing may occur either during high-temperature treatment of the raw materials or during the in-situ crystallisation of $CaCO_3$ within the binder during carbonation.

This work presents a preliminary experimental attempt to isolate and characterise the TL signal associated with the carbonate fraction in historical mortars, introducing a novel methodological approach aimed at distinguishing this signal from the quartz contribution. The study explores the potential of the carbonate phase as a possible chronometer for luminescence dating, a direction that has so far received little attention. In parallel, the thesis contributes methodologically by addressing the procedures for equivalent dose determination, which remain a critical step in luminescence dating of complex materials such as mortars.

The experimental work was carried out in two successive phases, designed to progressively advance the development and testing of a TL-based approach for mortar dating. In the first phase, controlled reference samples were prepared and analysed in order to characterise the luminescent behaviour of quartz, calcite, and their mixtures. Quartz and calcite were first investigated separately through TL glow curve deconvolution, which allowed the identification of their characteristic peaks and the extraction of kinetic parameters. The study was then extended to controlled mixtures of the two minerals, irradiated with known doses, to assess the possibility of discriminating their respective contributions within composite signals. This step provided the methodological basis for isolating the carbonate fraction within the composite TL signal and for studying its dosimetric behaviour.

In the second phase, the developed approach was applied to the dating of archaeological mortars from the Roman bath complex of the *Terme della Rotonda* in Catania, Italy. The D_e of quartz extracted from the mortars was determined by SG-OSL and used as a reference chronology. In parallel, the TL-based protocol was applied directly to unprepared mortars, with deconvolution

procedures employed to derive independent D_e estimates. The annual dose rate ($\dot{D}_R$) was then determined and combined with the D_e values to obtain absolute age estimates. The comparison of SG-OSL and TL chronologies under real-case conditions provided a rigorous test of the proposed methodology, demonstrating its potential to expand the methodological approaches available for luminescence dating of complex building materials.

The experimental work was carried out at two research facilities. The methodological development and TL measurements on reference and archaeological mortars were conducted at the *PH3DRA laboratories* (Physics for Dating Diagnostics Dosimetry Research and Applications) of the University of Catania, Italy, whereas the SG-OSL measurements and the annual dose rate determinations on the samples from the *Terme della Rotonda* were performed at the *Archéosciences Bordeaux* laboratory, Université Bordeaux Montaigne, France.

The thesis is structured into four chapters, each advancing the investigation of luminescence dating of mortars:

Chapter 1 establishes the theoretical foundations of luminescence phenomena, focusing on the physical principles that govern the storage and release of energy in crystalline materials exposed to ionising radiation. The mechanisms of TL and OSL are presented in detail, including kinetic models used to interpret glow curves. The chapter concludes with a discussion of the luminescent properties of quartz and calcite, the two dosimetric phases investigated in this thesis, highlighting their suitability for dating applications.

Chapter 2 provides the state of the art on luminescence dating, with specific emphasis on its application to historical mortars. It reviews the conditions for the applicability of the method and introduces the luminescence age equation and its two key components: the equivalent dose (D_e) and the annual dose rate ($\dot{D}_R$). The procedures for estimating D_e are discussed, including regenerative protocols and the Single-Aliquot Regenerative-dose (SAR) method, as well as the statistical models used to interpret heterogeneous dose distributions. The second part addresses the determination of the annual dose rate, describing the contributions of α, β, γ, and cosmic radiation, and the experimental approaches employed, such as high-resolution gamma spectrometry and *in situ* dosimetry.

Chapter 3 presents controlled laboratory experiments on quartz, calcite, and their mixtures, individually characterised through TL glow-curve deconvolution to identify their characteristic peaks and kinetic parameters. Analysis of mixed samples demonstrated the feasibility of isolating the carbonate component and studying its behaviour with dose, thereby establishing a methodological basis for its potential use as an independent chronometer. The results of this work are presented in the publication *Discrimination of Thermoluminescent Signals from Natural Quartz and Carbonate Crystals Mixture* [18].

Chapter 4 applies the developed methodology to archaeological mortars from the Roman bath complex of the *Terme della Rotonda*. The D_e of quartz extracted from the mortars was determined by SG-OSL as a reference chronology, while the TL-based deconvolution protocol was applied to unprepared mortars to separate quartz and carbonate signals and derive independent D_e estimates. These values, combined with annual dose rate determinations, al-

lowed reconstruction of absolute ages. The direct comparison of SG-OSL and TL chronologies under real-case conditions provides a rigorous validation of the proposed approach and highlights its potential for luminescence dating of complex heritage materials.

A comprehensive appendix is included in this thesis, providing the complete analytical documentation of the TL investigations on the archaeological mortars, including the full data analysis workflow.

1 Luminescence Physics

The present chapter establishes the theoretical foundations required to interpret luminescence as a dating tool for crystalline materials exposed to ionising radiation. Building on the general introduction, where the objectives and scope of this thesis were outlined, the focus here is on the physical principles that govern the storage and release of energy in minerals of dating interest.

The discussion begins with a general overview of luminescence, distinguishing between fluorescence and phosphorescence, and then introduces the electronic structure of crystals with emphasis on the role of defects as trapping and recombination centres. These concepts are essential for understanding how a latent signal is created and preserved within natural dosimetric materials.

Subsequently, the theoretical basis of Thermoluminescence (TL) is presented in detail. Particular attention is given to the processes of thermal release from metastable traps, the generation of glow curves, and their interpretation through different kinetic models. Since TL represents the core technique applied in the experimental part of this thesis, this section provides the framework for later analyses of glow curve structures and their deconvolution.

In addition, the theoretical aspects of Optically Stimulated Luminescence (OSL) are introduced to provide the necessary basis for understanding its application in the Single-Grain OSL (SG-OSL) technique on quartz grains.

The chapter concludes with a discussion of quartz and calcite, the two minerals central to this research, highlighting their luminescent responses and their suitability as natural dosimeters for dating purposes.

This theoretical background serves as the necessary foundation for the methodological developments discussed in Chapter 2, where the principles introduced here are applied to the study of historical mortars and their chronological assessment.

1.1 Introduction to luminescence phenomenon

Luminescence is the emission of light by a material as a result of non-thermal excitation, and it can be triggered by a wide range of interactions, including mechanical stress, chemical reactions, and ionising radiation. This phenomenon has gained increasing relevance over the past five decades owing to its wide range of applications in scientific and technological fields, such as dosimetry, materials science, archaeology, and geochronology [19, 20, 21].

Numerous theoretical models have been successfully developed to explain the luminescence behavior of synthetic or highly controlled crystalline materi-

als. These models are well supported by experimental evidence and allow reliable predictions of luminescence responses under laboratory conditions. However, when it comes to natural crystals, the situation becomes more complex. Luminescence signals from naturally occurring materials often exhibit significant variability and unpredictability, reflecting the uncontrolled conditions of their geological formation. As a result, a unified and comprehensive theoretical model that can describe their luminescence behavior remains elusive.

Nonetheless, some of the physical models originally formulated to describe luminescence in controlled systems can still be applied to interpret experimental results from natural crystals. In this context, the objective of this chapter is to present the theoretical foundations of the luminescence phenomenon, focusing in particular on those aspects that are relevant to the use of natural minerals as dosimetric materials in dating applications.

The luminescence process applied in dating techniques can be described as a sequence of two main stages. In the first stage, the material absorbs energy from an external source. This input promotes electrons and holes and drives the system into a non-equilibrium state, where charge carriers can become trapped in metastable energy levels within the forbidden band gap of the crystal lattice. In the framework of luminescence dating, the external source of interest is ionizing radiation, responsible for the progressive accumulation of trapped charges within the material over time. In the second stage, a stimulation process supplies the energy required for the trapped electrons to escape their traps and recombine radiatively with holes, thus leading to the emission of photons.

If stimulation occurs by heating, the phenomenon is termed thermoluminescence (TL); if the stimulation is optical, the emission is referred to as optically stimulated luminescence (OSL). In both cases, the intensity of the emitted signal depends on the number of radiative transitions, which is determined by the population of trapped charges. Consequently, the luminescence intensity is directly related to the absorbed dose, defined as the amount of energy deposited per unit mass since the last resetting event.

This chapter will therefore introduce the essential physical concepts underlying the luminescence phenomenon, followed by an overview of the principles of TL and OSL dating. Particular attention will be given to the mechanisms of energy absorption and storage, the processes of charge trapping and recombination, and the determination of the equivalent dose, key components for understanding the methodological developments presented in the following chapters. Finally, the luminescent properties of the main dosimetric materials employed in this study will be discussed, providing the necessary background for interpreting the experimental results described later in the thesis.

1.1.1 Luminescence and essential conditions for its occurrence

Luminescence is generally defined as the emission of electromagnetic radiation resulting from a non-thermal excitation of atomic or molecular origin. This distinguishes it from thermal radiation, in which the emitted energy originates from heat. For this reason, luminescence is often referred to as *cold light*, in

contrast to *incandescent light* produced by thermal excitation [19]. Luminescent materials are able to absorb energy, store a portion of it, and subsequently convert it into light. These materials typically exhibit a crystalline structure. When radiation interacts with the lattice, the energy can be reabsorbed or re-emitted as light at a longer wavelength, in accordance with Stokes' law. The emitted radiation usually lies in the visible range, although ultraviolet or infrared emissions may also be observed depending on the properties of the material.

Different types of luminescence are categorized according to the source of excitation: *photoluminescence*, *cathodoluminescence*, *chemiluminescence*, *bioluminescence*, and *triboluminescence*, corresponding to excitation by photons, electrons, chemical reactions, biochemical processes, and mechanical stress, respectively. The type of luminescence relevant to this work is that induced by ionising radiation, which provides the physical basis for dating archaeological materials.

The emission lifetime t_c allows a broad classification into *fluorescence*, where $t_c < 10^{-8}$ s, and *phosphorescence*, where $t_c > 10^{-8}$ s [22, 23]. Fluorescence occurs simultaneously with irradiation and ceases immediately once the source is removed, whereas phosphorescence is characterized by a delay between excitation and maximum emission intensity $t_{\max}$, and it persists after irradiation ends (Fig. 1.1).

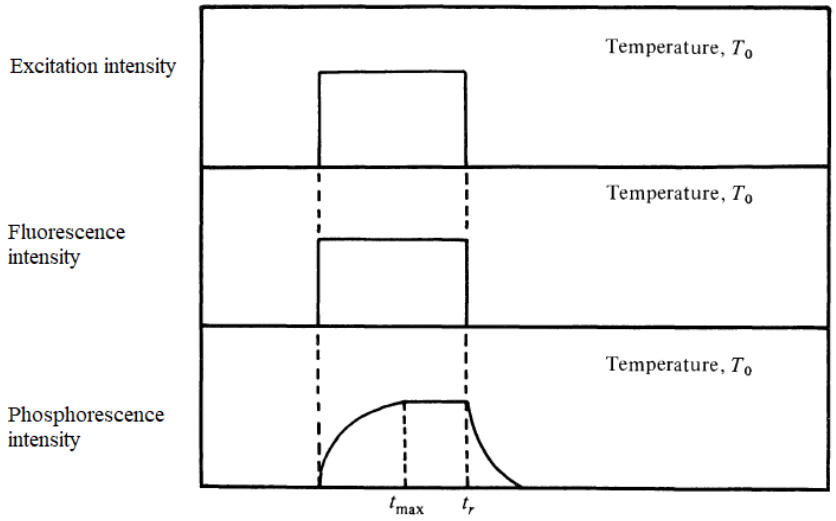

Figure 1.1: Temporal relationship between the excitation source and emission for fluorescence and phosphorescence. T_0 is the temperature at which irradiation occurs, $t_{\max}$ is the time of maximum emission intensity, and t_r is when irradiation ends and phosphorescence decay begins. Adapted from [19].

The energy states in a solid, as described by band theory, originate from the discrete energy levels of isolated atoms or ions. When atoms form a solid, their energy levels broaden into bands: the *valence band* (V), filled with electrons at absolute zero, and the *conduction band* (C), typically empty in insulators. The energy difference between them, the *band gap*, defines the electronic and optical properties of the material. Within this scheme, the *Fermi level* E_F plays a central role, representing the energy at which the probability of occupation by an electron is 50% at thermal equilibrium. In insulators, the Fermi level lies

inside the band gap, providing a reference for the energetic position of defect states and determining their tendency to capture or release charge carriers. In the context of luminescence, it is therefore essential for evaluating the stability and occupancy of traps and recombination centers that govern the emission process.

In real crystals, however, the ideal band structure is perturbed by the presence of structural imperfections and impurities, which introduce localized energy states within the band gap. The nature of these defects can be very diverse and, in the case of natural minerals, their exact identification often remains uncertain, making it difficult to determine which specific centers are responsible for the observed luminescence.

In real crystalline solids, luminescence can arise from different mechanisms of excitation energy transport. Two main processes are generally considered: the migration of excitons, i.e. bound electron–hole pairs that propagate through the lattice, and the migration of free charge carriers, namely electrons and holes that move before being captured by trapping or recombination centers. Although both mechanisms may occur, in natural crystalline solids of dosimetric relevance the dominant process is ionization, which separates electrons from their lattice sites and creates complementary vacancies known as holes.

During irradiation, electrons may be promoted to the conduction band and subsequently captured in localized defect states. Upon stimulation, the trapped charges may be released, return to the conduction band, and recombine at luminescence centers, giving rise to the emission of photons. Luminescence in a sample can thus be described as a two-step process: (1) *induction*, where ionising radiation generates free electrons and holes, most of which recombine instantly but a fraction of which diffuse and become trapped at defect sites; and (2) *stimulation*, where trapped charges are released and subsequently recombine at specific sites capable of radiative transitions.

Defect states can play different roles in this process. On the one hand, *electron traps* and *hole traps* store charge carriers until they are released by stimulation. On the other hand, *recombination centers* (or *luminescent centers*) are the sites where radiative recombination takes place, and they can be further classified as *electron centres* or *hole centres* depending on the type of carrier involved. A schematic representation of these defect states, together with the valence band, conduction band, and the Fermi level at absolute zero, is shown in Figure 1.2. In this specific condition, all electrons occupy states in the valence band below the Fermi level, while the conduction band remains empty. This schematic representation provides a conceptual framework for understanding how traps and recombination centres are distributed within the band gap, and how their energetic position relative to the Fermi level determines their role in charge storage and radiative recombination.

The TL signal generated during stimulation is therefore proportional to the number of trapped charge carriers available for recombination, providing a direct link between trap occupancy and luminescence intensity. A schematic representation of the distribution of traps, recombination centers, and the Fermi level in an insulator at absolute zero is shown in Figure 1.2.

The stability of a trap is determined by its depth or activation energy,

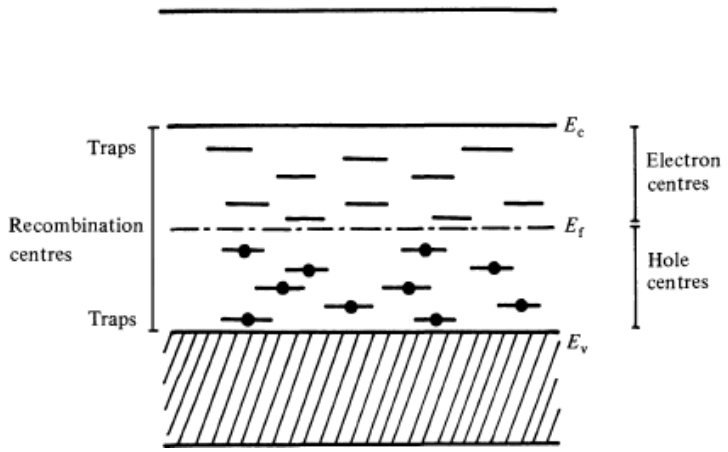

Figure 1.2: Schematic representation of energy levels in an insulator at absolute zero. The diagram shows electron and hole traps, as well as recombination centres, in relation to the valence band (E_V), conduction band (E_C), and the Fermi level (E_F). At $T = 0$ K, all electrons occupy states in the valence band below the Fermi level, while the conduction band remains empty. Recombination centres are drawn in the middle of the band gap only schematically, to emphasize their role as radiative recombination sites, without a precise energetic position. Adapted from [19].

which represents the energy required to release the trapped carrier. Shallow traps correspond to short-lived states and are associated with phosphorescence, whereas deeper traps may retain charges for extremely long timescales, up to hundreds or thousands of years under natural conditions. It is precisely these long-lived traps that are responsible for the luminescence signal of interest in dating applications.

When stimulation is provided by heat, the resulting emission is termed TL, whereas stimulation by photons produces OSL. Both phenomena originate from the same fundamental mechanism of charge trapping and recombination, differing only in the nature of the stimulation.

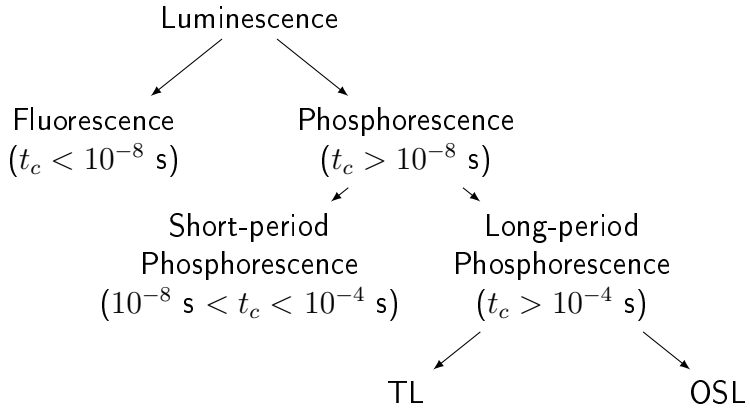

Figure 1.3: Schematic classification of luminescence phenomena based on emission time and stimulation type.

Over the past decades, TL has retained a central role despite the more recent and widespread diffusion of OSL. TL remains a fundamental technique, offering not only a reliable dating tool but also essential insights into the trapping and recombination processes that govern luminescence.

1.2 Thermoluminescence and theory of the glow curves

An electron confined in a trap within the crystal lattice can be conceptually compared to a ball resting at the bottom of a gravitational potential well. The depth of the trap depends on the specific nature of the defect structure and represents the binding energy of the charge carrier (either an electron or a hole) to the defect site within the lattice. Only when sufficient thermal energy is provided can the carrier escape from the trap, in analogy to a ball that must overcome the potential barrier to leave the well.

During thermal stimulation, traps with different depths release their charge carriers at different temperatures. The resulting light emission, plotted as a function of temperature, produces the characteristic TL signal profile known as a *glow curve*. This curve is the superposition of several glow peaks, each associated with a specific trap population. In practice, the glow curve of a typical luminescent material is composed of multiple contributions, some of which are well resolved while others overlap, reflecting the coexistence of different trap types.

A typical thermoluminescence glow curve is shown in Figure 1.4. The shape of the curve reflects the combined effect of traps with different activation energies, while the intensity of the emission depends on the balance between thermal release, retrapping, and recombination probabilities. The separation of individual components, each corresponding to a specific trap, requires deconvolution procedures that will be discussed later in Chapter 3.

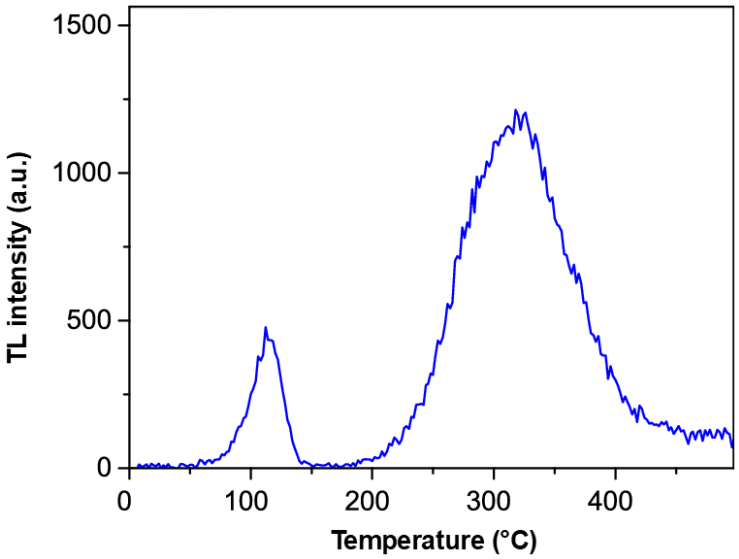

Figure 1.4: Example of a TL glow curve recorded from quartz. The observed peaks at different temperatures reflect the presence of traps with different activation energies. The intensity and shape of each peak depend on the balance between thermal release, retrapping, and recombination probabilities. Adapted from [24].

In the following discussion, the analysis is restricted to the case of an isolated single glow peak. This simplification implies that the emission originates from a population of traps of a single kind, characterized by a uniform trap depth.

Consider a population of electrons confined in such defects, commonly referred to as *filled traps*. At low temperatures, these electrons occupy the ground state of the trap, located at an energy E below the conduction band minimum.

The probability of finding an electron at an energy ΔE above the ground state at a given temperature T is governed by the Boltzmann distribution:

$$\frac{n}{n_0} = \exp\left(-\frac{\Delta E}{kT}\right), \tag{1.1}$$

where n_0 is the total number of trapped electrons and n is the number of electrons with energy ΔE above the trap minimum. Of particular interest is the fraction of electrons that reach an energy equal to the trap depth E, since these are the carriers that can escape into the conduction band and contribute to TL upon recombination. For a trap depth of 1 eV at room temperature, this fraction is of the order of 10^{-13}.

Although such a probability is extremely small, traps can nevertheless be emptied efficiently due to the high frequency at which escape attempts occur. This effect is expressed by the term

$$p = s \exp\left(-\frac{E}{kT}\right), \tag{1.2}$$

where s is the *frequency factor*, corresponding to the lattice vibrational frequency. The parameter p represents the probability per unit time for an electron to escape from the trap.

At any given instant only a small fraction of the trapped electron population acquires, through thermal fluctuations, an energy comparable to the trap depth, enabling them to be thermally released into the conduction band. Once these carriers escape, the system rapidly re-establishes thermal equilibrium: the remaining trapped electrons redistribute their energies according to the Boltzmann distribution, and a new fraction attains the energy required for release.

This process is inherently dynamic. At each infinitesimal time interval, a subset of carriers is thermally excited and released, while the rest of the population re-adjusts to equilibrium. As the temperature increases, the probability of reaching the activation energy grows, thereby accelerating the release rate and leading to the progressive emptying of the traps.

This cumulative mechanism explains how thermoluminescence emission can occur efficiently even when the instantaneous escape probability for individual carriers is extremely low. It also highlights the combined importance of the trap depth (activation energy) and the frequency factor in governing the kinetics of TL emission. A more detailed analysis of the role and interpretation of the frequency factor is presented in the following section.

1.2.1 Frequency factor

The thermal release of an electron from a trap of depth E involves a two-step process. First, the electron must be thermally excited to an energy level approximately E above the trap ground state. The fraction of electrons in the trap population that acquires such energy is given by the Boltzmann factor

$\exp(-E/kT)$. However, even after reaching this energy, the electron is not immediately free: it may either fall back into the trap or successfully transition into the conduction band under the influence of continued thermal agitation.

The probability per unit time that an electron in the excited state will escape into the conduction band is quantified by the *frequency factor* s. In general, any transition rate depends on three parameters: (i) the number of available final states in the conduction band, (ii) the thermal velocity of the electron, and (iii) the transition cross-section. These factors combine to give:

$$s = N_c \sigma v, \tag{1.3}$$

where N_c is the effective density of states in the conduction band (cm^{-3}), v is the average thermal velocity of electrons ($\mathrm{cm\,s}^{-1}$), and σ is the transition cross-section (cm^2). The product $N_c \sigma v$ therefore has units of s^{-1} and expresses the number of attempts per second that a thermally activated electron makes to escape from the trap into the conduction band. Typical values for s lie in the range 10^{12}–$10^{14}\,\mathrm{s}^{-1}$, comparable to the lattice vibrational (Debye) frequency.

The parameters N_c and v exhibit an explicit temperature dependence, given by:

$$N_c = 2\left(\frac{2\pi m^* kT}{h^2}\right)^{3/2}, \tag{1.4}$$

$$v = \left(\frac{3kT}{m^*}\right)^{1/2}, \tag{1.5}$$

where m^* is the effective electron mass, k is Boltzmann's constant, and h is Planck's constant.

The transition cross-section σ has also been shown to vary with temperature, with an approximate dependence of $T^{-3/2}$ proposed by Lewandowski and McKeever [25]. Combining these relations gives the overall temperature dependence of the frequency factor:

$$s \propto T^{1/2}. \tag{1.6}$$

Despite this dependence, the value of s remains very large, typically of the order of $10^{13}\,\mathrm{s}^{-1}$. Consequently, over the temperature interval relevant to TL glow curve measurements (approximately 300–700 K), its variation is small, and it is generally acceptable to treat s as constant.

Finally, according to the principle of detailed balance, the probability that an electron escapes from a trap into the conduction band is equal to the probability of the reverse process, namely the capture of a conduction-band electron back into the trap. This implies that the cross-section σ is the same for both directions of the transition [26].

1.2.2 Thermoluminescence models

The interpretation of thermoluminescence glow curves relies on theoretical models that describe the kinetics of trap depopulation and charge recombination during thermal stimulation. The most widely adopted framework is the

one-trap one-recombination-center (OTOR) model, which considers a single electron trap and a single recombination center. Depending on the balance between recombination and retrapping probabilities, different kinetic regimes can be derived from this general scheme.

The first formulation was given by Randall and Wilkins, who assumed negligible retrapping. This limiting case of the OTOR scheme leads to first-order (FO) kinetics, where the luminescence intensity depends solely on the rate of trap emptying and is independent of the initial trap filling. Garlick and Gibson extended the model by including competitive retrapping, giving rise to second-order (SO) kinetics, another special case of the OTOR model in which the glow curve shape depends on trap occupancy.

To cover conditions that fall between these two extremes, May and Partridge proposed the General Order Kinetics (GOK) model. This empirical formalism provides a unified expression that includes FO and SO as limiting cases and allows for intermediate or non-integer kinetic orders. The GOK model has therefore become a versatile tool for analyzing experimental glow curves, particularly in natural minerals where idealized conditions are rarely met.

In this thesis, the GOK model will be adopted to perform deconvolutions of the thermoluminescence glow curves of the studied materials. This approach allows the kinetic parameters of the individual peaks to be extracted, providing quantitative insight into the trapping and recombination processes that control the luminescent response of these minerals.

1.2.2.1 One Trap One Recombination center (OTOR) model

A simplified energy-level model describing thermoluminescence emission involves one type of electron trap and one type of hole recombination center. This configuration, known as the One Trap One Recombination center (OTOR) model, is schematically illustrated in Figure 1.5 [27]. During irradiation, traps and recombination centers are filled with electrons and holes, respectively. Upon heating, electrons are thermally released into the conduction band and can either recombine radiatively at recombination centers (emitting luminescence) or fall back into empty traps, a process known as retrapping.

The OTOR model represents the fundamental framework of TL theory, since it incorporates the essential processes that govern luminescence: charge trapping during irradiation, thermal release of carriers, and their subsequent recombination. Despite its simplicity, this model captures the key competition between retrapping and recombination, and provides the basis from which more elaborate kinetic models, such as the first-order, second-order, or general-order formalisms, can be derived. For this reason, OTOR is regarded as the principal reference model for interpreting thermoluminescence kinetics. The dynamics of the described system are governed by three fundamental rates:

- **Excitation rate:**

$$R_{\text{ex}} = ns \exp\left(-\frac{E}{kT}\right) \tag{1.7}$$

- **Retrapping rate:**

$$R_{\text{ret}} = n_c A_n (N - n) \tag{1.8}$$

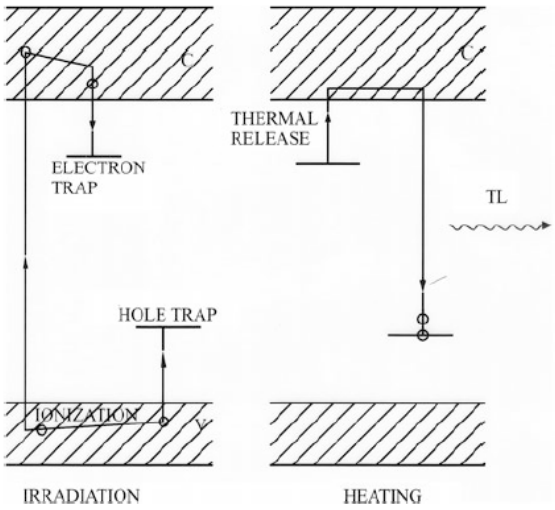

Figure 1.5: Schematic representation of the One Trap One Recombination center (OTOR) model. During irradiation (left), electrons are excited from the valence band to the conduction band and subsequently trapped at electron traps, while holes are captured by hole traps. Upon heating (right), the electrons are thermally released from the traps and may recombine with holes at recombination centers, emitting thermoluminescence (TL). Adapted from [20].

- **Recombination rate:**

$$R_{\text{rec}} = n_c A_h h \tag{1.9}$$

In these expressions, n and N denote the concentration of filled and total active traps, h the concentration of available recombination centers, n_c the concentration of free electrons, and E the trap depth. The coefficients A_n and A_h depend on the respective electron capture cross-sections and the thermal velocity t in the conduction band: $A_n = \sigma_n t$, $A_h = \sigma_h t$.

Assuming quasi-equilibrium conditions, where all free electrons quickly relax either by retrapping or recombination, the fraction F of excited carriers contributing to luminescence is given by:

$$F = \frac{R_{\text{rec}}}{R_{\text{rec}} + R_{\text{ret}}} \tag{1.10}$$

This fraction depends on the competition between retrapping and recombination. In more complex models, additional non-radiative relaxation pathways (e.g., deep trap recapture) would modify the denominator of Equation 1.10, altering the luminescence efficiency.

Before discussing the details of the different kinetic models, it is useful to introduce the main geometrical parameters that describe the shape of a thermoluminescence (TL) glow peak. These quantities, illustrated in Figure 1.6, provide a practical framework for characterizing TL curves and will serve as a reference for a clearer understanding of the theoretical models presented in the following sections.

As shown in the figure, the maximum intensity of the peak is denoted by I_m, while the corresponding temperature is indicated as T_m. The peak width at half of the maximum intensity defines the full width at half maximum (ω),

which is a measure of the overall broadening of the glow peak. The high-temperature half-width (δ) corresponds to the distance between T_m and the point on the descending part of the curve at which the intensity drops to half of I_m. These parameters are not only descriptive but also form the basis for calculating dimensionless factors, such as the shape factor $\mu = \delta/\omega$, which are widely used to distinguish between different kinetic orders of TL processes.

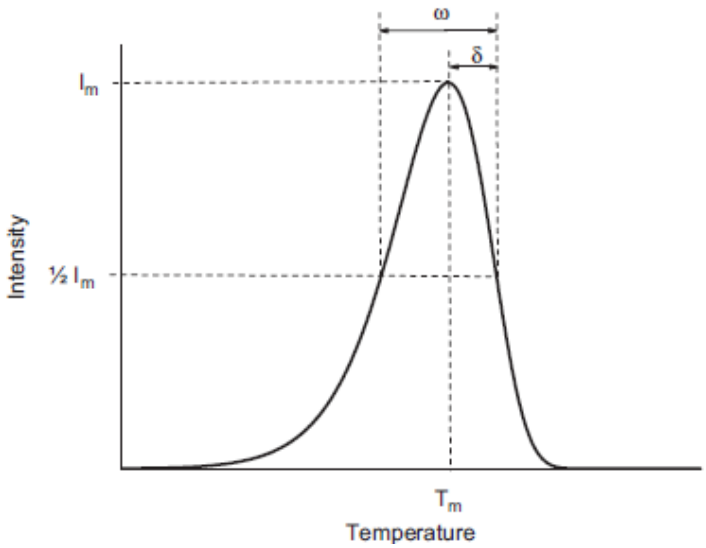

Figure 1.6: Definition of the main parameters used to describe a TL glow peak: I_m is the peak intensity, T_m the temperature at which the peak occurs, ω the full width at half maximum (FWHM), and δ the high-temperature half-width. These quantities are used to calculate geometrical factors such as the shape factor $\mu = \delta/\omega$, commonly employed in kinetic analysis. Adapted from [28].

1.2.2.2 Randal and Wilkins model

The Randall and Wilkins model (RW) represents the simplest case of thermoluminescence (TL) emission, based on the *one trap one recombination center* (OTOR) scheme [27, 29]. The model assumes negligible retrapping, i.e., all thermally released electrons recombine radiatively. Under these conditions, the fraction F of excited carriers that contribute to luminescence is equal to 1, and the TL intensity I is directly proportional to the excitation rate R_{ex}:

$$I = cR_{\text{ex}} = cns \exp\left(-\frac{E}{kT}\right) \tag{1.11}$$

Assuming linear heating with constant rate $\beta = \frac{dT}{dt}$, the trap depopulation follows:

$$\frac{dn}{n} = -\left(\frac{s}{\beta}\right) \exp\left(-\frac{E}{kT}\right) dT \tag{1.12}$$

Integrating this relation yields the time-dependent trap population $n(T)$, which leads to the TL intensity as a function of temperature:

$$I(T) = n_0 s \exp\left(-\frac{E}{kT}\right) \exp\left[-\int_{T_0}^{T} \left(\frac{s}{\beta}\right) \exp\left(-\frac{E}{kT'}\right) dT'\right] \tag{1.13}$$

The glow curve generated by this model exhibits *first-order (FO) kinetics*. The main features and dependencies of the glow curve are:

- **Effect of trap depth E:** As E increases, the peak temperature T_m shifts to higher values. This is due to the greater thermal energy required to release more strongly bound charges. The peak becomes broader and shifts rightward, as shown in Figure 1.7.
- **Effect of frequency factor s:** An increase in s leads to an earlier release of charges, thus lowering T_m and narrowing the peak width ω. This behavior is depicted in Figure 1.8.
- **Effect of heating rate β:** Increasing β causes T_m to shift to higher temperatures and increases the peak height. However, the peak area remains constant if normalized by β, as shown in Figure 1.9.
- **Effect of initial trap filling n_0:** The peak temperature T_m and shape remain unchanged with different values of n_0. Only the peak intensity scales proportionally with n_0, making the model suitable for dosimetric applications where intensity is proportional to radiation dose.

1.2.2.3 Garlick and Gibson model

The Garlick and Gibson (GG) model refines the Randall–Wilkins (RW) approach by including retrapping of electrons [30]. Still based on the OTOR framework, it assumes that upon thermal excitation, the electron can either recombine radiatively at a recombination center or be retrapped in a vacant trap.

The recombination fraction F is:

$$F = \frac{A_h n}{A_h n + A_n (N - n)} \tag{1.14}$$

In the special case $A_h = A_n$, this simplifies to $F = \frac{n}{N}$. Consequently, the TL intensity becomes:

$$I(T) = -\frac{dn}{dt} = \left(\frac{n}{N}\right) n s \exp\left(-\frac{E}{kT}\right) = \frac{n^2}{N} s \exp\left(-\frac{E}{kT}\right) \tag{1.15}$$

Assuming constant heating ($dT/dt = \beta$), the glow curve follows:

$$I(T) = n_0^2 \frac{s}{N} \exp\left(-\frac{E}{kT}\right) \left[1 + \frac{n_0 s}{\beta N} \int_{T_0}^{T} \exp\left(-\frac{E}{kT'}\right) dT'\right]^{-2} \tag{1.16}$$

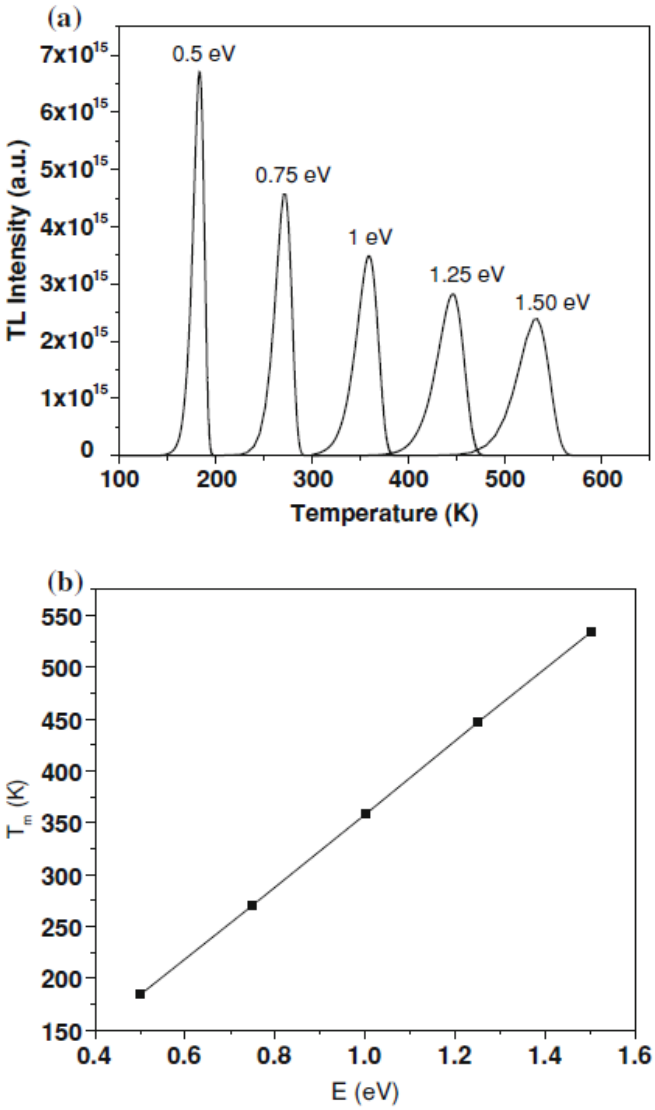

Figure 1.7: Effect of trap depth E on TL glow curve: (a) shift of peak with increasing E; (b) linear relationship between T_m and E. Adapted from [20].

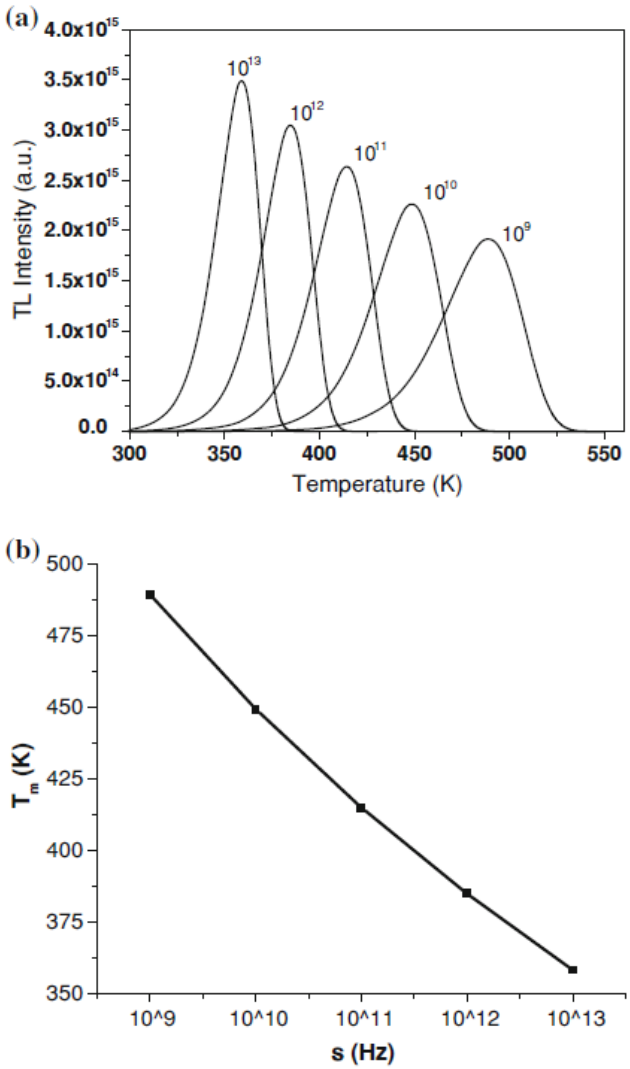

Figure 1.8: Effect of frequency factor s on TL glow curve: (a) shift of peak to lower T with increasing s; (b) logarithmic dependence of T_m on s. Adapted from [20].

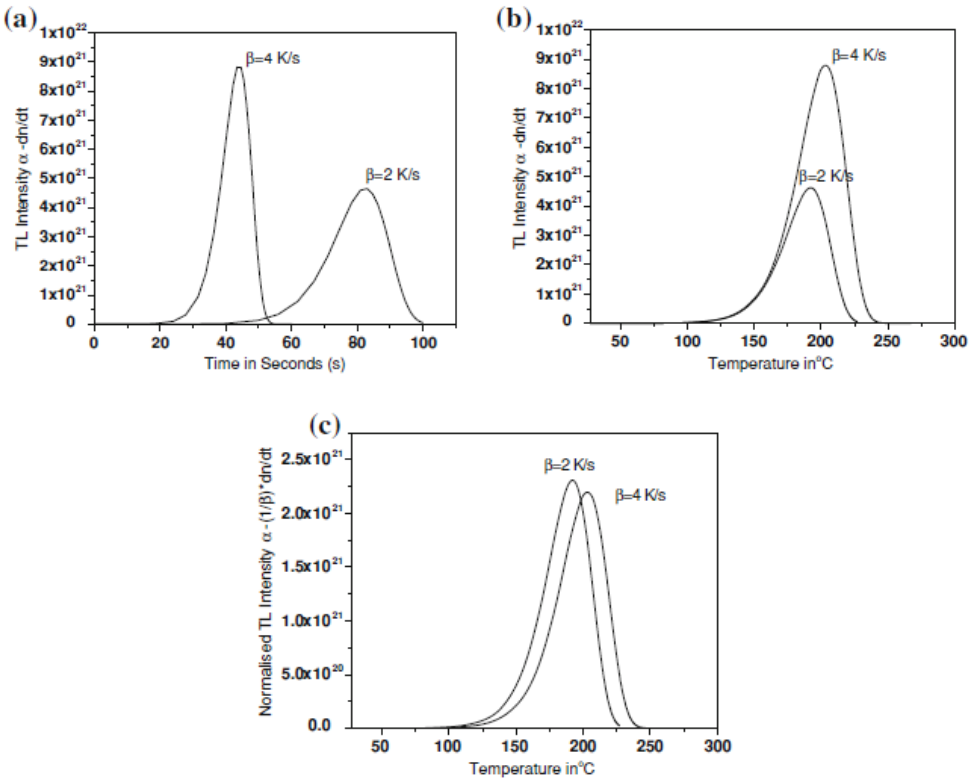

Figure 1.9: Effect of the heating rate β on the shape and intensity of TL glow curves. The figure shows glow curves recorded at $\beta = 2\,\mathrm{K/s}$ and $\beta = 4\,\mathrm{K/s}$ plotted as: (a) TL intensity versus time, (b) TL intensity versus temperature, and (c) normalized TL intensity (I/β) versus temperature. As β increases, the glow peak becomes sharper and shifts to higher temperatures, with a corresponding increase in peak intensity. However, when normalized by β, the area under the curve remains conserved, in agreement with first-order kinetics. Input parameters: $E = 1.1\,\mathrm{eV}$, $s = 10^{11}\,\mathrm{s}^{-1}$, and $n_0 = 10^{23}\,\mathrm{m}^{-3}$. Adapted from [20].

The effect of the initial trap occupancy ratio n_0/N on the shape of the glow curve is illustrated in Figure 1.10. As the relative dose decreases, i.e., for lower n_0/N, the TL peak shifts to higher temperatures and becomes broader, while the peak intensity diminishes. This behavior is characteristic of second-order (SO) kinetics and contrasts with the first-order case, where the peak position and shape remain independent of dose.

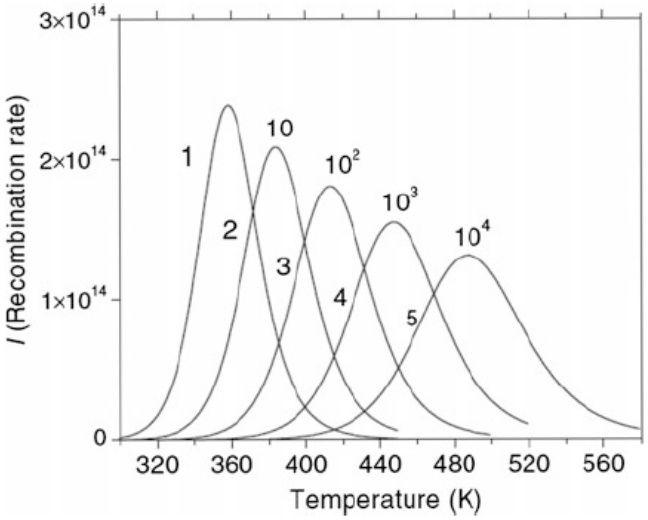

Figure 1.10: Glow curves predicted by the Garlick–Gibson model (second-order kinetics) for different values of the ratio n_0/N. The trap parameters are $E = 1\,\text{eV}$, $s = 10^{12}\,\text{s}^{-1}$, and $\beta = 1\,\text{K}\,\text{s}^{-1}$. Curves 1–5 correspond respectively to $n_0/N = 1, 10^{-1}, 10^{-2}, 10^{-3}, 10^{-4}$, with intensities of curves 2–5 scaled by factors $10, 10^2, 10^3$ and 10^4 for clarity. The figure illustrates the shift of the glow peak to higher temperatures and its progressive broadening as n_0/N decreases. Adapted from [20].

This behavior characterizes *second-order (SO) kinetics* TL. Key effects include:

- The glow peak decays more gradually post-maximum compared to the first-order model.
- For fixed E, s, and β, the peak temperature T_m is slightly higher in SO than in FO, except when traps are saturated ($n_0 \approx N$).
- Reducing the ratio $\frac{n_0}{N}$ (dose lower relative to trap capacity) results in glow peaks that are shifted to higher T_m and become broader; both width and asymmetry increase—a contrast with FO kinetics, where shape is independent of dose.
- Dependencies on E, s, and β qualitatively mirror those in the FO case, such as T_m increasing with E or β.

1.2.2.4 General order kinetic (GOK) model

The General Order (GO) kinetic model, proposed by May and Partridge [31], extends the classical first- and second-order kinetics by introducing a generalized expression for TL intensity that can describe all intermediate cases. The TL intensity is defined as:

$$I = -\frac{dn}{dt} = s' n^b \exp\left(-\frac{E}{kT}\right) \tag{1.17}$$

where s' is an empirical pre-exponential factor and b is the kinetic order. The model reduces to first-order (FO) kinetics for $b = 1$, and to second-order (SO) kinetics for $b = 2$. Intermediate or non-integer values of b describe non-FO/SO behaviors.

Upon solving the differential equation, the TL intensity as a function of temperature becomes:

$$I(T) = s n_0 \left(\frac{n_0}{N}\right)^{b-1} \exp\left(-\frac{E}{kT}\right) \left[\frac{s(b-1)}{\beta}\left(\frac{n_0}{N}\right)^{b-1} \int_{T_0}^{T} \exp\left(-\frac{E}{kT'}\right) dT' + 1\right]^{-\frac{b}{b-1}} \tag{1.18}$$

where N is the total trap concentration, n_0 is the initial trap occupancy, β is the heating rate, and s is the frequency factor.

A more compact formulation of Eq. 1.18 can be obtained by introducing the condition for the temperature of maximum intensity, T_m. At the peak temperature T_m, the condition for maximum intensity is given by $\left(\frac{dI}{dT}\right)_{T_m} = 0$. This condition leads to a relation that links the kinetic parameters E, s, β, and the kinetic order b with the peak maximum temperature T_m.

By combining this relation with the general solution of Eq. 1.18, the TL intensity can be rewritten in a normalized form that depends explicitly on the maximum intensity I_m and peak position T_m. The resulting expression, derived by Kitis et al. [32], is:

$$I(T) = \frac{\frac{I_m\, b}{(b-1)^{b-1}} \exp\left(\frac{E}{kT}\frac{T-T_m}{T_m}\right)}{\left[(b-1)\left(1-\frac{2kT}{E}\right)\left(\frac{T}{T_m}\right)^2 \exp\left(\frac{E}{kT}\frac{T-T_m}{T_m}\right) + 1 + (b-1)\frac{2kT_m}{E}\right]^{\frac{b}{b-1}}} \tag{1.19}$$

Equation 1.19 represents a solution for the general order kinetic model that directly incorporates the peak maximum parameters. This formulation is particularly useful in practical fitting procedures, since the intensity at any temperature can be expressed in terms of measurable quantities such as I_m and T_m, while the shape of the glow curve is controlled by the kinetic order b and the activation energy E.

The evolution of TL glow curves with varying parameters reveals several key trends:

- **Kinetic order b:** As b increases, the glow peaks become broader and shift to higher temperatures. This behavior reflects an increased probability of retrapping, which delays the complete release of trapped charges. The peak shape factor $\mu = \delta/\omega$, already defined in Figure 1.6, increases monotonically with b [20].

- **Trap occupancy n_0/N:** Lower values of n_0/N, corresponding to low dose conditions, result in a shift of the glow peak T_m towards higher temperatures and broader peaks. This shift does not occur in FO kinetics, providing a practical criterion to distinguish FO from non-FO peaks.

- **Pre-exponential factor s':** The parameter s' is not an independent constant but depends on both b and N. It can be related to the standard frequency factor s by the empirical relation [33]:

$$s' = \frac{s}{N^{b-1}} \tag{1.20}$$

which leads to an alternative expression for TL intensity:

$$I = \left(\frac{n}{N}\right)^{b-1} ns \exp\left(-\frac{E}{kT}\right) \tag{1.21}$$

Figure 1.11 illustrates the evolution of glow curves computed for various values of b and n_0/N. A clear trend of peak broadening and shift to higher temperatures is observed as b increases and n_0/N decreases.

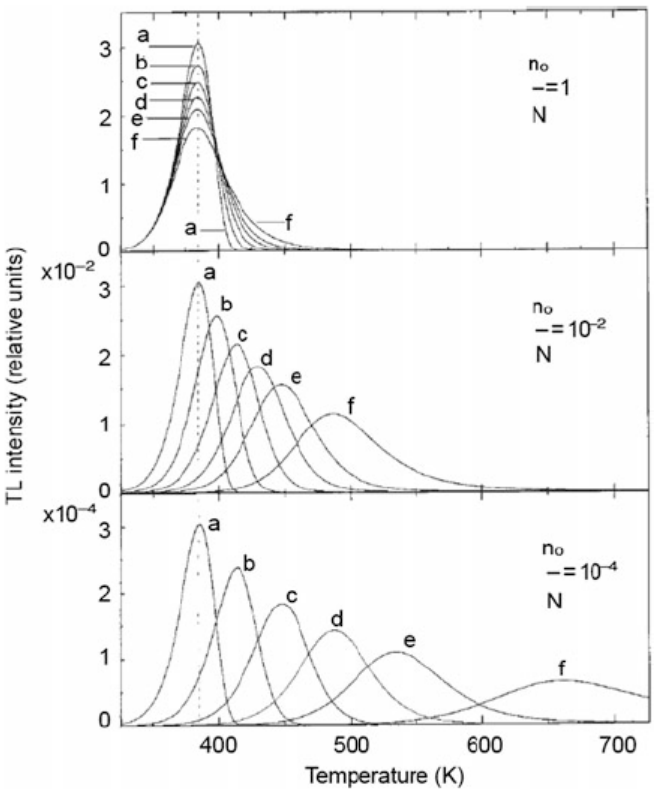

Figure 1.11: Simulated glow curves based on the General Order kinetics model for different values of kinetic order b and trap occupancy n_0/N. Adapted from [20].

The GOK model thus provides a flexible theoretical framework that can accommodate a wide range of TL behaviors, offering a more comprehensive tool for fitting and interpreting experimental glow curves, especially in cases where retrapping plays a significant role.

1.3 Optically Stimulated Luminescence (OSL)

In this thesis, OSL is introduced in direct connection with the single-grain measurements on quartz, which will be described in detail in Chapter 4. Only the essential theoretical concepts are presented, as they provide the basis for interpreting OSL curve shapes and for understanding the principles underlying the SG-OSL dating protocol. The discussion is therefore focused on the key processes of optical stimulation, charge release, and recombination, which together define the theoretical framework required for the subsequent experimental application.

OSL is governed by the same fundamental processes as TL, with the key distinction that the stimulation energy in OSL is provided by photons instead of thermal energy. In practice, the sample is stimulated with light of a specific wavelength, while the luminescence emission is detected at a different, usually shorter, wavelength. Both techniques rely on the presence of trapped charge carriers and their recombination at luminescent centers. However, it is not guaranteed that the same defect centers participate in both processes in a given material [34].

Optical transitions between localized defect levels and delocalized energy bands provide the physical basis for the stimulation of radiation-induced trapped charges, giving rise to OSL. This process occurs when a photon of suitable energy interacts with a trapped charge, promoting it to the conduction band (for electrons) or to a localized level in the valence band (for holes). Once in the delocalized band, the charge may recombine radiatively with an oppositely charged center or be retrapped by an empty defect site. In this way, an OSL signal is generated, whose intensity is proportional to the number of trapped charges available for release under optical stimulation, and to the probability of their recombination at luminescent centers. Under constant stimulation conditions, the OSL intensity thus reflects the progressive depletion of the trap population, linking the signal to the absorbed radiation.

1.3.1 OSL model

Several models have been proposed to describe the luminescence decay curves obtained during OSL measurements, depending on the number and type of traps and recombination centers considered. A comprehensive treatment of these models can be found in Chen and Pagonis [27]. In the framework of this thesis, the analysis is restricted to the simplest case, namely a model with a single electron trap and a single recombination center. The discussion is further limited to the continuous-wave OSL (CW-OSL) stimulation mode, in which the sample is illuminated with light of constant intensity and the luminescence emission is recorded during stimulation [35]. The luminescence signal is observed to decrease progressively with stimulation time as the optically sensitive traps are emptied, until a constant background level is reached. The resulting decay curve constitutes the characteristic CW-OSL signal, which is routinely monitored from the onset of illumination until this background is established.

An example of a typical CW-OSL decay curve is shown in Figure 1.12,

where the exponential decrease of the signal towards a stable background can be clearly observed.

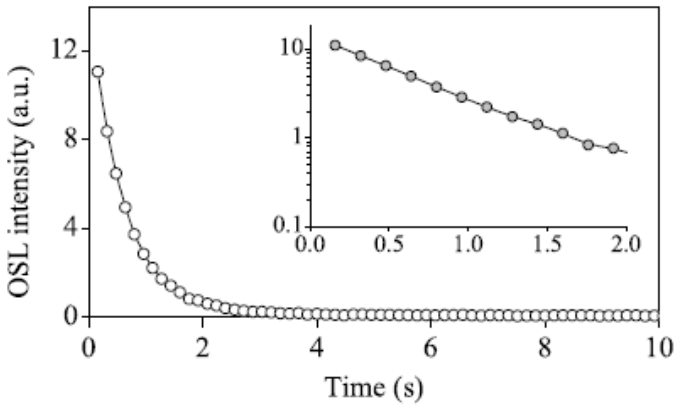

Figure 1.12: Example of a CW-OSL decay curve obtained from a sedimentary quartz sample. The curve shows the characteristic exponential decrease of luminescence intensity as the optically sensitive traps are progressively emptied, until a stable background level is reached. Inset: the same data plotted on a logarithmic scale to highlight the exponential behaviour. Adapted from [12].

1.3.1.1 One trap and one recombination center model

In this model, a single type of electron trap and a single type of radiative recombination center are considered. Upon optical stimulation, electrons are released from traps into the conduction band with probability per unit time:

$$p = \sigma(\lambda)\phi, \tag{1.22}$$

where $\sigma(\lambda)$ is the photoionisation cross-section, which quantifies the probability that a photon of suitable energy will release an electron from its trap, and ϕ is the photon flux of the stimulating light. The photon flux is defined as the number of photons incident per unit area and per unit time (photons $\mathrm{m}^{-2}\,\mathrm{s}^{-1}$). Under CW-OSL conditions, ϕ is assumed to remain constant during the measurement, corresponding to a stimulation at constant light intensity. The value of σ depends strongly on the photon energy and exhibits a threshold behaviour: below a certain energy E_t, photoionisation is not possible, while above the threshold the probability of transition increases with increasing photon energy.

If n denotes the instantaneous population of trapped electrons, the detrapping rate is:

$$\frac{dn}{dt} = -pn. \tag{1.23}$$

The rate at which electrons get trapped (or retrapped) in the trap T is proportional to the concentration of electrons in the conduction band and to the concentration of available trapping sites in the trap, i.e.:

$$\frac{dn}{dt} = p_t n_c (N - n), \tag{1.24}$$

where p_t is the trapping probability, n_c is the concentration of electrons in the conduction band, N is the total concentration of electron traps, and n is the concentration of filled traps.

The recombination rate (i.e., the transition rate of electrons from the conduction band to the recombination center R) is proportional to the concentration of electrons in the conduction band and to the concentration of available holes h in the recombination center, so that:

$$\frac{dh}{dt} = -p_r n_c h, \tag{1.25}$$

where p_r denotes the recombination probability.

The rate equations that describe the traffic of electrons between the conduction band, traps, and recombination centers are therefore:

$$\frac{dn_c}{dt} = -\frac{dn_u}{dt} - \frac{dn}{dt} - \frac{dh}{dt} = pn - p_t n_c(N-n) - p_r n_c h, \tag{1.26}$$

$$\frac{dn}{dt} = -pn + p_t n_c(N-n), \tag{1.27}$$

$$\frac{dh}{dt} = -p_r n_c h, \tag{1.28}$$

where dn_u/dt is the detrapping rate from the trap T under optical stimulation [Eq. 1.23].

If it is assumed that all holes created in the initial ionisation process are trapped in recombination centers, then the following condition holds:

$$n + n_c = h, \tag{1.29}$$

which is the well-known charge neutrality condition.

In this model, the OSL intensity I_{OSL} (photons/s) is equal to the rate at which recombination occurs:

$$I_{\mathrm{OSL}}(t) = -\frac{dh}{dt} = -\frac{dn_c}{dt} - \frac{dn}{dt} \approx -\frac{dn}{dt}, \tag{1.30}$$

where the quasi-equilibrium approximation has been assumed, i.e. $n_c \ll n$ (the concentration of electrons in the conduction band is much smaller than the concentration of trapped electrons), and $|dn_c/dt| \ll |dn/dt|$.

Under these conditions, an approximate expression for the OSL intensity can be derived as:

$$I_{\mathrm{OSL}}(t) \approx pn\left(1 - \frac{p_t(N-n)}{p_r h + p_t(N-n)}\right). \tag{1.31}$$

This expression is referred to as the General One-Trap (GOT) equation for OSL [36].

1.3.1.1.1 CW-OSL decay curve If retrapping is assumed to be negligible, i.e. $p_r h \gg p_t(N-n)$, the General One-Trap (GOT) equation reduces to a first-order differential equation:

$$I_{\mathrm{OSL}}(t) = -\frac{dn}{dt} = pn, \tag{1.32}$$

whose solution yields a simple exponential decay:

$$I_{\mathrm{OSL}}(t) = I_0 \exp\left(-\frac{t}{\tau}\right), \tag{1.33}$$

where I_0 is the initial intensity of the OSL signal at $t = 0$ and τ is the characteristic decay time, given by $(\sigma(\lambda)\phi)^{-1}$ with ϕ the photon flux of the stimulation light.

In real materials, however, the situation is more complex. Natural quartz, for example, typically contains more than one type of optically active trap, each with a different photoionisation cross-section. Since all traps are stimulated simultaneously under CW-OSL conditions, the measured signal is not described by a single exponential but can be represented as a sum of exponentials:

$$I_{\mathrm{OSL}}(t) = \sum_{i=1}^{m} I_{0i} \exp\left(-\frac{t}{\tau_i}\right), \tag{1.34}$$

where m is the number of distinct trap populations, each associated with a characteristic lifetime τ_i and initial intensity I_{0i}.

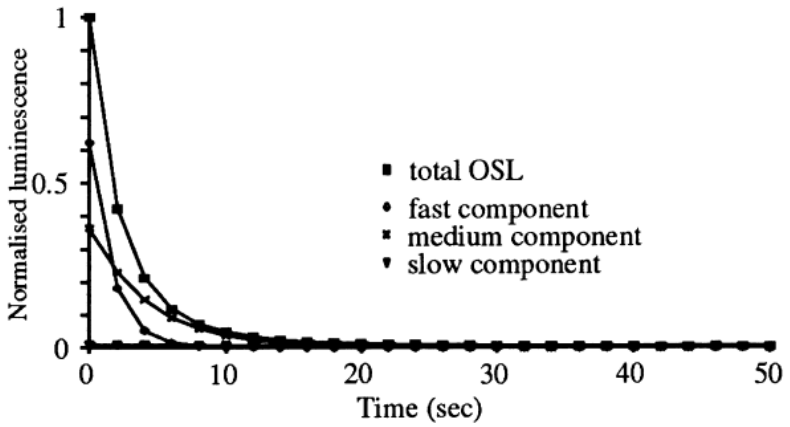

Figure 1.13: Decomposition of a CW-OSL decay curve from quartz into exponential components. The fast component dominates the early part of the decay and corresponds to easy-to-bleach traps, while medium and slow components represent progressively harder-to-bleach traps that may retain residual charges even after prolonged stimulation. Adapted from [37].

Traps associated with the *fast component* are generally referred to as *easy to bleach*, because they are emptied rapidly upon optical stimulation and are most likely to be completely reset during exposure to daylight. These traps dominate the initial part of the OSL decay and provide the most reliable dosimetric information. Conversely, *slow components* correspond to *hard to bleach* traps,

which release charge only gradually and may retain a residual signal even after extended stimulation. This residual must be carefully accounted for, since it can bias equivalent dose determinations. An intermediate *medium component* is also often observed, with properties between the two extremes.

Although the multi-exponential formalism provides a practical description of CW-OSL curves, it relies on the assumption of negligible retrapping. When retrapping is significant, the decay becomes slower than exponential and higher-order kinetics must be invoked. Moreover, the presence of optically inactive traps ($\sigma = 0$) introduces additional competition, further modifying the decay shape [34].

1.4 Quartz as a natural dosimeter

In the framework of the present thesis, one of the main materials under investigation is quartz, which is widely recognised as one of the most important natural dosimeters in luminescence dating [38]. Like a few other minerals, quartz has the ability to record the amount of ionising radiation to which it has been exposed, storing it as a latent signal within its crystal lattice. For this latent signal to be useful as a dosimeter, it must be reset by specific environmental events, such as exposure to daylight, or heating, thereby defining a reproducible zeroing point. Once reset, quartz begins to accumulate a new luminescence signal, which provides a measurable record of the subsequent radiation history of the material [39].

The latent signal stored in quartz can be accessed through different techniques, among which TL and OSL have gained particular relevance. These two approaches are complementary and represent the most widely employed techniques for quartz in archaeological applications, providing powerful and versatile tools for reconstructing the chronology of archaeological contexts and historical buildings.

For this reason, the following sections present in detail the TL and OSL properties of quartz, which form the theoretical basis for their application in the dating of historical mortars investigated in this thesis.

1.4.1 TL properties of quartz

TL in quartz arises from the release of trapped electrons upon heating, followed by recombination at specific luminescence centres. As already introduced before, two main physical parameters governing the TL signal are the depth of the traps and the energy of the emitted photons. The trap depth defines the temperature at which a peak appears in the TL glow curve, while the emission energy depends on the type of recombination centre involved.

TL peaks in quartz are commonly observed at approximately 110°C, 202°C, 325°C, and 375°C, for a heating rate of 5°C/s [40, 41, 42]. The position of these peaks is controlled primarily by the depth of the associated trap and by the frequency factor. However, peak positions can vary due to different heating rates or signal interference from adjacent peaks. Notably, low-temperature peaks are generally unstable over time and are usually observed only in artificially irradiated samples.

The spectral emission of TL in quartz spans a wide range of wavelengths. Three major emission bands are reported [43, 38]:

- **Near UV-Violet band** (360–440 nm): The TL emission between 360 and 440 nm in quartz is likely associated with a $(H_3O_4)^0$ centre linked to a silicon vacancy and is commonly observed around 380 nm, near the 110°C TL peak. This emission displays first-order kinetics. Additional emissions in this spectral range are found at higher temperatures, in particular at 325°C, with corresponding wavelengths up to 430 nm.

- **Blue band** (around 482 nm): this emission is commonly observed in the TL signal near 375°C. It is likely associated with the $(AlO_4)^0$ centre substituting for Si, although other defects may contribute.

  The emission band is relatively broad in both temperature and wavelength, with asymmetry extending toward lower temperatures and higher photon energies. Secondary peaks with similar spectral features have also been reported at around 260–280°C and above 450°C.

- **Red-orange band** (600–650 nm): this emission typically appears near 320°C in natural TL signals. There is no clear link between this emission and a particular type of defect. It shows a broad and intense luminescence emission bands. After laboratory irradiation, TL peaks are observed at progressively increasing temperatures with corresponding shifts in photon energy from 1.90 eV (650 nm) to 2.00 eV (620 nm).

For dating purposes, the TL peaks of quartz centred at approximately 325 °C and 375 °C are regarded as the most reliable, since they exhibit sufficient thermal stability over geological timescales [38].

Spectral studies have shown that the emission profile of quartz can vary depending on its geological origin. For instance, quartz of volcanic origin tends to emit in the red, while granitic or metamorphic quartz shows stronger blue or violet emission.

A synthetic overview of thermoluminescence emission bands in quartz is presented in Figure 1.14, adapted from [43]. The diagram summarizes the main TL emission wavelengths as a function of glow peak temperature. It distinguishes between emissions observed in natural samples, artificially irradiated ones, and those not consistently present in all quartz types. Most emissions fall within the violet (360–400 nm), blue (460–500 nm), and red-orange (600–650 nm) spectral regions, and are associated with glow peaks from 100°C to 400°C.

To complement this summary, Figure 1.15 shows a three-dimensional TL emission surface obtained from a natural quartz sample. It displays the intensity of TL as a function of both temperature and emission wavelength. The plot highlights the presence of multiple broad emission bands and reveals the complex nature of TL in quartz, including overlapping peaks and spectral shifts that occur as temperature increases. This type of representation provides valuable insight into the evolution of emission centres and their thermal behaviour.

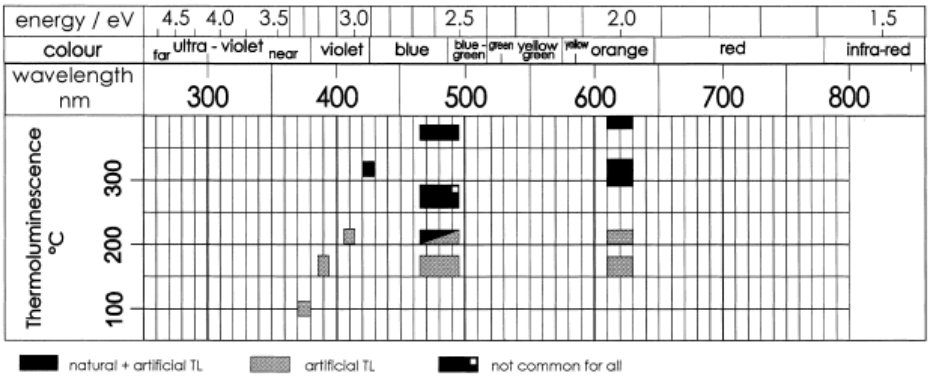

Figure 1.14: Summary of major TL emission bands in quartz as a function of glow peak temperature. The diagram indicates the spectral position and occurrence (natural, artificial, or variable) of each emission band [43].

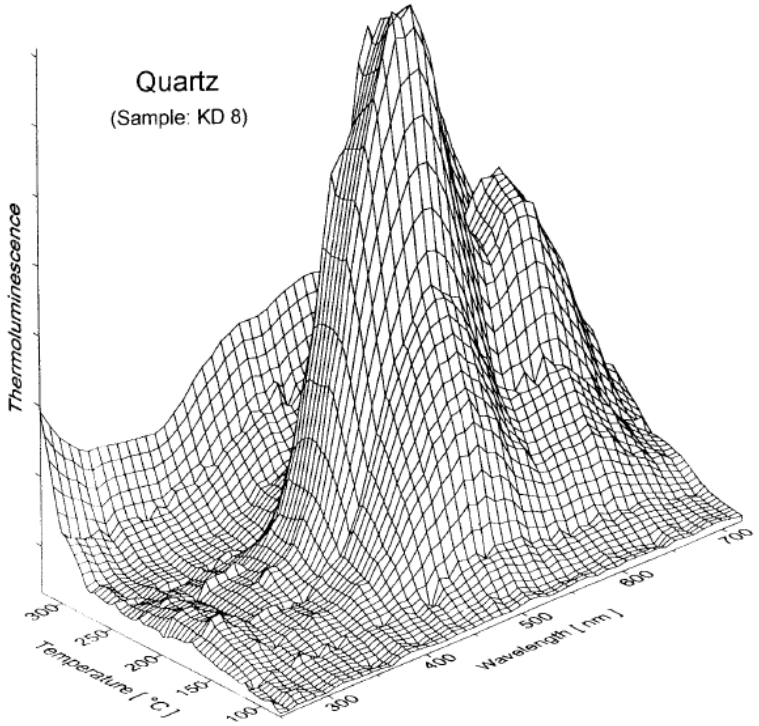

Figure 1.15: Three-dimensional TL emission surface for a natural quartz sample, showing TL intensity as a function of temperature and emission wavelength. Peaks in the blue and red-orange regions are evident [43].

1.4.2 OSL emission properties in quartz

The optically stimulated luminescence (OSL) emission in quartz is typically detected in the near-UV region, with a dominant peak at around 365–380 nm. This band has been reported using different stimulation sources, including blue LEDs with a peak emission at 470 nm and Nd:YVO4 solid state diode-pumped laser emitting at 532 nm [44, 45].

Although quartz is extensively used in luminescence dating, relatively few studies have investigated its optical stimulation spectrum in detail. Notably, [46] and [47] systematically measured the OSL stimulation response of sedimentary quartz over a photon energy range of 1.9 to 2.9 eV, corresponding

approximately to wavelengths from 650 to 430 nm. Their results indicate that the stimulation efficiency increases exponentially with photon energy, thereby confirming the effectiveness of using blue light (around 470–480 nm) for OSL stimulation in practical dating applications.

Spectrally resolved OSL emissions are less complex than TL, with quartz generally exhibiting only a single emission band near 365 nm. This simplicity supports its application in dating protocols. However, the presence of feldspar inclusions (which can emit at longer wavelengths) must be carefully excluded.

The OSL curve from quartz is usually said to be composed of three exponential components: a fast, medium, and slow component, with characteristic lifetimes of approximately 0.4 s, 10 s, and 150 s, respectively. These components reflect the presence of multiple optically active traps with different detrapping probabilities, contributing simultaneously to the measured signal.

Figure 1.16 shows a continuous-wave optically stimulated luminescence (CW-OSL) decay curve obtained from a sedimentary quartz sample. Stimulation was performed using blue LEDs with a central wavelength around 470–480 nm, and the luminescence was detected using 7.5 mm Hoya U-340 filters, which efficiently transmit the near-UV emission around 365 nm while blocking the stimulation light [48].

The curve exhibits the typical rapid initial decrease in intensity, characteristic of the fast OSL component in quartz. This behaviour is commonly interpreted as the dominance of a single kinetic component (fast component), which is particularly suitable for dating applications due to its high reset efficiency and reproducibility.

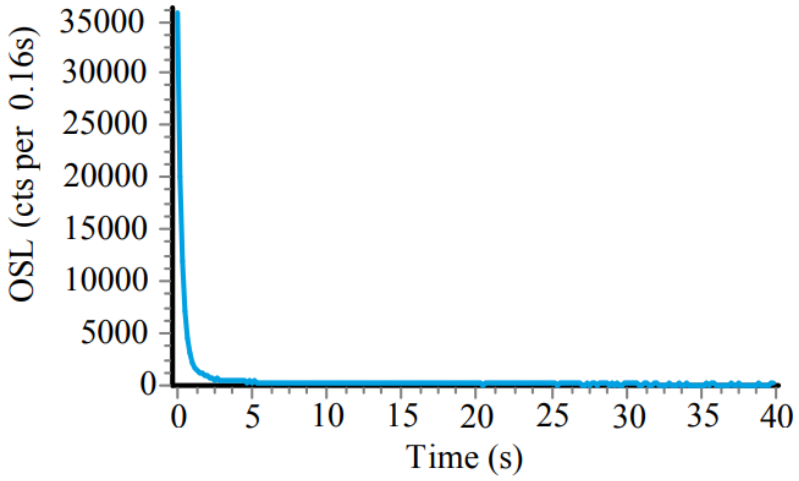

Figure 1.16: CW-OSL decay curve obtained from a sedimentary quartz sample. The sample was stimulated using blue LEDs and the luminescence detected through 7.5 mm Hoya U-340 filters. Adapted from [48].

1.5 Carbonates as a natural dosimeter

Calcium carbonate ($CaCO_3$) is a chemical compound that naturally occurs in several crystalline forms, known as polymorphs. The three main polymorphs of $CaCO_3$ are calcite, aragonite, and vaterite. Among these, *calcite* is the most

thermodynamically stable form under ambient temperature and pressure conditions. Therefore, while calcium carbonate refers to the chemical composition, *calcite* specifically designates the mineral phase in which $CaCO_3$ crystallises in the trigonal system.

In addition to quartz, which is the most widely employed natural dosimeter in luminescence dating, early studies have shown that calcium carbonate may also exhibit luminescence properties that make it suitable for dosimetric purposes [49]. Under appropriate conditions of impurity content and structural order, calcite can store a latent luminescence signal generated by exposure to ionising radiation, in a manner analogous to quartz. Although its dosimetric behaviour has been less extensively investigated, these findings indicate that carbonate materials may provide valuable chronological information, particularly in archaeological contexts where they represent a major component of historical mortars.

In the framework of this thesis, calcite will be extensively considered as one of the main materials under investigation, with particular emphasis on its role in the experimental tests. Although its luminescence behaviour has been less explored than that of quartz, calcite could represents a valuable candidate for dosimetric applications in archaeology, especially given its widespread occurrence in historical mortars as part of the binder. A detailed discussion of the experimental procedures and results involving calcite will be presented in Chapter 3. In order to provide the necessary background for these applications, the following section outlines the main characteristics of the TL signal in calcite, which are essential for assessing its potential as a dosimetric material.

1.5.1 Thermoluminescence properties of calcite

In calcite, TL peaks are commonly observed around 285°C and 350°C when using a heating rate of 5°C/s [50, 51]. The relative intensity and stability of these peaks vary depending on sample type, grain size and impurity content.

The 285°C TL peak is generally associated with Mn^{2+} ions substituting for Ca^{2+} in the lattice, which act as efficient luminescence centres and produce a characteristic orange-red emission around 620–650 nm [43, 52]. The efficiency of Mn^{2+} emission can be enhanced by sensitiser ions (e.g. Pb^{2+}) or quenched by the presence of Fe^{2+} and organic matter.

A representative TL emission surface for natural calcite is shown in Figure 1.17, which illustrates the intensity of the emitted light as a function of both temperature and wavelength. The dominant orange-red emission band near 620–650 nm is clearly visible, along with weaker components in the blue-green region. This figure highlights the spectral complexity and temperature dependence of TL in calcite [43].

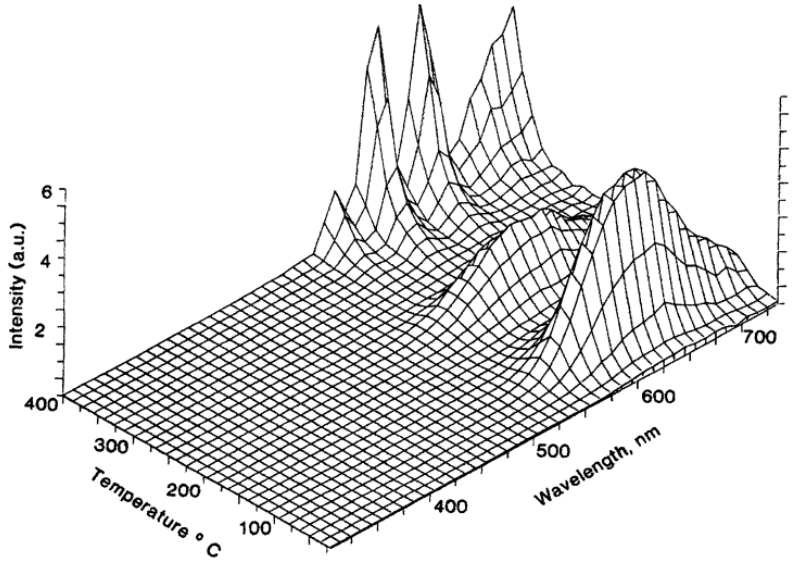

Figure 1.17: Three-dimensional TL emission surface of natural calcite, showing luminescence intensity as a function of temperature and emission wavelength. The strong orange-red band near 620–650 nm is attributed to Mn^{2+} centres. Adapted from [43].

2 Luminescence dating applied on historical buildings

Following the theoretical framework outlined in Chapter 1, this chapter presents a comprehensive overview of the methodological principles underlying luminescence dating, with specific emphasis on its application to historical mortars. The aim is to provide the conceptual and analytical basis required to interpret the experimental work developed in the following chapters.

The chapter begins with a review of the main applications of TL and OSL to built cultural heritage, tracing the evolution of the method and highlighting the current limitations that still prevent its routine use. This overview provides the basis for the objectives of this thesis, which focuses on addressing some of these limitations by developing a novel luminescence dating protocol.

The discussion then focuses on the luminescence age equation and its two fundamental components: the equivalent dose (D_e) and the annual dose rate ($\dot{D}_R$). Particular attention is given to the procedures for estimating D_e, including regenerative protocols, the Single-Aliquot Regenerative-dose (SAR) method. The statistical treatment of D_e distributions is also introduced, with reference to models commonly used to interpret heterogeneous or partially bleached samples.

The second part of the chapter deals with the evaluation of the annual dose rate. The contributions of α, β, γ, and cosmic radiation are described. The implications of radioactive disequilibrium in the U and Th decay chains are discussed, together with their potential impact on dose rate estimates. Finally, the main experimental approaches are outlined, including low-background gamma spectrometry for laboratory measurements of radionuclide concentrations and *in situ* dosimetry for field determination of environmental and cosmic dose rates.

By integrating these aspects, this chapter establishes the methodological framework required for the application of luminescence dating to mortars. This framework is then translated into practice in the following two chapters, which constitute the experimental core of this thesis and are devoted respectively to a methodological study on reference materials (Chapter 3) and to a case study on archaeological mortars (Chapter 4).

2.1 Conditions for the applicability of luminescence dating

As discussed in the Introduction, luminescence dating techniques rely on the capacity of natural minerals to accumulate and store the effects of ionising radiation over time, and to release this information in the form of light when appropriately stimulated. However, for this accumulation process to be chronologically meaningful and reproducible, a series of specific conditions must be met. These conditions for applicability, based on the physical mechanisms described in Chapter 1, serve to ensure that the measured luminescence signal corresponds to the time elapsed since a well-defined resetting event.

In practical terms, these conditions can be divided into three main categories: (1) material-related requirements, which concern the intrinsic properties of the dosimetric phase; (2) signal-related criteria, which refer to the behaviour of the luminescence signal in response to the amount of radiation absorbed over time (i.e., the dose); and (3) context-specific factors, which involve the depositional or structural environment in which the material was placed. In the following, these three aspects are addressed in detail.

- *Presence of a stable and sensitive dosimetric phase (material-related):* The material must contain minerals able to trap charge carriers over timescales relevant to archaeological or historical dating. Quartz is generally preferred for its thermal stability and well-characterised luminescence properties, while feldspar and carbonates may also be used under specific conditions.

- *Predictable dose–response behaviour (signal-related):* The luminescence intensity should increase in a quantifiable way with the absorbed radiation dose, allowing for the construction of a dose–response curve. Ideally, this relationship should be linear or well-approximated by a known saturating function, ensuring the accuracy of dose interpolation in the laboratory.

- *Existence of a clearly identifiable zeroing event (signal-related):* The last exposure to light (for OSL) or heat (for TL) must correspond temporally to the event that is intended to be dated, such as the construction of a wall or the firing of a ceramic. The zeroing must be complete and uniform across the grains being analysed; otherwise, residual signals may lead to age overestimation.

- *Integrity of the trapped charge population (signal-related):* The absence of any later disturbance (thermal, optical, or mechanical) that could result in partial signal loss is essential. For example, even short-term exposure to daylight during sampling or handling can affect the reliability of the OSL signal, particularly for shallow traps.

- *Chronological relevance of the reset event (signal-related):* The event that resets the luminescence signal must coincide with the archaeological event of interest. If, for instance, the exposure to light occurred during a

secondary use or alteration of the material, the resulting age will reflect that later episode rather than the original construction.

- *Environmental stability post-resetting (context-specific):* After the signal has been reset, the environmental conditions surrounding the sample must remain sufficiently stable over time to ensure a constant radiation exposure throughout the post-depositional period. Temporal variations in factors such as moisture content or radionuclide mobility can alter the rate at which dose is accumulated, thus compromising the reliability of the dating result.

- *Favourable dosimetric context (context-specific):* In addition to temporal stability, the spatial characteristics of the sample's environment must allow for a uniform exposure to environmental radiation. The surrounding radiation field should be sufficiently homogeneous, without localised hot spots or shielding heterogeneities, to ensure that the dose received by the sample is representative and accurately quantifiable.

The applicability conditions outlined above define the physical and contextual requirements necessary for interpreting the luminescence signal in chronological terms. When these conditions are fulfilled, the signal accumulated by the dosimetric material becomes a measurable physical quantity that correlates with the time elapsed since the last effective zeroing event. In this framework, the age of the sample can be estimated by establishing a quantitative relationship between the accumulated dose and the rate at which ionising radiation has been absorbed over time. This relationship is expressed by the luminescence dating equation, introduced in the following section.

2.2 Age equation

Luminescence dating is based on the principle that minerals accumulate a measurable signal during burial as a result of their exposure to ionising radiation. When the necessary conditions are satisfied, this signal can be quantitatively related to the time elapsed since the last effective zeroing event.

The total radiation absorbed by the sample since that event is referred to as the *palaeodose*. In practice, this quantity is determined indirectly: the natural luminescence signal is compared with signals induced by controlled laboratory irradiations, and the laboratory dose that reproduces the natural response is defined as the *equivalent dose* (D_e). The equivalent dose, expressed in grays (Gy), therefore quantifies the cumulative energy stored in the crystal lattice of the dosimetric material since its last reset [39].

The age of a sample is obtained by combining D_e with the *annual dose rate* $\dot{D}_R$, which represents the amount of energy absorbed per unit mass per year from the decay of natural radionuclides (^{238}U, ^{235}U, ^{232}Th, ^{40}K and ^{87}Rb) and from cosmic rays. The relationship is expressed by the fundamental luminescence dating equation:

$$\text{Age (years)} = \frac{D_e\,(\text{Gy})}{\dot{D}_R\,(\text{Gy/year})} \tag{2.1}$$

The physical mechanisms that give rise to the luminescence signal, namely charge trapping and recombination, have already been discussed in Chapter 1. The methodological aspects related to the experimental determination of both D_e and the $\dot{D}_{\mathrm{R}}$ will be addressed later in this Chapter.

Figure 2.1 schematically illustrates the accumulation and resetting of the luminescence signal: during burial, irradiation leads to a progressive increase in trapped charge carriers, which produce a measurable signal upon stimulation; exposure to light or heat resets the system, returning the signal to zero.

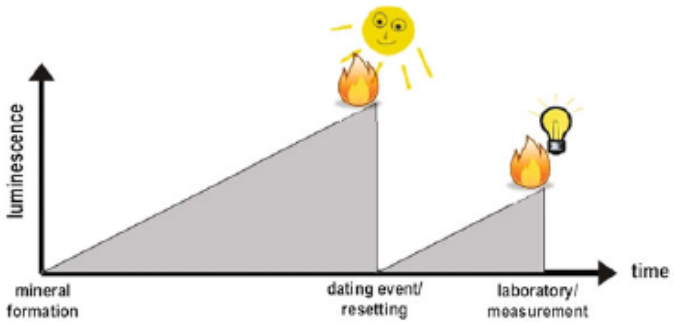

Figure 2.1: Schematic representation of the luminescence signal growth and resetting process. After mineral formation, ionising radiation leads to the accumulation of trapped charges, producing a luminescence signal. A resetting event, such as exposure to light or heat, brings the signal back to zero. From that point onward, the signal accumulates again until it is measured in the laboratory. Adapted from [53].

2.3 Luminescence dating of historical buildings

Having established the physical framework of luminescence dating, with the equivalent dose and the annual dose rate as the two key components of the age equation, the next step is to examine how these components can be determined in practice. The following sections focus on the dating of historical buildings, where luminescence techniques have been employed to identify construction phases through the direct analysis of masonry materials. Key studies based on TL and OSL are reviewed, outlining the main methodological advances and current challenges. Particular attention is given to the determination of the equivalent dose (D_e), which represents not only a crucial parameter for the application of the age equation but also the central physical quantity investigated in this thesis.

2.3.1 Thermoluminescence dating of bricks

Fired bricks and other ceramic structural components are well suited for TL dating because, during their manufacture, they undergo high-temperature treatment that resets the luminescence signal accumulated from natural environmental radiation. The temperatures reached during firing are typically sufficient to empty the electron traps in the crystal lattice of dosimetric minerals such as quartz and feldspar embedded in the clay matrix [2, 3]. This thermal resetting defines the *zeroing event*, which marks the starting point for signal accumulation.

Once removed from the kiln and incorporated into a structure, the bricks are exposed to environmental ionising radiation, and the luminescence signal begins to accumulate progressively. The age determined through TL measurements corresponds to the time elapsed since the last firing, under the assumption that no subsequent events have altered the trapped charge population.

In historical masonry, bricks are commonly available, compositionally homogeneous, and often well shielded from external environmental changes. These features enhance the reliability of TL-based age determinations [4]. When proper dosimetric reconstruction and calibration protocols are applied, uncertainties as low as 5–10% can be achieved.

Several limitations must nevertheless be considered. Accidental heating events, such as those caused by fires, may induce a partial or complete reset of the signal and lead to underestimation of the age [5]. Architectural alterations may also change the local radiation field, introducing uncertainties in the dose rate determination. In addition, bricks are frequently reused in later construction phases, which means that the TL age reflects the firing date rather than the time of incorporation into the new structure [6].

These limitations have led to increasing interest in alternative luminescence methods. OSL, in particular, has been proposed for dating materials such as mortars, where the last exposure to light may coincide more directly with the construction event.

2.3.2 Optically stimulated luminescence dating of mortars

In recent decades, OSL dating has been increasingly employed for the investigation of historical building mortars. These materials were typically produced using lime as the main binder, occasionally mixed with pozzolanic additives to improve their hydraulic behaviour, and more rarely with gypsum-based compositions. As a result, lime-based mortars represent the most widespread type in European and, particularly, Mediterranean masonry traditions [8, 9].

The relevance of these mortars for luminescence dating lies in their preparation process, during which the sandy aggregates containing quartz grains are repeatedly exposed to daylight through activities such as quarrying, transport, mixing, and placement. Exposure to full sunlight for only a few seconds is sufficient to induce a substantial reduction of the OSL signal in quartz, showing that even very short light exposures may effectively bleach the signal and reset the luminescence clock [54]. The final exposure to sunlight, which typically occurs immediately before the mortar sets within the masonry, defines the zeroing event. Once the material is shielded from light, the quartz grains begin to accumulate a new luminescence signal as a result of continuous exposure to environmental ionising radiation. The OSL age thus corresponds to the time elapsed since the last daylight exposure and is directly linked to the construction phase.

The feasibility of applying OSL to mortars was first demonstrated in the early 2000s. Bøtter-Jensen et al. [55] used quartz grains from mortars as dosimetric material, followed by successful applications on Byzantine mortars by Zacharias et al. [56]. Subsequent studies confirmed the method's applica-

bility to different architectural contexts, showing that coarser quartz grains tend to be better bleached and yield more accurate ages [57, 58]. Gueli et al. [59] and Stella et al. [60, 61] applied a multigrain fine-grain approach to medieval mortars and obtained OSL ages consistent with TL results from associated bricks. In this context, an aliquot refers to a portion of the studied material mounted on a metallic disc used in the luminescence reader and measured as a single unit. In conventional multigrain measurements, each aliquot typically contains thousands of grains, producing an averaged luminescence signal [1, 44, 12]. With the subsequent development of the Single-Aliquot Regenerative-dose (SAR) protocol (please refer to Section 2.4.2), it became possible to reduce the number of grains per aliquot and to analyse smaller fractions. These so-called small aliquots, usually containing a few tens to a few hundred grains, reduce averaging effects and provide greater sensitivity to the variability among individual grains [62, 63, 64, 12].

While the use of smaller aliquots represented a methodological advance, multigrain approaches could still mask the variability between grains and the presence of residual signals from incompletely bleached grains. Goedicke [7] therefore highlighted the importance of assessing the degree of bleaching and recommended the use of small aliquots or even single-grain measurements when bleaching is incomplete. The issue of incomplete bleaching is one of the main challenges in OSL dating of mortars. Although the OSL signal in quartz can be rapidly reset under ideal sunlight exposure, with a reduction of about 50% after only a few seconds of full sunlight [54], this does not necessarily ensure full resetting at the moment of mortar setting. Inadequate exposure, low light intensity, or filtered spectra may prevent complete zeroing [65, 11], leading to residual luminescence signals in some grains. Such incompletely zeroed samples are referred to as partially or poorly bleached. If not identified, these residual signals may cause an overestimation of the equivalent dose and thus of the calculated age [10, 66, 62, 63].

A useful indicator of incomplete bleaching is the scatter observed in the distribution of individual D_e values. Several studies have shown that partially bleached samples exhibit significant dispersion in their equivalent dose distributions [10, 67, 68, 69, 70]. However, large multigrain aliquots, consisting of thousands of grains, often average out grain-to-grain variability, potentially masking the presence of residual doses. Reducing the number of grains per aliquot to a few hundred (small aliquots) or even down to individual grains (SG-OSL) increases the probability of detecting poorly bleached components [12, 10, 11]. In this way, the best-bleached grains at the time of burial are more likely to be isolated, yielding equivalent doses that better reflect the true burial dose.

To describe the probability of selecting poorly bleached grains within an aliquot, Olley et al. [71] introduced a probabilistic model based on the binomial distribution. In this framework, the number of poorly bleached grains K in an aliquot of size n is treated as a binomial random variable with probability p that a given grain is poorly bleached, i.e. $K \sim \text{Binomial}(n, p)$. The probability of observing exactly k poorly bleached grains is

$$\Pr(K = k) = \binom{n}{k} p^k (1-p)^{n-k}. \tag{2.2}$$

In the special case $k = 0$, the probability that an aliquot contains only well-bleached grains is

$$\Pr(K = 0) = (1-p)^n. \tag{2.3}$$

This probability decreases monotonically with increasing p, and decreases exponentially with increasing n. For example, with $p = 0.045$ and $n = 100$, one obtains $\Pr(K = 0) = 0.955^{100} \approx 0.010$, i.e. about 1.0%. Increasing n to 101 lowers this probability below 1%. Therefore, the use of small aliquots or single-grain measurements increases the likelihood of isolating well-bleached grains, thereby enhancing the reliability of equivalent dose estimation in partially bleached or heterogeneous samples.

A practical way to implement this approach is through SG-OSL, where individual quartz grains are hand-picked and measured independently, each providing its own equivalent dose estimate. This method represents the natural extension of the progressive reduction in aliquot size, from thousands of grains in conventional multigrain measurements, to hundreds in small aliquots, and finally to individual grains [12]. The development of dedicated single-grain systems further enabled this advance [72, 73]. By isolating the luminescence response of each grain, SG-OSL provides a means of identifying the well-bleached subpopulation already discussed in relation to partial bleaching and improves the accuracy of age estimates in challenging cases of heterogeneous bleaching.

The first applications of SG-OSL to mortars emerged from accidental dosimetry studies and focused on modern materials [58, 74]. These works showed that multigrain aliquots tend to overestimate the dose due to averaging effects and demonstrated the advantage of single-grain measurements. Goedicke [7] concluded that SG-OSL is the only reliable technique when bleaching is extremely limited.

Recent archaeological applications have further confirmed the potential of SG-OSL. Urbanová et al. [75, 13, 76] successfully dated mortars from various historic sites, obtaining reliable results despite low grain sensitivity and significant dose dispersion. Panzeri et al. [14] combined SG-OSL and TL to date mortars and bricks from the UNESCO site of Modena, reporting consistent ages.

Despite its advantages, SG-OSL requires sensitive instrumentation and involves long measurement procedures, since each grain must undergo multiple SAR cycles of irradiation, stimulation, and readout.

Such high dispersion in D_e values requires appropriate statistical treatment. In this context, models such as the Central Age Model (CAM) and the Minimum Age Model (MAM) are commonly employed [77]. CAM assumes that most grains were effectively bleached and estimates the central tendency of the distribution. MAM, instead, isolates the component related to well-bleached grains and is preferred in cases of incomplete resetting. These statistical approaches are especially relevant when dating historical mortars, where heterogeneous bleaching conditions are frequently encountered. A detailed discussion of CAM and MAM is presented in Section 2.4.3.

2.3.3 A potential new approach to historical building dating

A potential experimental pathway in luminescence dating targets the carbonate fraction of historical lime mortars, namely the calcium carbonate that precipitates *in situ* during binder carbonation after placement. Because this phase forms within the wall fabric, it may provide a direct chronological link to the construction event and thus represents a promising dosimetric target for luminescence dating.

Lime mortars are produced through the *lime cycle*, a sequence of transformations illustrated in Figure 2.2, which begins with the calcination of geological limestone ($CaCO_3$) at temperatures above 800 °C. Calcination decomposes $CaCO_3$ into quicklime (CaO), releasing CO_2. In traditional mortar production, the quicklime (CaO) was often mixed directly with aggregates before or during hydration, a process known as hot mixing. During hydration, CaO reacts with water to form portlandite or hydrated lime ($Ca(OH)_2$) within the mixture. After application to masonry, the mortar progressively hardens through carbonation, as $Ca(OH)_2$ reacts with atmospheric CO_2 and reprecipitates as a new calcium carbonate phase within the wall fabric.

The $CaCO_3$ formed during carbonation is therefore a newly created phase, distinct from the geological carbonate originally used in calcination. This distinction has direct implications for luminescence dating: calcination destroys the initial carbonate structure, eliminating any pre-existing trapped-charge signal, while carbonation defines the onset of a new luminescence clock in the binder. In parallel, the aggregate fraction may be exposed to daylight during quarrying, transport, and mixing, providing the basis for conventional OSL and TL dating.

Historically, lime mortars were often prepared with aggregate-to-binder ratios close to 3:1 [61, 78, 79]. Aggregates, predominantly composed of quartz and feldspar, constitute the traditional dosimetric minerals for luminescence dating, whereas the carbonate-rich binder, despite its potential as a direct chronological marker of mortar setting, has so far received comparatively little attention.

The sequence illustrated in Figure 2.2 thus tracks the transformation from geological limestone to quicklime, to hydrated lime, and finally to the newly precipitated carbonate binder within the wall. In this thesis, particular emphasis is placed on investigating the luminescence properties of this carbonate fraction in order to evaluate its potential as a direct chronological marker of mortar setting, complementing the information traditionally derived from quartz-based luminescence dating.

A key point for chronological interpretation is that the $CaCO_3$ produced by carbonation is not the original geological $CaCO_3$ used at the start of the cycle. Carbonation then creates a newly formed $CaCO_3$ binder *in situ*. This distinction has direct implications for luminescence dating: First, the high-temperature calcination step eliminates prior luminescence in the geological carbonate. Second, the progressive precipitation of calcium carbonate during carbonation defines the formation of a new binder phase, which can in principle start a new luminescence clock for the carbonate fraction. In parallel,

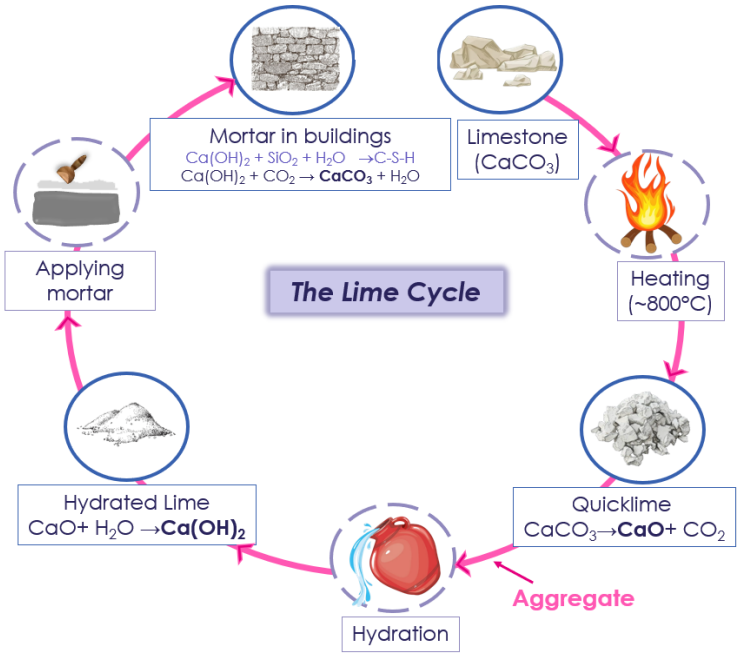

Figure 2.2: Schematic representation of the lime cycle. Geological limestone ($CaCO_3$) is calcined at ~800 °C to produce quicklime (CaO) with release of CO_2. In traditional practice, the quicklime is combined with aggregates before or during hydration, forming portlandite or hydrated lime ($Ca(OH)_2$) within the mixture. After application to masonry, the mortar hardens through carbonation, as $Ca(OH)_2$ reacts with atmospheric CO_2 and reprecipitates *in situ* as a new $CaCO_3$ binder. Adapted from [18].

the aggregate fraction, mainly composed of quartz and feldspar, is introduced after calcination and can be exposed to daylight during quarrying, transport, mixing, and placement, which provides the basis for conventional OSL dating of aggregates.

This thesis aims to develop a new methodology for luminescence dating based on the evaluation of the equivalent dose from the luminescence signals of the carbonate fraction within the mortar binder. Since this $CaCO_3$ forms *in situ* during carbonation, predominantly as calcite, which is the most stable and widespread crystalline polymorph of calcium carbonate [15], calcite was selected as the reference mineral in the experimental work. Its luminescence properties were investigated in order to assess its potential as a dosimetric phase for the direct dating of mortar setting.

The experimental work conducted in this thesis is structured into the following key phases:

- *Methodological study on reference materials:* this phase comprises the thermoluminescence characterization of quartz and calcite as individual components, as well as the investigation of their controlled mixtures. The aim was to analyze their thermoluminescence properties and dosimetric behavior under laboratory conditions, and to evaluate the feasibility of separating the contributions of the two mineral phases through signal deconvolution protocols.

- *Case study on archaeological mortars:* The approach established through the methodological study was subsequently applied to archaeological

mortars collected during a sampling campaign in Catania. In this phase, the developed protocol was used to obtain equivalent dose (D_e) values from the carbonate fraction, which, combined with the annual dose rate, provided absolute age estimates. To ensure validation, the same samples were also dated using the SG-OSL technique, the established reference for mortar dating, allowing a direct comparison between the two approaches.

The methodological study on the characterization of pure minerals and mixtures forms the basis of Chapter 3, while the case study on archaeological mortars constitutes the core of Chapter 4.

Ultimately, the goal of this research is to evaluate whether the carbonate binder fraction can serve as a complement to traditional quartz-based luminescence techniques, with the aim of improving the chronological accuracy of mortar dating, particularly in contexts affected by partial bleaching. By exploiting the complementary luminescence signals of quartz and calcite, the carbonate phase may support the interpretation of complex dose distributions and increase the reliability of age estimates for masonry structures.

To achieve this goal, it is first necessary to present the theoretical basis of luminescence dating. The following sections outline both the underlying physical principles and the measurement techniques required to determine the key parameters for age estimation. The discussion is organised into two parts: the first describes the principles and protocols used to estimate the equivalent dose (D_e), while the second addresses the evaluation of the annual dose rate ($\dot{D}_R$). Together, these parameters constitute the fundamental components of the luminescence age equation, and their accurate determination is essential for reliable dating results.

2.4 Equivalent Dose determination

As introduced in Section 2.2, the equivalent dose (D_e) is the total amount of ionising radiation absorbed by a luminescent mineral since its last complete zeroing event. Along with the annual dose rate ($\dot{D}_R$), it represents one of the two key quantities in the luminescence age equation.

The determination of D_e requires laboratory measurements in which the luminescence signal of a sample, obtained after controlled stimulation, is compared to the signals induced by known radiation doses. Accurate estimation of this parameter is essential for the reliability of luminescence dating, particularly when applied to historical mortars that often present incomplete bleaching and internal heterogeneity.

The following sections introduce the main protocols used for D_e determination in this thesis, namely the regenerative protocol and the Single-Aliquot Regenerative-dose (SAR), with particular attention to their implementation. The SAR, originally developed for OSL, has also been successfully adapted to thermoluminescence (TL) signals, which will be relevant for the applications presented in this work. Finally, statistical models for interpreting equivalent dose distributions are presented, as they are especially relevant for samples affected by partial bleaching or compositional variability.

2.4.1 The regenerative protocol

The estimation of the equivalent dose is based on a simple concept. The luminescence signal naturally stored in the sample (i.e., the *natural signal*) is first measured in the laboratory. This measurement corresponds to the emission induced by the stimulation of charge traps that have accumulated energy due to natural irradiation since the last zeroing event. The sample is then exposed to known laboratory doses D_i, and the resulting luminescence signals are recorded after each dose. Before each measurement, a thermal treatment known as *preheating* is applied to the sample. This step serves to remove unstable or shallow traps that could contribute unstable signal components. By ensuring that only thermally stable traps are stimulated, the preheating step improves the accuracy and reproducibility of the dose-response curve. By repeating the regeneration procedure for increasing dose values, a curve is constructed that describes how the luminescence intensity varies as a function of absorbed radiation, known as *dose-response* curve. The equivalent dose is then obtained by interpolating the initial natural signal onto this curve, and corresponds to the laboratory dose required to reproduce the observed natural luminescence intensity.

This regenerative approach is one of the measurements protocols performed on single aliquots. Each aliquot is treated and measured independently, allowing for the construction of its own dose-response curve [80].

Although the regenerative approach offers a conceptually simple framework for estimating the equivalent dose, its practical application is complicated by changes in luminescence sensitivity that occur as a result of laboratory procedures such as irradiation, heating, and optical stimulation. These variations compromised the reproducibility of dose measurements, as the luminescence intensity could no longer be assumed to scale linearly with the administered dose. To overcome these limitations, the regenerative scheme was refined through the introduction of the Single-Aliquot Regenerative-dose (SAR) protocol [64]. By incorporating internal test doses and specific correction steps, SAR allows for the monitoring and adjustment of sensitivity variations within the same aliquot, thereby improving the accuracy and reliability of equivalent dose determinations. The next section outlines the structure of this protocol.

2.4.2 The Single-Aliquot Regenerative-dose (SAR) protocol

The Single-Aliquot Regenerative-dose (SAR) protocol was developed to provide a reliable procedure for equivalent dose determination while explicitly correcting for sensitivity changes induced by irradiation, heating, and stimulation. This correction is achieved by administering a small test dose after each regenerative dose cycle and normalising the luminescence response to the signal obtained from the test dose [64, 81, 82]. In this way, the effects of sensitivity variation can be monitored throughout the sequence and effectively compensated.

The procedure starts with the measurement of the natural signal (L_N), obtained without preheating, in order to preserve the original charge distribution within the traps. Preheating is a thermal treatment at a fixed temperature

prior to optical stimulation, used to remove unstable signal components and stabilise the luminescence response. Immediately afterwards, a test dose (D_t), usually smaller than the expected D_e, is administered. The aliquot then undergoes a cutheat treatment (T_{CH}), a shorter heating step at a lower temperature than the preheat, designed to empty only the shallowest and least stable traps. The luminescence response to the test dose (T_N) is subsequently measured and used as a sensitivity monitor.

The aliquot is then subjected to a series of regenerative doses (D_i). After each dose, a preheat at a fixed temperature (T_{PH}, typically 160–300 °C) is applied, followed by optical stimulation to record the regenerative signal (L_i). To monitor sensitivity changes, a test dose is again applied after each regenerative dose, followed by a cutheat step and the measurement of the corresponding test dose signal (T_i).

Sensitivity-corrected signals are obtained by normalising each regenerative signal to its corresponding test dose response, i.e. $I_i = L_i/T_i$, while the natural signal is expressed as $I_N = L_N/T_N$. These corrected intensities are plotted against the given regenerative doses to construct a dose–response curve. The equivalent dose (D_e) is interpolated by matching the corrected natural signal I_N to the fitted curve [64, 82].

A summary of the SAR procedure is reported in Table 2.1, which lists the sequence of treatments and the corresponding observed signals.

Table 2.1: Parametrised single-aliquot regenerative-dose (SAR) sequence, including the natural measurement and one regenerative cycle. Adapted from [64].

Step	Treatment[a]	Observed
Natural measurement ($D_N = 0$ Gy)		
1	Optical stimulation at T_{stim} for Δt_{stim}	L_N
2	Give test dose, D_t	–
3	Cutheat at T_{CH} for Δt_{CH}	–
4	Optical stimulation at T_{stim} for Δt_{stim}	T_N
Regenerative cycle		
5	Give regenerative dose, D_i	–
6	Preheating at T_{PH} for Δt_{PH} at heating rate HR	–
7	Optical stimulation at T_{stim} for Δt_{stim}	L_i
8	Give test dose, D_t	–
9	Cutheat at T_{CH} for Δt_{CH}	–
10	Optical stimulation at T_{stim} for Δt_{stim}	T_i
11	Return to step 5 with next D_{i+1}	–

[a] Parameters: T = temperature, Δt = duration, HR = heating rate. The specific values of T_{PH}, Δt_{PH}, HR, T_{stim}, Δt_{stim}, D_t, T_{CH}, and Δt_{CH} are chosen according to the characteristics of the different samples.

Originally developed for measurements on small-aliquot [64], the SAR protocol was later adapted for single-grain applications in order to address with the specific challenges of analysing individual quartz grains. The modified version proposed by Ballarini et al. [83] retains the basic structure of the SAR sequence but introduces several adjustments to account for the lower signal intensities and higher variability inherent to single-grain measurements. These

include the use of relatively larger test doses to ensure statistically significant sensitivity monitoring, as well as optimised preheat and cutheat treatments designed to stabilise the luminescence signal without inducing excessive charge loss. In addition, more stringent dose recovery and recycling tests are applied to validate the protocol at the single-grain level. Together, these modifications enhance the robustness of the SAR protocol when applied to SG-OSL, enabling reliable equivalent dose estimation even in highly heterogeneous samples.

Although originally developed for OSL, the SAR protocol has also been adapted for thermoluminescence (TL) signals, with successful applications reported for heated quartz and related materials [84, 85, 86]. In this variant, optical stimulation is replaced by thermal stimulation, and the dose–response curve is derived from TL signals measured at specific temperature intervals. The overall sequence follows the same structure outlined in Table 2.1, with the only difference that stimulation is thermal rather than optical (Thermal stimulation at T_{stim} at heating rate HR).

2.4.2.1 Quality control tests

In the framework of the SAR protocol, a set of internal tests can be systematically performed to assess the reliability and accuracy of the measurement sequence. These tests are essential to verify that the protocol can correctly account for sensitivity changes, preheating effects, and other experimental variables, ensuring that the equivalent dose determinations are robust. In particular, the following checks were implemented: the *Dose Recovery Test*, the *Recycling Test*, and the *Recuperation Check* [81].

The *Dose Recovery Test* represents a specific and essential quality control procedure. It is designed to validate the ability of the SAR sequence to accurately determine a known laboratory dose under the same conditions applied for equivalent dose determination.

Its primary objective is to verify whether the measurement sequence and applied corrections can reliably determine a known laboratory dose. The procedure begins by resetting the natural luminescence signal of the sample, typically through thermal or optical stimulation. A known dose is first administered under controlled laboratory conditions; the luminescence signal generated by this dose is treated as the natural signal for the purposes of the test. The aliquot is then subjected to the full SAR measurement protocol, which includes pre-heating, regenerative dose cycles, and test dose monitoring. A dose-response curve is constructed based on the regenerative measurements, and the equivalent dose (D_e) is determined by interpolating the signal corresponding to the given dose on this curve. The accuracy of the procedure is evaluated by comparing the determined equivalent dose with the known administered dose (D_{given}).

The ratio between these two quantities defines the Recovery Ratio (R):

$$R = \frac{D_e}{D_{given}} \tag{2.4}$$

where R ideally approaches unity. A recovery ratio close to 1 indicates that the protocol accurately reproduces the given dose and that factors such

as sensitivity change corrections, test dose normalization, and preheat treatments are appropriately accounted for. Conversely, significant deviations from unity may highlight issues such as inadequate sensitivity correction, or other experimental artefacts [81].

The *Recycling Test* assesses the reproducibility of the luminescence response when a regenerative dose is repeated at a later stage of the SAR sequence. Specifically, this test compares the sensitivity-corrected luminescence signal, denoted as L_x/T_x, obtained for the recycled regenerative dose with that measured during its first administration. The recycling ratio is defined as:

$$\text{Recycling ratio} = \frac{(L_x/T_x)_{\text{recycled}}}{(L_x/T_x)_{\text{initial}}} \tag{2.5}$$

An ideal value of this ratio is close to unity, indicating that the luminescence response is stable and that sensitivity changes have been properly corrected. Significant deviations from unity may reveal sensitivity drift, dose misadministration, or issues in the applied correction procedures.

The *Recuperation Check* evaluates the sensitivity-corrected luminescence signal L_x/T_x measured after applying a regenerative dose of zero within the SAR sequence. This signal, referred to as the recuperation signal, should ideally be negligible. The recuperation ratio is defined as:

$$\text{Recuperation ratio} = \frac{(L_x/T_x)_{\text{zero dose}}}{(L_x/T_x)_{\text{given dose}}} \tag{2.6}$$

where the denominator corresponds to the sensitivity-corrected signal from the known administered dose in the dose recovery test. A low recuperation ratio confirms that no spurious charge transfer, or contributions from light-insensitive traps are present. Elevated recuperation signals could lead to dose overestimation and suggest the need for additional preheating or stimulation steps, as discussed by Murray and Wintle [81].

Together, these tests provide a comprehensive evaluation of the SAR protocol's performance, ensuring that the sensitivity-corrected equivalent doses derived from the luminescence measurements are reliable for dating purposes.

Once the luminescence signals have been measured and the equivalent doses determined using the SAR protocol, it becomes necessary to analyse the resulting data distributions to obtain a representative dose value for age calculation. This step is particularly critical when dealing with single-grain or small-aliquot measurements, where natural variability and partial bleaching can introduce significant dispersion in the data. The following section introduces the main statistical models employed to interpret such distributions, with particular attention to their theoretical assumptions and applicability conditions in the context of historical mortars.

2.4.3 Equivalent dose modelling and age models

Once individual equivalent dose (D_e) values have been obtained, they must be combined through appropriate statistical methods to derive a representative value for age calculation. These values may originate either from single-grain measurements, where each grain provides an individual estimate, or from

multigrain aliquots, where each aliquot yields an averaged signal from a population of grains. In both cases, the number of measurements performed, the degree of scatter observed in the data, and the archaeological context all influence the selection of an appropriate statistical model.

These models, commonly referred to as *age models*, are statistical tools designed to estimate the most representative equivalent dose from a set of individual determinations [87]. In this section, the most commonly used age models for luminescence dating are introduced, with a focus on their assumptions, applicability, and interpretation. The basis for model selection and the presentation of D_e distributions are also discussed, as they are essential in age determinations. Graphical tools such as radial plots or density plots are often employed to visualise the spread and relative precision of individual D_e values [77]. Among these, the radial plot [88] is especially useful, as it enables a simultaneous evaluation of the statistical dispersion and the uncertainty of each data point, thereby guiding the selection of the most appropriate age model. The number of grains or aliquots measured, the degree of scatter in the data, and the archaeological context all influence the selection of an appropriate statistical model.

2.4.3.1 Central Age Model (CAM)

The Central Age Model (CAM), introduced by Galbraith et al. [77, 88], is one of the most commonly used statistical models for calculating the equivalent dose (D_e) in luminescence dating. It assumes that the distribution of individual D_e values follows a log-normal distribution, which becomes symmetric when the logarithm of the doses is taken.

This model is best applied in situations where the majority of grains in the sample were well bleached at the time of the zeroing event, such as during exposure to sunlight or heat before burial. In contrast, samples that include grains which were not fully reset before burial *partially bleached*, tend to exhibit asymmetric D_e distributions, often with a pronounced tail towards higher dose values.

The CAM estimates the central value of the dose distribution by accounting for the overdispersion in the data, which includes both the natural variability of the sample and the analytical uncertainties. After a logarithmic transformation of the individual measured doses d_i, each value is expressed as:

$$D_i = \delta_i + \epsilon_i \tag{2.7}$$

where D_i is the natural logarithm of the measured dose for an aliquot or a grain i, δ_i denotes the theoretical expected dose value on the logarithmic scale, that is, the value around which each measurement is assumed to fluctuate, while ϵ_i is the random error term, assumed to be normally distributed with mean zero and variance s_i^2.

The total variance of the measured data is then:

$$v = \sigma^2 + s_i^2 \tag{2.8}$$

where σ represents the intrinsic dispersion (overdispersion) of the dose distribution and s_i^2 is the individual measurement uncertainty.

The CAM estimates the mean of the logarithmic dose distribution, δ, by computing the weighted average of the D_i values:

$$\delta = \frac{\sum w_i D_i}{\sum w_i} \tag{2.9}$$

with weights defined as the inverse of the total variance:

$$w_i = \frac{1}{\sigma^2 + s_i^2} \tag{2.10}$$

The central dose is then obtained by exponentiating the weighted mean δ:

$$D_{\text{CAM}} = \exp(\delta) \tag{2.11}$$

The CAM also provides an estimate of the relative scatter in the data through the parameter known as *overdispersion*, defined as:

$$\text{OD} = \sigma \times 100 \tag{2.12}$$

This value, expressed as a percentage, quantifies the additional variability in the dose distribution not explained by individual measurement uncertainties alone.

The CAM has become the standard model for describing dose distributions in well-bleached samples. It provides a statistically robust estimate of the equivalent dose when the observed dispersion is due mainly to measurement error and intrinsic variability, rather than to partial bleaching.

In cases where the data include very small or negative D_e values and a logarithmic transformation is not appropriate, the CAM can also be applied using non-log-transformed data, as proposed by Arnold et al. [89].

2.4.3.2 Minimum Age Model (MAM)

The Minimum Age Model (MAM), proposed by Galbraith et al. [77], is designed for samples where not all grains were fully bleached at the time of the zeroing event, leading to asymmetric D_e distributions with a tail toward higher doses. This situation is typical in cases of incomplete bleaching.

Like the CAM, the MAM assumes a log-normal distribution of individual equivalent doses, but introduces the concept of a minimum dose γ, representing the true dose received by the well-bleached grain population. The observed D_e distribution is modeled as a mixture of two components: a proportion p of grains that were adequately bleached and a remaining fraction $1 - p$ that includes grains affected by residual signals due to partial bleaching.

The measured individual dose d_i is log-transformed to obtain:

$$D_i = \delta_i + \epsilon_i \tag{2.13}$$

where D_i is the natural logarithm of the measured dose for grain i, δ_i denotes the expected log dose value, that is, the theoretical quantity which the model assumes each measurement is centred on, and ϵ_i is the measurement error, assumed to be normally distributed with mean zero and variance s_i^2.

The total variance is then:

$$v_i = \sigma^2 + s_i^2 \tag{2.14}$$

The true dose distribution is modeled as a truncated normal distribution starting at the minimum dose γ. The log-dose distribution for the partially bleached grains follows a normal distribution with mean μ and standard deviation σ, truncated below at γ. The resulting probability density function is:

$$f(z) = p \cdot \delta(z - \gamma) + (1 - p) \cdot \frac{\phi\left(\frac{z-\mu}{\sigma}\right)}{\sigma \cdot \Phi\left(\frac{\mu-\gamma}{\sigma}\right)} \tag{2.15}$$

In this expression, p represents the proportion of well-bleached grains, $\phi(\cdot)$ is the standard normal probability density function, and $\Phi(\cdot)$ is the cumulative distribution function of the standard normal distribution. The parameters μ and σ correspond to the mean and standard deviation of the log dose distribution of the partially bleached grains, while γ defines the minimum log dose, acting as the truncation threshold of the distribution.

The model parameters p, μ, σ, and γ are estimated via maximum likelihood. The minimum dose is then obtained by back-transforming γ:

$$D_{\text{MAM}} = \exp(\gamma) \tag{2.16}$$

This value is interpreted as the equivalent dose associated with the well-bleached grain population of the sample and should be used for age calculation in heterogeneous samples affected by partial bleaching.

Before applying the MAM, it is necessary to fix an expected overdispersion (σ_b) that characterises the well-bleached grain population. This parameter is not estimated from the analysed dataset, but is assumed *a priori* based on values reported in the literature, typically in the range of 0.10–0.20 (i.e., 10–20%) [77]. It represents the residual scatter expected among grains that were fully reset before burial and is added in quadrature to the individual measurement uncertainties, thereby accounting for both analytical error and intrinsic sample variability during the model fitting procedure.

The MAM has become a widely adopted tool for interpreting dose distributions in partially bleached samples.

2.4.3.3 Graphical representation of equivalent dose distributions: radial plots and density plots

The graphical representation of equivalent dose (D_e) distributions is essential for assessing the internal structure of the dataset, identifying possible outliers, and selecting an appropriate statistical model for age calculation. Among the most effective tools available are the *radial plot* and the *density plot*, which provide complementary perspectives on the same dataset. Examples of both representations are shown side by side in Figure 2.3.

The radial plot, introduced by Galbraith [77, 88], is designed to simultaneously display both the magnitude and precision of individual D_e values on a two-dimensional plane. Each data point is represented by a transformed coordinate pair derived from the natural logarithm of the D_e value and its

associated standard error. Specifically, each data point is plotted with a horizontal position that increases with the precision of the measurement: more precise measurements, having smaller standard errors, are plotted farther from the origin. This is achieved by using the inverse of the standard error on the x-axis. The angular position of the point (its angle relative to the vertical axis) represents how much the measured dose differs from a chosen central value (often the geometric mean or the estimate from a statistical age model). In this way, the radial plot conveys both how far a measurement deviates from the centre and how reliable that measurement is, allowing the viewer to visually assess both the deviation and the reliability of each data point within the distribution.

Mathematically, let $z_i = \ln(D_{e,i})$ and s_i be the standard error of z_i. The radial plot positions each point at a horizontal distance $1/s_i$, and a vertical displacement proportional to $(z_i - \bar{z})/s_i$, where $\bar{z}$ is the estimated central value of the log-transformed doses. In this way, the plot emphasizes the spread and relative influence of each point on the overall distribution. This representation is particularly advantageous in the presence of overdispersed or mixed populations. Unlike other graphical methods, the radial plot does not require binning and visually incorporates measurement precision into the spatial layout of the points. Clusters of high-precision points distant from the main population can thus be easily identified and interpreted, which is particularly useful in scenarios involving partial bleaching or heterogeneities in grain behaviour.

An example of how to read the radial plot is provided by the red point in Figure 2.3a. This point represents the central dose estimate obtained from the dataset. Its horizontal position, at a precision of about 10, corresponds to a relative standard error close to 10%. Its angular position aligns with the radial scale at approximately 55 Gy, indicating the equivalent dose associated with this estimate. This example illustrates how the position of a point on the radial plot simultaneously conveys the equivalent dose value and the reliability of the corresponding measurement.

The density plot, in contrast, displays the distribution of equivalent dose values in a way that directly reflects their frequency and relative abundance. Unlike the radial plot, which integrates both dose magnitude and precision, the density plot focuses on the visualisation of the overall shape and spread of the dose distribution. Each individual D_e value is represented by a symmetric kernel function, typically Gaussian, centred on the estimated dose. These kernels are then summed to produce a continuous curve that approximates the underlying probability density function of the data. Mathematically, the density plot represents the kernel density estimate (KDE) of the D_e distribution and is defined as:

$$f(D) = \frac{1}{nh} \sum_{i=1}^{n} K\left(\frac{D - D_{e,i}}{h}\right) \tag{2.17}$$

where D is the dose variable, $D_{e,i}$ is the equivalent dose of the i-th grain or aliquot, $K(\cdot)$ is the kernel function, usually a standard normal distribution, and h is the bandwidth parameter that controls the smoothness of the resulting curve.

A key advantage of the density plot is its ability to highlight multimodality and asymmetry in the dose distribution, which may arise due to partial

bleaching, mixed populations, or other forms of internal heterogeneity. Peaks in the density plot correspond to clusters of similar D_e values, and the shape of the distribution can guide the selection of an appropriate statistical model. For example, a single, narrow peak may support the use of CAM, while multiple peaks or skewed tails may indicate the need for MAM or other mixture models.

When used together, radial and density plots provide complementary insights: while the radial plot emphasizes measurement precision and the relationship of each data point to a central value, the density plot highlights the overall structure and modality of the dataset. Their combined use therefore offers a robust graphical framework for interpreting luminescence dating data.

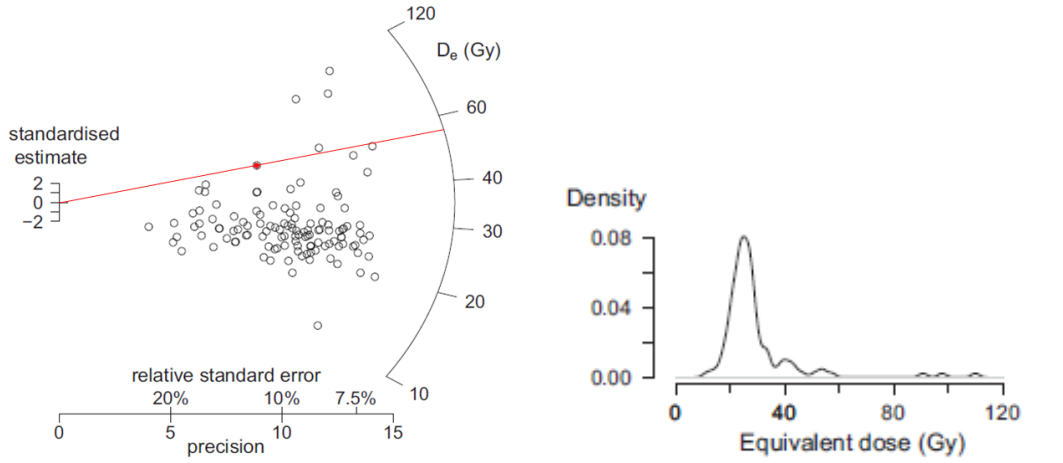

(a) Radial plot. Each point's distance from the origin reflects its precision, while the angle encodes the deviation from the central value.

(b) Density plot. Peaks indicate clusters of similar dose values and highlight the overall shape of the distribution.

Figure 2.3: Examples of graphical representations of equivalent dose (D_e) distributions. (a) Radial plot emphasising the relationship between precision and deviation from a central value. (b) Density plot illustrating the overall structure and modality of the distribution. Adapted from [88].

2.5 Annual dose rate determination

In luminescence dating, the annual dose rate ($\dot{D}_R$) quantifies the amount of ionising radiation absorbed by a sample in one year since its last signal-resetting event. Together with the equivalent dose (D_e), it constitutes one of the two key quantities of the age equation (Section 2.2). While the previous section addressed the procedures for determining D_e, the following discussion focuses on the evaluation of $\dot{D}_R$, which requires distinct physical considerations and analytical approaches.

In the framework of this thesis, the assessment of $\dot{D}_R$ plays a central role, as it is required for dating archaeological mortars both through the established SG-OSL technique and within the new methodological approach proposed in this study. Although the evaluation of the annual dose rate is not the main focus of the research, it remains a fundamental parameter in the luminescence age equation. For this reason, the following section introduces the main physi-

cal concepts and methodological aspects relevant to its determination, ensuring the reliability of the chronological results.

This section first outlines the physical basis of dose rate evaluation. It then introduces the experimental techniques employed to measure the internal and external dose components, including low-background gamma spectrometry for laboratory determination of radionuclide concentrations and *in situ* dosimetry for direct field assessment of the environmental and cosmic dose rate.

2.5.1 Individual contributions to the annual dose rate

The annual dose rate includes contributions from alpha, beta, and gamma radiation emitted by naturally occurring radionuclides, as well as from cosmic rays. The main radionuclides responsible for the irradiation of minerals in archaeological materials are those with very long half-lives, which remain active over geological and archaeological timescales and therefore contribute significantly to the natural radiation field. These include potassium (^{40}K, with a natural isotopic abundance of 0.0117%), which emits both beta and gamma radiation; the uranium series (^{238}U, 99.29% and ^{235}U, 0.71%) and the thorium series (^{232}Th, 100%), which emit alpha particles as well as beta and gamma radiation along their decay chains; and rubidium (^{87}Rb), which contributes beta radiation but only as a minor component. The relative importance of these contributions depends on the concentrations of the radionuclides in the surrounding geological context. In addition, a cosmic-ray component is always present: it becomes increasingly relevant at high altitudes or in environments with low radionuclide content and therefore cannot be neglected in dose rate estimation [1, 90].

The way these radiations interact with minerals depends on their energy and, in the case of alpha and beta particles, also on their charge. In all cases, the interaction is further influenced by medium properties such as density (ρ, expressed in $\mathrm{g\,cm^{-3}}$) and the atomic-to-mass number ratio (Z/A).

For example, in materials like quartz, alpha particles are highly ionising but affect only the outer 20–40 μm of a grain. Beta particles penetrate up to a few millimetres, interacting with both the grain and its immediate surroundings. Gamma rays are much more penetrating, traversing tens of centimetres, while cosmic rays reach the sample from the Earth's surface and atmosphere, contributing uniformly to the dose. These differences in penetration depth are schematically illustrated in Figure 2.4, which compares the effective ranges of the main radiation types. Alpha particles, with a range of only a few tens of micrometres, interact within the outermost rim of mineral grains. Beta particles, with a penetration of up to a few millimetres, affect both the grain and its immediate surroundings. In contrast, gamma rays, with ranges of several tens of centimetres, contribute to irradiation over much larger volumes of material.

In the context of luminescence dating, an archaeological sample is continuously irradiated by natural radionuclides located both within the sample and in its surrounding environment. The relative contribution of these sources depends on their spatial distribution and can be expressed as the sum of three components:

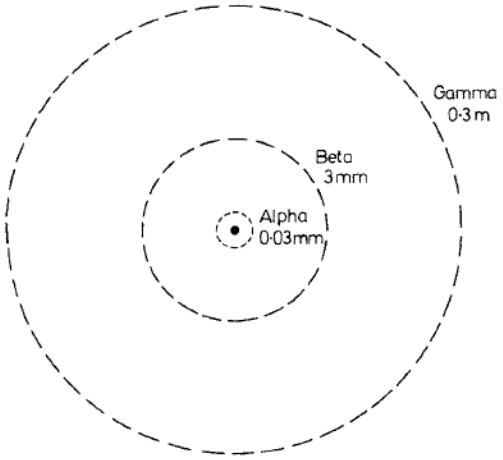

Figure 2.4: Penetration ranges of ionising radiation in materials like quartz. Alpha particles affect only the outer $\sim 30\,\mu$m, beta particles up to ~ 3 mm, and gamma rays irradiate from several centimetres to decimetres. Adapted from [91].

$$\dot{D}_{\mathrm{R}} = \dot{D}_{\mathrm{inc}} + \dot{D}_{\mathrm{int}} + \dot{D}_{\mathrm{env}} \tag{2.18}$$

Here, $\dot{D}_{\mathrm{inc}}$ denotes the dose produced by radionuclides included within the mineral grains themselves, $\dot{D}_{\mathrm{int}}$ represents the contribution from radionuclides dispersed in the binder matrix or bulk of the sample, and $\dot{D}_{\mathrm{env}}$ corresponds to the external dose arising from the surrounding sediments or building materials. This distinction between internal and external components is essential for accurately assessing the annual dose rate. In the notation of Eq 2.18, each of the terms implicitly encompasses the different radiation components (α, β, and γ), which contribute to the overall irradiation of the mineral grains together with the cosmic component in the case of the external environment.

In the present study, several of these contributions can be excluded for the following reasons:

- The dose rate from inclusions within the mineral grains ($\dot{D}_{\mathrm{inc}}$) is assumed to be negligible in this study, as no significant internal radioactive inclusions are expected within the investigated materials.

- The penetration depth of alpha particles in mineral matrices does not exceed $\sim$20 μm, while beta particles reach a maximum of 2–3 mm. Since the analysed sample corresponds to a mortar fragment extracted from the selected architectural structure, the external surface layer (2–3 mm) is removed during sample preparation, thus the external α and β components ($\dot{D}_{\alpha,\mathrm{env}}$, $\dot{D}_{\beta,\mathrm{env}}$) can be neglected.

- The γ contribution originating from the sample itself ($\dot{D}_{\gamma,\mathrm{int}}$) can also be disregarded. As pointed out by Aitken [1], in the case of archaeological materials of limited dimensions, such as mortars from architectural structures, the internal γ dose is negligible compared to that from the surrounding environment. The total γ dose rate can therefore be attributed entirely to the external environment.

Taking these aspects into account, the total dose rate equation simplifies to:

$$\dot{D}_{\mathrm{R}} = \dot{D}_{\alpha,\mathrm{int}} + \dot{D}_{\beta,\mathrm{int}} + \dot{D}_{\gamma,\mathrm{env}} + \dot{D}_{\mathrm{cosm}} \tag{2.19}$$

Finally, accurate estimation of the annual dose rate also requires accounting for the attenuation of ionising radiation due to water content in the burial environment. The presence of water reduces the energy deposited by α, β, and γ radiation, and this effect is corrected using two empirical factors: the W factor, which quantifies the water absorption capacity of the sample, and the F factor, representing the average field water saturation. The corrected dose contributions are thus expressed as:

$$\dot{D}_{\alpha,\mathrm{corr}} = \frac{\dot{D}_{\alpha}}{1 + 1.50 \cdot WF} \tag{2.20}$$

$$\dot{D}_{\beta,\mathrm{corr}} = \frac{\dot{D}_{\beta}}{1 + 1.25 \cdot WF} \tag{2.21}$$

$$\dot{D}_{\gamma,\mathrm{corr}} = \frac{\dot{D}_{\gamma}}{1 + 1.16 \cdot WF} \tag{2.22}$$

2.5.2 Assessment of radioactive equilibrium and its implications for dose rate evaluation

The dating method relies on the assumption that the annual dose rate remained constant over time, provided the sample's burial environment has not been altered. However, field observations frequently challenge this assumption because archaeological sites often undergo physical and geochemical changes. In particular, radioactive disequilibria caused by the migration or selective retention of radionuclides can lead to significant variations in environmental radioactivity, ultimately affecting age calculations if not accounted for properly.

Radioactive equilibrium corresponds to the condition in which all members of a decay chain exhibit equal activities that match the one of the long-lived parent isotope. Disequilibrium arises when one of the daughter nuclides is added or lost due to processes, such as radon gas escape, dissolution, or selective mobilization driven by water circulation, redox variations, or changes in pH. These processes can affect the dose rate when they occur on timescales that are comparable to the half-life of the affected radionuclide. If no further disturbance occurs, the decay chains tend to re-establish secular equilibrium over time. For this reason, the identification and quantification of any disequilibrium are essential to correctly determine the mean annual dose rate, which is the effective quantity used in luminescence age calculation.

Uranium and thorium have distinct chemical behaviours. Thorium is largely immobile and is retained in insoluble mineral phases or adsorbed onto clays. Uranium is more reactive and can be mobilized under oxidizing conditions, especially in the hexavalent form, which produces the soluble uranyl ion UO_2^{2+}. The tetravalent form of uranium is much less soluble and tends to remain incorporated in minerals such as uraninite and coffinite. Radium, although less

mobile than uranium, can still migrate or become adsorbed onto clay minerals or incorporated into carbonate matrices.

Natural uranium occurs as a mixture of three isotopes. Two of these isotopes, ^{238}U and ^{235}U, are the starting points of two natural radioactive decay chains. The third isotope, ^{234}U, is a radiogenic daughter of ^{238}U. In total, there are three natural radioactive series. The thorium series starts with ^{232}Th and includes isotopes with mass number divisible by four. The uranium series starts with ^{238}U and includes isotopes with mass number equal to four times an integer plus two. The actinium series starts with ^{235}U and includes isotopes with mass number equal to four times an integer plus three. Among these, the uranium series is the most relevant in luminescence dating because of its abundance.

Near the surface, both uranium and thorium can be mobilized in oxidising conditions, although in very different ways. Thorium is usually found in insoluble phases or adsorbed onto clay surfaces, while uranium is often transported in solution as uranyl complexes or as part of the detrital mineral fraction. In primary rocks and minerals, both elements are typically in the +4 oxidation state. However, uranium can also exist in +5 and +6 oxidation states. The +6 state is the most stable under oxidising conditions and forms the uranyl ion UO_2^{2+} according to the reaction:

$$U^{4+} + 2H_2O \rightleftharpoons UO_2^{2+} + 4H^+ + 2e^- \tag{2.23}$$

The uranyl ion may form complexes depending on pH and the presence of other dissolved species. Uranium in the +4 state remains insoluble under slightly acidic to alkaline conditions, and its solubility is controlled by the precipitation of uraninite or coffinite. In contrast, uranium in the +6 state is much more soluble. The mobility of uranium is also enhanced by alpha decay recoil, which damages the mineral lattice and facilitates its release.

Radium can also be mobile, although to a lesser extent than uranium. It can be incorporated into secondary mineral phases such as calcite or retained by adsorption onto clays. Thorium is considered poorly mobile because of its low solubility and strong affinity for insoluble phases.

Geochemical processes that selectively enrich or deplete radionuclides alter the annual dose. They do so not only by modifying the local abundance of radioactive elements but also because the system gradually evolves back toward secular equilibrium once the perturbation ceases. Disequilibrium arises when the addition or removal of a parent or daughter nuclide occurs at a rate comparable to the half-life of the affected daughter. The study of these processes is therefore necessary to determine the effective dose rate experienced by the sample and to reconstruct its time-averaged dose history.

The different types of disequilibrium commonly encountered in natural samples, including uranium enrichment, radium loss, and radon escape, can be visualised through schematic representations of the decay chains. These diagrams highlight the deviation from equilibrium activity levels and help to understand the potential influence of specific geochemical processes on the dose rate absorbed by the sample.

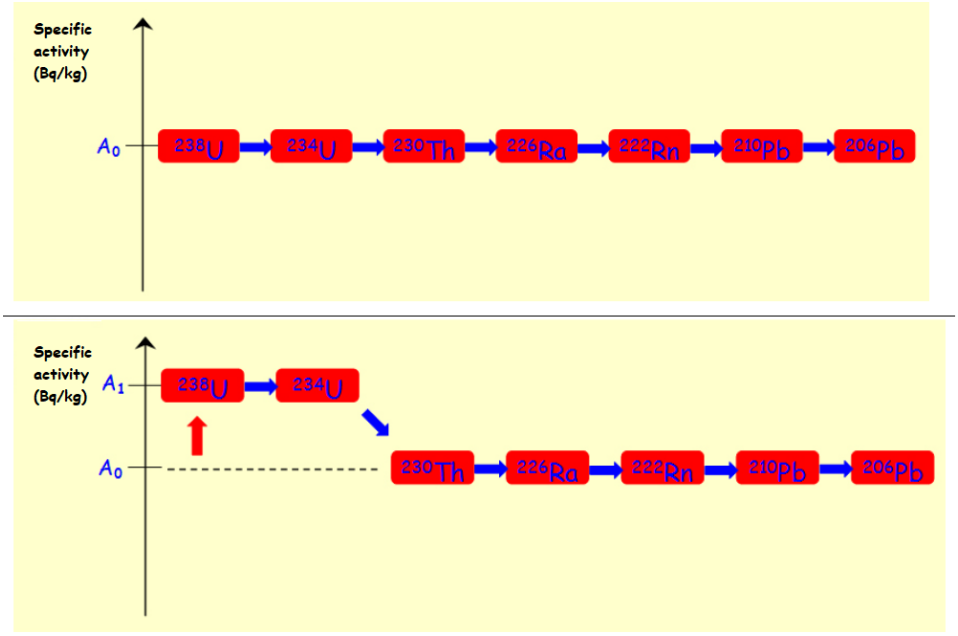

Figure 2.5: Simplified diagram of the ^{238}U decay chain in secular equilibrium (top) and in a uranium enrichment scenario (bottom). The initial increase in ^{238}U and ^{234}U results in an activity excess in the upper part of the chain [92].

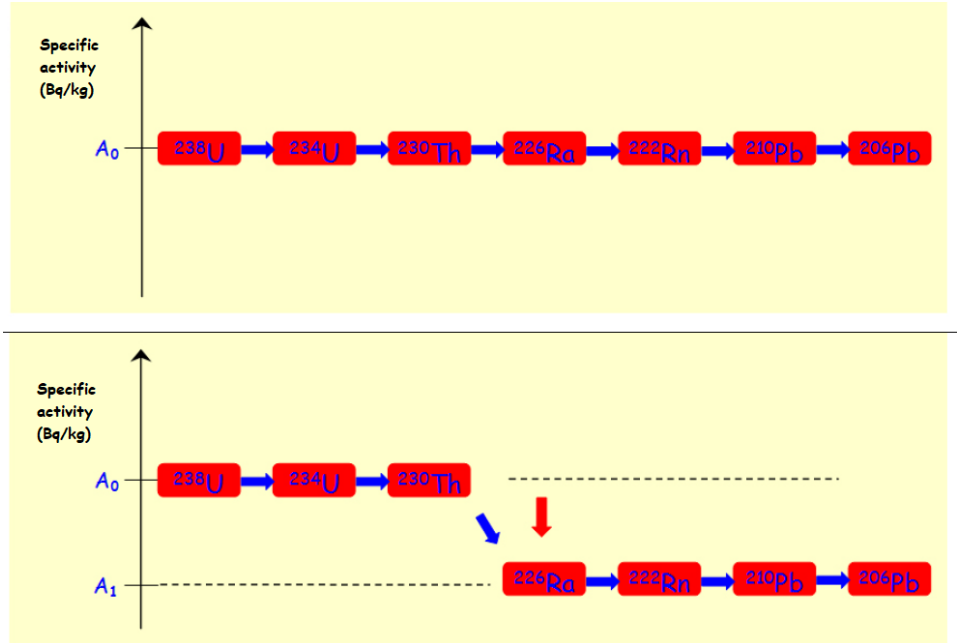

Figure 2.6: Simplified diagram of the ^{238}U decay chain in secular equilibrium (top) and in a radium loss scenario (bottom). The reduction in ^{226}Ra activity leads to a decrease in the activity of its daughters [92].

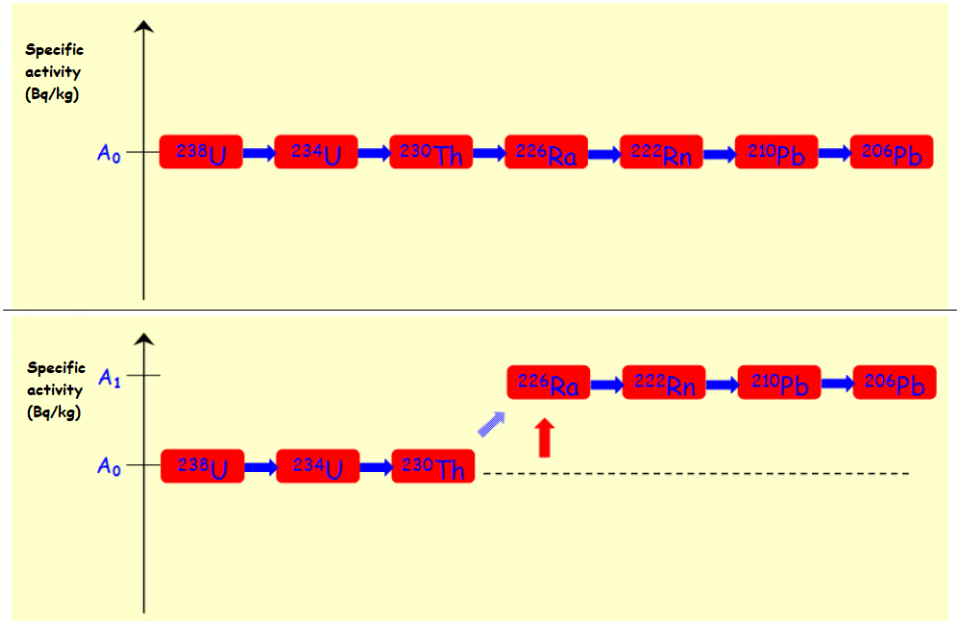

Figure 2.7: Simplified diagram of the ^{238}U decay chain in secular equilibrium (top) and in a radium enrichment scenario (bottom). The addition of ^{226}Ra produces a localised increase in activity in the lower part of the chain [92].

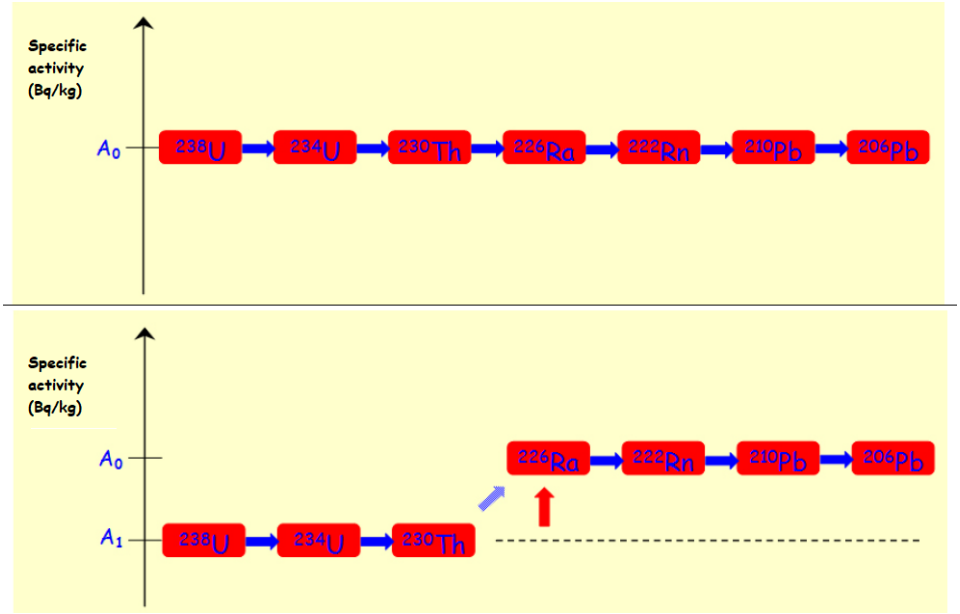

Figure 2.8: Simplified diagram of the ^{238}U decay chain in secular equilibrium (top) and in a radium removal scenario (bottom). The loss of ^{226}Ra reduces the activity of subsequent daughters [92].

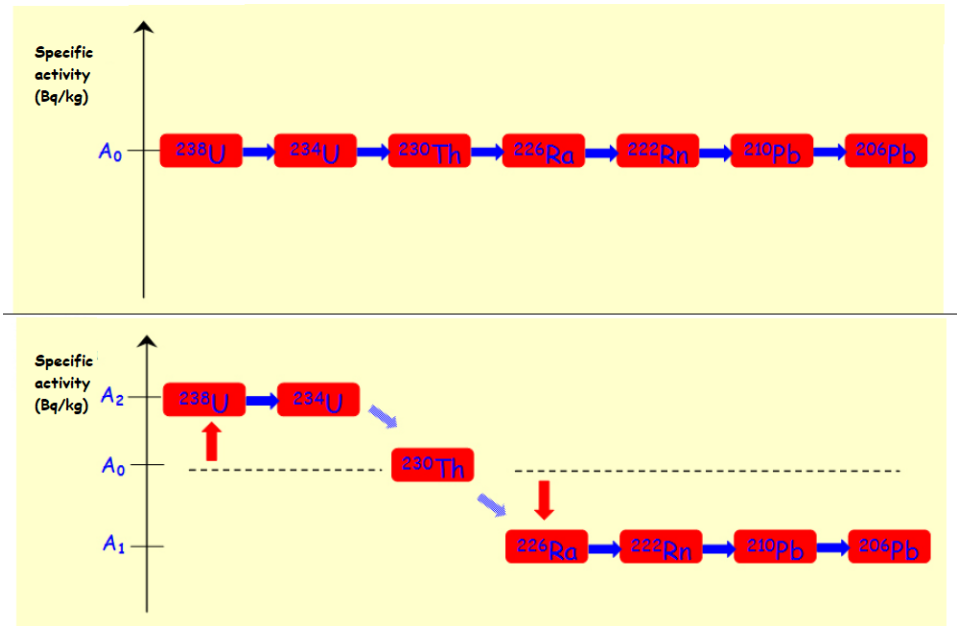

Figure 2.9: Simplified diagram of the ^{238}U decay chain in secular equilibrium (top) and in a combined uranium enrichment and radium depletion scenario (bottom). The imbalance produces a strong deviation in the activity profile across the chain [92].

Figures 2.5 to 2.9 present schematic representations of the ^{238}U decay chain under different geochemical conditions. Each figure compares the ideal case of secular equilibrium (top) with a specific disequilibrium scenario (bottom). In secular equilibrium, all radionuclides in the chain exhibit equal specific activities, corresponding to a stable and time-invariant dose rate. Deviations from this condition may arise when one or more radionuclides are selectively added to or removed from the system.

Figure 2.5 illustrates the case of uranium enrichment, where an increase in the concentration of ^{238}U and ^{234}U leads to an excess in the upper part of the chain. The downstream radionuclides remain unchanged until equilibrium is progressively restored by radioactive decay. Figure 2.6 shows a scenario of radium depletion, in which the activity of ^{226}Ra and its daughters is reduced.

In Figure 2.7, the system is affected by radium enrichment, which enhances the activity of the lower part of the decay chain. This may artificially increase the external dose rate if the origin of the enrichment is not properly identified. Figure 2.8 depicts the partial removal of radium, a condition that may occur due to leaching or low retention in the surrounding matrix, with a corresponding decrease in the activity of its short-lived daughters.

Figure 2.9 presents a complex situation in which uranium is enriched while radium is simultaneously depleted. This combination produces an imbalanced activity profile along the decay chain, which can lead to significant errors in dose rate estimation if not appropriately corrected. These graphical models highlight the importance of assessing the internal consistency of the decay chain through high-resolution spectrometric analysis and applying correction factors when disequilibrium is detected.

2.5.3 Measurements of the individual components of the annual dose

The reliability of luminescence dating depends critically on the accurate determination of the $\dot{D}_R$, as any uncertainty directly propagates into the calculated age [93]. Its evaluation requires complementary approaches to characterise both the internal and environmental contributions.

The internal component is typically determined in the laboratory using low-background gamma spectrometry, which measures the activity concentrations of ^{40}K, ^{238}U, ^{235}U, and ^{232}Th. These values are then converted into dose rates ($\dot{D}_{\alpha,\mathrm{int}}$, $\dot{D}_{\beta,\mathrm{int}}$) through standard conversion factors, with corrections for grain size and attenuation effects [94].

The environmental component is instead assessed through *in situ* dosimetry, which provides site-specific estimates of the external γ dose ($\dot{D}_{\gamma,\mathrm{env}}$) together with the cosmic-ray contribution ($\dot{D}_{\mathrm{cosm}}$).

The following sections describe these two techniques, which together allow for a comprehensive evaluation of the annual dose rate.

2.5.3.1 Low-background gamma spectrometry for internal dose rate determination

The use of low-background gamma spectrometry in the context of luminescence dating has been widespread since the late 1970s [95]. The major advantage of gamma emission spectrometry is its sensitivity to the elements of interest in TL and OSL dating.

This technique allows for the determination of the activity concentrations of naturally occurring gamma-emitting radionuclides such as ^{40}K, ^{235}U, and the decay products of ^{238}U and ^{232}Th. From these activities, the concentrations of K, U, and Th can be calculated, assuming secular equilibrium within the uranium and thorium series.

Given the relatively low concentrations of radionuclides in samples used for luminescence dating — typically 0.5–5 ppm of uranium, 2–20 ppm of thorium, and 0.2–4% of potassium — the detection of the gamma spectrum they emit requires the use of highly efficient shielding around the detector [95]. For this purpose, high-purity germanium (HPGe) detectors are employed, which are capable of detecting low-intensity gamma emissions with high resolution.

The standard procedure consists of placing a powdered sample, typically between 10 and 120 grams, into a sealed container with fixed geometry and acquiring the gamma spectrum over a prolonged measurement time, usually ranging from 16 to 64 hours, in order to obtain statistically significant results.

Once the gamma spectrum has been acquired, the peaks with the highest intensity and methodological relevance are selected for analysis. By processing the spectra, the intensity of each selected peak (I_i) is obtained, typically expressed as the number of photons detected per unit time. These raw intensity values must be corrected for self-absorption effects within the sample, particularly when measuring low-activity materials. The correction factor for self-absorption (S_{abs}) depends on the photon energy, the density (ρ) of the sample, and its thickness (x), and is given by the equation:

$$S_{\text{abs}} = \exp\left(\frac{\mu\,\rho\,x}{2}\right) \tag{2.24}$$

where μ is the mass attenuation coefficient, which, in the energy range of interest, can be considered independent of the chemical composition of the sample [96].

After this correction is applied, the net intensity I_i becomes proportional to the activity A_i of the emitting isotope, according to:

$$I_i = A_i\, f_i\, \epsilon_i \tag{2.25}$$

where f_i is the branching ratio of the gamma emission (available in literature tables, e.g., [97, 98, 99]), andϵ_i is the absolute detection efficiency of the system for registering gamma photons that deposit their full energy at the specific energy E_i.

In the case of decay chains such as those of uranium and thorium, where multiple peaks are used to estimate the activity, the apparent activity of the parent element (e.g., ^{238}U or ^{232}Th) is obtained by a weighted average of the individual peak activities, assuming secular equilibrium within the series.

The elemental concentration C of potassium, uranium, or thorium is then derived from the measured activity using the following relationship:

$$C = \frac{A\, T_{1/2}\, M}{\ln 2\, N_{\text{av}}\, \alpha\, m} \tag{2.26}$$

where:

- A is the activity of the radionuclide [Bq],
- $T_{1/2}$ is the half-life of the parent isotope,
- M is the molar mass of the parent element,
- N_{av} is Avogadro's number,
- α is the natural isotopic abundance,
- m is the sample mass.

2.5.3.2 *In situ* dosimetry for environmental and cosmic dose assessment

The enviromental component of the annual dose rate, which includes gamma radiation from surrounding materials, and cosmic radiation, can be evaluated through *in situ* dosimetry. This method employs a portable gamma probe that enables the real-time measurement of the ambient gamma and cosmic radiation directly at the sampling location.

The probe is typically positioned at the same depth and geometry as the sampled material, allowing for a representative characterisation of the radiative environment surrounding the sample. The measurement provides a direct estimation of the local dose rate, expressed in units of dose per unit time (e.g., μGy/h), which can be converted to annual dose rate values. When necessary, standard correction procedures can be applied to account for water content, density variations, and geometry.

This technique is fast, non-destructive, and allows for multiple measurements to be carried out across the site. These features make *in situ* dosimetry with a portable gamma probe particularly valuable in archaeological and architectural contexts, where rapid dose assessment is required and installation of passive dosimeters may not be feasible [100].

3 Discrimination of thermoluminescent signals from natural quartz and carbonate crystals mixture

The previous chapter introduced the theoretical and methodological background of luminescence dating, with particular emphasis on the challenges associated with the application of this technique to historical mortars. Building on this framework, the present chapter is devoted to a methodological study aimed at characterizing the thermoluminescence signals of selected reference materials. These consist of quartz (Qz_{ref}), calcite (Cal_{ref}), and a controlled mixture of the two (Mix_{ref}). The analysis of these materials provides the experimental basis for the development of a protocol that can subsequently be applied to archaeological samples.

The first part of the chapter focuses on the TL characterization of quartz and calcite considered individually. For each material, glow curves were analysed through curve deconvolution, with the aim of identifying the main peaks contributing to the TL signal and of extracting the associated kinetic parameters. This step was essential to determine which TL components can be regarded as characteristic of each mineral phase and to assess their dosimetric properties.

In the second part of the study, the controlled mixture (Mix_{ref}) is examined. The mixture was prepared from known proportions of Qz_{ref} and Cal_{ref}, both irradiated with well-defined doses prior to mixing. The composite TL glow curves of the mixture are deconvoluted to assess the degree of overlap between the luminescence contributions of quartz and calcite. The aim of this analysis is to evaluate if the characteristic peaks identified in the individual materials can still be distinguished within the mixture and to assess its dosimetric properties.

The results presented in this chapter therefore represent a key methodological step, providing the foundation for the application of the developed approach to complex materials such as historical mortars for dating purposes. This application will be the subject of the Chapter 4, where the methodology is tested on archaeological samples.

3.1 Materials

This section describes the reference materials and their preparation, which formed the basis for the methodological characterization carried out in this study.

3.1.1 Samples Qz_{ref} and Cal_{ref}

Quartz extracted from a marine sediment, named Qz_{ref}, and calcite obtained from a stalagmite, named Cal_{ref}, were selected as reference materials for this study.

The preparation of Qz_{ref} followed a *coarse grain* protocol aimed at isolating grains in the 180–212 µm diameter range [101, 102, 103, 104, 105]. During the entire preparation process, the sample was kept at room temperature and shielded from light to avoid signal loss. The sediment was first sieved to obtain grains below 500 µm, then treated with 10% H_2O_2 for 48 h to remove organic matter and with 20% HCl for 120 min to dissolve carbonate components. After sieving to retain grains in the 100–300 µm range, the material, consisting of quartz, feldspars and heavy minerals, underwent density separation in sodium polytungstate with $\rho = 2.62$ g/cm^3 to isolate quartz fraction. The obtained quartz sample was etched in 40% HF for 50 min, removing approximately 30 µm of the grain surface to eliminate the alpha-irradiated outer shell. A final cleaning step with 10% HCl for 25 min removed fluorides precipitated during HF etching. After rinsing, drying, and sieving, the final fraction of 180–212 µm was obtained.

The preparation workflow for Qz_{ref} is summarised in Figure 3.1.

The preparation of Cal_{ref} consisted of the mechanical disaggregation of the stalagmite, with the isolation of coarse grains in the 180–212 µm diameter range. To avoid the influence of light-bleached material, the outermost 10 mm layer was first removed with a hand file [106]. The remaining inner portion was then gently crushed and sieved, and the resulting grains were subsequently treated with a 1% acetic acid solution for approximately 7 min to minimise potential spurious triboluminescence (tribo-TL) induced during crushing [49, 107, 108]. The preparation workflow for Cal_{ref} is summarised in Figure 3.2.

The preparation procedures allowed obtaining quartz and calcite fractions that were then used for thermoluminescence measurements.

3.1.2 Sample Mix_{ref}

In addition to the individual monocrystalline fractions, a controlled mixture was prepared using Qz_{ref} and Cal_{ref} as starting materials. The mixture consisted of 75% quartz and 25% calcite by weight, a proportion chosen to approximate the typical binder-to-aggregate ratio commonly observed in historical lime mortars [78, 79, 61, 109, 110].

Prior to mixing, both fractions were first bleached to remove any pre-existing luminescence signal and subsequently irradiated with different doses: 41.4 Gy for quartz and 10.4 Gy for calcite. The difference in irradiation doses

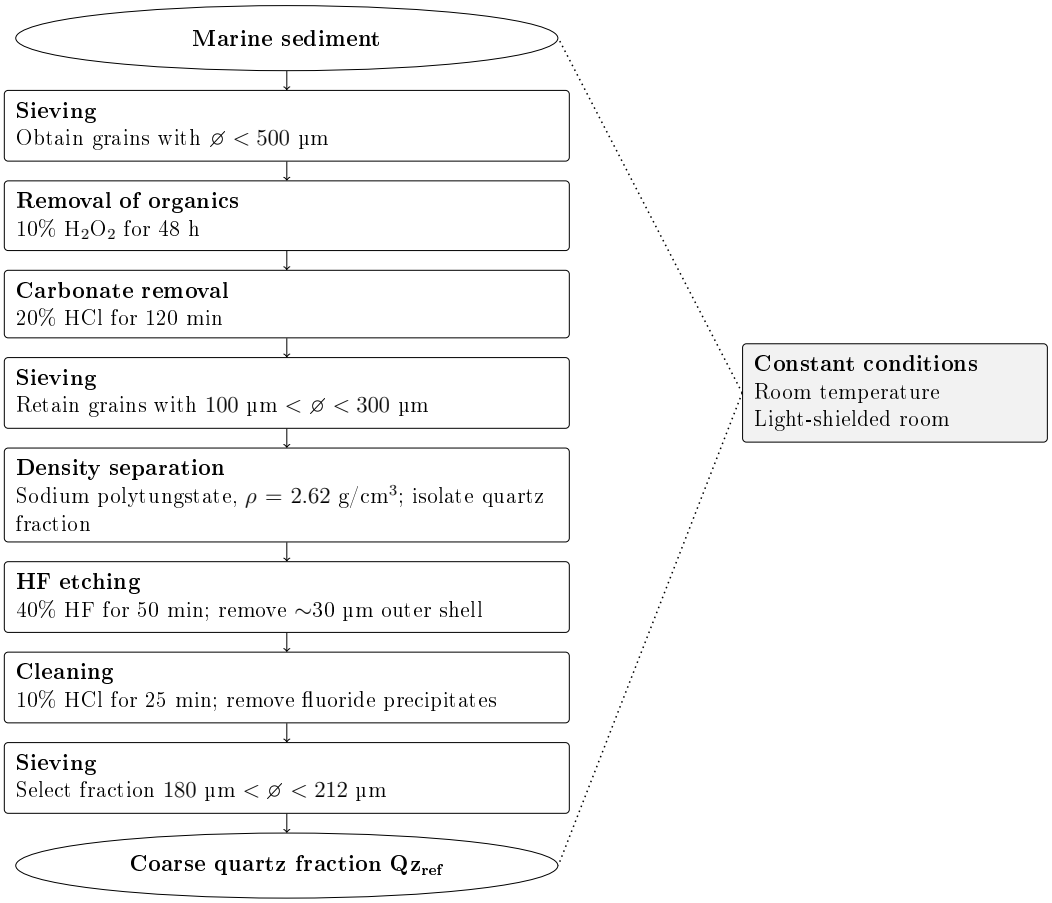

Figure 3.1: Flowchart of the preparation steps for the monocrystalline quartz fraction that constitutes the sample denoted as Qz_{ref}.

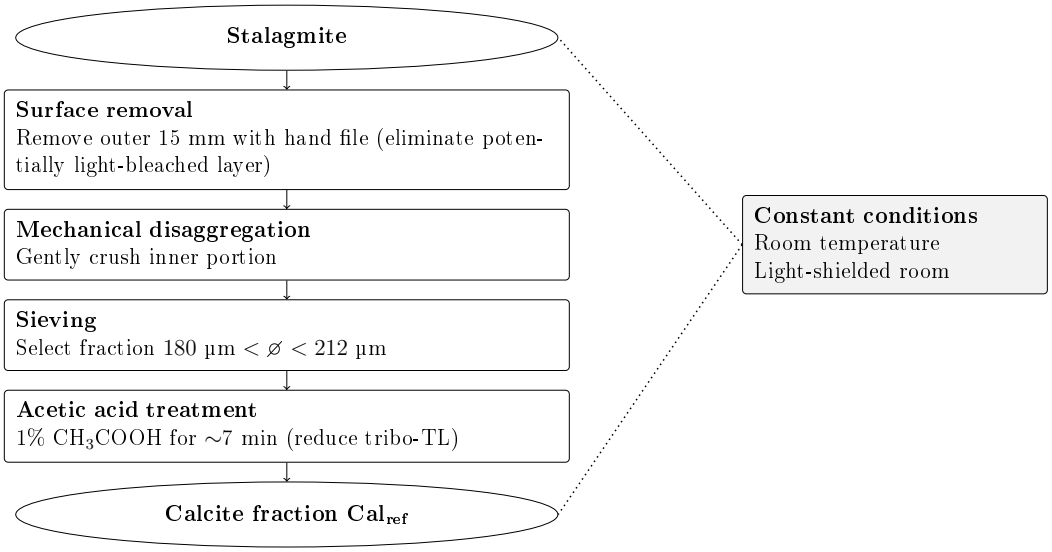

Figure 3.2: Flowchart of the preparation steps for the monocrystalline calcite fraction that constitutes the sample denoted as Cal_{ref}.

arises from the fact that the luminescence signal of calcite begins to accumulate only after mortar hardening, when new crystals are formed during the carbonation process. Quartz, on the other hand, undergoes optical resetting during mortar preparation, but if bleaching is incomplete it retains part of its geological dose. This residual component is then added to the dose accumulated during the burial of the mortar, so that at the time of measurement the equivalent dose of quartz is higher than that of the carbonate fraction. In the present experiment, this additional geological contribution due to partial bleaching was simulated by assigning quartz a dose approximately four times greater than that of calcite. The resulting 4:1 ratio was chosen to reproduce a realistic scenario in which the carbonate fraction carries a fully reset signal of low equivalent dose, while quartz preserves a larger residual signal inherited from its geological history.

The irradiated fractions were then combined in a beaker, dispersed in acetone, and homogenised in an ultrasonic bath for 5 minutes. The suspension was subsequently dried in a G®-Therm 015 oven at 35°C for 48 hours to ensure complete evaporation of the solvent. This procedure yielded a homogeneous dry mixture suitable for thermoluminescence measurements.

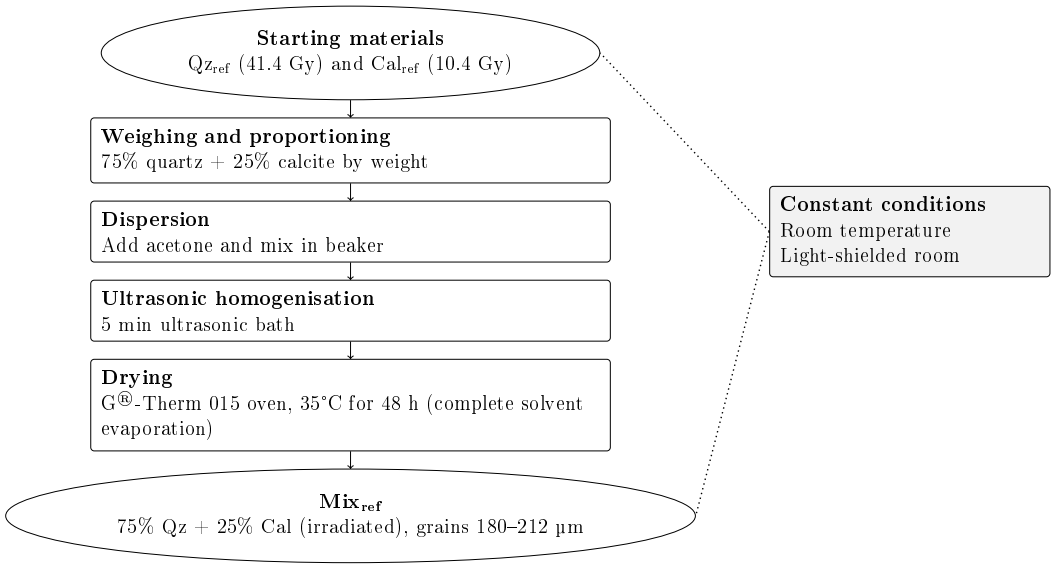

Figure 3.3: Flowchart of the preparation steps for the controlled mixture Mix_{ref} obtained from Qz_{ref} and Cal_{ref}.

3.2 Methods

This section presents the experimental methods and analytical procedures adopted for the methodological study. Consistent with the structure of the research workflow, the content is organised into two main parts. The first part describes the instrumentation employed for luminescence measurements: the Risø DA-15 TL/OSL reader.

The second part details the measurement protocols applied to the reference materials Qz_{ref}, Cal_{ref}, and Mix_{ref}, together with the corresponding strategies for data analysis.

3.2.1 Luminescence measurements instrument: Risø TL/OSL DA-15 reader

The measurements for the methodological part of this thesis were carried out using a Risø TL/OSL DA-15 reader, a system widely employed in luminescence dating. The instrument is equipped for both TL and OSL analyses; however, in this methodological study and throughout the thesis it was used exclusively for TL measurements. A photograph of the instrument is shown in Fig. 3.4.

Figure 3.4: Automated luminescence reader used in this study: Risø TL/OSL DA-15.

The DA-15 is equipped with a carousel that can hold up to 48 stainless steel sample cups or discs, each 1 cm in diameter. For this study, the reference samples Qz_{ref}, Cal_{ref}, and Mix_{ref} were mounted on these cups. Each cup contained a thin monolayer of the samples fixed with silicone spray, which allowed TL measurements to be carried out under reproducible conditions (Fig. 3.5).

The heating system of the DA-15 provides precise temperature control up to 700 °C, with programmable rates between 0.1 and 30 °C/s, ensuring stable and reliable TL analyses. The heating unit, positioned under the sample, also acts as a lifting mechanism that brings the cup into the measurement position. It consists of a Kanthal strip with a central depression, designed to improve thermal contact and ensure proper sample alignment [12, 35, 55].

Temperature regulation is achieved by a type K (Alumel–Chromel) thermocouple located directly under the cup, providing accurate feedback control. To prevent oxidation and maintain stable conditions during high-temperature operation, the heating chamber is continuously flushed with nitrogen [55].

A close-up of the heating unit configuration is shown in Fig. 3.6.

Luminescence detection is performed by an EMI 9835 QA photomultiplier

Figure 3.5: Stainless steel cups mounted in the Risø carousel, each containing a monolayer of sample grains fixed with silicone spray. These holders were used for multigrain TL measurements in this study.

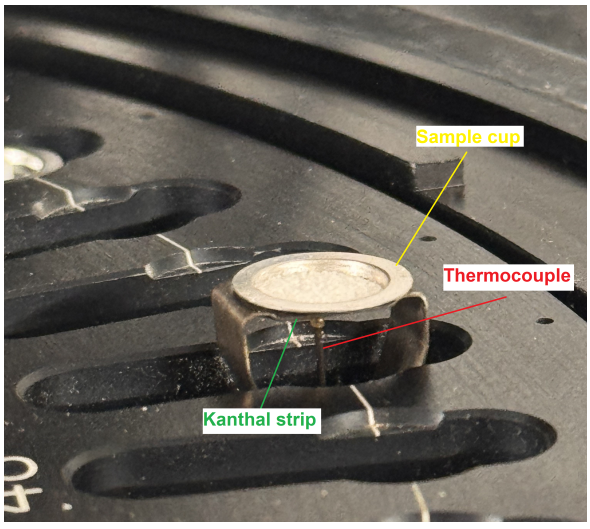

Figure 3.6: Close-up view of the heating unit in the Risø TL/OSL DA-15 reader. The stainless steel sample cup is positioned above the Kanthal strip, which ensures efficient thermal contact, while the thermocouple provides real-time temperature feedback for accurate regulation.

tube (PMT), used in photon-counting mode. The geometry of the sample measurement position and the PMT is optimised to a 55 mm distance, ensuring a detection solid angle of 0.4 sr.

Since the spectral emission of carbonates falls within the orange region of the spectrum (570–650 nm), the use of a dedicated optical filter was necessary to detect this signal (see Section 1.5 in Chapter 1 for further details). In this study, the BG-39 filter, a broad band-pass type with transmission extending into the green–orange range, was adopted as detection filter for TL analyses. The choice of this filter resulted from preliminary tests that indicated its suitability for detecting both the carbonate emission (around 570 nm) and the quartz emission (around 365 nm). The BG-39 filter and its transmittance curve are shown in Fig. 3.7.

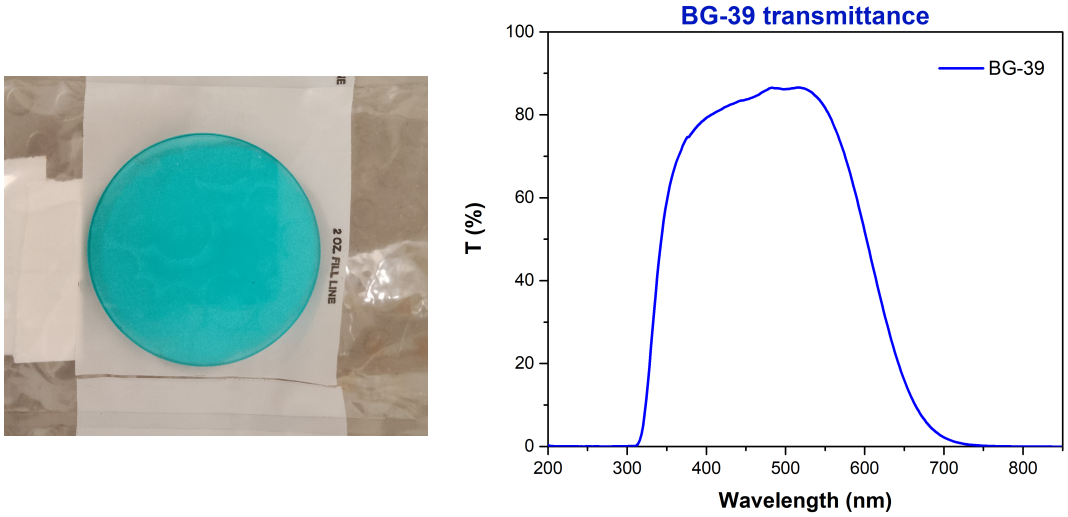

Figure 3.7: BG-39 optical filter employed for the detection of carbonate emissions: photograph (left) and measured transmittance curve (right), obtained with a Perkin-Elmer Lambda 1050 UV-VIS-NIR spectrophotometer.

The system is further equipped with a built-in ^{90}Sr/^{90}Y beta source, which delivered a dose rate of 4.14 Gy/min (1 February 2023).

For further technical details on the DA-15 system and its components, the reader is referred to the comprehensive descriptions available in the literature [12, 35, 55].

3.2.2 Measurements on reference materials

This section focuses on the experimental investigation of the reference materials, with the aim of establishing the characteristic TL response of quartz and calcite under controlled laboratory conditions.

3.2.2.1 Measurements on Qz_{ref} and Cal_{ref}

A total of 25 aliquots were prepared for each of the reference samples Qz_{ref} and Cal_{ref}, mounted in cups and measured by TL using the Risø TL/OSL DA-15 system.

The first experimental step focused on characterizing the TL response of the reference samples under controlled laboratory conditions. In this context, artificial signals were employed for two main reasons. First, Qz_{ref} and Cal_{ref} were obtained from materials with different geological origins and dosimetric histories, making their natural luminescence signals not directly comparable. Second, the use of artificial irradiation allows the creation of reproducible experimental conditions, which are essential for a consistent methodological study. The investigation of these signals was therefore aimed at establishing the TL behaviour of each phase, thus providing reference conditions for the subsequent application of the method to mortars.

The natural luminescence signal of the aliquots was removed by thermal annealing at 450 °C, carried out with a controlled heating rate of 5 °C/s. Each aliquot was then subjected to a well-defined experimental sequence. A laboratory beta dose of 14 Gy was administered, after which the samples underwent a preheating stage at 220 °C for 10 s to remove electrons from unstable traps. The TL signal was then acquired by thermal stimulation from room temperature up to 450 °C at a constant heating rate of 5 °C/s, with detection through a BG-39 optical filter to ensure spectral selectivity.

The complete measurement sequence applied to the aliquots is reported in Table 3.1.

Table 3.1: Measurement sequence applied for TL acquisition of artificial signals from Qz_{ref} and Cal_{ref} aliquots.

Sequence step	Treatment	Observed
1	Thermal annealing (@450 °C, 5 °C/s)	–
2	Beta irradiation: 14 Gy	–
3	Preheating (@220 °C, 10 s)	–
4	Thermal stimulation (@450 °C, 5 °C/s)	L_x

To assess the dosimetric response of the two samples, a Dose Recovery Test was carried out on the same set of aliquots (see Section 2.4.2.1, Eq. 2.4). After annealing, two beta doses were administered: 41.40 Gy to the aliquots of Qz_{ref} and 10.40 Gy to those of Cal_{ref}. These irradiation doses were treated as the "natural" dose to be recovered, and the aliquots were subsequently measured using a TL SAR protocol in order to derive a D_e estimate to be compared with D_{given} as part of the recovery test.

The detailed TL SAR sequence adopted for the Dose Recovery Test is summarised in Table 3.2.

3.2.2.2 Measurements on Mix_{ref}

For Mix_{ref}, a first set of 5 aliquots was analysed with the purpose of characterising the composite TL signal of the mixture. The measurement procedure consisted of a preheating step at 220 °C for 10 s, followed by TL readout up to 450 °C at a heating rate of 5 °C/s. The signal recorded in this configuration reflects the luminescence arising from the artificial irradiation previously administered to the quartz and calcite fractions prior to mixing and was therefore

Table 3.2: TL SAR measurement sequence applied during the Recovery Test on Qz_{ref} and Cal_{ref} aliquots.

Sequence step	Treatment	Observed
1	Preheating (@220 °C, 10 s)	–
2	Thermal stimulation (@450 °C, 5 °C/s)	L_{given}
3	Give test dose, D_T = 7 Gy	–
4	Cut heat (@180 °C)	–
5	Thermal stimulation (@450 °C, 5 °C/s)	T_{given}
6	Give dose, D_i	–
7	Preheating (@220 °C, 10 s)	–
8	Thermal stimulation (@450 °C, 5 °C/s)	L_x
9	Give test dose, D_T = 7 Gy	–
10	Cut heat (@180 °C)	–
11	Thermal stimulation (@450 °C, 5 °C/s)	T_x
12	Repeat steps 6–11 for D_i = 6.90 Gy, 13.80 Gy, 27.60 Gy, 41.40 Gy, 55.20 Gy	–

treated, within the context of this study, as the "natural" signal of the mixture (L_N). The adopted measurement sequence is summarised in Table 3.3.

Table 3.3: Measurement sequence applied for TL signal acquisition from Mix_{ref} aliquots.

Step	Treatment	Observed
1	Preheating (@220 °C, 10 s)	–
2	Thermal stimulation (@450 °C, 5 °C/s)	L_N

A second set of 25 aliquots was analysed by applying a TL SAR protocol in order to reconstruct the equivalent dose associated with the artificial irradiations previously administered to the quartz and calcite fractions. The measurement sequence applied to these aliquots is summarised in Table 3.4.

Table 3.4: TL SAR measurement sequence applied to Mix_{ref} aliquots.

Step	Treatment	Observed
1	Preheating (@220 °C, 10 s)	–
2	Thermal stimulation (@450 °C, 5 °C/s)	L_N
3	Give test dose, $D_T = 7$ Gy	–
4	Cut heat (@180 °C)	–
5	Thermal stimulation (@450 °C, 5 °C/s)	T_N
6	Give dose, D_i	–
7	Preheating (@220 °C, 10 s)	–
8	Thermal stimulation (@450 °C, 5 °C/s)	L_x
9	Give test dose, $D_T = 7$ Gy	–
10	Cut heat (@180 °C)	–
11	Thermal stimulation (@450 °C, 5 °C/s)	T_x
12	Repeat steps 6–11 for $D_i = 6.90$, 13.80, 27.60, 41.40, 55.20 Gy	–

3.2.3 Analysis

For all TL datasets considered in this methodological study, namely Qz_{ref}, Cal_{ref}, and Mix_{ref}, the same data analysis workflow was applied.

Following the measurement sequences, each measured glow curve was analysed individually through deconvolution in order to separate overlapping components.

Deconvolutions were performed with a home-made stand-alone application named *Dosimetric Deconvolution Chart*. The software provides an interactive graphical interface for fitting complex glow curves and implements the GOK formalism, which describes kinetic behaviour between first and second order (please refer to Section 1.2.2.4 and Eq. 1.19 for the general expression of the model). The user defines the number of deconvolution peaks and supplies initial values for the peak temperature T_m, the maximum intensity I_m at T_m, the activation energy E, and the kinetic order b. These values are then iteratively optimised during the fitting process. During optimisation the software displays simultaneously the experimental curve, the individual components and the global fit, and reports residuals and fit metrics in real time.

For each deconvolution, the residuals between experimental and fitted data were calculated and normalised with respect to the maximum absolute residual, providing a direct check of the fit quality. In addition to this qualitative control, the goodness of fit was quantitatively assessed using the Figure of Merit (FOM) [111], a widely employed indicator in thermoluminescence studies to evaluate the agreement between experimental and fitted glow curves [112].

$$\text{FOM} = \frac{\sum_{i=1}^{n} \left| y_i^{\text{exp}} - y_i^{\text{fit}} \right|}{\sum_{i=1}^{n} |y_i^{\text{exp}}|} \,, \tag{3.1}$$

where y_i^{exp} and y_i^{fit} denote the experimental and fitted intensities at point i. The FOM values are generally expressed as percentages, with a threshold of 5%, which is considered indicative of good agreement.

For all TL signals, deconvolutions were applied to both regenerative (L_x) and test (T_x) signals in order to separate the individual contributions of each component. The notation P_j is used throughout this work to denote each deconvolution peak, where $j = 1, 2, \ldots, N_p$ and N_p is the total number of peaks identified for a given glow curve. The initial fitting parameters associated with each P_j, namely the peak temperature $T_m(P_j)$, the activation energy $E(P_j)$, and the kinetic order $b(P_j)$, provided the starting point for the optimisation procedure.

For each peak, the integrals of the luminescence intensity corresponding to regenerative and test doses, $L_x(P_j)$ and $T_x(P_j)$, were calculated. The sensitivity-corrected signal was then obtained as

$$I(P_j) = \frac{L_x(P_j)}{T_x(P_j)} \,, \tag{3.2}$$

and used to construct dose–response curves as a function of the applied regenerative doses. The equivalent dose of each peak, $D_e(P_j)$, was determined by interpolating the natural signal $L_N(P_j)/T_N(P_j)$ on the corresponding curve.

In the case of $\mathrm{Qz}_{\mathrm{ref}}$ and $\mathrm{Cal}_{\mathrm{ref}}$, the equivalent dose values obtained for each deconvolution peak, $D_e(P_j)$, were used to quantify the accuracy of the SAR protocol through the dose–recovery test. Specifically, for each peak the recovery ratio (Eq. 2.4) was calculated as

$$R(P_j) = \frac{D_e(P_j)}{D_{\mathrm{given}}} \,, \tag{3.3}$$

A recovery ratio $R(P_j)$ close to unity indicates that the measured equivalent dose correctly reproduces the given dose, thereby confirming the reliability of the applied procedure.

In contrast, for $\mathrm{Mix}_{\mathrm{ref}}$ the equivalent dose values of each peak were further analysed with radial plots obtained with the *RadialPlotter* software, which allowed a more comprehensive assessment of the distribution of $D_e(P_j)$ values across the analysed aliquots.

3.3 Results

This section summarises the TL behaviour of the reference materials. First, single-phase glow curves of $\mathrm{Qz}_{\mathrm{ref}}$ and $\mathrm{Cal}_{\mathrm{ref}}$ are deconvolved to define peak structure and kinetic parameters. Second, $\mathrm{Mix}_{\mathrm{ref}}$ is analysed to verify peak correspondence and to separate the relative contributions of quartz and calcite. Third, TL SAR measurements are used to reconstruct equivalent doses associated with the known artificial irradiations, supported by sensitivity monitoring and L/T dose–response analysis. A concise comparison with literature values closes the section and anticipates the application to archaeological mortars in the next chapter.

3.3.1 Characterization of the reference samples Qz_{ref} and Cal_{ref}

Glow curves for both quartz and calcite aliquots were acquired following the measurement sequence in Table 3.1. Figure 3.8 presents a representative example of the deconvolution analysis performed on the TL signal of a single aliquot, along with the corresponding residuals.

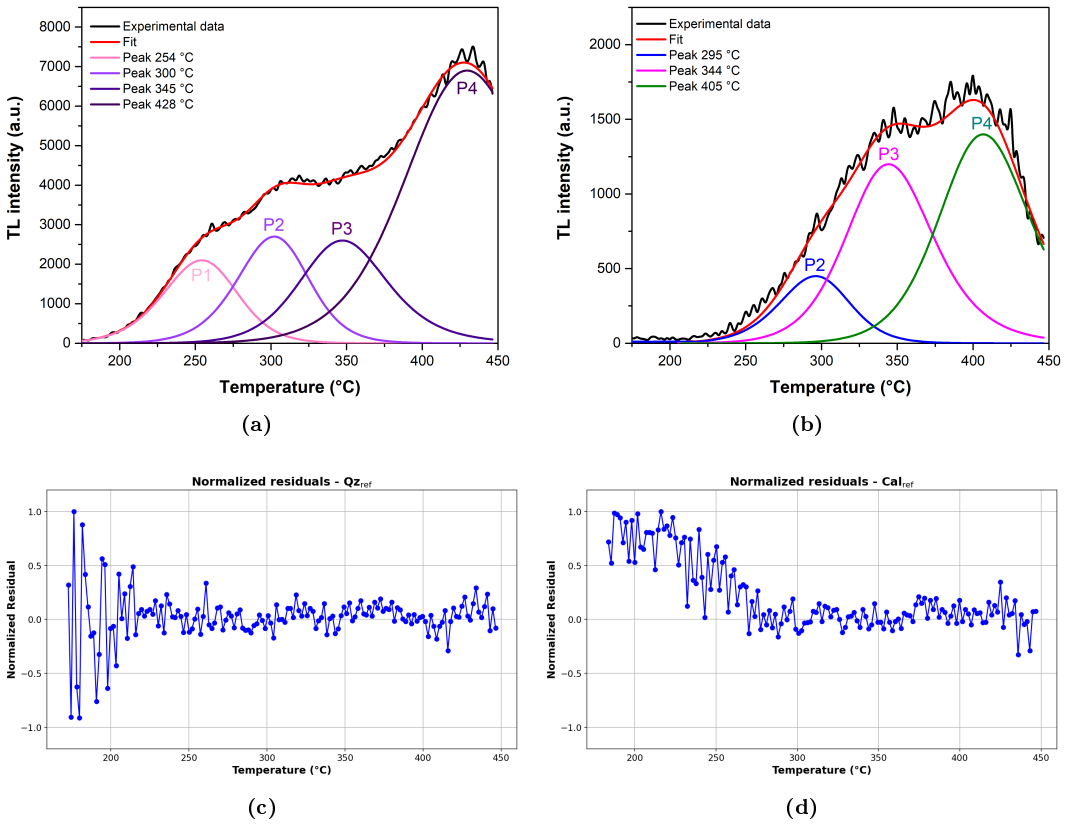

Figure 3.8: Thermoluminescence signal deconvolution of irradiated aliquots. (a) Quartz glow curve with fitted peaks at 254 °C, 300 °C, 345 °C, and 428 °C. (b) Calcite glow curve with fitted peaks at 295 °C, 344 °C, and 405 °C. Residuals are reported in (c) and (d), respectively.

As shown in Figure 3.8a, the quartz TL glow curve is well described by four peaks, centred at 254 °C, 300 °C, 345 °C, and 428 °C. In contrast, the calcite signal in Figure 3.8b is described by three peaks, located at 295 °C, 344 °C, and 405 °C. Notably, unlike quartz, calcite does not exhibit a distinct low-temperature peak.

The deconvolutions were performed by minimising the Figure of Merit (FOM), obtaining values lower than 3% for the two representative aliquots shown in Figure 3.8. These values indicate a high degree of statistical reliability of the fit for each individual case. The corresponding residuals, shown in Figures 3.8c and 3.8d, confirm the robustness of the fits across the temperature interval considered. In both cases, the residuals remain close to zero, confirming that the fitted curves reproduce well the experimental data. For calcite, the residuals show a slightly larger spread than those of quartz, which may be explained by higher signal noise.

The deconvolution procedure was applied to all 25 aliquots of quartz and calcite, respectively. Averaging the FOM values obtained from each individual deconvolution yielded mean values of $1.5\% \pm 0.4\%$ for quartz and $1.8\% \pm 0.4\%$ for calcite. These results confirm the overall reliability and consistency of the deconvolution procedure applied to all measured aliquots.

Peak P4 of the quartz deconvolution (428 °C) was excluded from subsequent dosimetric analysis, as its parameters are strongly affected by uncertainties in the background subtraction. Similarly, the highest-temperature peak identified in the calcite glow curve (405 °C) was also excluded for the same reason. In this temperature range, the background mainly arises from the incandescence of the sample itself during heating, which intensifies with increasing temperature and interferes with the discrimination of the actual TL emission. These high-temperature components are therefore not considered representative of the intrinsic luminescence properties of quartz and calcite, and their inclusion could introduce additional uncertainties in dose estimation procedures.

Following the deconvolution of the 25 aliquots of quartz and calcite, a set of kinetic parameters was obtained for each deconvolved TL peak. These parameters include the maximum temperature of the peak (T_m in °C), activation energy (E in eV), and kinetic order (b). For each identified peak, average values and the corresponding standard errors of the mean were calculated across all aliquots. The results of this analysis are reported in Table 3.5, which includes the mean deconvolution parameters for quartz and calcite peaks P1 to P4. Peaks P4 were excluded from kinetic evaluation due to uncertainties arising from background subtraction, as discussed previously.

The parameters reported in Table 3.5 summarise the thermal and kinetic characteristics of the TL glow peaks identified in quartz and calcite. For both minerals, three reproducible peaks (P1 to P3) were observed between 254 and 345 °C for quartz and between 295 and 344 °C for calcite. Their activation energies range from 1.29 to 1.59 eV. The kinetic orders vary between 1.52 and 1.86, consistent with general-order kinetics, that is intermediate between first- and second-order behaviour.

These results are consistent with the expected behaviour of stable TL components in quartz and carbonates. Peak P1 was identified only in quartz, confirming its specificity for this mineral phase. In contrast, peaks P2 and P3 show very similar kinetic parameters in both minerals, indicating that the charge carriers involved have comparable thermal stability under the applied measurement conditions. This outcome provides a solid basis for discriminating and modelling TL signals in composite materials such as historical mortars.

A detailed comparison between the TL deconvolution parameters obtained in this study and those reported in the literature for quartz is presented in Table 3.6. The values refer to the three main peaks identified (P1, P2, P3), and include the peak temperature (T_m), activation energy (E), and kinetic order (b). The literature data have been averaged where multiple values are available, in order to provide a more robust reference for comparison.

As presented in Table 3.6, the thermoluminescence parameters derived in this study for quartz peaks P1, P2, and P3 exhibit a generally good agreement with those reported in the literature. For peak P1, the measured peak temperature ($T_m = 254 \pm 4$ °C) is consistent with the average literature value of

Table 3.5: Mean deconvolution parameters obtained from 25 aliquots of quartz and calcite. Values refer to peak temperature (T_{m}), activation energy (E), and kinetic order (b). Uncertainties represent standard errors of the mean.

	Quartz			Calcite		
Peak	T_{m} (°C)	E (eV)	b	T_{m} (°C)	E (eV)	b
P1	254 ± 4	1.29 ± 0.04	1.52 ± 0.04	–	–	–
P2	300 ± 3	1.50 ± 0.04	1.57 ± 0.04	295 ± 4	1.50 ± 0.04	1.57 ± 0.04
P3	345 ± 3	1.59 ± 0.04	1.86 ± 0.04	344 ± 4	1.59 ± 0.04	1.86 ± 0.04
P4	428 ± 10	–	–	405 ± 12	–	–

Table 3.6: Comparison between TL deconvolution parameters obtained in this study and average values reported in the literature for quartz peaks P1, P2, and P3. Values include peak temperature (T_m), activation energy (E), and kinetic order (b).

Peak	**Parameter**	**This study**	**Average values (literature)** [113, 114]
P1	T_m (°C)	254 ± 4	263 ± 9
	E (eV)	1.29 ± 0.04	1.30 ± 0.10
	b	1.52 ± 0.04	1.24 ± 0.03
P2	T_m (°C)	300 ± 3	316 ± 9
	E (eV)	1.50 ± 0.04	1.35 ± 0.10
	b	1.57 ± 0.04	1.44 ± 0.10
P3	T_m (°C)	345 ± 3	347 ± 5
	E (eV)	1.59 ± 0.04	1.46 ± 0.10
	b	1.86 ± 0.04	1.81 ± 0.10

$263 \pm 9\,°C$. The activation energy ($E = 1.29 \pm 0.04\,eV$) is in good agreement to the average reported value ($1.30 \pm 0.10\,eV$), confirming the reliability of the deconvolution model adopted. The kinetic order parameter ($b = 1.52 \pm 0.04$), although slightly higher than the reference value (1.24 ± 0.03), falls within a reasonable range of variation and may reflect differences in sample origin or trapping configurations.

In the case of peak P2, the experimental peak temperature ($300 \pm 3\,°C$) is slightly lower than the average value found in the literature ($316 \pm 9\,°C$). The activation energy obtained ($1.50 \pm 0.04\,eV$) exceeds the average reported value ($1.35 \pm 0.10\,eV$), although the deviation remains within the experimental uncertainty typical of TL kinetic analyses. The kinetic order parameter ($b = 1.57 \pm 0.04$) is compatible with the literature average (1.44 ± 0.10).

For peak P3, the measured parameters show excellent correspondence with literature data. The peak temperature ($345 \pm 3\,°C$) matches the reported average ($347 \pm 5\,°C$), and the activation energy ($1.59 \pm 0.04\,eV$) is slightly elevated relative to the reference value ($1.46 \pm 0.10\,eV$), yet remains within an acceptable range. Similarly, the kinetic order ($b = 1.86 \pm 0.04$) is in very good agreement with the average literature value (1.81 ± 0.10).

Overall, the results support the robustness and reproducibility of the deconvolution approach applied in this work. The minor deviations observed are attributable to differences in the defects configuration and thermal history, and do not compromise the overall consistency of the kinetic interpretation, which is strongly supported by the close agreement observed across most of the deconvolution parameters.

As shown in Table 3.7, a direct comparison between the kinetic parameters derived in this work and the average values reported in the literature is presented for calcite peaks P2 and P3, as already done for quartz.

As shown in Table 3.7, for peak P2, the measured peak temperature is $295 \pm 4\,°C$, which is moderately higher than the average value from literature, $267 \pm 13\,°C$. The activation energy obtained in this study, $1.50 \pm 0.04\,eV$, is in very good agreement with the literature average of $1.53 \pm 0.04\,eV$. Likewise, the kinetic order parameter $b = 1.57 \pm 0.04$ shows strong consistency with the

Table 3.7: Comparison between TL deconvolution parameters obtained in this study and average values reported in the literature for calcite peaks P2 and P3. Values include peak temperature (T_{m}), activation energy (E), and kinetic order (b).

Peak	Parameter	This study	Average values (literature) [115, 116, 117, 118, 119]
P2	T_{m} (°C)	295 ± 4	267 ± 13
	E (eV)	1.50 ± 0.04	1.53 ± 0.04
	b	1.57 ± 0.04	1.64 ± 0.16
P3	T_{m} (°C)	344 ± 4	348 ± 16
	E (eV)	1.59 ± 0.04	1.76 ± 0.07
	b	1.86 ± 0.04	1.90 ± 0.06

average literature value of 1.64 ± 0.16.

For peak P3, the measured peak temperature is $344 \pm 4\,^{\circ}\mathrm{C}$, closely matching the average value of $348 \pm 16\,^{\circ}\mathrm{C}$ from literature works. The activation energy determined, $1.59 \pm 0.04\,\mathrm{eV}$, is slightly lower than the reported literature average of $1.76 \pm 0.07\,\mathrm{eV}$, yet the deviation remains within acceptable bounds for thermoluminescence kinetic analysis. The kinetic order parameter $b = 1.86 \pm 0.04$ is in excellent agreement with the literature value of 1.90 ± 0.06.

In conclusion, the comparison confirms a high degree of consistency between the TL parameters obtained in this study and those reported in the literature, particularly with regard to the activation energy and kinetic order, which display minimal deviations. The slightly greater variability observed in peak temperature values can be attributed to differences in sample provenance and the distribution of intrinsic defects, all of which can influence recombination dynamics.

As described in Section 3.2.2.1, the Dose Recovery Test was applied to 25 aliquots of $\mathrm{Qz_{ref}}$ and 25 aliquots of $\mathrm{Cal_{ref}}$ to assess the accuracy of dose reconstruction through deconvolution. All TL curves obtained in the recovery test were subjected to deconvolution. For each deconvolution peak, $P_{\mathrm{Qz}}\,1$, $P_{\mathrm{Qz}}\,2$, and $P_{\mathrm{Qz}}\,3$ in $\mathrm{Qz_{ref}}$, and $P_{\mathrm{Cal}}\,2$ and $P_{\mathrm{Cal}}\,3$ in $\mathrm{Cal_{ref}}$, the equivalent dose (D_e) was determined by interpolation on the respective dose–response curve. The Recovery Ratio (R) was then calculated as the ratio between the reconstructed and the administered dose, providing a peak-specific evaluation of measurement accuracy.

Figure 3.9 presents the results of the SAR protocol applied in the Dose Recovery Test. Panels a and b display the TL glow curves of representative aliquots of quartz and calcite measured after successive regenerative doses, illustrating the evolution of the luminescence signal with increasing temperature. Panels c and d show the corresponding sensitivity-corrected signal ratios T_x/T_n for the main deconvolution peaks. The ratio, where T_x denotes the test dose signal and T_n the natural dose signal, was monitored across all cycles to assess both sensitivity correction and signal stability, which are essential for reliable equivalent dose determination.

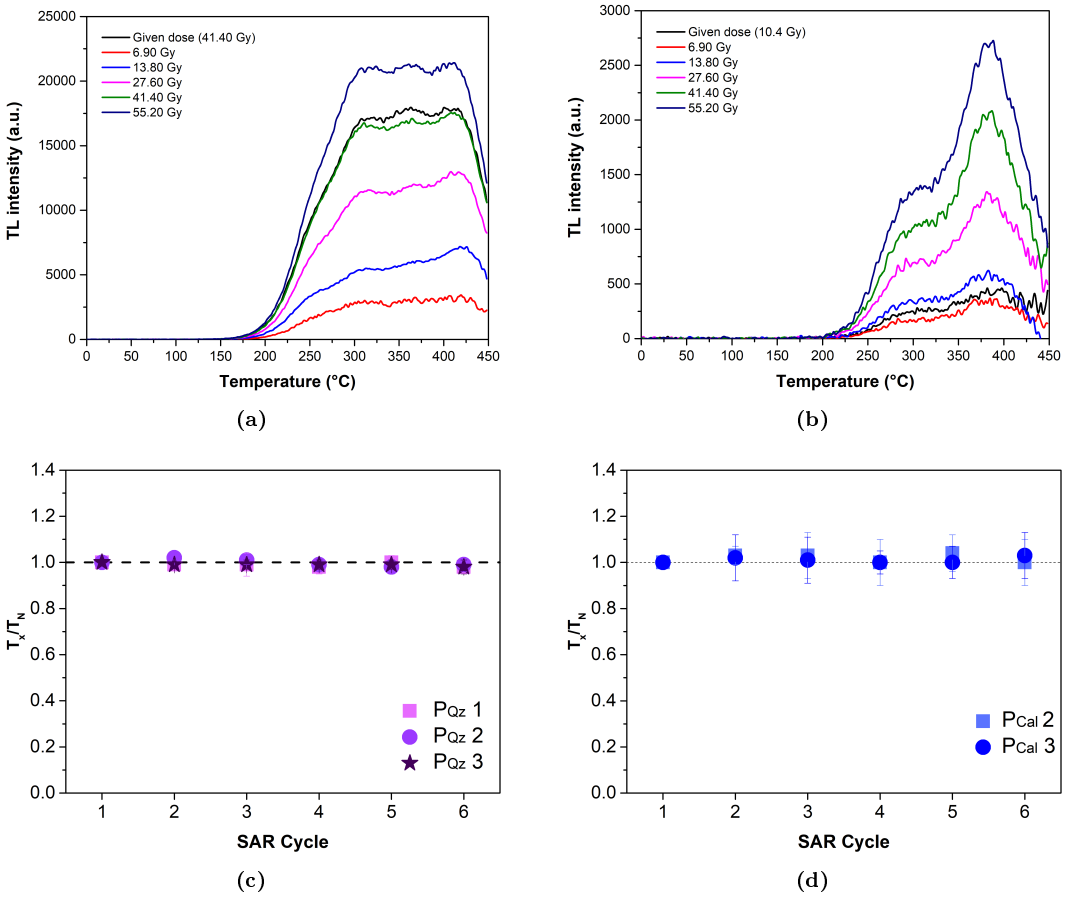

Figure 3.9: Evaluation of signal stability and sensitivity correction during the SAR protocol. (a)–(b) TL glow curves obtained from a representative aliquot of quartz and calcite subjected to increasing regenerative doses. (c)–(d) Evolution of the sensitivity-corrected signal ratio T_x/T_n for each deconvolution peak, as observed in the same example aliquot.

As shown in Figures 3.9c and 3.9d, the T_x/T_n ratio of quartz remains consistently close to unity for all three deconvolution peaks, with minimal fluctuation across cycles, indicating effective sensitivity correction. Calcite shows a similarly stable behaviour for peaks P2 and P3, with slightly higher variability, yet still consistent with proper sensitivity correction.

The dose–response behaviour of the main TL deconvolved peaks was investigated by plotting the sensitivity-corrected signal (L_x/T_x) as a function of the administered dose (Figure 3.10). For quartz ($\mathrm{Qz_{ref}}$), peaks 1, 2, and 3 exhibit linear growth, with slopes of 0.153 ± 0.002 ($R^2 = 0.997$), 0.175 ± 0.004 ($R^2 = 0.998$), and 0.158 ± 0.002 ($R^2 = 0.997$), respectively. For calcite ($\mathrm{Cal_{ref}}$), peaks 2 and 3 also follow a linear trend, with slopes of 0.143 ± 0.002 ($R^2 = 0.997$) and 0.133 ± 0.002 ($R^2 = 0.996$). These results demonstrate that both quartz and calcite display a linearity of the dosimetric signal over the investigated dose range.

Finally, in the Table 3.8 reports the average Recovery Ratio (R) values obtained for each deconvolution peak in quartz and calcite.

The results presented in Table 3.8 show that, for both quartz and calcite, the average Recovery Ratios (R) associated with the main TL peaks are close to unity. In quartz, R values increase from 0.92 ± 0.30 for P1 to 0.96 ± 0.26 for P3, suggesting a slightly improved agreement between administered and measured

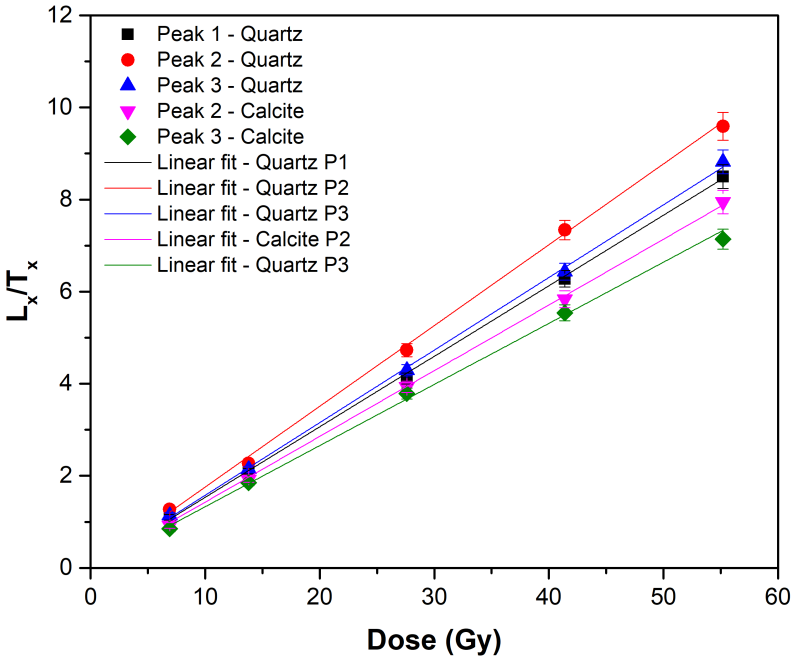

Figure 3.10: Dose–response curves of sensitivity-corrected signals (L_x/T_x) for deconvolution peaks 1–3 of quartz and peaks 2–3 of calcite. The solid lines represent the best-fit linear regressions, with slopes and coefficients of determination reported in the text.

Table 3.8: Average Recovery Ratio (R) values obtained for each deconvolution peak of quartz and calcite. A value close to 1 indicates accurate dose reconstruction. The uncertainty represents the standard deviation of the R values obtained from the 25 aliquots analysed for each material.

Peak	**Quartz** R	**Calcite** R
P1	0.92 ± 0.30	–
P2	0.94 ± 0.27	0.97 ± 0.27
P3	0.96 ± 0.26	0.99 ± 0.27

doses at higher temperatures. The relatively large standard deviations reflect intrinsic variability among aliquots, possibly related to differences in sensitivity changes or signal stability across measurements.

For calcite, recovery was evaluated for peaks P2 and P3, which yielded R values of 0.97 ± 0.27 and 0.99 ± 0.27, respectively. These results confirm the capability of the selected TL components to provide accurate dose estimates under the applied SAR protocol.

3.3.2 Characterization of the Mix_{ref}

To evaluate the dosimetric performance of the proposed methodology under conditions simulating real mortars, the controlled mixture Mix_{ref} of pre-irradiated quartz and calcite grains was analysed. This configuration reproduces the luminescence behaviour expected in historical mortars and provides a test case for applying the deconvolution approach under mixed mineral conditions.

Deconvolution of the TL signals revealed the thermoluminescent compo-

nents of the composite glow curve and allowed extraction of their kinetic parameters, using initial fitting conditions derived from the separate characterization of the reference samples $\mathrm{Qz_{ref}}$ and $\mathrm{Cal_{ref}}$.

As shown in Figure 3.11a, the TL glow curve of a representative mixed aliquot was deconvolved into four distinct peaks. Peak 1 (P_1), centred at approximately 254 °C, is exclusively associated with the quartz component, while peaks 2 (P_2) and 3 (P_3), located around 300 °C and 345 °C respectively, result from the overlap of TL signals emitted by both quartz and calcite. Peak 4 (P_4), observed at temperatures of 417 °C, was excluded from subsequent dose evaluations due to the significant influence of background subtraction in this temperature region, in accordance with the approach adopted for the individual mineral phases.

All the analysed aliquots of the mixture showed TL glow curves that could be consistently described by this same four-peak structure, with peak positions corresponding closely to those identified in the example shown.

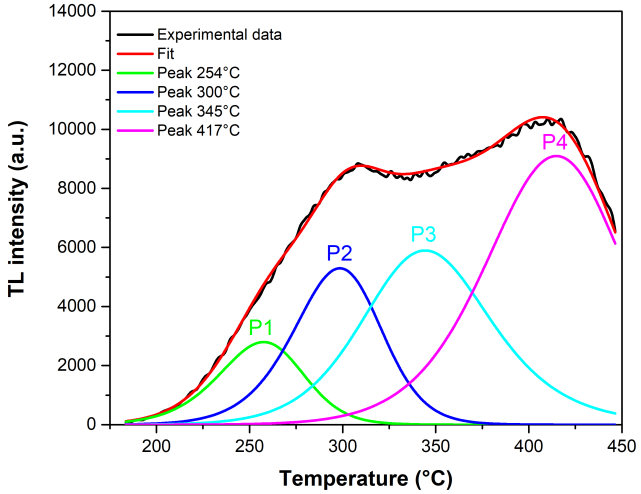

(a) Deconvolution of the TL glow curve of the quartz–calcite mixture. Four peaks were used to model the experimental signal, with a resulting FOM of 1.6%.

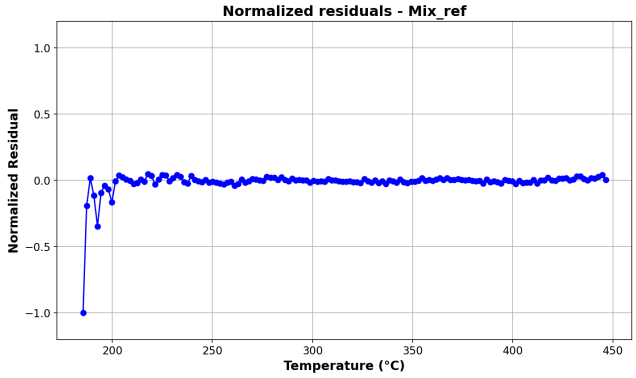

(b) Residuals of the fit expressed as a percentage difference between experimental and modelled data, as a function of temperature.

Figure 3.11: TL signal deconvolution of a mixed aliquot of quartz and calcite. The residuals in panel (b) confirm the overall goodness of fit, with deviations mostly within ±10%. The increased dispersion observed below 227 °C is likely due to the reduced signal-to-noise ratio in this region.

The quality of the fit was first evaluated for the representative aliquot shown in Figure 3.11a, which yielded a FOM of 1.6%. The residuals plotted below the glow curve further support the reliability of the deconvolution, remaining close to zero and mostly within the normalised range of –1 to 1.

Extending the analysis to all aliquots of the mixture, the deconvolution procedure consistently produced FOM values below 2.5%, confirming the robustness of the fitting approach.

The mean kinetic parameters obtained from the deconvolution of the 25 analysed aliquots are summarised in Table 3.9.

Table 3.9: Kinetic parameters obtained from the deconvolution of the TL signal of a mixed quartz-calcite aliquot. T_{m} is the peak temperature, E the activation energy, and b the kinetic order. Uncertainties on T_{m}, E, and b are standard errors derived from the deconvolution fitting.

Peak	T_{m} (°C)	b	E (eV)
P_1	254 ± 4.0	1.42 ± 0.04	1.25 ± 0.04
P_2	300 ± 3.0	1.45 ± 0.03	1.42 ± 0.03
P_3	345 ± 4.0	1.83 ± 0.05	1.37 ± 0.04
P_4	417 ± 4.0	–	–

As indicated in Section 3.2.2.2, the SAR TL protocol was applied to the mixed aliquots. D_e values for peaks P_1, P_2, and P_3 were derived from the deconvoluted signals by interpolation on the corresponding dose–response curves, thus reflecting the irradiation history of the quartz and calcite fractions prior to mixing.

The results are shown in the Radial Plots in Figure 3.12.

Figure 3.12 displays the radial plot representation of the equivalent dose (D_e) values obtained from the deconvolution peaks P_1, P_2, and P_3 in the mixed aliquots. In a Radial Plot, D_e values are shown using a logarithmic scale on the radial axis. The 2σ error for each point is represented on the left side of the plot, while the horizontal scale at the bottom provides a standard orthogonal (x, y) coordinate system that allows evaluating the relative error and precision of each measurement. The equivalent dose corresponding to each point can be directly read from the radial axis on the right, and the central value of the distribution is indicated by a solid line extending from the y-axis of errors to the radial axis.

The distribution of D_e values associated with peak P_1 is centred around $40.04 \pm 0.22\,\mathrm{Gy}$, which, within experimental uncertainty, coincides with the irradiation dose applied to quartz prior to mixing. This supports the interpretation that peak P_1 in the deconvolution of the mixed TL signal originates exclusively from the quartz component.

The D_e values obtained from peak P_2 also cluster around a central value of $40.12 \pm 0.30\,\mathrm{Gy}$. The agreement with the D_e values of peak P_1 confirms that the second peak, although associated with contributions from both minerals, is still predominantly influenced by quartz luminescence.

In contrast, the D_e values related to peak P_3 show a systematic shift toward higher values, centring around $50.02 \pm 0.35\,\mathrm{Gy}$. This increase reflects the growing contribution from the calcite fraction in this temperature region,

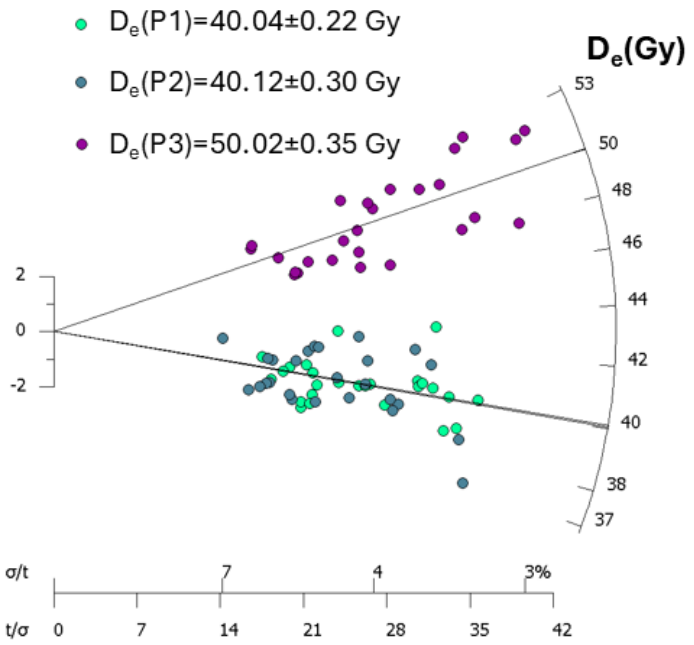

Figure 3.12: Radial plot showing the distribution of equivalent dose (D_e) values obtained from the deconvolution peaks P_1, P_2, and P_3 in the mixed aliquots. Each point represents a single D_e measurement. The radial axis on the right gives the dose in Gy on a logarithmic scale, while the bottom axis expresses the relative error. The solid line indicates the central value of the distribution.

which retains a higher residual signal due to its distinct irradiation history. The displacement of the $D_e(P_3)$ population relative to $D_e(P_1)$ and $D_e(P_2)$ on the radial scale confirms the difference in the luminescence signal contributions within these peaks.

Based on the distributions of the equivalent dose values associated with each deconvolution peak, and considering the relative contributions of quartz and calcite to the composite signal, the specific contribution of calcite was isolated. This was achieved by calculating the difference between the D_e of peak P_3 and those of P_1 and P_2. The resulting differential values are shown in the Radial Plot of Figure 3.13, where the reference line corresponds to the known irradiation dose of calcite in the mixture (10.40 ± 0.20 Gy).

Each data point represents an individual D_e value obtained by subtracting the contributions of P_1 and P_2 from that of P_3. The data are distributed around a central value that, within the experimental uncertainty, coincides with the known calcite dose. Specifically, the resulting central values are 10.26 ± 0.49 Gy for $D_e(P_3 - P_1)$ and 10.46 ± 0.56 Gy for $D_e(P_3 - P_2)$, both of which are in excellent agreement with the reference dose.

This result confirms that the proposed differential method allows for the isolation of the calcite signal within the mixed TL response. By subtracting the contributions associated with quartz-only peaks (P_1 and P_2) from the mixed peak (P_3), it is possible to reconstruct the absorbed dose of the carbonate fraction in the mixture with good accuracy.

The equivalent dose (D_e) derived from peak 1 of quartz reflects the laboratory dose administered to the quartz fraction prior to mixing, and in this experimental framework it can be regarded as an analogue of the residual dose

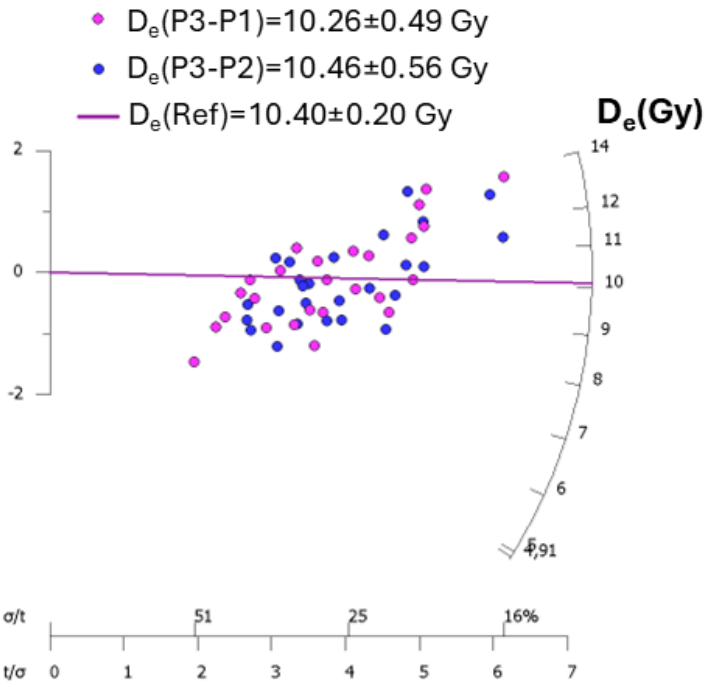

Figure 3.13: Radial Plot showing the distributions of equivalent dose differences used to isolate the calcite signal: $D_e(P_3 - P_1) = 10.26 \pm 0.49\,\text{Gy}$ and $D_e(P_3 - P_2) = 10.46 \pm 0.56\,\text{Gy}$. The solid reference line indicates the known irradiation dose of calcite in the mixture, $10.40 \pm 0.20\,\text{Gy}$. The clustering of the data points around this value confirms the feasibility of isolating the carbonate contribution by subtraction.

expected in incompletely bleached grains.

Conclusions

The methodological study presented in this chapter allowed a detailed characterisation of the TL response of quartz (sample Qz_{ref}) and calcite (sample Cal_{ref}), both individually and in controlled mixtures (sample Mix_{ref}).

The deconvolution analyses of the monocrystalline fractions confirmed the presence of reproducible peaks in the 250–350 °C range, whose kinetic parameters are consistent with values reported in the literature. Peak P1 was found to be specific to quartz, while peaks P2 and P3 were common to both minerals, showing comparable activation energies and kinetic orders. Dose recovery tests demonstrated that the selected TL components provide accurate and stable estimates of the administered laboratory doses, with recovery ratios close to unity. In addition, dose–response analyses confirmed the linearity of the main peaks, supporting their dosimetric reliability.

The analysis of the controlled mixture (Mix_{ref}) showed that the TL contributions of quartz and calcite can be discriminated through deconvolution. In particular, the differential approach applied to peaks P2 and P3 enabled the isolation of the carbonate signal, with results in excellent agreement with the known irradiation dose of calcite. This finding is particularly relevant, as it demonstrates the feasibility of extracting carbonate-specific information from complex luminescence signals.

Overall, the results of this methodological investigation provide a robust experimental and analytical basis for the application of the proposed approach to archaeological mortars. The characterisation of the reference samples demonstrated that the luminescence signals of quartz and calcite can be reliably deconvolved, yielding consistent kinetic parameters and enabling the discrimination of their respective contributions even in mixed systems. The analysis of the controlled mixture further confirmed the feasibility of isolating the carbonate fraction, which is the target dosimeter for the dating of mortars.

Starting from these results, the following chapter presents the application of the developed deconvolution methodology to archaeological samples collected from historical mortars. This case study represents a crucial step in testing the methodology under real conditions, where luminescence signals are more complex due to the geological variability of the minerals and the effects of partial bleaching. The analysis will address these challenges and assess the potential of the proposed approach for deriving reliable equivalent dose estimates in mortars.

4 Case study: application of the methodological approach to mortars from the *Terme della Rotonda* (Catania, Italy)

The methodological framework developed in Chapter 3 is here applied to archaeological mortars collected from the site of the *Terme della Rotonda* in Catania. This case study represents a crucial step of the research, as it allows the assessment of the feasibility of the proposed TL-based approach when applied to complex historical materials, through its direct comparison with the SG-OSL technique, which currently serves as the reference method for mortar dating with luminescence.

The chapter is structured into four main sections. A preliminary part introduces the archaeological site, outlining its historical context, architectural stratigraphy, and the sampling strategy adopted for the mortars analysed in this study. This information provides the necessary framework to interpret the luminescence results in relation to the construction phases of the building.

The first section presents the determination of the equivalent dose (D_e) by means of SG-OSL, applied to the coarse-grain quartz fraction extracted from the mortars, hereafter denoted as $\mathrm{Mor}_{\mathrm{qz}}$. This technique is adopted because it currently provides the most reliable estimates of D_e in mortar dating, and therefore offers reference values against which the TL-based results can be compared.

The second section focuses on the application of the methodological basis introduced in Chapter 3 to the TL signals of unprepared mortars, denoted as $\mathrm{Mor}_{\mathrm{unprep}}$.

In this case, deconvolution procedures are applied to the composite TL glow curves in order to isolate the contributions of the quartz and carbonate fractions, from which an estimate of D_e can be derived. Since the two approaches involve different preparation protocols, distinct luminescent fractions, and independent measurement systems, both sections include a detailed description of sample preparation, the experimental procedure, and the subsequent data analysis carried out to extract the D_e values. In particular, the TL measurements were carried out at the *PH3DRA laboratories* (Physics for Dating Diagnostics Dosimetry Research and Applications) of the University of Catania, while the SG-OSL measurements were performed at the *Archéosciences Bordeaux* laboratory, Université Bordeaux Montaigne, using different instrumentation and procedures specific to each facility.

The third section is dedicated to the determination of the annual dose rate, which is common to both methods. Although no original methodological development was carried out in this part of the work, it provides the dosimetric framework required to transform D_e values into absolute ages.

Finally, the chronological framework of the *Terme della Rotonda* is reconstructed by combining the equivalent and annual dose estimates. The results obtained from SG-OSL and TL are compared, and their consistency and differences are critically discussed in order to assess the reliability and potential of luminescence dating applied to archaeological mortars.

4.1 Archaeological context and mortar sampling at the *Terme della Rotonda*

The choice of the *Terme della Rotonda* in Catania as a case study was motivated by several factors. First, the complex represents one of the most significant archaeological sites in the city, characterised by multiple construction phases ranging from the Roman to the Byzantine and medieval periods, thus offering an articulated chronological framework against which luminescence ages can be evaluated. Second, the preservation of both heated environments (e.g., *calidarium* and *frigidarium*) and unheated spaces provides an opportunity to assess the effect of prolonged thermal exposure and different light conditions on the luminescence signals of mortars. Third, the mortars are generally well preserved, which allows both the extraction of quartz grains for SG-OSL analyses and the study of bulk carbonate fractions through TL measurements. Finally, the availability of independent archaeological and historical information enables a direct comparison with luminescence results, making the site an ideal benchmark to explore the potential and limitations of the proposed approach applied to historical mortars.

The archaeological site is located in the historic center of Catania and is centered around a square building with a domed circular hall, known as the *Rotonda*, which constitutes the only portion of the complex still covered by masonry. The overall layout of the complex is illustrated in Fig. 4.1, which presents a digital reconstruction of the preserved structures and surrounding archaeological remains.

Figure 4.1: Digital reconstruction of the *Terme della Rotonda* complex in Catania, showing the preserved Rotonda building and the surrounding archaeological remains. The image provides a general overview of the site morphology and the spatial arrangement of the thermal structures [120].

Archaeological investigations have demonstrated that the structure was originally part of a Roman bath complex built in multiple phases. The earliest construction is dated to the 1st–2nd century AD (First Roman Phase), with substantial modifications during the 3rd–4th centuries AD (Second Roman Phase). The complex appears to have been abandoned between the end of the 6th and the first half of the 7th century AD, after which it was reused and possibly converted into a church during the Byzantine period [120, 121].

The preserved architectural elements, including underfloor heating systems (*pilae*), vertical terracotta tubes (*tubuli*), and immersion pools, support the interpretation of the site as a thermal facility. The functional layout of Roman baths typically consisted of a gradual sequence from cold to hot environments, including a *frigidarium*, a *tepidarium*, and a *calidarium* equipped with hypocaust systems and heated pools. In the plan of the *Terme della Rotonda* (Fig. 4.2), the circular hall (C) has been identified as the *frigidarium*, while the southern rooms (A, B1, B2, B3, E, F, D), which preserve evidence of hypocaust systems, correspond to the *calidaria* and other heated areas. The remaining intermediate rooms may have served as *tepidaria* [120]. Most of these structures were uncovered during modern excavations and are now exposed to the open air, whereas the central hall remains enclosed under its original dome. This distribution of thermal features provides a key criterion when assessing the degree of luminescence signal resetting in the sampled mortars.

The functional organisation of the complex and the corresponding sampling areas are illustrated in the plan reported in Fig. 4.2. The color-coded areas correspond to the construction phases identified by Branciforti [121]: purple for the First Roman Phase, orange for the Second Roman Phase, green for the Byzantine period, and blue for later medieval modifications.

This stratigraphic framework was taken into account when evaluating each sample.

Sampling operations were carried out in collaboration with the building engineers responsible for the structural assessment of the site, to obtain specimens representative of the original construction materials and unaffected by later restorations or repairs. All collected mortars correspond to filling materials, directly associated with the primary construction phases. Given their high hardness and compactness, the mortars were sampled manually using a hammer and chisel, allowing the controlled removal of small fragments without compromising the integrity of the structure.

Whenever possible, irregular fragments measuring a few centimetres in length and width and at least 1 cm in thickness were extracted to a comparable depth, providing sufficient material (ideally 50–60 g) for both quartz extraction and bulk analyses. The sampling depth was selected to allow the subsequent removal of the superficial millimetres in the laboratory, ensuring the isolation of an unexposed inner core suitable for luminescence measurements.

Particular care was taken to avoid contamination from surface materials and to minimise exposure to daylight during extraction, as the luminescence signal records the last light exposure experienced by the material. Sampling was therefore carried out on inner portions of the walls, and the extracted fragments were immediately wrapped in aluminium foil to prevent accidental bleaching.

A summary of the collected mortar samples, including their presumed chronological attribution and thermal classification is reported in Table 4.1.

Table 4.1: Summary of the six mortar samples collected from the *Terme della Rotonda* complex. The table reports the classification of the sampling area as thermally affected (Hot) or unheated (Cold) and the presumed chronological attribution. Sample codes indicate the sector of provenance (e.g., Rot_B1, Rot_C, Rot_D) and the progressive number of the collected mortar specimen (M1, M3, etc.).

Sample Code	Thermal Zone	Presumed Age
Rot_B1_M1	Hot	1st century AD
Rot_D_M3	Hot	3rd century AD
Rot_D_M5	Hot	3rd century AD
Rot_C_M11	Cold	1st century AD
Rot_C_M12	Cold	1st century AD
Rot_C_M14	Cold	7th century AD

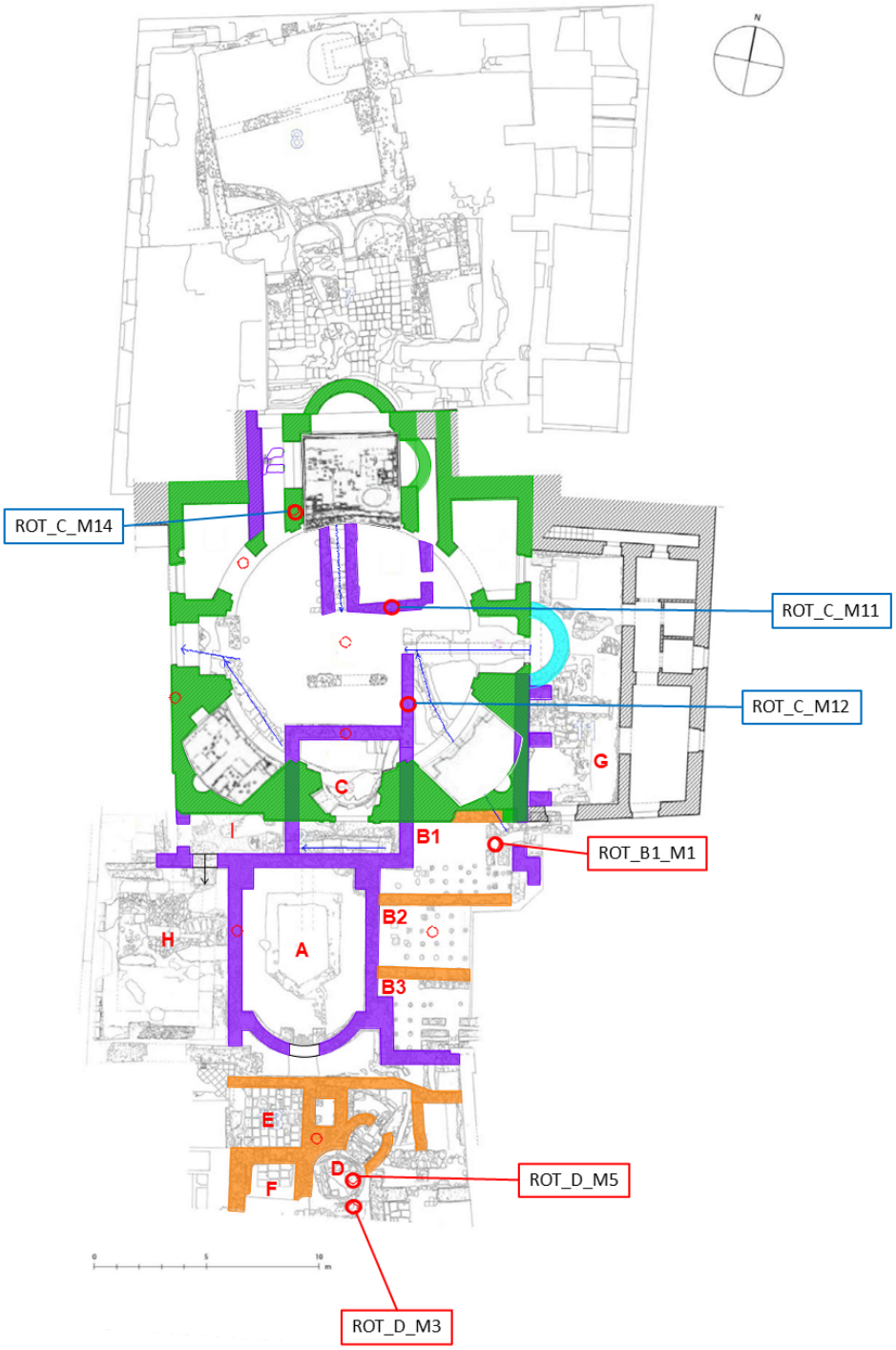

Figure 4.2: Plan of the *Terme della Rotonda* complex indicating the functional distribution of the thermal rooms (frigidarium, calidaria, tepidaria), together with the location and codes of the six collected mortar samples. The different colors correspond to the construction phases proposed by Branciforti [121]: purple = 1st–2nd century AD (First Roman Phase), orange = 3rd century AD (Second Roman Phase), green = 7th century AD (Byzantine period), and blue = late medieval modifications.

Mortars were subsequently prepared following two distinct strategies. Each of the six collected samples was divided into two portions: one portion was processed to extract quartz grains (200–250 µm), hereafter referred to as $\mathrm{Mor_{qz}}$, for SG-OSL measurements and the determination of independent D_e estimates through established procedures. The other portion was analysed as bulk powder, hereafter referred to as $\mathrm{Mor_{unprep}}$, in order to investigate the luminescence signal associated with the carbonate fraction and the residual quartz, and to apply the TL approach developed in this thesis.

4.2 D_e determination using SG-OSL on extracted pure quartz

SG-OSL measurements were carried out on the coarse-grain quartz fraction extracted from the mortars ($\mathrm{Mor_{qz}}$). This approach provides independent estimates of the D_e and represents the reference framework against which the TL-based results can be compared.

The following subsections describe the preparation of the quartz extracts, the measurement procedure, the criteria adopted for data analysis and the D_e results.

4.2.1 Materials for SG-OSL: $\mathrm{Mor_{qz}}$

The quartz used for SG-OSL dating was extracted from mortar samples through a chemical and physical preparation procedure. The aim of this procedure was to isolate quartz grains in the 200–250 µm size fraction that were not exposed to light during sampling, under the assumption that the coarser fraction is better bleached in the case of mortar [58, 57]. To achieve this, compact mortar samples were first carefully processed: the outermost portion, which may have been briefly exposed to light during sampling, was removed using manual tools such as a metal file, as this approach minimises the risk of contaminating the inner material.

After removing the external layer, the internal part of the sample was gently crushed into powder and dry-sieved to obtain the fraction below 500 µm. The sample was then treated with a 10% HCl solution for 120 minutes to remove carbonate phases. To ensure complete dissolution, a second identical treatment was applied. After thorough rinsing with distilled water, a 30% H_2O_2 solution was used to remove organic matter over a 48-hour period.

Subsequently, feldspar separation was carried out by immersion in a mixture of H_2SiF_6 and HNO_3 in a 9:1 volume ratio for one week [75]. If residual feldspar grains were identified during OSL measurements, the acid etching procedure was repeated for an additional week. After a final rinse in distilled water, the purified grains were dried and sieved to obtain the coarse-grain fraction in the range of 200–250 µm.

For clarity of notation, $\mathrm{Mor_{SG}}$ refers to the set of mortar samples prepared for SG-OSL measurements. Individual mortars are identified by their field codes (e.g. Rot_B1_M1, Rot_D_M3), which are reported in the corresponding tables.

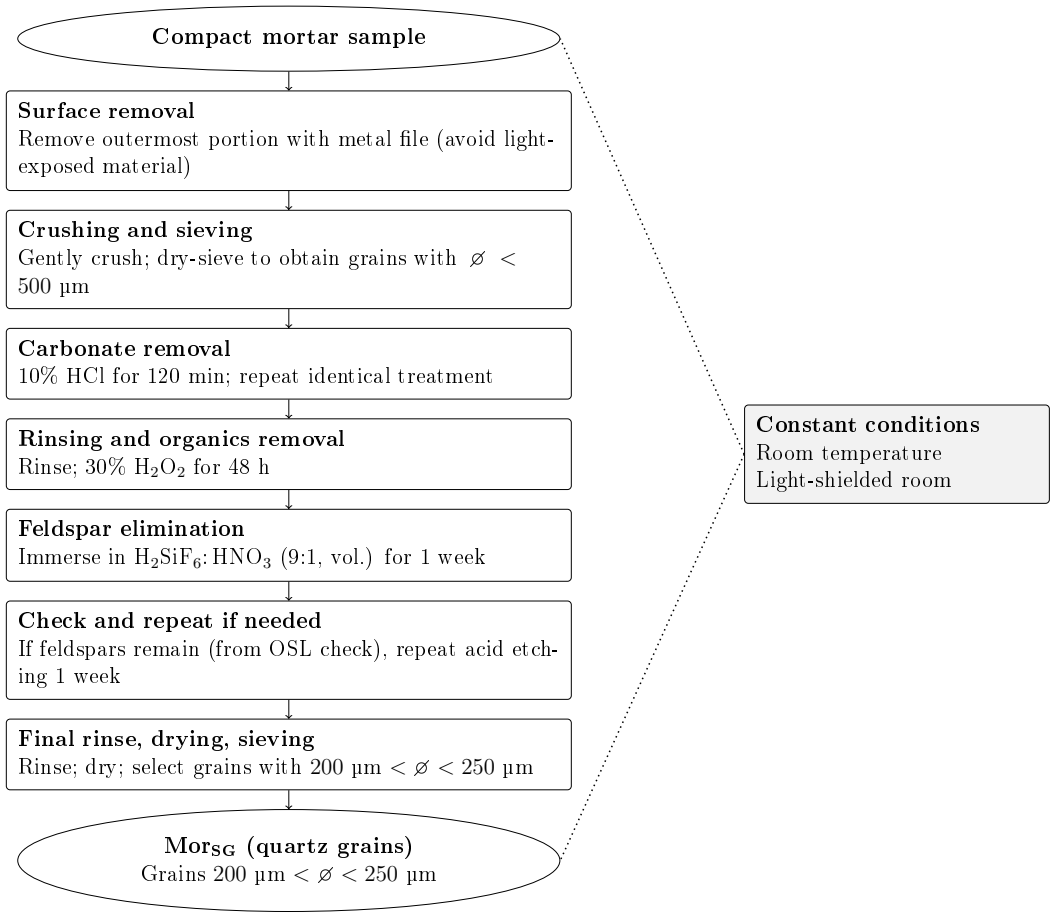

Figure 4.3: Flowchart of the preparation steps for quartz extraction from mortar samples Mor_{SG} for SG-OSL measurements (final fraction 200 µm < ⌀ < 250 µm).

4.2.2 Methods

The description of the methods is organised into three parts: the instrumentation employed for SG-OSL measurements, the measurement protocol adopted for quartz grains, and the data analysis strategy used to derive equivalent dose (D_e) values.

4.2.2.1 Instrument for SG-OSL: Risø TL/OSL DA-20 reader

All single-grain luminescence measurements in this study were performed using a Risø TL/OSL DA-20 reader, specifically designed for SG-OSL analyses (Fig. 4.4).

Figure 4.4: Risø TL/OSL DA-20 reader employed for SG-OSL measurements in this study.

The single-grain (SG) attachment introduces key modifications to the standard configuration, enabling spatially resolved luminescence measurements at the individual grain scale.

The sample carousel of the DA-20 accommodates up to 48 positions, allowing automated handling of single-grain discs during measurement sequences.

In this configuration, standard sample cups are replaced with stainless steel discs, 9.8 mm in diameter, perforated with 100 cylindrical holes arranged in a 10 × 10 matrix. Each hole measures 300 µm in diameter and depth, with a centre-to-centre spacing of 600 µm. Several hundred grains are poured onto the disc, and individual grains are carefully inserted into the holes using a fine brush.

Figure 4.5 shows a quartz grain mounted in one of the disc holes prepared for SG-OSL analysis.

The system also allows conventional TL measurements through a programmable heating unit capable of reaching 700 °C, thus enabling the investi-

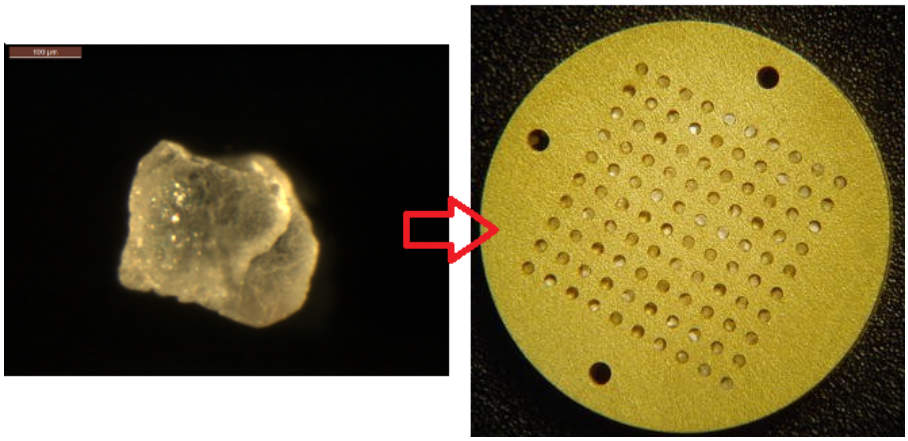

Figure 4.5: A quartz grain mounted on a single-grain disc with holes of 300 µm in diameter. Each disc contains 100 holes arranged in a 10 × 10 grid and has a total diameter of 9.8 mm. Adapted from [122].

gation of both optically and thermally stimulated luminescence signals when required.

Optical stimulation in SG-OSL mode is provided by a solid-state Nd:YVO_4 diode-pumped laser emitting at 532 nm with a nominal power of 10 mW. The intensity is regulated by a software-controlled neutral density filter, while an electromechanical shutter governs access to the measurement chamber. The laser is focused through three lenses to a ∼20 µm spot at the sample plane. Beam steering is achieved by two motor-driven mirrors with position encoders, allowing accurate targeting of each grain location with a precision better than 3 µm. This configuration enables automated sequential stimulation of the 100 grain positions on the disc.

A schematic representation of the system is shown in Fig. 4.6.

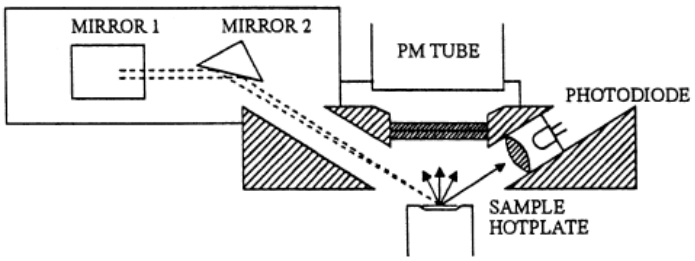

Figure 4.6: Schematic diagram of the optical detection system of the Risø TL/OSL DA-20 reader, showing the sample hotplate, the beam steering mirrors, the photomultiplier tube (PMT), and the photodiode used for signal detection. Adapted from [73].

To ensure precise alignment, three larger holes located at the disc periphery serve as reference points. During calibration, the laser scans these holes while a photodiode records changes in reflectivity, from which the system calculates the disc centre and rotation angle (better than 2 µm and 0.02°, respectively). During this procedure, the laser operates at only 2% of its maximum power to avoid accidental bleaching. Accuracy tests reported an average positioning error below 35 µm, with maximum deviations slightly above 100 µm, values attributed to disc manufacturing tolerances. In all cases, the laser spot remained

fully contained within the hole, and internal reflections ensured uniform illumination of the grain.

A schematic representation of the sample disc and the corresponding reflectivity signal obtained during the scan is shown in Fig. 4.7.

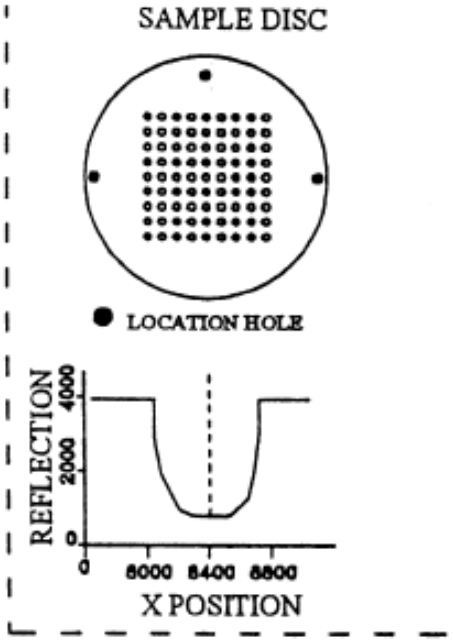

Figure 4.7: Sample disc used in the Risø single-grain OSL attachment. The three larger peripheral holes are employed as reference points for alignment. During calibration, the laser scans these location holes while a photodiode records the reflected signal, allowing the calculation of the disc centre and rotation angle. The graph illustrates the characteristic drop in reflectivity when the laser beam passes over a location hole, which is used for precise positioning. Adapted from [73].

The high power density delivered inside the grain hole (up to 10 W/cm^2) allows rapid depletion of the OSL signal, with quartz typically showing a 50% decrease in less than 0.1 s. Luminescence detection is performed by a PMT EMI 9235QA operated in photon-counting mode, providing high sensitivity to the weak emissions of individual grains. Since the spectral emission of quartz falls within the UV-blue region (centered around 365 nm), a dedicated optical filter was used to selectively detect this signal. The Hoya U-340 filter, characterised by high transmission in the UV-blue range, was employed as the most suitable option.

Figure 4.8 shows the optical filter and its transmittance curve, obtained through spectrophotometric measurements with a Perkin-Elmer Lambda 1050 UV-VIS-NIR spectrophotometer.

Finally, the built-in ^{90}Sr/^{90}Y beta source delivered a dose rate of 6.00 Gy/min (15 July 2024).

For further technical details on the DA-20 system and the SG-OSL attachment, the reader is referred to the comprehensive descriptions available in the literature [12, 73, 123].

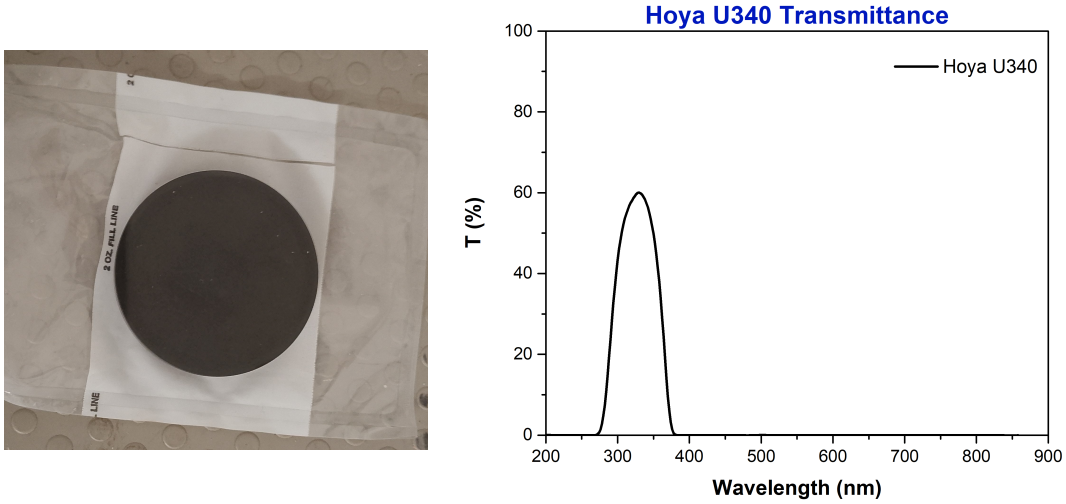

Figure 4.8: Hoya U-340 optical filter used for the detection of quartz emissions in SG-OSL: photograph (left) and measured transmittance curve (right), obtained with a Perkin-Elmer Lambda 1050 UV-VIS-NIR spectrophotometer.

4.2.2.2 Measurements

Quartz grains from sample Mor_{SG}, prepared as described in Section 4.2.1, were mounted on single-grain discs and analysed by SG-OSL with the TL/OSL DA-20 system to determine the equivalent dose.

Equivalent dose determinations were performed with the SAR protocol (refer to Chapter 2, Section 2.4.2).

Preliminary tests were first performed on selected grains to obtain an initial estimate of the expected equivalent dose for each mortar sample. These measurements were carried out under identical SAR conditions for all samples (preheat at 190 °C, cut-heat at 160 °C, test dose of 2.2 Gy, and regeneration doses of 0.6, 1.1, 2.2, 4.4, and 8.8 Gy). The results provided a first evaluation of the dose range and were used to guide the selection of the definitive regeneration dose schemes subsequently applied to each sample.

Based on these tests, the SAR parameters were carefully optimised for young samples. Due to the young age of the samples and their correspondingly low sensitivity, the test dose had to be set much higher than the expected archaeological dose compared to the standard SAR protocol [13, 124]. Applying a very low test dose would have resulted in a loss of response to the optical stimulation. Instead, higher test doses were applied to ensure reliable detection: 2.2 Gy for most samples, and 2.5 Gy for sample *Rot_D_M3* [13].

A preheat of 190 °C was selected to enhance signal reproducibility while avoiding thermal destabilisation of low-temperature traps [125], and a cut-heat of 160 °C was adopted to minimise thermal transfer that could bias the dose estimates [13, 7, 126].

As part of the quality control, a zero-dose was administered at the end of the sequence to check for recuperation, and the first regeneration dose was repeated to perform the recycling test. Further details on these procedures are provided in Chapter 2, Section 2.4.2.1. The definitive regeneration dose parameters used for each sample are listed in Table 4.2.

Table 4.2: Measurement parameters used for the determination of equivalent doses in the SG-OSL analysis of quartz grains extracted from mortars.

Sample	Preheat (°C)[a]	Cut-heat (°C)	Test dose (Gy)	Regeneration doses (Gy)[b]
Rot_B1_M1	190	160	2.2	1.1, 1.7, 2.8, 3.9, 6.6, 0, 1.1
Rot_D_M3	190	160	2.5	0.7, 1.3, 2.5, 5.1, 10.2, 0, 0.7
Rot_D_M5	190	160	2.2	0.6, 1.1, 2.2, 4.4, 5.5, 0, 0.6
Rot_C_M11	190	160	2.2	0.7, 1.1, 1.7, 2.8, 5.5, 0, 0.7
Rot_C_M12	190	160	2.2	0.9, 1.3, 2.2, 3.9, 5.5, 0, 0.9
Rot_C_M14	190	160	2.2	0.6, 1.1, 2.2, 4.4, 8.8, 0, 0.6

[a] Preheat applied for 10 s at the indicated temperature with a heating rate of 5 °C/s.
[b] The values of regeneration doses include a zero-dose point and a repeated first dose point, used for recuperation and recycling tests, respectively.

4.2.2.3 Analysis

Single-grain OSL signals were integrated over the first 0.05 s of stimulation and corrected by subtracting the last 0.2 s of the 1 s stimulation interval, in order to isolate the contribution of the fast component . For each grain, the regenerated signals (L_x/T_x) were normalised to the test dose and fitted with a linear function to construct the individual growth curve. The D_e was then obtained by projecting the natural signal (L_N/T_N) onto this curve. When the natural signal fell within the range of regeneration doses, D_e was estimated by interpolation.

The uncertainty on each individual D_e, calculated with the Analyst software (version 4.57), includes contributions from counting statistics, interpolation of the regenerated doses, and instrumental reproducibility. The latter was fixed at 2.7% in accordance with previous studies, reflecting the performance of the Risø system [13].

Grains were retained for analysis based on the following criteria, commonly adopted in SG-OSL studies [12, 13, 126, 127, 128]:

1. The error associated with the T_N signal was less than 30%;
2. The signal was more than 3σ above background.

These criteria were applied to exclude grains affected by poor signal-to-noise ratios or by large uncertainties in the sensitivity correction, conditions that would compromise the reliability of the equivalent dose calculation. Their application ensures that only grains providing reproducible and statistically robust OSL signals contribute to the final equivalent dose distribution. The impact of these selection criteria on the final equivalent dose was assessed by comparing the values obtained from all grains yielding a measurable signal with those derived from the subset of grains that met the selection requirements. In this study, no significant differences were observed between the two estimates.

The equivalent dose values obtained from the accepted grains were represented using both radial and density plots, which enabled a visual evaluation of the scatter in the data. The dispersion of individual equivalent doses, often larger than what can be explained by analytical uncertainties alone, is described by the *overdispersion* (OD). As the OD reflects factors such as heterogeneous bleaching or intrinsic grain properties, it was considered as an indicator of the degree of bleaching and of the microdosimetric heterogeneity

of the sample. In this study, OD values were obtained with the RadialPlotter software [129], which was also used to generate the radial plots and the density plots employed for the analysis. On the basis of the observed OD, either the Central Age Model (CAM) or the Minimum Age Model (MAM) was applied to derive the most reliable estimate of the equivalent dose distribution for each sample (please refer to Chapter 2, Section 2.4.3).

4.2.3 D_e results

As reported by several studies on SG-OSL applied to historical mortars [13, 126], only a small fraction of the extracted grains is capable of producing a measurable luminescence signal upon optical stimulation.

In this study, the percentage of grains showing a detectable luminescence response was evaluated for each sample, corresponding to the ratio between the number of accepted grains and the total number of analysed grains. The results are summarised in Table 4.3.

Table 4.3: Summary of SG-OSL analysis: number of total and accepted grains, percentage of luminescent grains, test dose, and regeneration dose set used in the SAR protocol.

Sample	**#Measured grains**	**Accepted grains (%)**
Rot_B1_M1	2300	2.7
Rot_D_M3	4200	1.8
Rot_D_M5	3500	1.5
Rot_C_M11	1900	3.7
Rot_C_M12	1100	5.7
Rot_C_M14	5900	1.1

The number of measured grains varied considerably among the analysed samples, ranging from about 1100 (Rot_C_M12) to nearly 5900 (Rot_C_M14), depending on the amount of material available for mounting. The proportion of accepted grains was between 1.1% and 5.7%.

These values fall within the range commonly reported for historical mortars [126, 90, 76, 75]. Rot_C_M12 displayed the highest proportion of accepted grains (5.7%), which may reflect more favourable bleaching conditions or the presence of a quartz fraction with higher luminescence sensitivity. In contrast, Rot_C_M14 yielded the lowest percentage (1.1%), indicating a more restricted population of quartz grains suitable for single-grain analysis.

Despite these differences, the absolute number of accepted grains was sufficient in all cases to ensure a statistically reliable assessment of the equivalent dose distributions, which are discussed in the following section.

D_e values for the investigated mortars were determined by applying the SAR protocol under the measurement conditions described in Section 4.2.2.2.

To explore the distribution of single-grain equivalent doses, density plots were constructed for each of the six samples (Figure 4.9). To complement this approach, radial plots were employed to simultaneously visualise the spread of D_e values and their associated uncertainties (please refer to Chapter 2, Section 2.4.3.3).

This dual representation allows both the shape of the dose distribution and the internal scatter of the dataset to be evaluated. It also provides a robust framework for the application of statistical models such as the Central Age Model (CAM) and the Minimum Age Model (MAM)(please refer to Chapter 2, Section 2.4.3).

For sample *Rot_B1_M1*, the histogram displays a unimodal profile with a relatively symmetric shape centred around intermediate doses. The KDE curve confirms the dominance of a single grain population. In the corresponding radial plot, however, a wide scatter of the points is observed, reflecting high overdispersion (OD). This indicates that despite the unimodal appearance of the density plot, the dataset is affected by substantial internal variability, which could be attributed to incomplete bleaching or microdosimetric heterogeneities.

Sample *Rot_D_M3* shows a markedly broader and more heterogeneous distribution. The histogram reveals a main peak at lower D_e values with a long tail extending toward higher doses, while the KDE highlights the asymmetry and suggests the coexistence of multiple grain populations. The radial plot confirms this interpretation, showing a spread of data points with high OD values, consistent with variable bleaching conditions.

The equivalent dose distribution of *Rot_D_M5* is clearly bimodal, with two distinct peaks: a dominant mode at lower doses and a second, well-developed mode at higher values. The KDE curve emphasises this dual structure, indicating at least two grain populations with different exposure histories. The radial plot further supports this view, displaying a wide scatter of points distributed in two distinct clusters, again pointing to heterogeneous bleaching.

For sample *Rot_C_M11*, the histogram is unimodal. Both the histogram and KDE indicate a single grain population with very limited dispersion. This observation is reinforced by the radial plot, which shows a dense cluster of points with low OD values, suggesting a more uniform bleaching conditions and a homogeneous dosimetric environment.

The distribution of *Rot_C_M12* is also unimodal, with a bell-shaped profile and a single central peak. The KDE confirms the absence of secondary modes. The radial plot mirrors this behaviour, showing a compact distribution of points with low OD.

Finally, sample *Rot_C_M14* displays a unimodal distribution with moderate dispersion around the central values. The KDE curve supports this observation, showing a symmetric peak with minor skewness. The radial plot indicates a slightly broader scatter than *Rot_C_M11* and *Rot_C_M12*, but still significantly more compact than the bimodal distribution of *Rot_D_M5*. This suggests overall homogeneous bleaching conditions, with only limited internal variability.

In summary, the combined use of density plots and radial plots highlights the contrast between samples affected by heterogeneous bleaching (*Rot_B1_M1*, *Rot_D_M3*, *Rot_D_M5*) and those characterised by compact and uniform equivalent dose distributions (*Rot_C_M11*, *Rot_C_M12*, *Rot_C_M14*). Elevated OD values in the first group are commonly linked to incomplete or heterogeneous bleaching during mortar preparation or to microdosimetric heterogeneities due to uneven radioelement distribution at the grain scale [13, 75].

OD is a key criterion for model selection in equivalent dose (D_e) evaluation

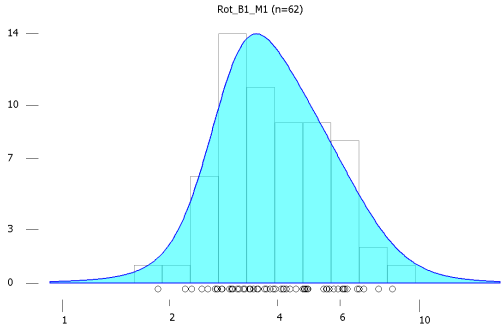

(a) Density plot (Rot_B1_M1)

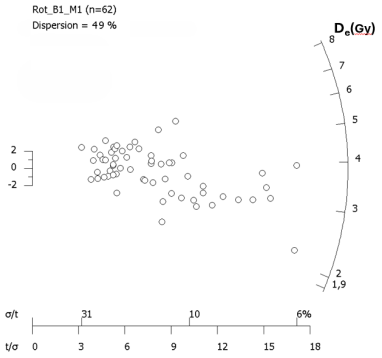

(b) Radial plot (Rot_B1_M1)

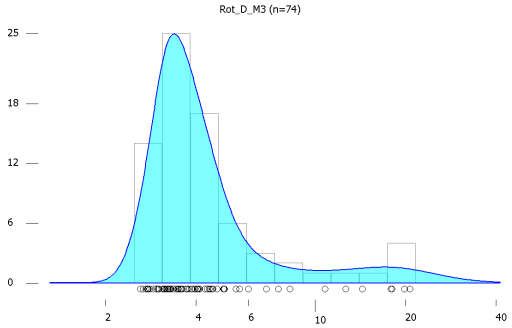

(c) Density plot (Rot_D_M3)

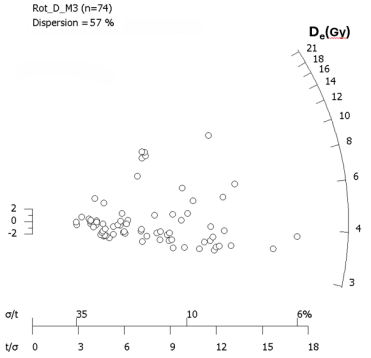

(d) Radial plot (Rot_D_M3)

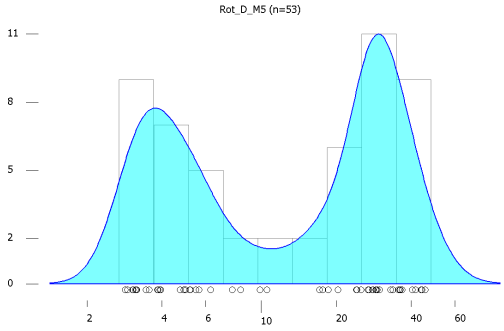

(e) Density plot (Rot_D_M5)

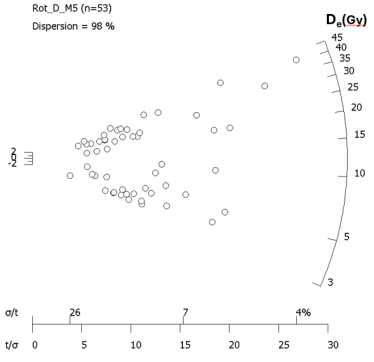

(f) Radial plot (Rot_D_M5)

Figure 4.9: Density and radial plots of the equivalent dose (D_e) for the six mortar samples. Each row shows the density distribution on the left and the corresponding radial plot on the right.

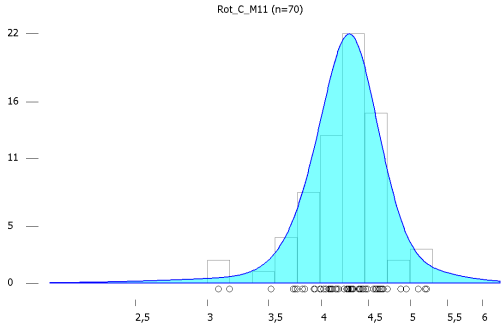

(g) Density plot (Rot_C_M11)

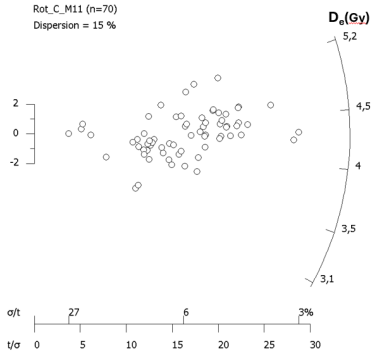

(h) Radial plot (Rot_C_M11)

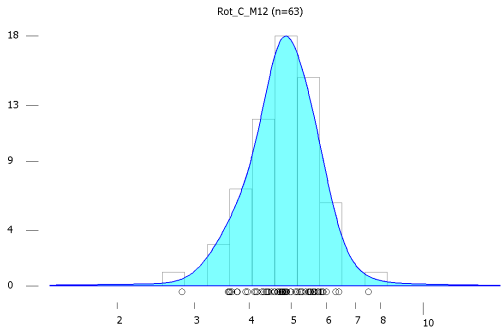

(i) Density plot (Rot_C_M12)

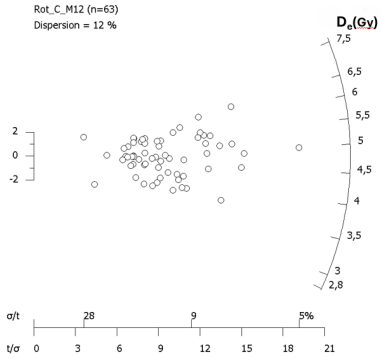

(j) Radial plot (Rot_C_M12)

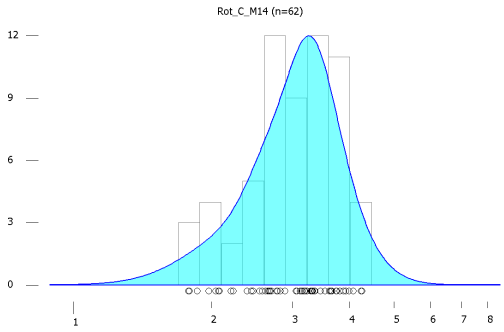

(k) Density plot (Rot_C_M14)

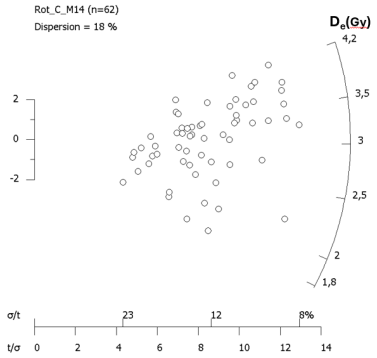

(l) Radial plot (Rot_C_M14)

Figure 4.9: Density and radial plots of the equivalent dose (D_e). Continued.

[126]. Values approaching or exceeding 50% are considered critical, as they are unlikely to result from measurement error and instead reflect incomplete bleaching or microdosimetric variability [13]. For this reason, in this study samples with OD $< 50\%$ were treated with the Central Age Model (CAM), assuming a distribution dominated by well-bleached grains. For OD values around 50% or higher, the Minimum Age Model (MAM) was applied [89, 13]. The OD estimates, the selected model, and the resulting D_e values are summarised in Table 4.4.

Table 4.4: OD values, statistical model applied, and equivalent dose (D_e) for each sample.

Sample	**OD (%)**	**Model**	D_e **(Gy)**
Rot_B1_M1	49	MAM	3.86 ± 0.16
Rot_D_M3	57	MAM	3.30 ± 0.10
Rot_D_M5	98	MAM	3.46 ± 0.10
Rot_C_M11	15	CAM	4.29 ± 0.37
Rot_C_M12	12	CAM	4.70 ± 0.10
Rot_C_M14	18	CAM	3.04 ± 0.10

The results in Table 4.4 highlight the variability among the analysed mortars. Samples *Rot_B1_M1*, *Rot_D_M3*, and *Rot_D_M5* show OD values well above the 50% threshold, supporting the use of the Minimum Age Model (MAM).

In contrast, *Rot_C_M11*, *Rot_C_M12*, and *Rot_C_M14* present OD values below 20%, indicating that most grains were adequately reset before burial. These samples were therefore modelled using the Central Age Model (CAM). The corresponding D_e values show low uncertainties, supporting the reliability of these age estimates.

4.3 D_e determination using TL-based approach on unprepared mortars

The following sections present the application of the results derived from the methodological study discussed in Chapter 3 to the mortar.

TL measurements were performed on bulk mortar samples subjected to a minimal preparation procedure.

This approach enables the determination of D_e values through the analysis of glow curves, thus providing a complementary framework for comparison with the SG-OSL results.

The following subsections describe the adopted preparation protocol, the measurement procedure, the strategy for curve analysis and deconvolution, and the D_e values obtained from the thermoluminescence signals.

4.3.1 Materials for TL-based approach: $\text{Mor}_{\text{unprep}}$

A portion of the six mortars collected from the *Terme della Rotonda* was used for the application of the TL methodology on bulk material, referred to

as $\mathrm{Mor}_{\mathrm{unprep}}$. Unlike $\mathrm{Mor}_{\mathrm{SG}}$, these samples were examined in their untreated state, without any etching or mineralogical separation.

Before measurement, the outermost 2 mm were removed to eliminate material potentially exposed to light during sampling. The remaining fraction was gently crushed and sieved to isolate grains in the range of 180–212 µm, without chemical treatment in order to preserve the original mortar composition.

This procedure aimed to verify whether the TL signal of the carbonate fraction can be detected within the complexity of the bulk mortar matrix. The experimental workflow for $\mathrm{Mor}_{\mathrm{unprep}}$ is summarised in Figure 4.10.

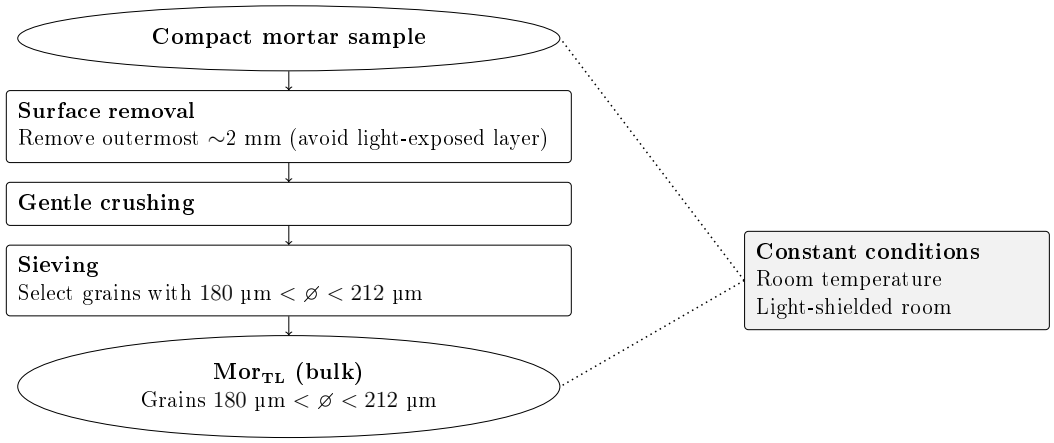

Figure 4.10: Flowchart of the preparation steps for bulk TL measurements on mortar samples $\mathrm{Mor}_{\mathrm{unprep}}$ (final fraction 180 µm $< \varnothing <$ 212 µm); no etching or mineralogical separation was applied.

For clarity of notation, similarly to the SG-OSL samples, $\mathrm{Mor}_{\mathrm{unprep}}$ denotes the group of six mortars subjected to minimal preparation for TL measurements, whereas the individual samples are identified by their field codes (e.g. Rot_B1_M1, Rot_D_M3), as reported in the corresponding tables.

4.3.2 D_e determination methods

This section describes the instrumentation, the luminescence measurement sequences, and the data analysis performed on the $\mathrm{Mor}_{\mathrm{unprep}}$ samples.

4.3.2.1 Instrument for TL-based approach

The TL measurements on the $\mathrm{Mor}_{\mathrm{unprep}}$ samples were carried out with the Risø TL/OSL DA-15 reader, operated in the same configuration described in Chapter 3, Section 3.2.1, including the use of the same optical filters.

4.3.2.2 Measurements on $\mathrm{Mor}_{\mathrm{unprep}}$

The six $\mathrm{Mor}_{\mathrm{TL}}$ samples selected for the assessment of the proposed methodology were subjected to a TL measurements.

Unlike the reference samples $\mathrm{Qz}_{\mathrm{ref}}$, $\mathrm{Cal}_{\mathrm{ref}}$, and $\mathrm{Mix}_{\mathrm{ref}}$, which were investigated using artificial signals, the mortars provide a natural signal that directly reflects the dose accumulated in the material. This natural signal was therefore used to derive the equivalent dose.

To date, this study presents the first application of luminescence measurements to unprepared historical mortars, a material for which no standardised measurement protocols currently exist. All acquisition parameters were therefore defined through dedicated experimental tests designed to optimise the procedure for this specific matrix.

Preliminary tests indicated that the untreated sample, when subjected to a high number of heating cycles, underwent a deterioration process that altered its dosimetric properties. Considering the response of the material, two changes in the measurement protocol parameters were therefore required compared to the approach used for the other samples. The maximum stimulation temperature was reduced to 430 °C, which was sufficient to acquire the luminescence signal without producing visible damage, and a simplified regenerative protocol (please refer to Chapter 2, Section 2.4.1) was adopted to limit the number of heating cycles and reduce thermal stress. Tests confirmed the stability of the signal, as no significant variation in the sensitivity correction ratio T_x/T_N was observed.

The choice of the optimal preheating temperature is crucial for the application of the TL regenerative protocol, as it ensures the removal of unstable signal components and minimizes thermal transfer effects. To identify the most suitable condition for each sample, a series of test measurements was performed by comparing the natural TL glow curve with those obtained from artificially irradiated aliquots preheated at increasing temperatures.

For each mortar sample, TL measurements were carried out after irradiation with a dose comparable to the estimated natural equivalent dose. The resulting glow curves were normalized in the intensity interval [0, 1] to enable direct visual comparison, emphasizing similarities in peak shape and position. The optimal preheating temperature was selected as the one for which the normalized artificial glow curve best matched the natural TL signal.

Figure 4.11 shows the results of these comparisons for all six mortar samples. For each sample, the natural TL glow curve is plotted together with the normalized artificial curves acquired at different preheating temperatures, allowing a direct assessment of the homotheticity between the signals.

In sample Rot_B1_M1, a preheating temperature of 240°C produced the best agreement in terms of peak shape and position, while in the case of sample Rot_D_M3 the optimal match was achieved at 250°C.

For sample Rot_D_M5, the best correspondence with the natural signal was observed at 260°C. In the case of samples Rot_C_M11, Rot_C_M12, and Rot_C_M14, the optimal correspondence with the natural glow curve was obtained with a preheating of 210°C, which ensured the best match in terms of both peak position and overall shape of the TL signal.

After selecting the optimal preheating temperature, preliminary tests were performed to define the range of regeneration doses for each mortar sample. For each sample, two aliquots were measured to obtain an approximate equivalent dose by comparing the intensity of the natural signal with that of an artificially induced signal. The resulting estimate was used to choose a set of four to five regeneration doses centred on the expected value and sufficiently spaced to capture the linear response without approaching saturation. This range was then adopted in the subsequent regeneration sequence of the measurement

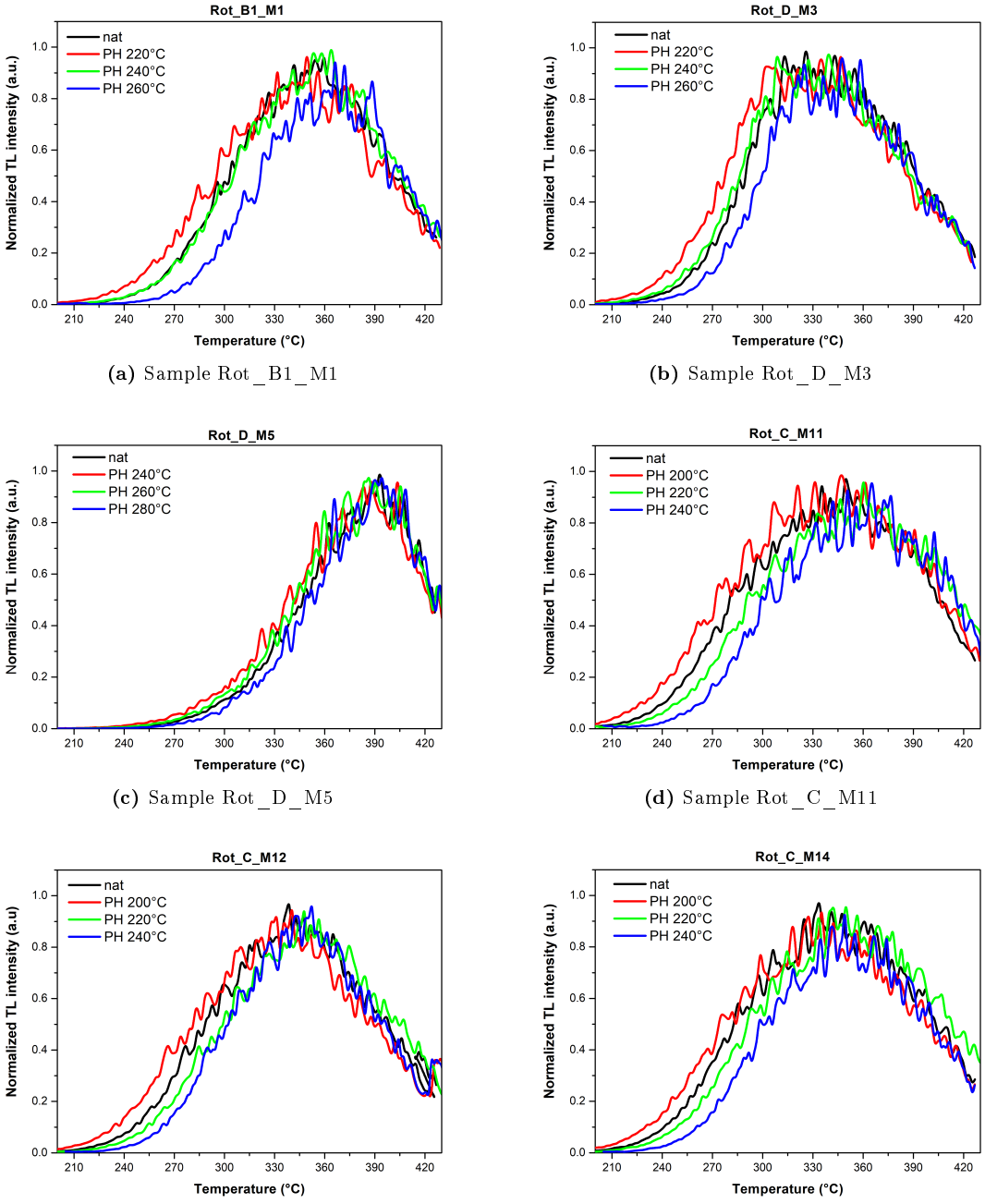

(a) Sample Rot_B1_M1 **(b)** Sample Rot_D_M3

(c) Sample Rot_D_M5 **(d)** Sample Rot_C_M11

(e) Sample Rot_C_M12 **(f)** Sample Rot_C_M14

Figure 4.11: Comparison between normalized TL glow curves obtained after different preheating temperatures and the corresponding natural signal for each mortar sample. The optimal preheating temperature was identified based on the best agreement in curve shape with the natural signal.

protocol.

A summary of the selected preheating conditions for each sample and related TL regeneration parameters is provided in Table 4.5.

Table 4.5: Preheating temperatures and regenerative doses applied for the determination of individual equivalent doses on unprepared mortar samples Mor_{TL}. The preheat was applied for 120 s at the indicated temperature with a heating rate of 5°C/s.

Sample	Preheat (°C)	Regeneration doses (Gy)
Rot_B1_M1	240	6.90, 17.30, 27.60, 38.00
Rot_D_M3	250	10.40, 20.70, 31.10, 41.40, 51.80
Rot_D_M5	260	13.80, 27.60, 41.40, 55.20, 69.00
Rot_C_M11	210	5.50, 11.00, 16.60, 22.10, 27.60
Rot_C_M12	210	10.40, 20.70, 31.10, 41.40, 51.80
Rot_C_M14	210	13.80, 27.60, 41.40, 55.20, 69.00

Finally, TL measurements were carried out on five aliquots per sample using a regeneration sequence in which each dose step was performed individually. The full procedure is reported in Table 4.6.

Table 4.6: Measurement sequence applied during the regenerative protocol on Mor_{TL} samples.

Step	Treatment	Observed
1	Thermal stimulation (@430 °C, 5 °C/s)	L_N
2	Give regeneration dose D_i	–
3	Preheating (@sample-specific temperature, 120 s)	–
4	Thermal stimulation (@430 °C, 5 °C/s)	L_x
5	Repeat steps 2–4 for all regeneration doses	–

4.3.2.3 Analysis

The TL signals of the mortar aliquots were analysed using the same deconvolution workflow adopted in the methodological study on the reference materials. Glow curves were deconvolved into individual components with the *Dosimetric Deconvolution Chart* software, employing as initial parameters the kinetic values previously identified for Mix_{ref}. The fitting and evaluation criteria (residual and FOM) were the same as those described in Section 3.2.3. This ensured methodological consistency and allowed the direct comparison of the deconvolution results from mortars and reference samples.

4.3.3 D_e results

Based on the measurement sequence described in Table 4.6 and the TL regeneration protocol parameters summarised in Table 4.5, thermoluminescence curves were acquired for five aliquots of each analysed mortar sample, reflecting the evolution of the TL signal as a function of the administered dose.

In the case of samples Rot_C_M11, Rot_C_M12, and Rot_C_M14, the regeneration curves (Figure 4.12a, left; Figure 4.12b, left; Figure 4.12c, left) show a progressive increase in TL intensity with dose, confirming both the reproducibility of the luminescence response and the homothetic behaviour of the glow curves as the administered dose increases.

The subsequent deconvolution of the signals revealed four distinct peaks, including a low-temperature component at about 283–285 °C overlapping with the main peaks centred at 315–322 °C and 355–359 °C. As representative examples, the deconvolution of the natural signals, shown together with the corresponding residuals, are presented in Figure 4.12a (right), Figure 4.12b (right), and Figure 4.12c (right).

The residuals remain randomly distributed around zero, without systematic trends, confirming the reliability of the fitting procedure.

All the deconvolutions presented for samples Rot_C_M11, Rot_C_M12, and Rot_C_M14 were considered acceptable only when the Figure of Merit (FOM) was below 2.5%. This criterion ensured high-quality fits, minimizing discrepancies between the experimental data and the reconstructed curves, and guaranteeing consistency across both natural and regenerated signals. The average FOM values obtained from the 5 aliquots were $2.2\% \pm 0.4\%$ for Rot_C_M11, 2.3%±0.4% for Rot_C_M12, and 2.1%±0.4% for Rot_C_M14, confirming the reliability of the deconvolution results.

In the case of samples Rot_B1_M1, Rot_D_M3, and Rot_D_M5, the regeneration curves (Figure 4.13a, left; Figure 4.13b, left; Figure 4.13c, left) display a progressive increase in TL intensity with dose. A clear preservation of the glow-curve shape with increasing dose is observed, with homothetic behaviour of the signals.

The deconvolution of the signals revealed three main components: 315 ± 2 °C, 357 ± 3 °C, and 397 ± 6 °C for Rot_B1_M1; 315 ± 2 °C, 357 ± 2 °C, and 397 ± 5 °C for Rot_D_M3; and 317 ± 3 °C, 359 ± 2 °C, and 397 ± 10 °C for Rot_D_M5. Representative deconvolutions of the natural signals, together with the corresponding residuals, are shown in Figure 4.13a (right), Figure 4.13b (right), and Figure 4.13c (right).

The residuals remain symmetrically distributed around zero without systematic deviations, confirming the robustness of the fits. All deconvolutions for Rot_B1_M1, Rot_D_M3, and Rot_D_M5 were accepted only when the FOM was below 3%. The mean values obtained from the five aliquots were $1.8\% \pm 0.4\%$ for Rot_B1_M1, $2.2\% \pm 0.3\%$ for Rot_D_M3, and $1.9\% \pm 0.4\%$ for Rot_D_M5, further supporting the reliability of the deconvolution procedure.

The parameters obtained from the deconvolution of TL glow curves for the analysed mortar samples are summarised in Table 4.7. For each identified peak, the table reports the maximum temperature T_m, the activation energy E, and the kinetic order parameter b. The high-temperature peak centred at $T_m \approx 397$ °C was identified in all samples but excluded from the analysis of kinetic parameters, since at high temperatures the influence of background subtraction becomes significant and may introduce additional errors in the results.

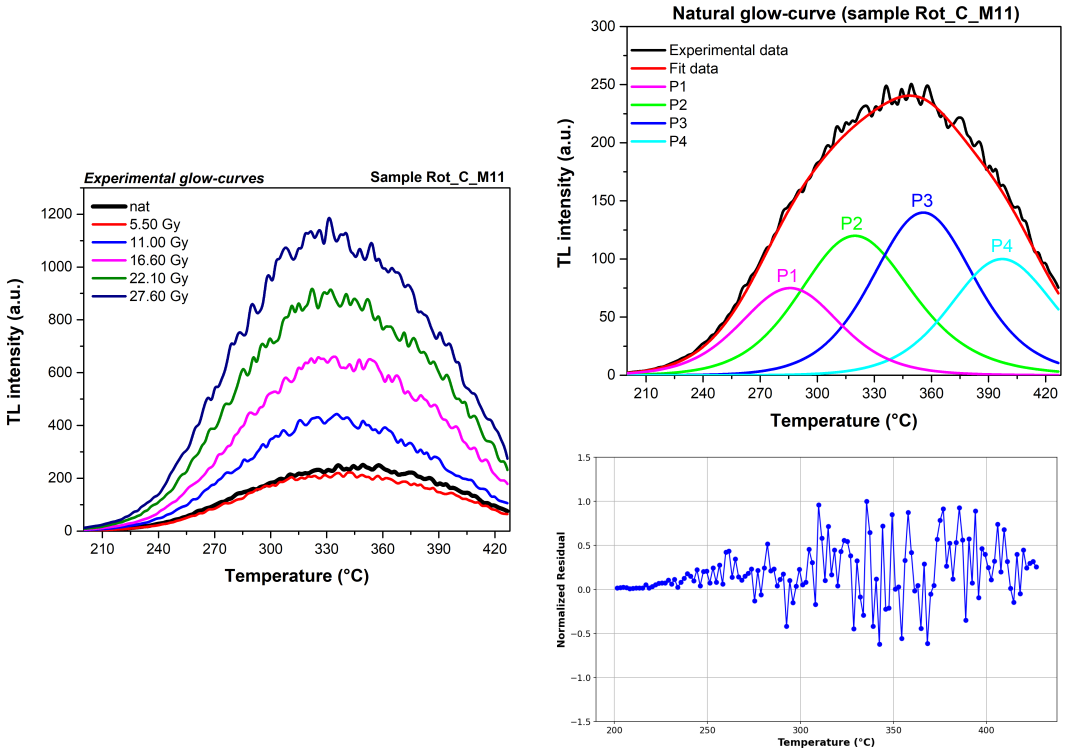

(a) Sample Rot_C_M11: regeneration curves (left) and deconvolution of the natural TL signal with corresponding residuals (right).

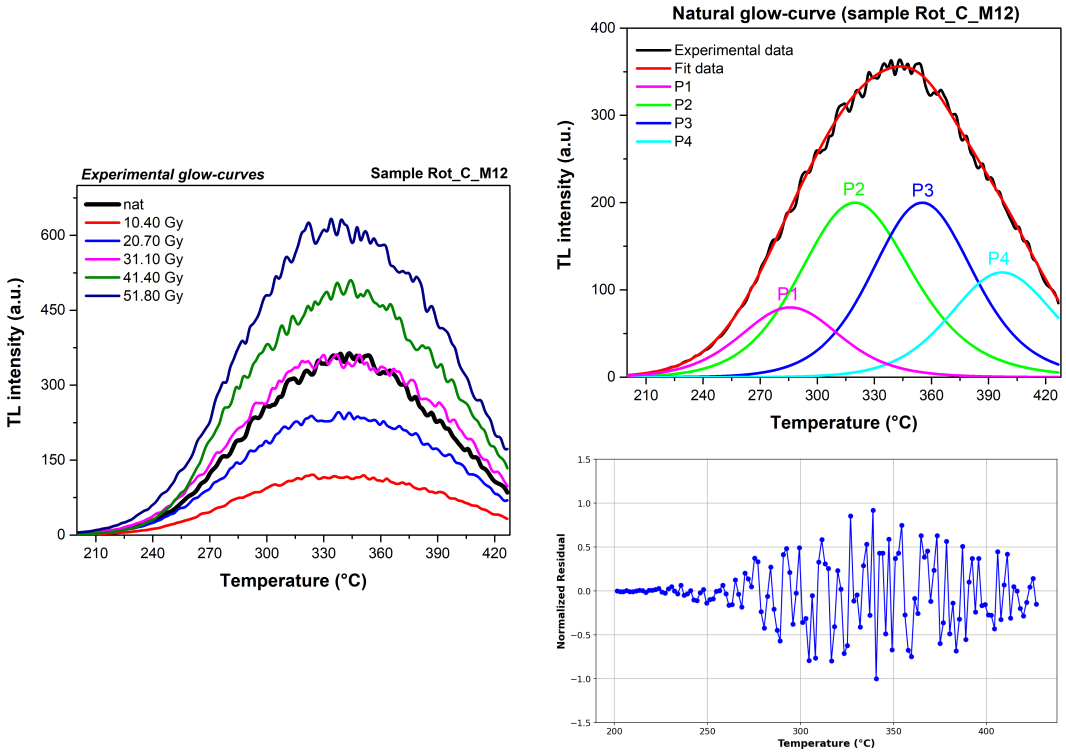

(b) Sample Rot_C_M12: regeneration curves (left) and deconvolution of the natural TL signal with corresponding residuals (right).

Figure 4.12: Comparison of regeneration curves (left) and natural TL deconvolution with residuals (right) for mortar samples Rot_C_M11 and Rot_C_M12.

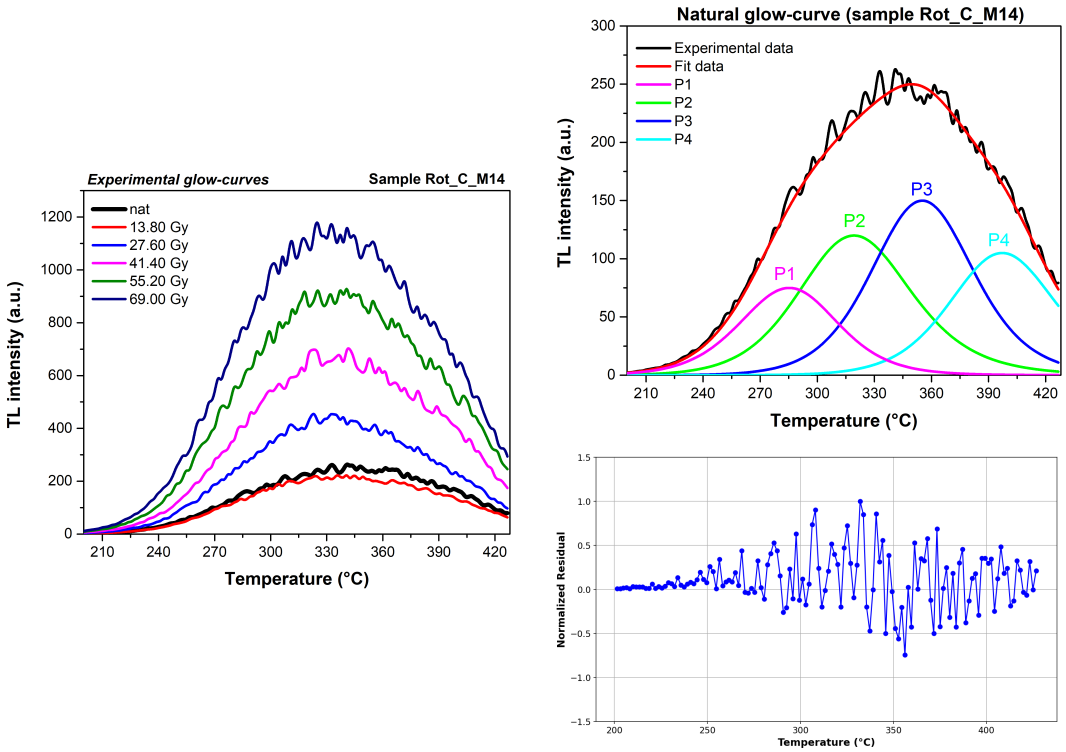

(c) Sample Rot_C_M14: regeneration curves (left) and deconvolution of the natural TL signal with corresponding residuals (right).

Figure 4.12: Comparison of regeneration curves (left) and natural TL deconvolution with residuals (right) for mortar sample Rot_C_M14.

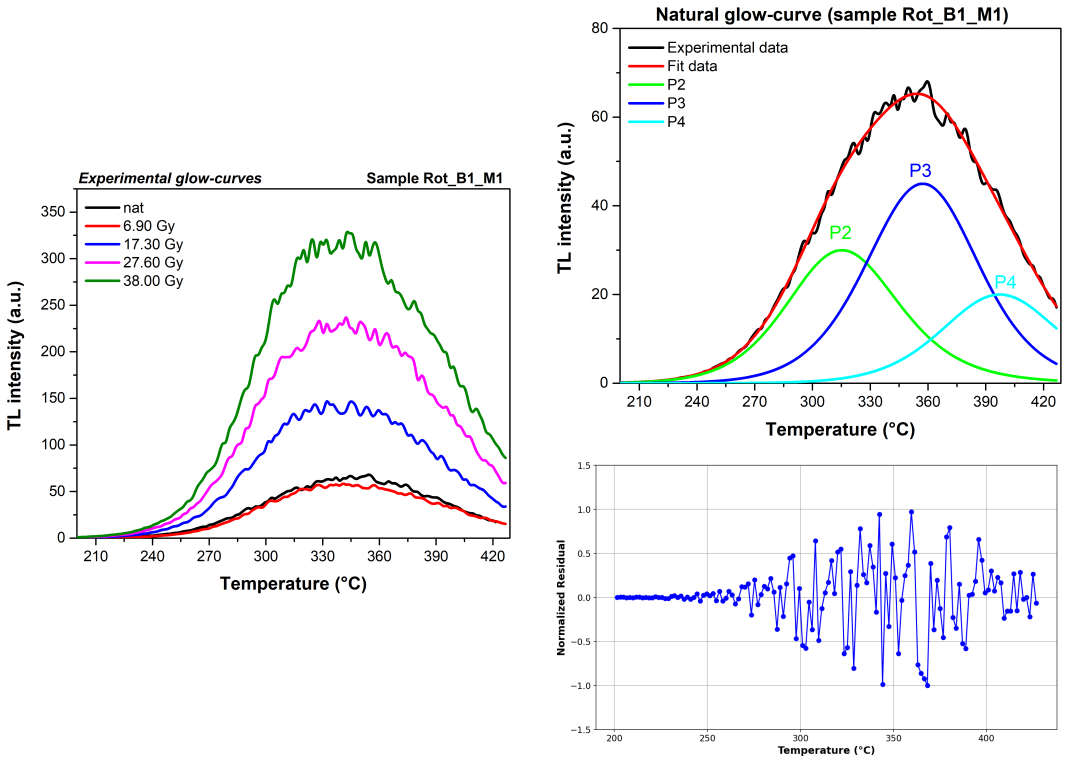

(a) Sample Rot_B1_M1: regeneration curves (left) and deconvolution of the natural TL signal with corresponding residuals (right).

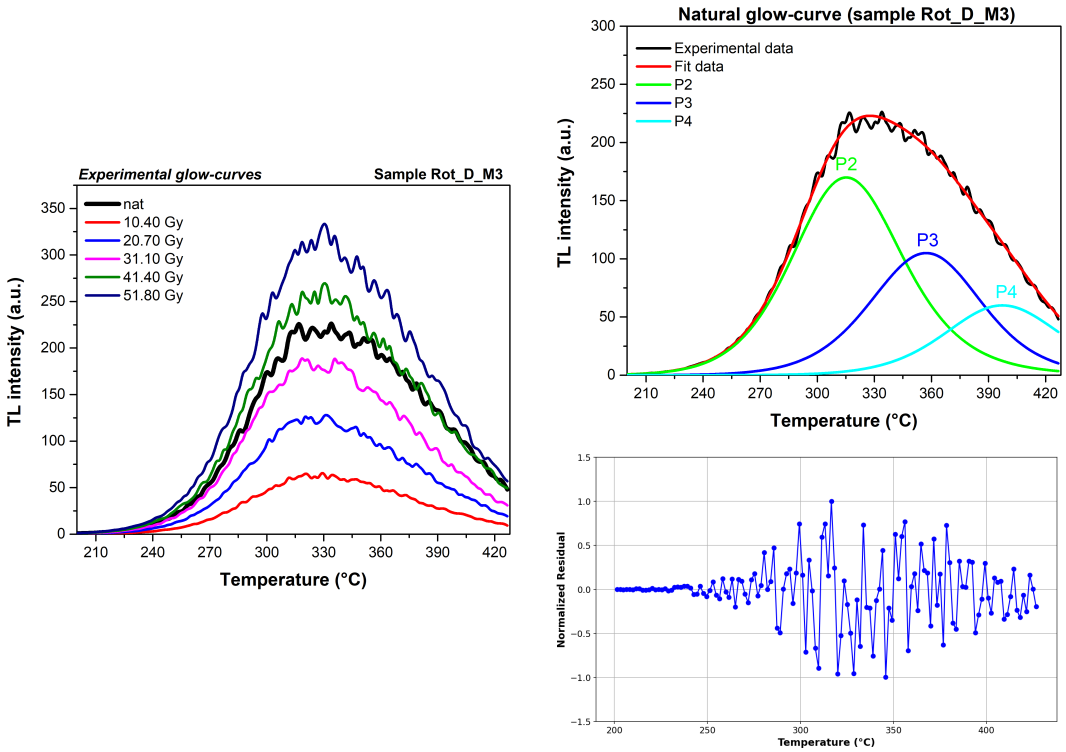

(b) Sample Rot_D_M3: regeneration curves (left) and deconvolution of the natural TL signal with corresponding residuals (right).

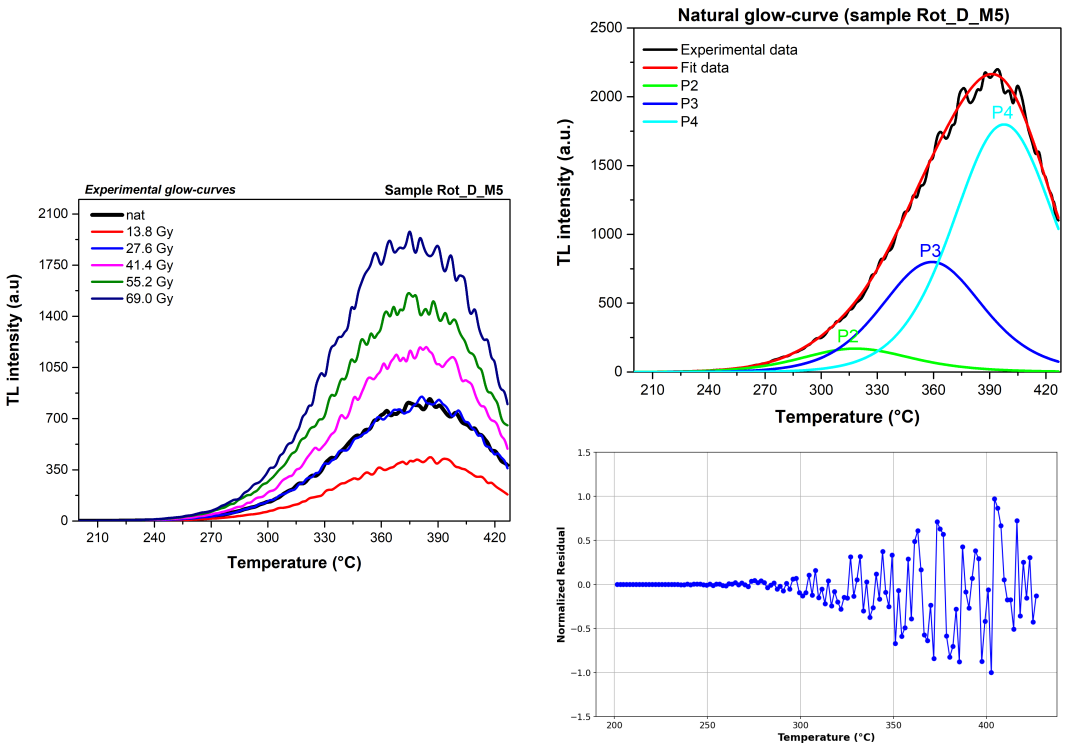

(c) Sample Rot_D_M5: regeneration curves (left) and deconvolution of the natural TL signal with corresponding residuals (right).

Figure 4.13: Comparison of regeneration curves (left) and natural TL deconvolution with residuals (right) for mortar sample Rot_B1_M1, Rot_D_M3, Rot_D_M5.

Table 4.7: Mean thermoluminescence (TL) deconvolution parameters obtained from multiple aliquots of each analysed mortar sample. For each deconvolution peak, the table reports the maximum temperature (T_m), the activation energy (E), and the kinetic order parameter (b). Reported values represent the average of results obtained for the measured aliquots per sample. The associated uncertainties correspond to the error on the mean calculated from the individual deconvolution results. Peaks with $T_m \approx 397$ °C (P4) were excluded from the analysis of kinetic parameters due to their low intensity and the increasing influence of background subtraction at high temperature. For these peaks, only the temperature position is reported. For samples displaying only three resolvable peaks, P1 is marked with "–" to indicate the absence of a low-temperature component; in these cases, P2, P3, and P4 correspond to the first, second, and third peaks actually observed.

Sample	Peak	T_m (°C)	E (eV)	b
Rot_B1_M1	P1	–	–	–
	P2	315 ± 2	1.40 ± 0.04	1.90 ± 0.04
	P3	357 ± 3	1.51 ± 0.04	1.69 ± 0.04
	P4	397 ± 6	–	–
Rot_D_M3	P1	–	–	–
	P2	315 ± 2	1.40 ± 0.04	1.90 ± 0.04
	P3	357 ± 2	1.51 ± 0.04	1.69 ± 0.04
	P4	397 ± 5	–	–
Rot_D_M5	P1	–	–	–
	P2	317 ± 3	1.40 ± 0.04	1.90 ± 0.04
	P3	359 ± 2	1.70 ± 0.04	1.80 ± 0.04
	P4	397 ± 10	–	–
Rot_C_M11	P1	283 ± 2	1.35 ± 0.04	1.74 ± 0.04
	P2	322 ± 4	1.40 ± 0.04	1.90 ± 0.04
	P3	358 ± 2	1.70 ± 0.04	1.80 ± 0.04
	P4	397 ± 9	–	–
Rot_C_M12	P1	283 ± 3	1.45 ± 0.04	1.74 ± 0.04
	P2	319 ± 2	1.40 ± 0.04	1.90 ± 0.04
	P3	358 ± 1	1.70 ± 0.04	1.80 ± 0.04
	P4	397 ± 5	–	–
Rot_C_M14	P1	285 ± 3	1.35 ± 0.04	1.73 ± 0.04
	P2	319 ± 2	1.40 ± 0.04	1.90 ± 0.04
	P3	355 ± 3	1.70 ± 0.04	1.80 ± 0.04
	P4	397 ± 8	–	–

The thermoluminescence (TL) deconvolution parameters obtained for the analysed mortar samples show peak temperatures (T_m) distributed between approximately 283 °C and 359 °C, excluding the highest-temperature peaks near 397 °C (P4) which were not considered in the analysis of kinetic parameters due to the increasing influence of background subtraction at high temperature. Among the most frequently identified components, P2 (centred at 315–322 °C) and P3 (centred at 355–359 °C) are the most recurrent across the samples. An additional low-temperature component, P1 (283–285 °C), was identified only in Rot_C_M11, Rot_C_M12, and Rot_C_M14, and displays kinetic parameters consistent with thermally less stable traps.

The number of deconvolution peaks also appears to be related to the archaeological context of sampling. Mortars from Rot_C_M11, Rot_C_M12, and Rot_C_M14, all collected from room C of the thermal complex (the *frigidarium*, a cold area not subjected to heating), consistently show four components (P1–P4). In contrast, mortars Rot_B1_M1, Rot_D_M3, and Rot_D_M5, which were taken from heated sectors of the baths, display only three main peaks (P2–P4). This difference suggests that in the latter case the low-temperature component (P1) was removed by thermal bleaching induced by prolonged exposure to high temperatures during the period of use of the site as a thermal complex.

The activation energies (E) associated with these deconvolved components range between 1.35 and 1.70 eV, while the kinetic order parameters (b) fall within the interval 1.73–1.90. This internal consistency across multiple samples and aliquots suggests the presence of trap populations with comparable thermal stability and recombination dynamics. In particular, P2 generally displays $E \approx 1.40$ eV and $b \approx 1.90$, whereas P3 tends to show slightly higher activation energies ($E \approx 1.70$ eV) and slightly lower kinetic orders ($b \approx 1.80$).

A comparison was conducted between the results obtained for the mortars and those derived from the deconvolution of a TL glow curve measured on a reference mixture of quartz and calcite (Table 3.9). In this mixture, three dominant peaks were identified at $T_m = 254 \pm 4$ °C (P1), $T_m = 300 \pm 3$ °C (P2), and $T_m = 345 \pm 3$ °C (P3), with activation energies of $E = 1.25 \pm 0.04$ eV, $E = 1.42 \pm 0.03$ eV, and $E = 1.37 \pm 0.04$ eV, and kinetic order values of $b = 1.42 \pm 0.04$, $b = 1.45 \pm 0.03$, and $b = 1.83 \pm 0.05$, respectively.

The comparison reveals that there is an overall similarity in the kinetic characteristics of the TL peaks observed in the mortars and in the quartz–calcite reference mixture, along with a systematic shift in the peak temperatures. In particular, P3 in the mortars (355–359 °C) appears shifted by approximately 10–15 °C with respect to P3 of the mixture ($T_m = 345 \pm 3$ °C). Similarly, P2 in the mortars (315–322 °C) occurs at higher temperatures than P2 of the mixture ($T_m = 300 \pm 3$ °C).

The systematic offset in T_m can be attributed to the greater structural and compositional complexity of the mortars compared to the quartz–calcite mixture. In heterogeneous matrices, such as mortars, variations in crystal structure, grain–matrix interactions, and the presence of defects or inclusions may modify the thermal release conditions of trapped charges, shifting the peak positions toward higher temperatures.

Despite this temperature shift, the activation energy (E) and kinetic order

(b) values remain consistent with those of the reference mixture. This agreement suggests that the same types of luminescence centres, associated with the quartz and calcite phases, are involved in both systems, although their behaviour appears slightly perturbed by the complex microstructural environment of the mortar.

Therefore, the same analytical framework described in Chapter 3 was applied for the estimation of the dose in the mortar matrix. For each aliquot, the integrals of the deconvolution peaks were calculated and used to construct dose–response curves as a function of the administered laboratory dose. The natural signal was then interpolated on these regressions to obtain the corresponding D_e. For both mortar types, whether showing three (P2–P4) or four (P1–P4) resolvable peaks, the D_e was determined from the difference $D_e(P_3) - D_e(P_2)$.

In the latter case (Rot_C_M11, Rot_C_M12, and Rot_C_M14), peaks P2 and P3 were analysed in detail for D_e calculation, following the methodological approach described in Chapter 3. Figure 4.14 illustrates, for one aliquot of each of these samples, the evolution of these two peaks as a function of the administered laboratory dose (top panels), together with the corresponding dose–response curves obtained from their integrals (bottom panels). The observed linear growth of the signals with increasing dose confirms the reproducibility of the measurements and the reliability of the deconvolution procedure.

The dose–response curves were fitted with linear functions of the form $y = a \cdot x$, where a represents the slope of the line and quantifies the variation of luminescence intensity with dose. All regressions yielded R^2 values between 0.998 and 0.999, confirming the reproducibility of the deconvolution procedure and the internal consistency of the experimental protocol.

The highest slopes were observed in the mortars with four deconvolution peaks. In Rot_C_M11, P2 reached $a = 2167.22 \pm 34.04$ and P3 $a = 1144.84 \pm 18.21$, both with $R^2 \approx 0.998$. In Rot_C_M14, the slopes were $a = 1812.70 \pm 18.42$ for P2 and $a = 1361.10 \pm 10.73$ for P3, also with $R^2 = 0.998$. Finally, in Rot_C_M12, the fitted slopes were $a = 1161.70 \pm 14.33$ for P2 and $a = 773.28 \pm 8.04$ for P3, with $R^2 = 0.998$ and $R^2 = 0.999$, respectively. These results confirm the good quality of the fits and the linear increase of TL intensity with dose across all investigated peaks.

The interpolation of the natural signals $L_N(P_2)$ and $L_N(P_3)$ onto the regressions provided the corresponding $D_e(P_2)$ and $D_e(P_3)$ values, from which the equivalent dose was consistently determined as $D_e(P_3) - D_e(P_2)$.

In the mortars showing three deconvolution peaks (P2–P4; Rot_B1_M1, Rot_D_M3, and Rot_D_M5), the analysis focused on peaks P_2 and P_3, which were used for the evaluation of D_e. As illustrated in Figure 4.15, the upper panels report the dose-dependent evolution of the P2 and P3 signals for one aliquot of each sample, while the lower panels display the corresponding dose–response functions obtained from their integrals.

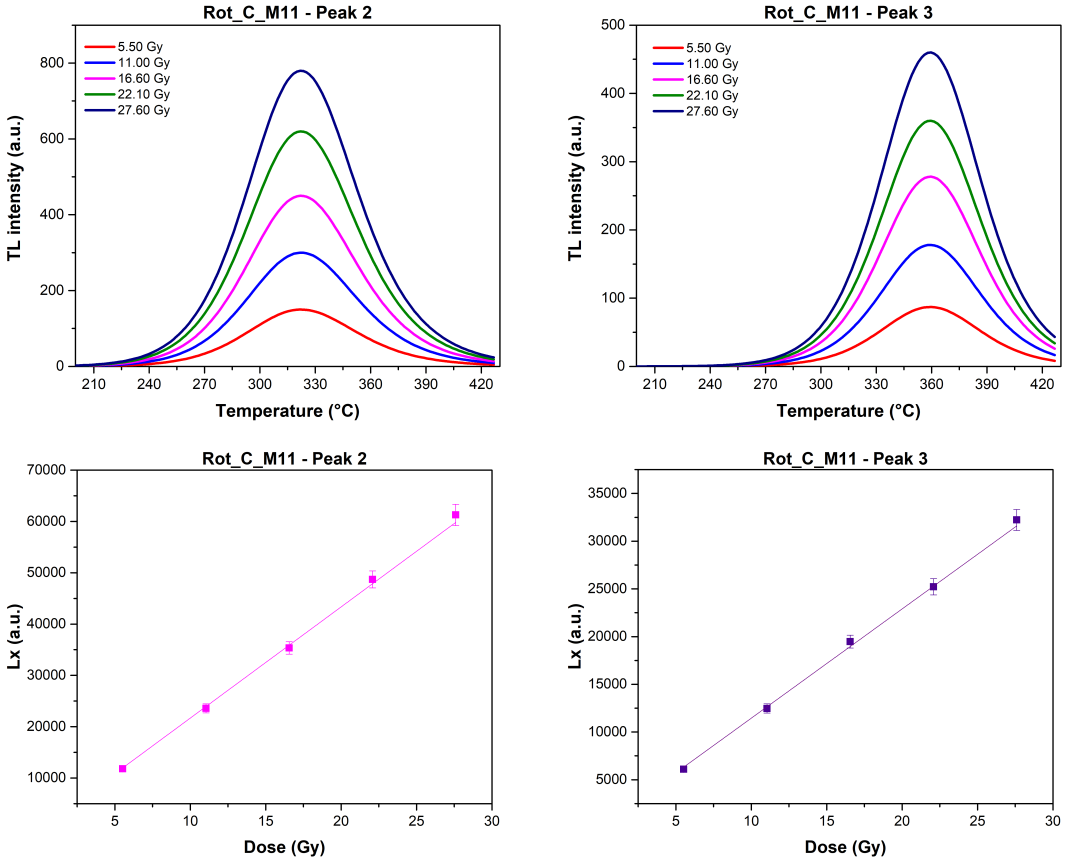

(a) Rot_C_M11. Top: dose-dependent evolution of the deconvolved peak signals P_2 (left) and P_3 (right). Bottom: linear dose–response fits obtained from the integrals under P_2 and P_3, yielding $D_e(P_2)$ and $D_e(P_3)$. The equivalent dose was determined as $D_e(P_3) - D_e(P_2)$.

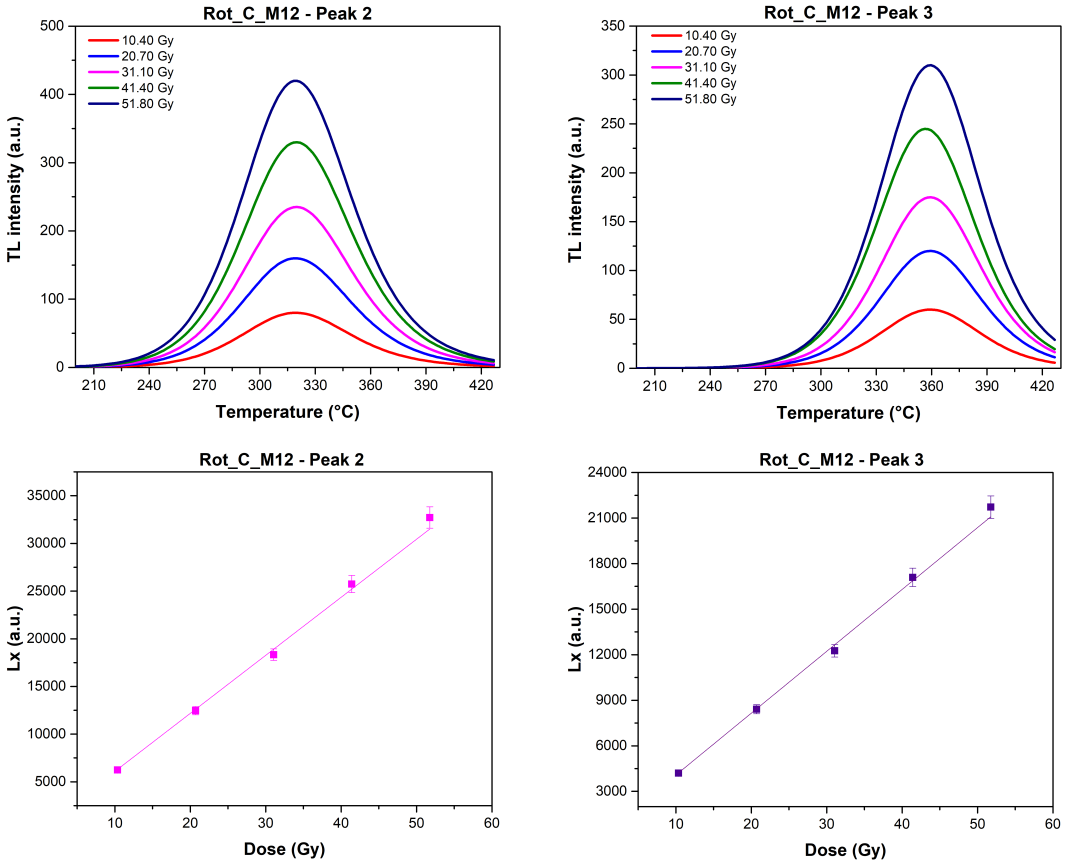

(b) Rot_C_M12. Top: dose-dependent evolution of the deconvolved peak signals P_2 and P_3. Bottom: linear dose–response fits from the corresponding peak integrals, yielding $D_e(P_2)$ and $D_e(P_3)$. The equivalent dose was determined as $D_e(P_3) - D_e(P_2)$.

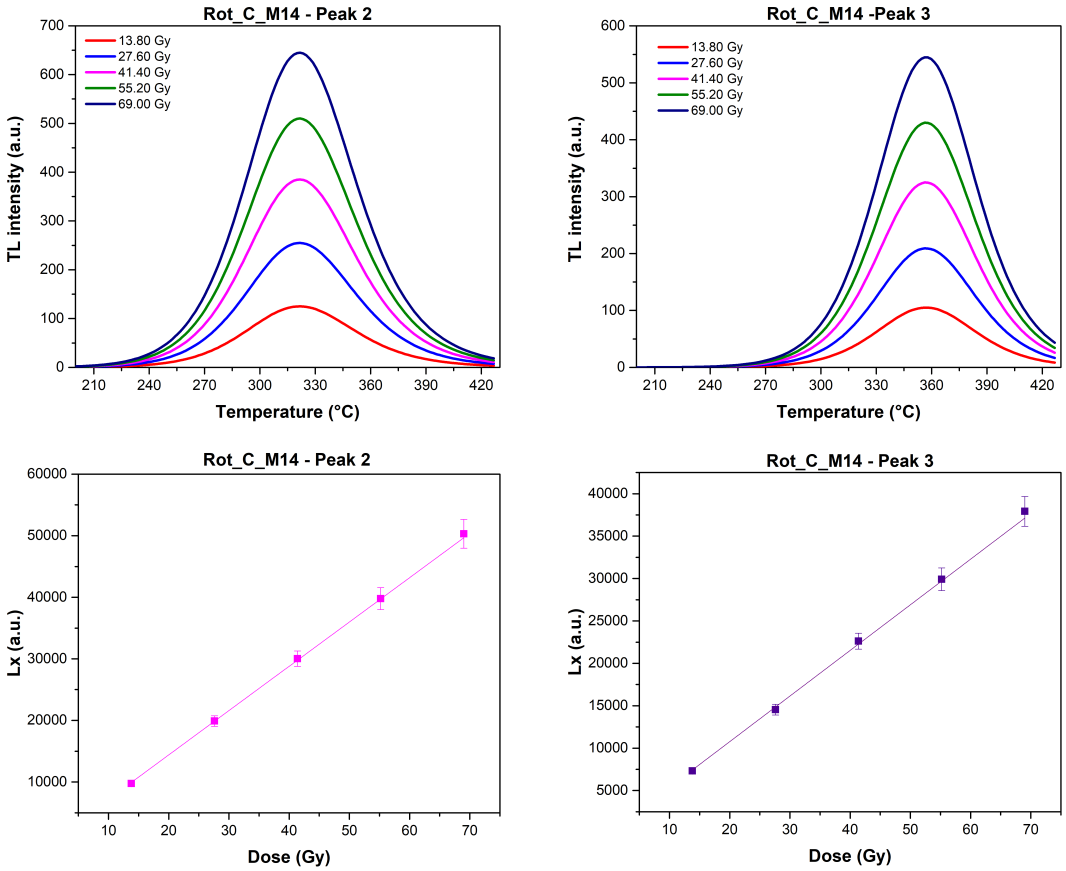

(c) Rot_C_M14. Top: dose-dependent evolution of the deconvolved peak signals P_2 and P_3. Bottom: linear dose–response fits from the corresponding peak integrals, yielding $D_e(P_2)$ and $D_e(P_3)$. The equivalent dose was determined as $D_e(P_3) - D_e(P_2)$.

Figure 4.14: Cold-sector mortars with four deconvolution peaks. For each sample, the upper panels show the dose-dependent evolution of the deconvolved peak signals, while the lower panels present the linear dose–response fits based on the corresponding peak integrals used to derive $D_e(P_i)$.

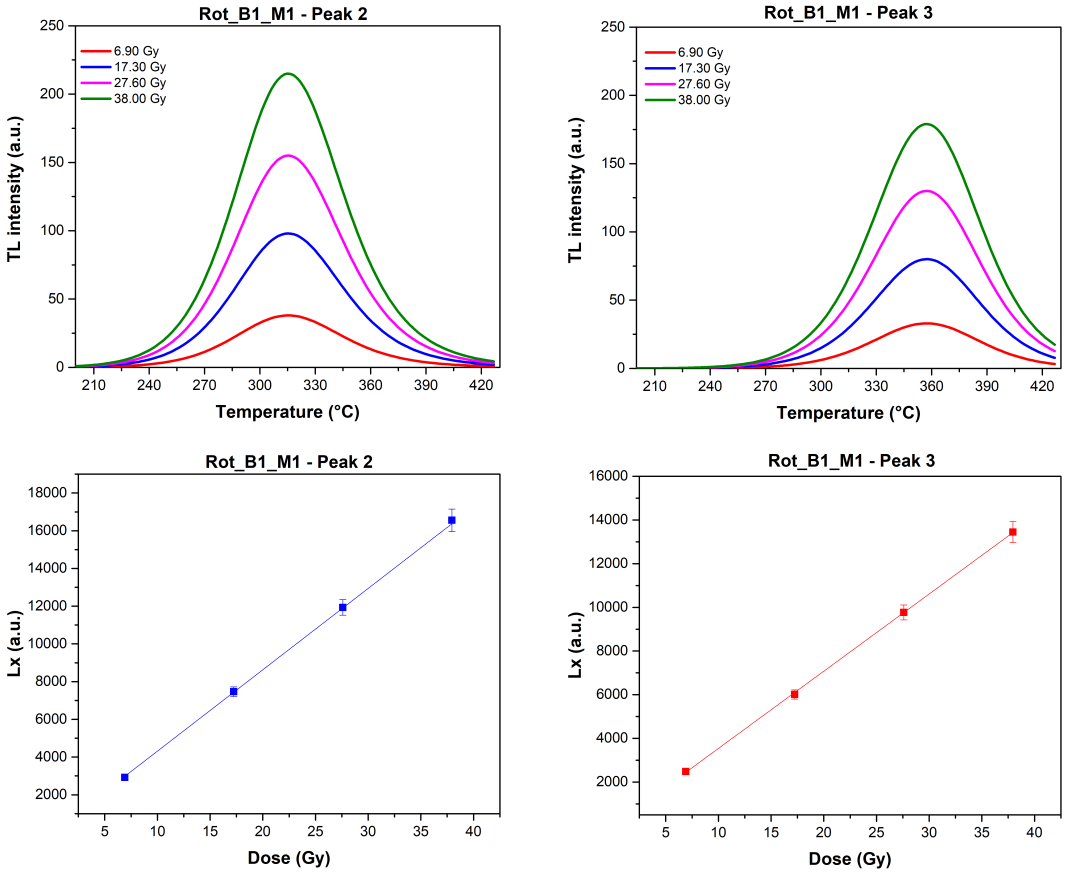

(a) Rot_B1_M1. Top: dose-dependent evolution of the deconvolved peak signals P_2 (left) and P_3 (right). Bottom: linear dose–response fits obtained from the integrals under P_2 and P_3, yielding $D_e(P_2)$ and $D_e(P_3)$. The equivalent dose was determined as $D_e(P_3) - D_e(P_2)$.

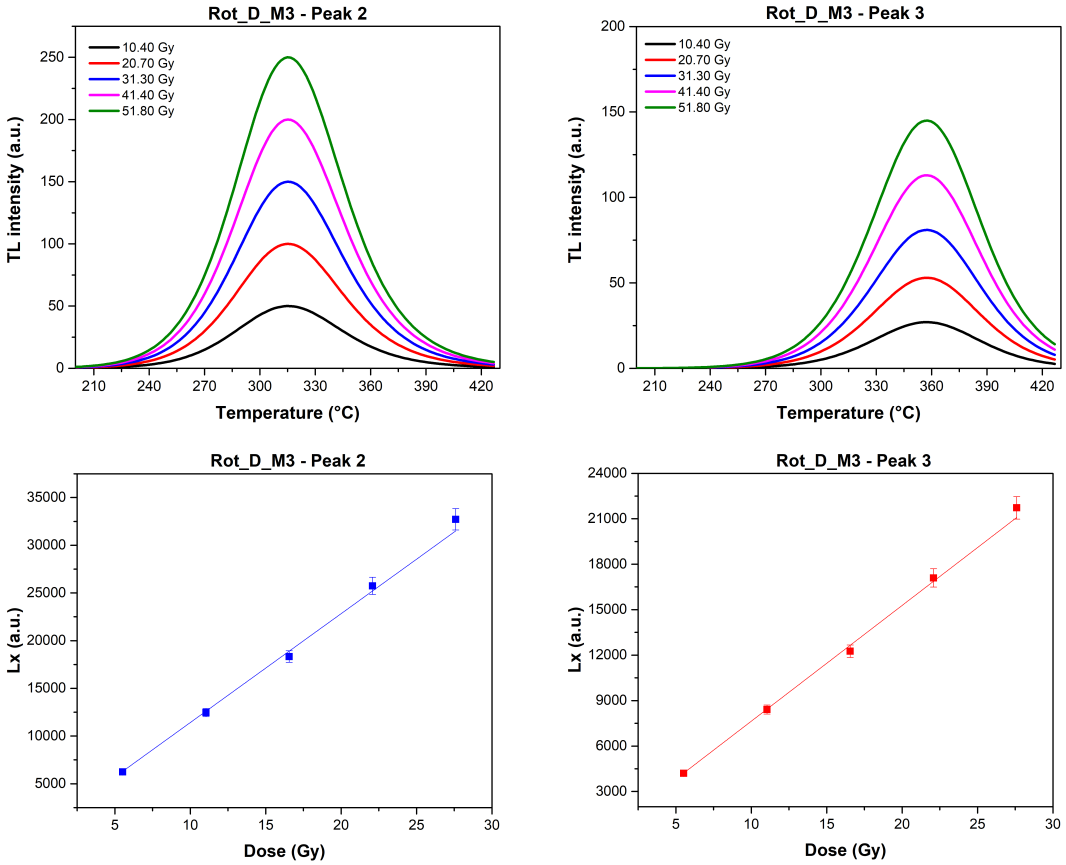

(b) Rot_D_M3. Top: dose-dependent evolution of the deconvolved peak signals P_2 and P_3. Bottom: linear dose–response fits from the corresponding peak integrals, yielding $D_e(P_2)$ and $D_e(P_3)$. The equivalent dose was determined as $D_e(P_3) - D_e(P_2)$.

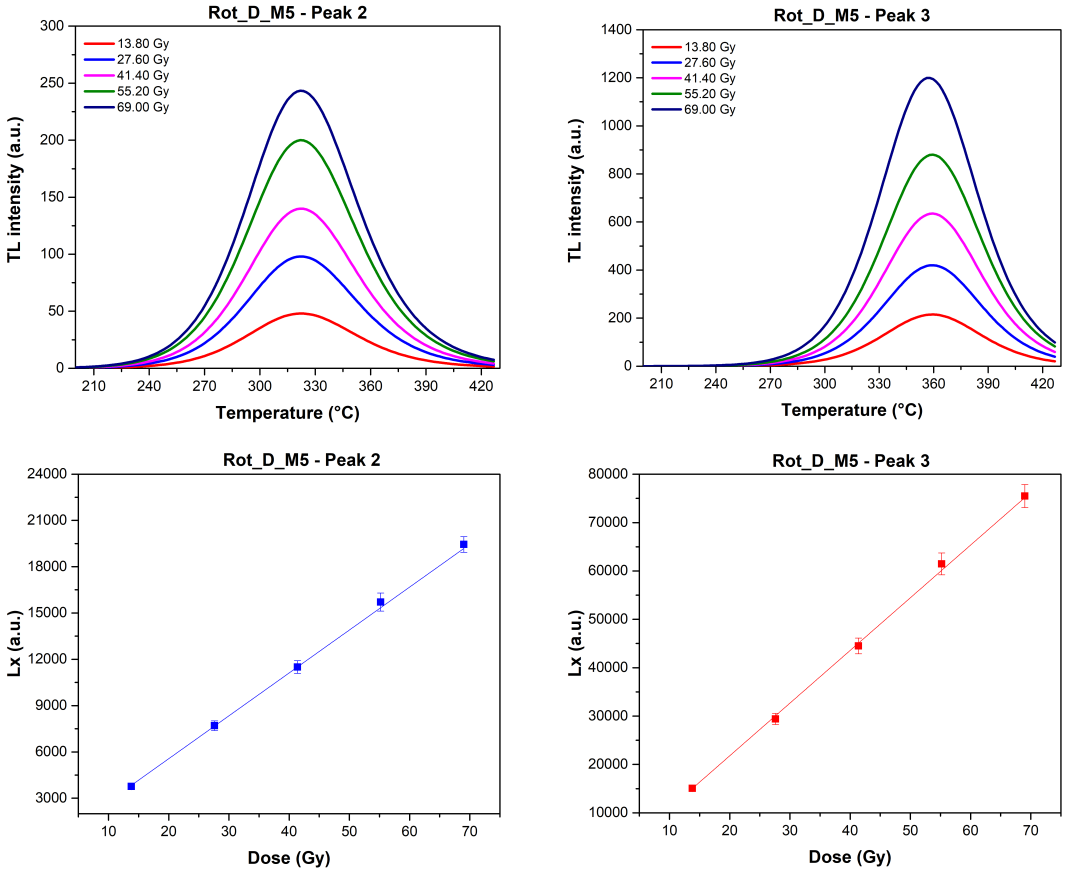

(c) Rot_D_M5. Top: dose-dependent evolution of the deconvolved peak signals P_2 and P_3. Bottom: linear dose–response fits from the corresponding peak integrals, yielding $D_e(P_2)$ and $D_e(P_3)$. The equivalent dose was determined as $D_e(P_3) - D_e(P_2)$.

Figure 4.15: Hot-sector mortars with three deconvolution peaks (P2–P4). For each sample, the upper panels show the dose-dependent evolution of the deconvolved peak signals P_2 and P_3, while the lower panels present the linear dose–response fits based on the corresponding peak integrals used to derive $D_e(P_i)$.

Consistently with the previous set, the dose–response trends were well described by linear functions $y = a \cdot x$.

For Rot_B1_M1, the values were $a = 431.36 \pm 7.61$ for P2 and $a = 353.71 \pm 6.32$ for P3, both with $R^2 = 0.998$. In Rot_D_M3, P2 exhibited a steeper slope ($a = 371.92 \pm 5.97$, $R^2 = 0.999$) compared to P3 ($a = 199.50 \pm 3.22$, $R^2 = 0.997$), indicating a lower growth rate for the latter. In Rot_D_M5, P3 showed a significantly higher slope ($a = 1087.34 \pm 19.94$, $R^2 = 0.999$) than P2 ($a = 275.15 \pm 5.24$, $R^2 = 0.997$), suggesting that P3 contributed more prominently to the luminescence response.

Table 4.8 reports the resulting mean D_e values, averaged over the five aliquots measured per sample, together with their associated uncertainties derived through error propagation.

Table 4.8: Mean equivalent dose (D_e) values and associated uncertainties obtained from the TL signal of the $\text{Mor}_{\text{unprep}}$ mortar samples. For each sample, D_e was derived from five measured aliquots and corresponds to the average value. D_e was evaluated by interpolating the integral of the natural signal onto the corresponding linear dose–response curve. In all cases, D_e was determined as the difference $D_e(P_3) - D_e(P_2)$. Uncertainties were obtained by error propagation.

Sample	D_e **(Gy)**
Rot_B1_M1_unprep	3.78 ± 0.23
Rot_D_M3_unprep	3.45 ± 0.20
Rot_D_M5_unprep	3.56 ± 0.21
Rot_C_M11_unprep	4.21 ± 0.25
Rot_C_M12_unprep	4.68 ± 0.30
Rot_C_M14_unprep	2.95 ± 0.12

4.4 $\dot{D}_R$ determination

The determination of the annual dose rate ($\dot{D}_R$) represents a fundamental step for establishing the chronology of the studied site. This section presents the materials employed for dose rate evaluation, together with the instruments and methodologies adopted for measurements and data analysis. The discussion covers both the internal contributions, namely the alpha and beta dose rates ($\dot{D}_{\alpha,\text{int}}$ and $\dot{D}_{\beta,\text{int}}$), and the external components, associated with the environmental and cosmic dose rates. While no dedicated methodological study was carried out for the environmental dose, its evaluation remains essential to obtain reliable age estimates for the investigated mortars.

4.4.1 Materials for $\dot{D}_R$ measurements

For the $\dot{D}_R$ measurements, a portion of the bulk mortar together with the outermost layer removed during luminescence sample preparation was used. The latter, unsuitable for luminescence analyses due to light exposure, was finely ground and provided a suitable fraction for gamma spectrometry.

Approximately 10 grams of material were homogenised using a planetary ball mill (RETSCH PM 400) to obtain a fine powder with uniformly sized

grains. The powder was then transferred into polyethylene cylinders (16 mm outer diameter, 12 mm inner diameter, 55 mm height) and hermetically sealed with paraffin. An example of the containers employed is shown in Figure 4.16, where the internal volume filled with powdered mortar is also visible.

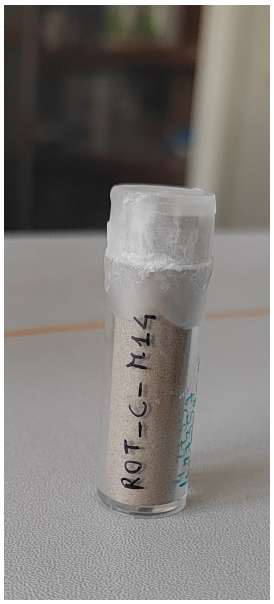

Figure 4.16: Polyethylene cylinder filled with powdered mortar, used for gamma spectrometry measurements.

The sealed samples were stored for four weeks prior to measurement to allow radioactive equilibrium between ^{226}Ra and ^{222}Rn. This step ensures that the activities of the short-lived radon daughters are representative of the parent radionuclide, thereby enabling accurate assessment of uranium-series contributions to the dose rate [130]. For a detailed discussion on the implications of radioactive disequilibrium, see Section 2.5.2 in Chapter 2.

4.4.2 Methods

This section describes the instrumentation and the procedures adopted for the determination of $\dot{D}_R$.

4.4.3 Instruments

The annual dose rate ($\dot{D}_R$) was determined through low-background gamma spectrometry in the laboratory and *in situ* measurements with a portable gamma probe at the sampling sites. Laboratory analyses with high-purity germanium (HPGe) detectors provided the radionuclide concentrations of the mortars, while the *in situ* measurements quantified the environmental gamma and cosmic radiation contributions. Together, these complementary techniques ensured a complete characterisation of the dose rate conditions at the site.

4.4.3.1 HPGe for gamma-spectrometry

The gamma spectrometry system employed in this study is based on a high-purity germanium (HPGe) detector, model EGPC 200 P17, manufactured by

Canberra-Eurisys. The detector has an active volume of 230 cm^3 and provides an energy resolution of 1.24 keV at 122 keV and 1.98 keV at 1.332 MeV, values that enable the reliable separation of closely spaced gamma peaks in complex spectra. It is a co-axial well-type detector, made of intrinsic high-purity germanium, and is operated under liquid nitrogen cooling to suppress electronic noise and minimise background radiation, thereby ensuring high sensitivity in low-background conditions.

Figure 4.17: HPGe gamma spectrometry detector (EGPC 200 P17, Canberra-Eurisys). Adapted from [131].

The system allows measurements in both arbitrary and standardised geometries. Arbitrary geometry is employed when sample integrity must be preserved; for the samples of this study, cylindrical tubes were preferred (please refer to Section 4.4.1), as they facilitate calibration and improve the reproducibility of results [92].

Energy calibration was performed using certified reference sources (^{60}Co, ^{137}Cs, and ^{152}Eu), covering the full energy range of interest (40 keV to 2700 keV). Efficiency calibration was conducted using matrix-matched standards of known composition and density to allow accurate conversion of net count rates into activity concentrations [75].

4.4.3.2 Gamma probe

The environmental gamma dose rate was assessed *in situ* using a portable gamma spectrometer (NaI:Tl), model Inspector (Canberra). The device is equipped with a 2"x2" thallium-doped sodium iodide (NaI:Tl) scintillation crystal coupled to a photomultiplier tube, allowing for both dose rate measurements and spectrometric analysis of the gamma radiation field. The instrument used is shown in Figure 4.18.

In gamma dose rate mode, the device acquires the entire gamma spectrum from the environment but integrates only the counts above a defined energy

Figure 4.18: Portable gamma spectrometer (Canberra Inspector 1000) used for *in situ* dose rate measurements.

threshold, typically set at 320 keV. This energy was experimentally determined as the point where the detection efficiencies for gamma emissions from ^{238}U, ^{232}Th, and ^{40}K converge [132]. By excluding low-energy gamma and X-rays, which contribute negligibly to the absorbed dose and are more affected by potential disequilibria or self-absorption, this approach improves the stability and accuracy of the dose rate estimation *in situ*.

4.4.4 Measurements and analysis

This section describes the procedures adopted for the determination of the annual dose rate ($\dot{D}_R$). Laboratory gamma spectrometry with an HPGe detector was used to measure uranium, thorium, and potassium concentrations in the mortars, while *in situ* dosimetry at the sampling sites assessed the contributions of environmental gamma and cosmic radiation.

4.4.4.1 Low-background gamma spectrometry

The mortar samples prepared as described in Section 4.4.1 for gamma spectrometry measurements were placed in the cylindrical cavity of the HPGe detector (Eurisys Mesures, EGPC 200 P17) and measured for 7 days to ensure sufficient counting statistics. Measured sectra were processed using a dedicated laboratory software following the established laboratory protocol on γ spectra analysis [95].

The spectral analysis began with the determination of the net area of each gamma peak. The underlying Compton background was estimated by selecting two regions of the spectrum, one on the low-energy side and one on the high-energy side of the peak. These regions were chosen sufficiently far from the maximum so as not to include the tails of the peak. A straight line was then interpolated between the two regions to represent the background beneath the peak. The background area thus obtained was subtracted from the gross peak area, leaving only the net contribution of the gamma emission of interest. The net area was normalised to the total acquisition time to express the net

intensity per unit time. The activity of each radionuclide was then calculated by comparison with a reference spectrum acquired from standard materials. For the calibration of the gamma spectrometry system, two standards were employed: a K_2SO_4 sample of certified purity (99.9 $\pm$ 0.1%) and the GS-N granite reference rock (3.85 $\pm$ 0.03% K, 42.2 $\pm$ 0.5 ppm Th, 8.05 $\pm$ 0.05 ppm U in equilibrium), in accordance with established laboratory protocols [130].

Self-absorption corrections were applied based on the elemental composition (please refer to Section 2.5.3.1 and Eq. 2.24), density, and geometry of the sample. Corrections were applied for spectral interferences in accordance with the established analysis protocol [75, 92, 95]. For example, at 186 keV, where both ^{226}Ra and ^{235}U contribute to the observed peak, the contribution from ^{235}U was estimated and subtracted from the total intensity. This estimation was based on the known isotopic ratio between ^{235}U and ^{238}U in natural samples, as well as on other characteristic gamma emissions of ^{235}U. Similar corrections were applied for other typical peak interferences, such as the 241.9 keV line of ^{214}Pb overlapping the 238.6 and 241.0 keV lines of the thorium series, and the 1459.1 keV line of ^{228}Ac overlapping the ^{40}K peak [92]. These corrections were essential to ensure accurate quantification of radionuclide concentrations and were systematically applied during data processing.

The gamma lines used for the determination of radionuclide concentrations are summarised in Table 4.9. These lines were selected based on their high emission probabilities, good spectral resolution, and minimal interference.

Potassium content was determined from the 1460.8 keV gamma line of ^{40}K. The thorium concentration was calculated as the mean activity derived from the gamma lines of ^{228}Ac, ^{212}Pb, and ^{208}Tl. Uranium content was evaluated by distinguishing between different parts of the ^{238}U decay chain:

- U(^{238}U), derived from the emissions of ^{234}Th, ^{234m}Pa, and ^{235}U;
- U(^{226}Ra), derived from the gamma lines of ^{214}Pb and ^{214}Bi, assuming equilibrium between ^{222}Rn and ^{226}Ra under laboratory conditions;
- U(^{210}Pb), derived from the 46.5 keV line.

The comparison between the concentrations of U(^{238}U), U(^{226}Ra), and U(^{210}Pb) was then used to verify the equilibrium state within the uranium decay series and to identify possible disequilibrium conditions that could affect dose rate calculations. The conversion of measured concentrations into dose rates was performed using the conversion factors published by Guérin et al. [94].

The annual dose rate components were corrected for porosity and grain-size effects. Porosity was accounted for through the water content factor (W), experimentally determined, and the saturation factor (F), estimated according to the sampling context (e.g., height, indoor or outdoor location), following the approach of Aitken [1]. The formulas used for the porosity correction are reported in Section 2.5.1 of Chapter 2. In this study, a value of $F = 0.3 \pm 0.2$ was adopted. The W factor was obtained by weighing a sample fragment under different moisture conditions: fully dry (after oven drying at 40°C for 48 hours) and fully saturated (after immersion in water until no further change in weight was observed).

Table 4.9: Gamma lines used for the determination of radionuclide concentrations in this study.

Series	Energy (keV)	Emitting Isotope
Potassium series	1460.8	K-40
Uranium series		
	46.5	Pb-210
	63.3	Th-234
	93.4	Th-234
Head of chain U(^{238}U)	143.0	U-235
	186.0	U-235
	186.0	Ra-226
	1001.0	Pa-234m
	295.2	Pb-214
	351.9	Pb-214
End of chain U(^{226}Ra)	609.3	Bi-214
	1120.3	Bi-214
	1764.5	Bi-214
Thorium series		
	238.6	Pb-212
	338.5	Ac-228
	583.2	Tl-208
	727.1	Bi-212
	860.5	Tl-208
	911.2	Ac-228
	969.0	Ac-228
	2614.5	Tl-208

Attenuation of the α and β components due to the limited penetration depth of these radiations in coarse grains was taken into account using the coefficients proposed by Brennan et al. [133] for α particles and by Mejdahl [134] for β particles. Accordingly, attenuation factors of $f_\beta = 0.9$ and $f_\alpha = 0.1$ were applied to the annual dose components. The α efficiency factor (k-value), which expresses the reduced luminescence efficiency of α particles due to their short penetration depth (about 20 µm), was not measured directly in this study; instead, a value of $k = 0.10 \pm 0.01$ was adopted [61, 60].

4.4.4.2 *In situ* dosimetry

The contribution of external gamma and cosmic radiation (see Section 2.5.1 and Eq. 2.19) was assessed through *in situ* dosimetry with a Canberra Inspector 1000 spectrometer.

The detector probe was placed at the sampling point within the masonry and operated in *Cumulative Dose Mode* for 10 minutes, recording the cumulative dose (µSv). These values were then converted into annual dose contributions by normalising to the acquisition time, under the assumption of constant exposure conditions throughout the year.

4.4.5 $\dot{D}_R$ results

The concentrations of potassium (K), uranium (U), and thorium (Th) measured by high-resolution gamma spectrometry, used to calculate $\dot{D}_{\alpha,\text{int}}$ and $\dot{D}_{\beta,\text{int}}$, are reported in Table 4.10. The methods used to quantify these radionuclides are described in Chapter 3, Section 4.4.4.

Table 4.10: Radionuclide concentrations (in % or ppm) with associated uncertainties for the analysed mortars.

Sample	K (%)	U(^{238}U) (ppm)	U(^{226}Ra) (ppm)	U(^{210}Pb) (ppm)	^{232}Th (ppm)
Rot_B1_M1	0.54 ± 0.03	1.34 ± 0.19	1.76 ± 0.05	0.20 ± 0.10	6.49 ± 0.12
Rot_D_M3	0.56 ± 0.03	1.51 ± 0.15	1.99 ± 0.04	2.03 ± 0.17	3.42 ± 0.08
Rot_D_M5	0.53 ± 0.01	2.37 ± 0.09	2.07 ± 0.02	2.21 ± 0.18	3.42 ± 0.05
Rot_C_M11	0.77 ± 0.01	1.89 ± 0.09	2.15 ± 0.02	1.98 ± 0.10	6.15 ± 0.06
Rot_C_M12	1.07 ± 0.02	1.67 ± 0.09	2.07 ± 0.03	1.99 ± 0.11	5.11 ± 0.06
Rot_C_M14	0.89 ± 0.02	2.23 ± 0.13	2.50 ± 0.03	2.19 ± 0.26	6.74 ± 0.08

Thorium content ranges from 3.42 to 6.74 ppm, suggesting a consistent presence of Th-rich minerals. Potassium concentrations are more variable (0.53–1.07%), likely reflecting a heterogeneous distribution of K-rich inclusions, possibly potassic feldspars. Uranium concentrations, measured both as ^{238}U and ^{226}Ra, vary between 1.34–2.37 ppm and 1.76–2.50 ppm, respectively.

To evaluate potential radioactive disequilibrium, the activity ratios $^{238}\text{U}/^{226}\text{Ra}$ and $^{226}\text{Ra}/^{210}\text{Pb}$ were calculated for each mortar (Table 4.11). The $^{238}\text{U}/^{226}\text{Ra}$ ratio provides information on the equilibrium state in the upper part of the uranium decay chain, whereas the $^{226}\text{Ra}/^{210}\text{Pb}$ ratio is used to detect possible radon loss or redistribution in the lower part. Under secular equilibrium, both ratios are expected to approach unity.

Deviations from equilibrium were assessed using the 2σ criterion [75]. The results show that some mortars deviate significantly from unity in the upper

Table 4.11: Activity ratios calculated for each sample to assess potential radioactive disequilibrium within the uranium decay chain.

Sample	$^{238}U/^{226}Ra$	$^{226}Ra/^{210}Pb$
Rot_B1_M1	0.76 ± 0.11	0.70 ± 0.06
Rot_D_M3	0.76 ± 0.08	0.98 ± 0.08
Rot_D_M5	1.14 ± 0.04	0.94 ± 0.08
Rot_C_M11	0.88 ± 0.04	1.09 ± 0.05
Rot_C_M12	0.81 ± 0.05	1.04 ± 0.06
Rot_C_M14	0.89 ± 0.05	1.14 ± 0.14

part of the chain (e.g. Rot_D_M5, Rot_C_M12, Rot_C_M14), whereas others (e.g. Rot_B1_M1, Rot_C_M11) are consistent with equilibrium within uncertainty. By contrast, most $^{226}Ra/^{210}Pb$ ratios are compatible with equilibrium, suggesting negligible radon loss in recent times. The exceptions are Rot_B1_M1, which shows a deficit in ^{210}Pb, and Rot_C_M11, which displays a slight excess, both indicative of mild disequilibrium in the lower chain.

A graphical comparison of ^{238}U and ^{226}Ra activities, normalized to ^{232}Th, is shown in Figure 4.19. Thorium provides a stable reference due to its low mobility, allowing relative variations to be enhanced. Most mortars deviate from the equilibrium line ($^{238}U = {}^{226}Ra$), with Rot_D_M5 lying below it and the other samples generally above.

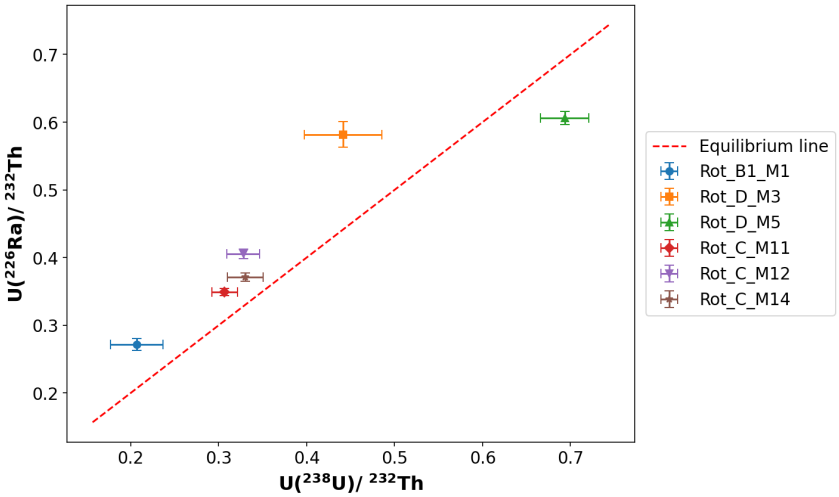

Figure 4.19: Scatter plot of $^{226}Ra/^{232}Th$ vs $^{238}U/^{232}Th$ for the analysed mortars. The red dashed line marks the equilibrium line ($^{238}U = {}^{226}Ra$). Most samples deviate from equilibrium, confirming radioactive disequilibrium in the upper part of the uranium decay series.

The observed disequilibrium cannot be ascribed unambiguously to uranium enrichment or radium depletion [135]. Given the limited number of samples, further investigation of its origin is not possible, as also noted in previous studies [75]. For dose rate evaluation, following the approach of Guibert et al. [130], it is assumed that the disequilibrium has remained constant since construction. The measured activities of ^{238}U and ^{226}Ra are therefore treated as time-averaged values, with the upper part of the chain (from ^{238}U to ^{234}U

and from ^{235}U to ^{231}Th) quantified using ^{238}U, and the lower part (from ^{230}Th to ^{206}Pb and from ^{231}Pa to ^{207}Pb) using ^{226}Ra.

The annual dose components $\dot{D}_\alpha$ and $\dot{D}_\beta$ were then calculated from the measured concentrations using standard conversion factors [136, 2], and corrected for porosity and grain-size effects as described in Chapter 3, Section 4.4.4. Table 4.12 reports the corrected contributions.

Table 4.12: Corrected annual dose contributions for the analysed samples. The corrections were applied using the porosity factor (W), experimentally measured, and the water saturation factor ($F = 0.30 \pm 0.20$). The combined environmental and cosmic dose rate is reported as $\dot{D}_{\mathrm{env,tot}}$.

Sample	W	$\dot{D}_{\alpha,\mathrm{corr}}$ (mGy/a)	$\dot{D}_{\beta,\mathrm{corr}}$ (mGy/a)	$\dot{D}_{\mathrm{env,tot}}$ (mGy/a)
Rot_B1_M1	0.20 ± 0.01	8.63 ± 0.16	0.90 ± 0.02	0.99 ± 0.02
Rot_D_M3	0.21 ± 0.01	7.10 ± 0.13	0.86 ± 0.02	0.91 ± 0.02
Rot_D_M5	0.23 ± 0.01	7.65 ± 0.07	0.89 ± 0.01	0.99 ± 0.02
Rot_C_M11	0.22 ± 0.01	9.39 ± 0.08	1.16 ± 0.01	0.93 ± 0.02
Rot_C_M12	0.24 ± 0.01	8.38 ± 0.08	1.37 ± 0.01	0.97 ± 0.02
Rot_C_M14	0.25 ± 0.01	10.55 ± 0.10	1.35 ± 0.01	0.99 ± 0.02

4.5 Chronology results

The luminescence dating results obtained from both quartz and mortar samples are summarised in Table 4.13. The SG-OSL protocol applied to quartz was used in this study as a reference chronology, since it is based on a well-established luminescence method that directly exploits the physical signal of individual grains and is widely considered the most reliable approach for mortar dating. The thermoluminescence analysis was performed directly on the mortar samples using the newly proposed methodology, which provided a second set of ages. These results were then compared with the quartz SG-OSL ages in order to evaluate the performance of the TL-based protocol and to test its ability to reproduce the chronological framework established by OSL.

The SG-OSL ages show a good agreement with the presumed chronology of the Rotonda baths. Samples Rot_D_M3 and Rot_D_M5 yielded ages of 1813 ± 80 a and 1850 ± 65 a, respectively, consistent with the second construction phase in the 2nd–3rd century AD. Sample Rot_C_M14 returned an age of 1316 ± 53 a, in line with the Byzantine reuse of the building during the second half of the 7th century AD. Samples Rot_C_M11 and Rot_C_M12 yielded ages of 2014 ± 179 a and 1983 ± 62 a, which fit within the 1st century AD when considering the uncertainties. Sample Rot_B1_M1 produced an age of 2053 ± 110 a, slightly older than the expected attribution but still compatible with the earliest phases of construction. The spatial distribution of the samples provides contextual insight: those from heated architectural features (Rot_B1_M1, Rot_D_M3, Rot_D_M5) exhibit higher overdispersion, likely due to thermally induced bleaching or trap modifications, while those from unheated contexts (Rot_C_M11, Rot_C_M12, Rot_C_M14) show lower dispersion and more stable signal preservation.

The TL ages obtained from the carbonate fraction mirror the same chronological framework. Samples Rot_B1_M1 (2007±140 a), Rot_C_M11 (1972± 125 a), and Rot_C_M12 (1979±135 a) confirm the attribution to the 1st century AD. Samples Rot_D_M3 (1895±125 a) and Rot_D_M5 (1902±120 a) are consistent with the 2nd–3rd century AD, while sample Rot_C_M14 returned an age of 1279±60 a, closely matching the Byzantine attribution. The relatively small uncertainty associated with this latter result underscores the robustness of the dose reconstruction. Overall, the TL-based methodology provides results in close agreement with both the archaeological expectations and the quartz SG-OSL ages.

The comprehensive dataset presented in Table 4.13 highlights the close correspondence between the two applied methodologies. For each sample, the SG-OSL and TL ages overlap within the uncertainty ranges, and both converge toward the same chronological framework suggested by archaeological evidence. The early construction phase in the 1st century AD is supported by samples Rot_B1_M1, Rot_C_M11, and Rot_C_M12; the second phase in the 2nd–3rd century AD is confirmed by Rot_D_M3 and Rot_D_M5; and the Byzantine reuse is clearly identified by Rot_C_M14. These results confirm that the new TL-based methodology could successfully reproduce the reference chronology established by SG-OSL on quartz.

This validation underscores its potential as a complementary tool for mortar dating and strengthens the reconstruction of the building history of the Rotonda baths, highlighting their continuity of use and transformation across different cultural periods.

Table 4.13: Comparison of luminescence dating results obtained from quartz (SG-OSL) and mortar (TL). For each sample, the equivalent dose (D_e), annual dose rate, calculated age, and absolute calendar date are reported with 1σ uncertainties. The presumed historical chronology is given for comparison.

	Quartz (SG-OSL)				Mortar (TL)				**Presumed historical age**
Sample	D_e (Gy)	$\dot{D}_R$ (mGy/a)	Age (a)	Date (AD)	D_e (Gy)	$\dot{D}_R$ (mGy/a)	Age (a)	Date (AD)	
Rot_B1_M1	3.86 ± 0.16	1.88 ± 0.06	2053 ± 110	-28 ± 110	3.78 ± 0.23	1.88 ± 0.06	2007 ± 140	18 ± 140	1st century AD (0–100)
Rot_D_M3	3.30 ± 0.10	1.82 ± 0.06	1813 ± 80	212 ± 80	3.45 ± 0.20	1.82 ± 0.06	1895 ± 125	130 ± 125	2nd–3rd century AD (100–300)
Rot_D_M5	3.46 ± 0.10	1.87 ± 0.04	1850 ± 65	175 ± 65	3.56 ± 0.21	1.87 ± 0.04	1902 ± 120	123 ± 120	2nd–3rd century AD (100–300)
Rot_C_M11	4.29 ± 0.37	2.13 ± 0.05	2014 ± 179	11 ± 179	4.21 ± 0.25	2.13 ± 0.05	1972 ± 125	53 ± 125	1st century AD (0–100)
Rot_C_M12	4.70 ± 0.10	2.37 ± 0.05	1983 ± 62	42 ± 62	4.68 ± 0.30	2.37 ± 0.05	1979 ± 135	46 ± 135	1st century AD (0–100)
Rot_C_M14	3.04 ± 0.10	2.31 ± 0.05	1316 ± 53	709 ± 53	2.95 ± 0.12	2.31 ± 0.05	1279 ± 60	746 ± 60	7th century AD (650–700)

Conclusions and perspectives

The present research was developed within the framework of luminescence dating applied to historical mortars, with the specific objective of addressing one of the main limitations of quartz OSL in this context: partial bleaching. The incomplete resetting of the geogenic luminescence signal during mortar preparation can lead to significant age overestimations, thereby reducing the reliability of chronological reconstructions. This issue motivated the search for an alternative dosimetric fraction naturally present in mortars, with the aim of expanding the methodological framework available for dating building materials.

In this perspective, the study explored the potential of the carbonate component as a natural dosimeter. A detailed examination of the chemical and physical transformations involved in the lime cycle highlighted at least two distinct zeroing events capable of resetting the luminescence signal of the carbonate phase. The first occurs during the calcination of limestone, when the material is exposed to temperatures above 800°C, and the second during the re-crystallisation of calcium carbonate in the carbonation process. Once these zeroing events were defined, the newly formed calcite could be regarded as a luminescent phase capable of absorbing and storing radiation after its reset. The exploitation of this fraction therefore represents a cautious but significant methodological innovation in the field of mortar dating.

The research was structured in two complementary phases. The first consisted of controlled laboratory experiments on quartz and calcite, both analysed as single mineral fractions and in binary mixtures designed to simulate simplified mortars. TL glow curve deconvolution was used to identify kinetic components, evaluate the dosimetric behaviour of each material. The SAR protocol was combined with peak-specific deconvolution in order to isolate the contribution of each mineral phase.

The second phase focused on the application of the methodology to archaeological mortars sampled from the Roman bath complex of the *Terme della Rotonda* in Catania. In this case, SG-OSL was employed as the reference protocol, providing robust age estimates and serving as a benchmark for comparison with the carbonate-based approach.

The experiments on binary mixtures confirmed that each mineral phase preserves its kinetic characteristic in composite systems. By applying peak-specific dose reconstruction, it was possible to obtain internally consistent D_e values for each mineral, comparable with those measured in single-phase samples. This shows that the dosimetric behaviour of quartz and calcite can be distinguished without performing a mineral separation, which is particularly significant when working directly with mortar matrices.

The application to archaeological mortars further confirmed the feasibility of the approach. TL glow curves measured on the selected samples were successfully deconvoluted into quartz- and calcite-related components, and D_e values were reconstructed by fitting the dose–response curves obtained from beta irradiations. These values showed reproducibility across aliquots and consistency with those measured on reference materials. Moreover, comparison with SG-OSL results indicated that the proposed TL-based methodology produced age estimates falling within the expected presumed age for the site, thereby validating its applicability under real-case conditions.

Nevertheless, several limitations must be acknowledged. The methodology was applied to a limited number of samples, all originating from the same archaeological context, which restricts the statistical significance of the conclusions. Another aspect that requires further investigation is the influence of mortar composition on the luminescence response. Variations in binder-to-aggregate ratio, as well as mineralogical heterogeneities, may affect the proportion of luminescent signals and their deconvolution. Systematic characterisation of mortars, for example by X-Ray Diffraction (XRD), would allow quantification of binder and aggregate contents, providing essential information for evaluating the reproducibility and reliability of the extracted dosimetric signals.

In light of these limitations, several perspectives for future research can be outlined. A first priority should be to apply the developed methodology to a larger number of mortars from different sites, in order to strengthen its statistical basis and evaluate its performance under diverse construction traditions and raw material compositions. A second objective should be to study systematically the role of mortar composition, particularly the binder-to-aggregate ratio, on the luminescence response of quartz and carbonate fractions. A third perspective is the definition of a dedicated chemical and physical separation protocol for calcium carbonate, analogous to quartz purification, to increase reproducibility and establish a standardised approach for routine application.

An important aspect emerging from this work is the methodological complementarity between the carbonate-based TL protocol and quartz OSL. The two approaches should not be considered as competing alternatives, but as techniques that can be combined depending on the preservation state of the samples and the bleaching conditions. The possibility of relying on two distinct luminescent fractions increases the resilience of chronological reconstructions, reducing the impact of partial bleaching and enhancing the reliability of mortar dating.

In summary, this thesis provides both methodological insights and an initial applied assessment. It has explored the potential of the carbonate fraction as a complementary dosimetric phase in mortars and has tested its feasibility in an archaeological case study. While the results are preliminary, they indicate that the integration of carbonate TL with quartz OSL may broaden the methodological framework for luminescence dating. This combination outlines a cautious but promising direction for future developments and further validation in the field of luminescence dating.

A Thermoluminescence data analysis of representative aliquots

This appendix includes all the data analyses performed on the mortar samples collected from the archaeological site of the *Terme della Rotonda* in Catania. The purpose is to provide a comprehensive overview of the TL analyses carried out on representative aliquots from each mortar, detailing every step of the data treatment and interpretation.

For each sample, the complete analytical workflow is presented, from the measurement conditions and preprocessing of the glow curves to the deconvolution procedure, extraction of kinetic parameters, and equivalent dose estimation. Each section corresponds to one representative aliquot per mortar and follows an identical structure, enabling a direct comparison among the different samples.

The appendix is organised so that each aliquot of a sample can be discussed and interpreted independently, allowing a presentation of the TL data analysis for every mortar investigated. In continuity with the structure adopted in the main body of the thesis, the order in which the mortars are discussed follows their provenance within the thermal complex. The analysis therefore begins with the mortars collected in zone C, corresponding to the cold sector of the baths (*frigidarium* area), where the samples systematically exhibited four deconvolution peaks. Subsequently, the discussion proceeds with the mortars from the heated zones of the complex, which are characterised by three TL components once subjected to thermoluminescence measurements.

This appendix therefore serves both as a methodological reference, illustrating the numerical treatment applied to the TL data, and as an analytical record supporting the discussion and conclusions reported in Chapter 4.

A.1 Sample Rot_C_M11

Sample Rot_C_M11 was collected from one of the wall of area C, identified as the *frigidarium* of the Terme della Rotonda complex. This unheated environment represents one of the cold rooms of the bath system and was selected to investigate the luminescence behaviour of mortars unaffected by thermal exposure.

A portion of the unprepared mortar extracted from this area was subjected to TL measurements in order to obtain the natural thermoluminescence signal of the sample.

Figure A.1: Sampling point of the Rot_C_M11 mortar, collected from the inner portion of a wall in area C, corresponding to the *frigidarium* of the Terme della Rotonda. The inner core of the mortar was extracted to minimise light exposure and surface contamination.

A.1.1 Measurement conditions

TL measurements on the unprepared mortar powder were carried out using a Risø TL/DA-15 reader equipped with a BG-39 optical filter. Each sample was subjected to a regenerative measurement protocol, following the sequence reported in Table A.1, which included five regeneration doses after the natural signal measurement.

Table A.1: Measurement sequence applied during the regenerative protocol for the unprepared mortar sample Rot_C_M11.

Step	Treatment	Observed
1	Thermal stimulation (@430 °C, 5 °C s^{-1})	L_N
2	Give regeneration dose D_i (where i = 5.50, 11.00, 16.60, 22.10, 27.60 Gy)	–
3	Preheat (@210 °C, 120 s)	–
4	Thermal stimulation (@430 °C, 5 °C s^{-1})	L_i
5	Repeat steps 2–4 for all regeneration doses D_i	–

A.1.2 Analysis and results

The experimental TL glow curves obtained for the unprepared mortar sample Rot_C_M11 are shown in Figure A.2. The natural TL signal and the regenerated curves corresponding to the applied doses of 5.50, 11.00, 16.60, 22.10, 27.60 Gy are reported.

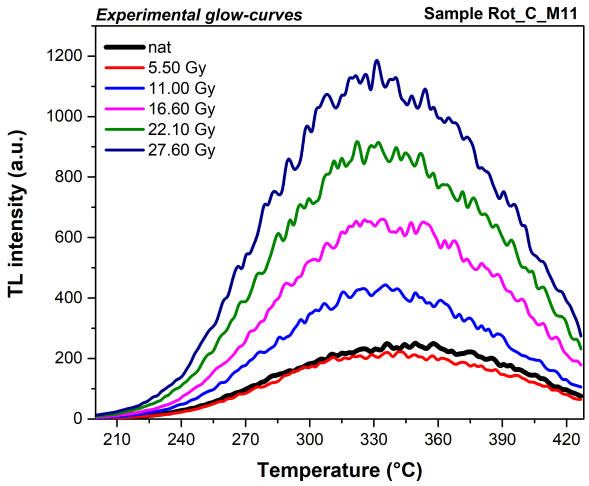

Figure A.2: Experimental TL glow curves obtained for the unprepared mortar sample Rot_C_M11 under regeneration mode. The natural signal (black) and the regenerated curves corresponding to doses of 5.50, 11.00, 16.60, 22.10, 27.60 Gy are shown.

For each glow curve shown in Figure A.2, a deconvolution was performed in order to separate the individual TL components contributing to the total signal. The deconvolution procedure was applied to the natural curve and to each regenerated curve corresponding to the selected doses (5.50, 11.00, 16.60, 22.10, 27.60 Gy). The fitting was carried out using the general order kinetic (GOK) model, following the same approach described in Chapter 4.

Figures A.3 present, for each regeneration dose, the deconvolution of the corresponding TL glow curve together with the table reporting the kinetic parameters of the individual peaks. For each dose step, the experimental data are fitted by the sum of the single TL components, and the figure also reports the FOM value that quantifies the goodness of each deconvolution.

The corresponding kinetic parameters for all regenerated curves are summarised in Table A.2.

Table A.2: Kinetic parameters derived from the deconvolution of the TL glow curves for sample Rot_C_M11. The same kinetic structure (P1–P3) was maintained across all regeneration doses.

Peak	T_m (°C)	E (eV)	b
P1	283	1.46	1.75
P2	322	1.39	1.93
P3	358	1.71	1.80
P4	397	-	-

Figures A.4a and A.4b show the variation in TL intensity of the second (P2) and third (P3) deconvolution peaks as a function of the administered

dose. The linear growth trend confirms the suitability of these components for constructing the dose–response curve used in the equivalent dose determination.

An integration was performed for the second (P2) and third (P3) deconvolution peaks. The resulting values were used to construct the dose–response curve shown in Figure A.5, where the experimental points represent the integrated TL signals as a function of the administered dose and the red line corresponds to the best-fit linear function used to fit the data.

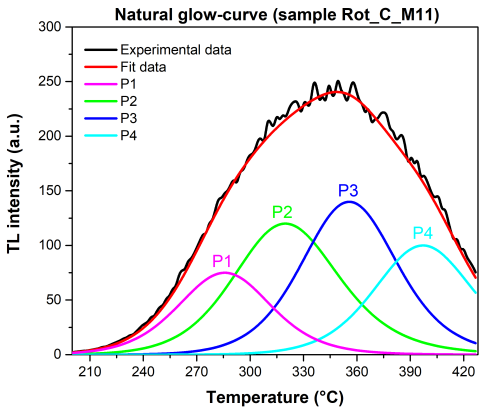

(a) Natural. FOM = 2.1%.

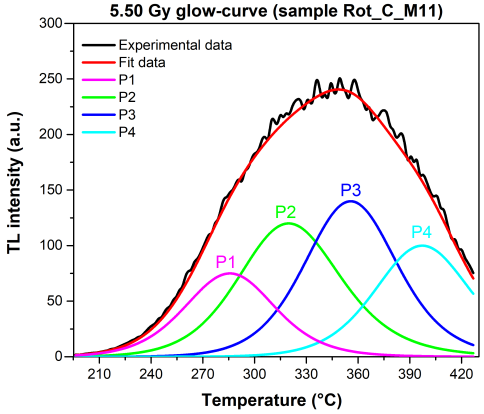

(b) 5.50 Gy. FOM = 2.4%.

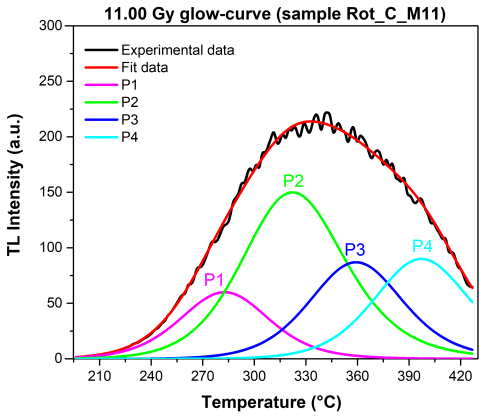

(c)11.00 Gy. FOM = 2.2%.

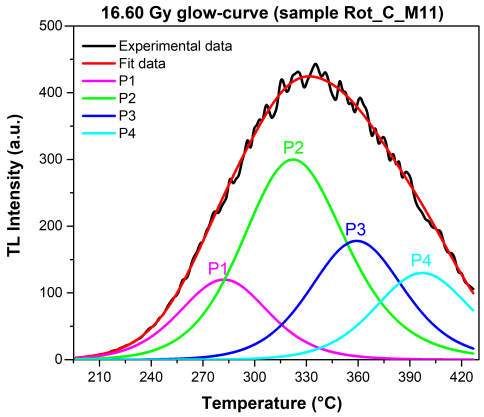

(d) 16.60 Gy. FOM = 2.5%.

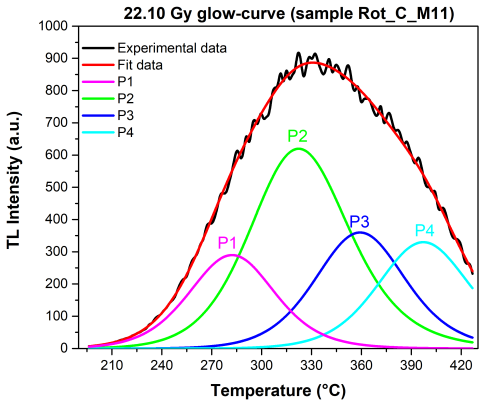

(e) 22.10 Gy. FOM = 2.3%.

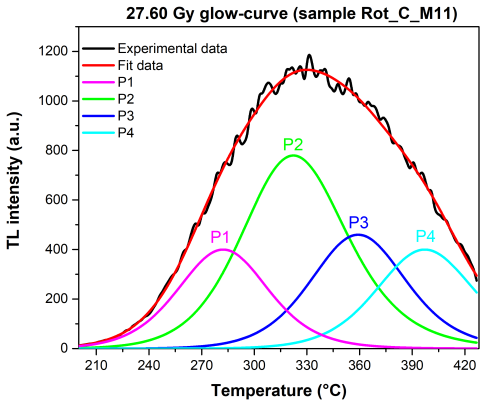

(f) 27.60 Gy. FOM = 2.4%.

Figure A.3: Deconvolution of the TL glow curves for sample Rot_C_M11 corresponding to the natural signal and to the regeneration doses of 5.50, 11.00, 16.60, 22.10, 27.60 Gy. Each plot shows the experimental data (black), the overall fit (red), and the individual TL components (P1–P3) in colour. The FOM values are indicated for each deconvolution, confirming the reliability and consistency of the fitting model.

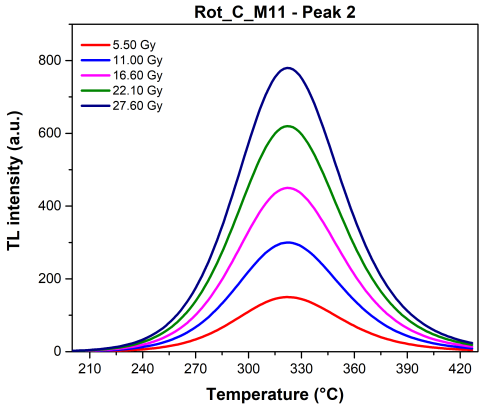

(a) TL intensity variation for Peak 2 (P2) at different regeneration doses.

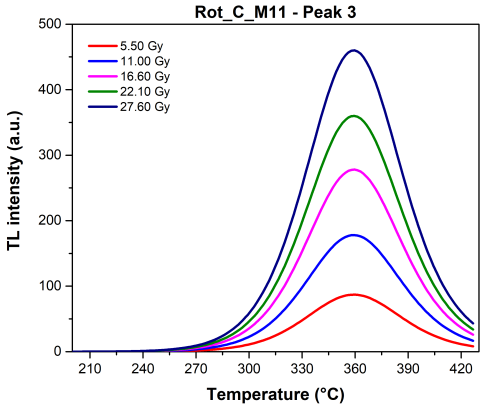

(b) TL intensity variation for Peak 3 (P3) at different regeneration doses.

Figure A.4: Variation in TL intensity of the second (P2) and third (P3) deconvolution peaks for sample Rot_D_M11 as a function of the administered dose.

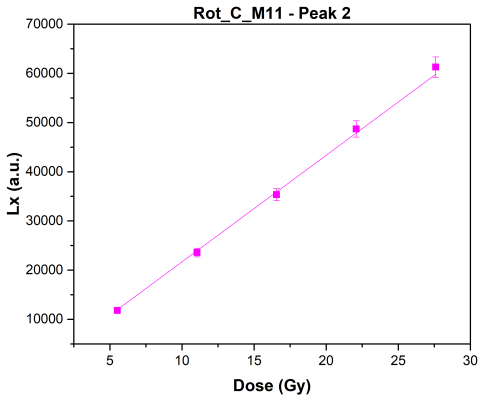

(a) Dose–response curve for Peak 2 (P2).

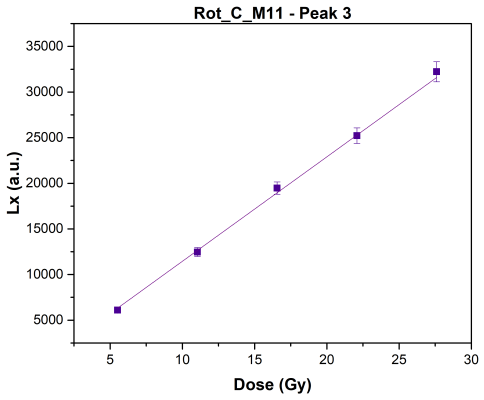

(b) Dose–response curve for Peak 3 (P3).

Figure A.5: Dose–response curves obtained from the integrated intensities of peaks P2 and P3 for sample Rot_C_M11. The experimental data points represent the integrated TL signal as a function of the administered dose, while the solid lines correspond to the best-fit linear functions used to estimate the equivalent dose.

The integrated data were fitted using linear functions of the form $y = ax$. For sample Rot_C_M11, the best-fit equations were $y = (2167.22 \pm 34.04)x$ for P2 and $y = (1144.84 \pm 18.21)x$ for P3, with correlation coefficients of $R^2 = 0.998$.

In these dose–response curves, the integral value corresponding to the natural signal was interpolated along the fitted line to determine the equivalent dose (D_e) of the sample.

The equivalent dose (D_e) values obtained from the dose–response curves of peaks P2 and P3 were 4.32 ± 0.18 Gy and 8.53 ± 0.36 Gy, respectively. As already specified for the previous samples, the uncertainty on the equivalent dose was estimated through standard error propagation, taking into account both the uncertainty of the linear fit parameters and that of the natural signal integral (Poisson counting error and FOM). This approach ensured that the combined effects of fitting and measurement uncertainties were properly reflected in the final D_e values.

The difference between the two estimates, $D_e(P3) - D_e(P2) = 4.21 \pm 0.25$ Gy, represents, according to the approach described in Chapter 4, the equivalent dose (D_e) of the untreated mortar sample. The uncertainty associated with the difference between the two D_e values was calculated by propagating the individual uncertainties of P2 and P3.

A.2 Sample Rot_C_M12

Sample Rot_C_M12 was collected from the inner portion of one of the hydraulic ducts located in area C. These conduits form part of the water-management system associated with the frigidarium and were built to regulate the circulation and drainage of cold water within this sector of the complex. The sampling point was chosen to access unexposed mortar preserved within the structure. As for the other specimens from area C, a portion of the unprepared material was subjected to TL measurements.

A.2.1 Measurement conditions

TL measurements on the unprepared mortar powder were carried out using a Risø TL/DA-15 reader equipped with a BG-39 optical filter. Each sample was subjected to a regenerative measurement protocol, following the sequence reported in Table A.3, which included five regeneration doses after the natural signal measurement.

Table A.3: Measurement sequence applied during the regenerative protocol for the unprepared mortar sample Rot_C_M12.

Step	Treatment	Observed
1	Thermal stimulation (@430 °C, 5 °C s^{-1})	L_N
2	Give regeneration dose D_i (where i = 10.40, 20.70, 31.10, 41.40, 51.80 Gy)	–
3	Preheat (@210 °C, 120 s)	–
4	Thermal stimulation (@430 °C, 5 °C s^{-1})	L_i
5	Repeat steps 2–4 for all regeneration doses D_i	–

Figure A.6: Sampling point of the Rot_C_M12 mortar, collected from the inner portion of one of the hydraulic ducts in area C. The sampling was performed by removing the inner mortar core to minimise light exposure and surface contamination.

A.2.2 Analysis and results

The experimental TL glow curves obtained for the unprepared mortar sample Rot_C_M12 are shown in Figure A.7. The natural TL signal and the regenerated curves corresponding to the applied doses of 10.40, 20.70, 31.10, 41.40, 51.80 Gy are reported.

For each glow curve shown in Figure A.7, a deconvolution was performed in order to separate the individual TL components contributing to the total signal. The deconvolution procedure was applied to the natural curve and to each regenerated curve corresponding to the selected doses (10.40, 20.70, 31.10, 41.40, 51.80 Gy). The fitting was carried out using the general order kinetic (GOK) model, following the same approach described in Chapter 4.

Figures A.8 present, for each regeneration dose, the deconvolution of the corresponding TL glow curve together with the table reporting the kinetic parameters of the individual peaks. For each dose step, the experimental data are fitted by the sum of the single TL components, and the figure also reports the FOM value that quantifies the goodness of each deconvolution.

The corresponding kinetic parameters for all regenerated curves are summarised in Table A.4.

Figures A.9a and A.9b show the variation in TL intensity of the second (P2) and third (P3) deconvolution peaks as a function of the administered dose. The linear growth trend confirms the suitability of these components for constructing the dose–response curve used in the equivalent dose determination.

An integration was performed for the second (P2) and third (P3) deconvolution peaks. The resulting values were used to construct the dose–response

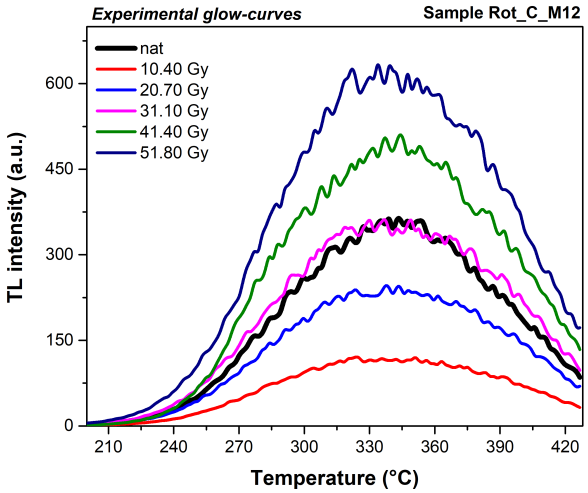

Figure A.7: Experimental TL glow curves obtained for the unprepared mortar sample Rot_D_M5 under regeneration mode. The natural signal (black) and the regenerated curves corresponding to doses of 10.40, 20.70, 31.10, 41.40, 51.80 Gy are shown.

Table A.4: Kinetic parameters derived from the deconvolution of the TL glow curves for sample Rot_B1_M12. The same kinetic structure (P1–P3) was maintained across all regeneration doses.

Peak	T_m (°C)	E (eV)	b
P1	283	1.42	1.75
P2	320	1.40	1.90
P3	358	1.71	1.80
P4	397	-	-

curve shown in Figure A.10, where the experimental points represent the integrated TL signals as a function of the administered dose and the red line corresponds to the best-fit linear function used to fit the data.

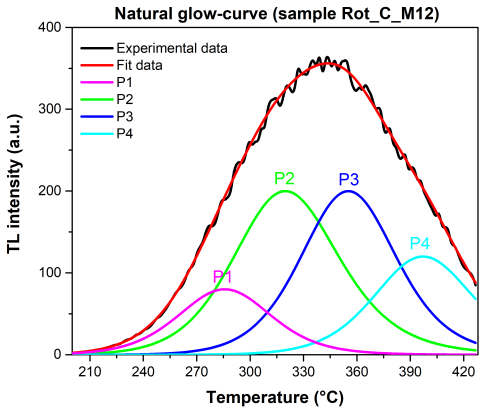

(a) Natural. FOM = 1.8%.

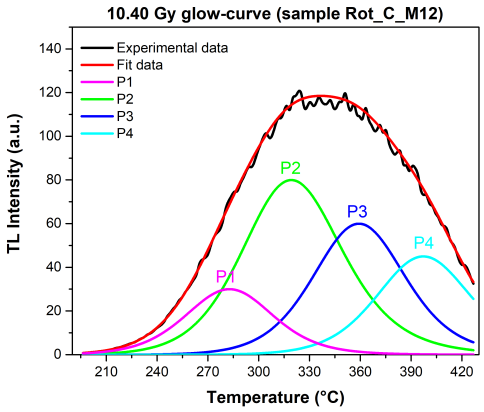

(b) 10.40 Gy. FOM = 2.0%.

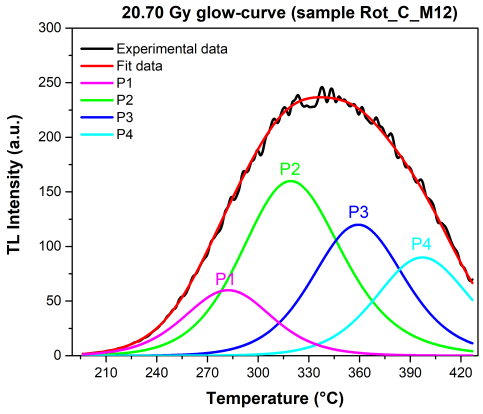

(c) 20.70 Gy. FOM = 2.1%.

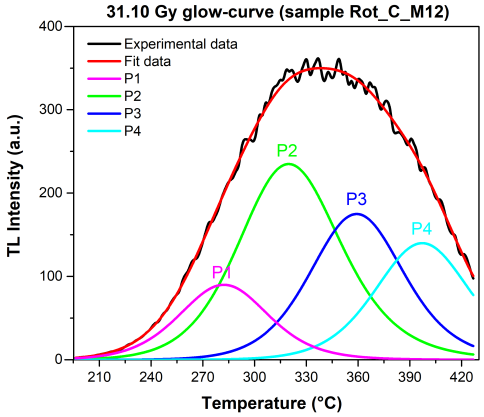

(d) 31.10 Gy. FOM = 2.2%.

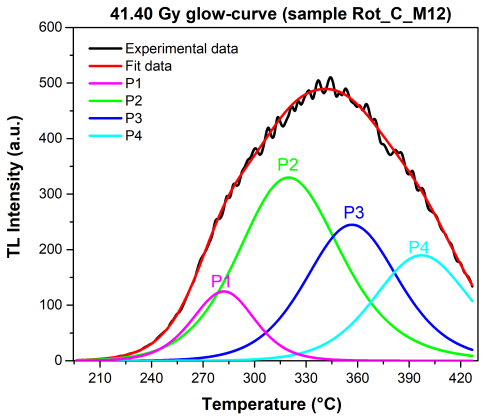

(e) 41.40 Gy. FOM = 2.3%.

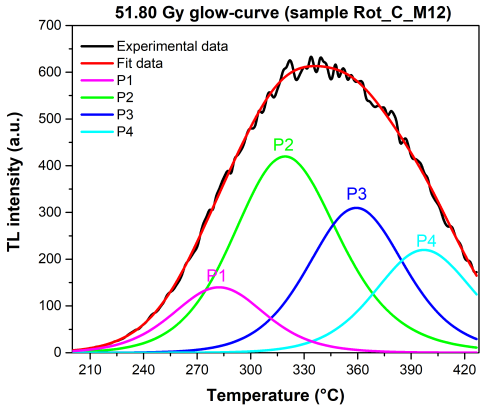

(f) 51.80 Gy. FOM = 2.1%.

Figure A.8: Deconvolution of the TL glow curves for sample Rot_C_M12 corresponding to the natural signal and to the regeneration doses of 10.40, 20.70, 31.10, 41.40, 51.80 Gy. Each plot shows the experimental data (black), the overall fit (red), and the individual TL components (P1–P3) in colour. The FOM values are indicated for each deconvolution, confirming the reliability and consistency of the fitting model.

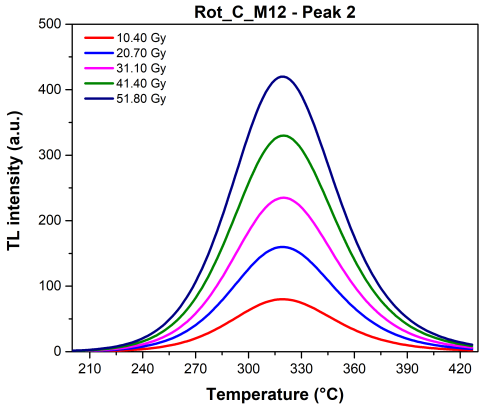

(a) TL intensity variation for Peak 2 (P2) at different regeneration doses.

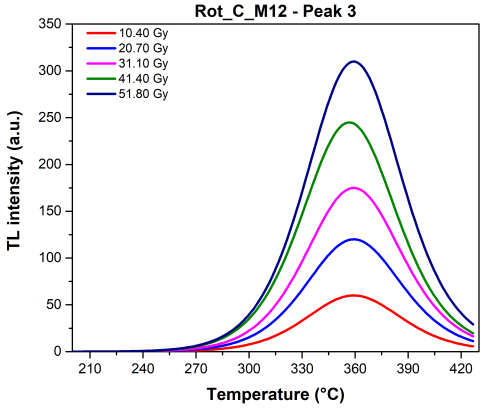

(b) TL intensity variation for Peak 3 (P3) at different regeneration doses.

Figure A.9: Variation in TL intensity of the second (P2) and third (P3) deconvolution peaks for sample Rot_C_M12 as a function of the administered dose.

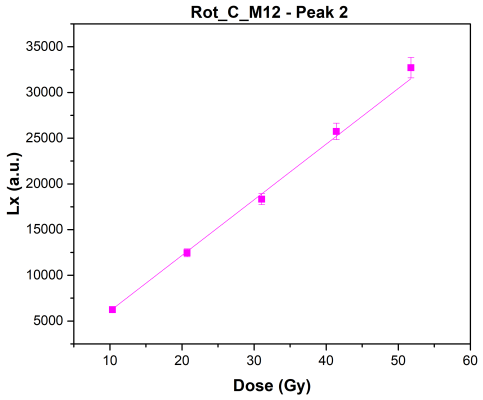

(a) Dose–response curve for Peak 2 (P2).

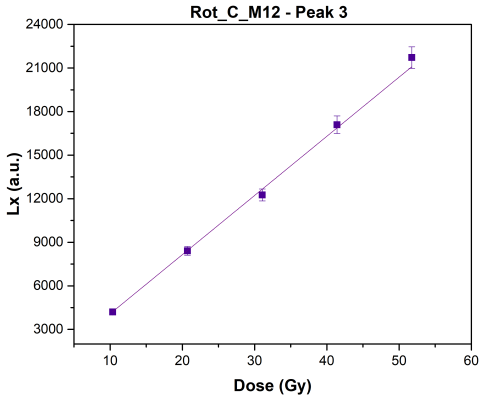

(b) Dose–response curve for Peak 3 (P3).

Figure A.10: Dose–response curves obtained from the integrated intensities of peaks P2 and P3 for sample Rot_C_M12. The experimental data points represent the integrated TL signal as a function of the administered dose, while the solid lines correspond to the best-fit linear functions used to estimate the equivalent dose.

The integrated data were fitted using linear functions of the form $y = ax$. For sample Rot_C_M12, the best-fit equations were $y = (1161.70 \pm 14.33)x$ for P2 and $y = (773.28 \pm 8.04)x$ for P3, with correlation coefficients of $R^2 = 0.998$ and $R^2 = 0.999$ respectively.

In these dose–response curves, the integral value corresponding to the natural signal was interpolated along the fitted line to determine the equivalent dose (D_e) of the sample.

The equivalent dose (D_e) values obtained from the dose–response curves of peaks P2 and P3 were 13.43 ± 0.18 Gy and 18.11 ± 0.24 Gy, respectively. As already specified for the previous samples, the uncertainty on the equivalent dose was estimated through standard error propagation, taking into account both the uncertainty of the linear fit parameters and that of the natural signal integral (Poisson counting error and FOM). This approach ensured that the combined effects of fitting and measurement uncertainties were properly reflected in the final D_e values.

The difference between the two estimates, $D_e(P3) - D_e(P2) = 4.68 \pm 0.30$ Gy, represents, according to the approach described in Chapter 4, the equivalent dose (D_e) of the untreated mortar sample. The uncertainty associated with the difference between the two D_e values was calculated by propagating the individual uncertainties of P2 and P3.

A.3 Sample Rot_C_M14

Sample Rot_C_M14 was collected from the inner portion of a wall in the cold area C, where the original mortar is still well preserved beneath the surface finishes. The sampling point was selected to access material that had remained protected from light exposure and later interventions, ensuring the reliability of the subsequent TL measurements.

A.3.1 Measurement conditions

TL measurements on the unprepared mortar powder were carried out using a Risø TL/DA-15 reader equipped with a BG-39 optical filter. Each sample was subjected to a regenerative measurement protocol, following the sequence reported in Table A.5, which included five regeneration doses after the natural signal measurement.

Table A.5: Measurement sequence applied during the regenerative protocol for the unprepared mortar sample Rot_C_M14.

Step	Treatment	Observed
1	Thermal stimulation (@430 °C, 5 °C s^{-1})	L_N
2	Give regeneration dose D_i (where i = 13.80, 27.60, 41.40, 55.20, 69.00 Gy)	–
3	Preheat (@210 °C, 120 s)	–
4	Thermal stimulation (@430 °C, 5 °C s^{-1})	L_i
5	Repeat steps 2–4 for all regeneration doses D_i	–

Figure A.11: Sampling point of the Rot_C_M14 mortar, extracted from the inner section of a wall in area C. The preserved underlying mortar was accessed to minimise light exposure and avoid surface contaminations.

A.3.2 Analysis and results

The experimental TL glow curves obtained for the unprepared mortar sample Rot_C_M14 are shown in Figure A.12. The natural TL signal and the regenerated curves corresponding to the applied doses of 13.80, 27.60, 41.40, 55.20, 69.00 Gy are reported.

For each glow curve shown in Figure A.12, a deconvolution was performed in order to separate the individual TL components contributing to the total signal. The deconvolution procedure was applied to the natural curve and to each regenerated curve corresponding to the selected doses (13.80, 27.60, 41.40, 55.20, 69.00 Gy). The fitting was carried out using the general order kinetic (GOK) model, following the same approach described in Chapter 4.

Figures A.13 present, for each regeneration dose, the deconvolution of the corresponding TL glow curve together with the table reporting the kinetic parameters of the individual peaks. For each dose step, the experimental data are fitted by the sum of the single TL components, and the figure also reports the FOM value that quantifies the goodness of each deconvolution.

The corresponding kinetic parameters for all regenerated curves are summarised in Table A.6.

Figures A.14a and A.14b show the variation in TL intensity of the second (P2) and third (P3) deconvolution peaks as a function of the administered dose. The linear growth trend confirms the suitability of these components for constructing the dose–response curve used in the equivalent dose determination.

An integration was performed for the second (P2) and third (P3) deconvolution peaks. The resulting values were used to construct the dose–response

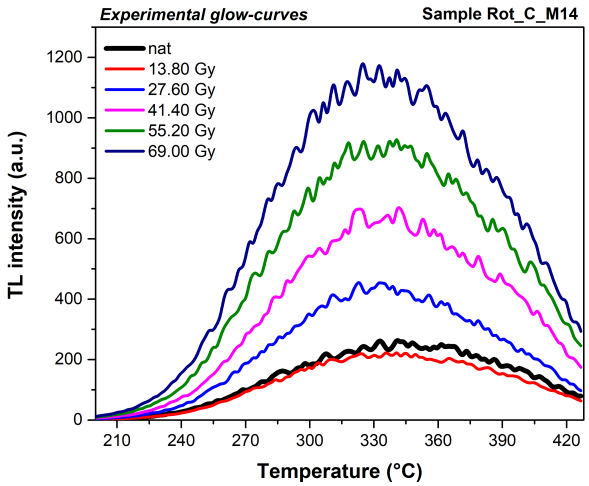

Figure A.12: Experimental TL glow curves obtained for the unprepared mortar sample Rot_C_M14 under regeneration mode. The natural signal (black) and the regenerated curves corresponding to doses of 13.80, 27.60, 41.40, 55.20, 69.00 Gy are shown.

Table A.6: Kinetic parameters derived from the deconvolution of the TL glow curves for sample Rot_C_M14. The same kinetic structure (P1–P3) was maintained across all regeneration doses.

Peak	T_m (°C)	E (eV)	b
P1	285	1.35	1.75
P2	319	1.40	1.90
P3	355	1.70	1.80
P4	397	-	-

curve shown in Figure A.15, where the experimental points represent the integrated TL signals as a function of the administered dose and the red line corresponds to the best-fit linear function used to fit the data.

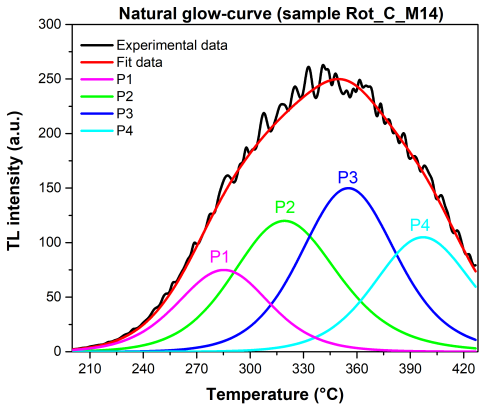

(a) Natural. FOM = 2.2%.

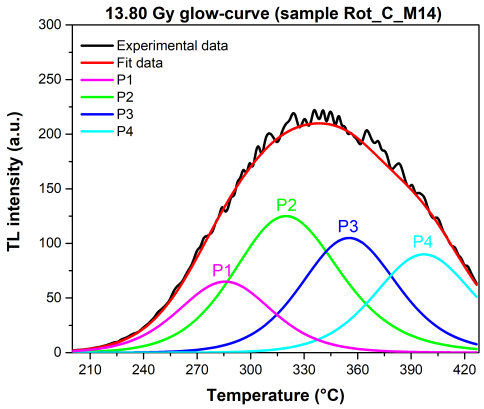

(b) 13.80 Gy. FOM = 2.1%.

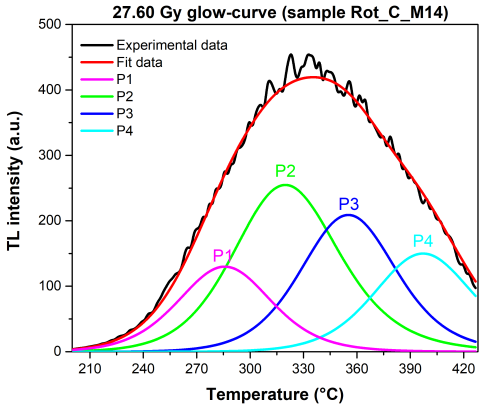

(c) 27.60 Gy. FOM = 2.4%.

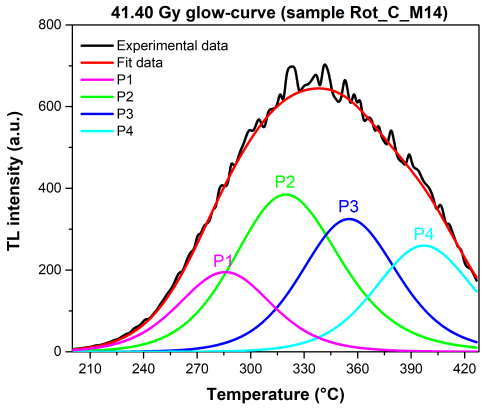

(d) 41.40 Gy. FOM = 2.5%.

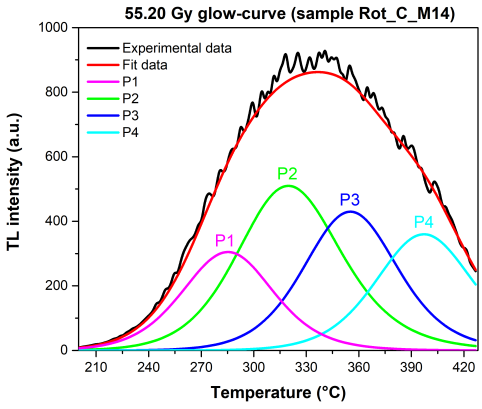

(e) 55.20 Gy. FOM = 2.3%.

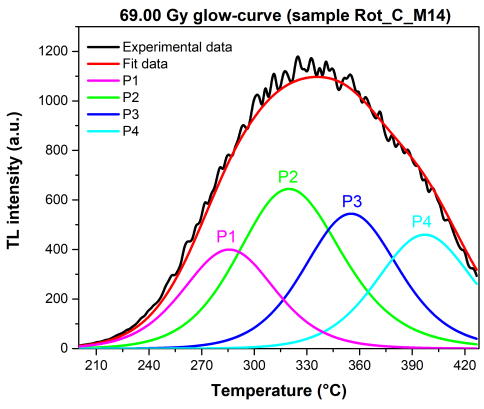

(f) 69.00 Gy. FOM = 2.3%.

Figure A.13: Deconvolution of the TL glow curves for sample Rot_C_M14 corresponding to the natural signal and to the regeneration doses of 13.80, 27.60, 41.40, 55.20, 69.00 Gy. Each plot shows the experimental data (black), the overall fit (red), and the individual TL components (P1–P3) in colour. The FOM values are indicated for each deconvolution, confirming the reliability and consistency of the fitting model.

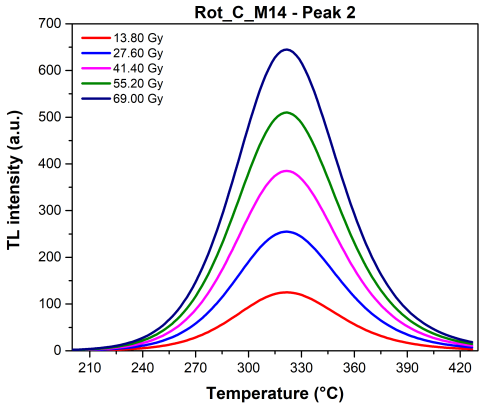

(a) TL intensity variation for Peak 2 (P2) at different regeneration doses.

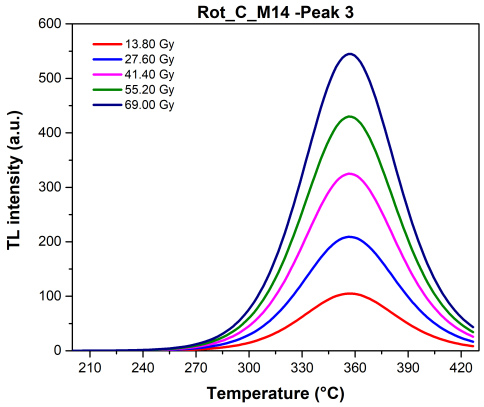

(b) TL intensity variation for Peak 3 (P3) at different regeneration doses.

Figure A.14: Variation in TL intensity of the second (P2) and third (P3) deconvolution peaks for sample Rot_C_M14 as a function of the administered dose.

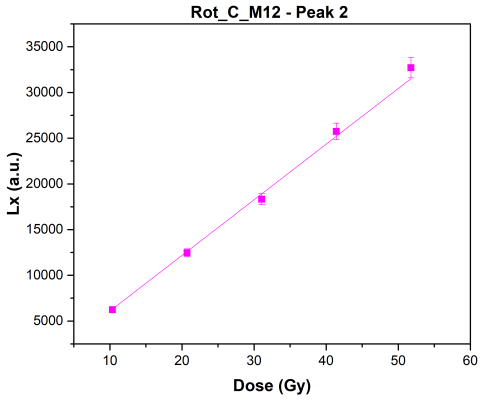

(a) Dose–response curve for Peak 2 (P2).

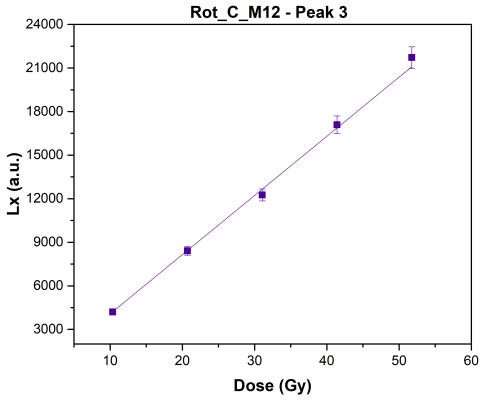

(b) Dose–response curve for Peak 3 (P3).

Figure A.15: Dose–response curves obtained from the integrated intensities of peaks P2 and P3 for sample Rot_C_M14. The experimental data points represent the integrated TL signal as a function of the administered dose, while the solid lines correspond to the best-fit linear functions used to estimate the equivalent dose.

The integrated data were fitted using linear functions of the form $y = ax$. For sample Rot_C_M12, the best-fit equations were $y = (1812.70 \pm 18.42)x$ for P2 and $y = (1361.10 \pm 10.73)x$ for P3, with correlation coefficients of $R^2 = 0.998$.

In these dose–response curves, the integral value corresponding to the natural signal was interpolated along the fitted line to determine the equivalent dose (D_e) of the sample.

The equivalent dose (D_e) values obtained from the dose–response curves of peaks P2 and P3 were 4.99 ± 0.07 Gy and 7.94 ± 0.10 Gy, respectively. As already specified for the previous samples, the uncertainty on the equivalent dose was estimated through standard error propagation, taking into account both the uncertainty of the linear fit parameters and that of the natural signal integral (Poisson counting error and FOM). This approach ensured that the combined effects of fitting and measurement uncertainties were properly reflected in the final D_e values.

The difference between the two estimates, $D_e(P3) - D_e(P2) = 2.95 \pm 0.12$ Gy, represents, according to the approach described in Chapter 4, the equivalent dose (D_e) of the untreated mortar sample. The uncertainty associated with the difference between the two D_e values was calculated by propagating the individual uncertainties of P2 and P3.

A.4 Sample Rot_B1_M1

The sample Rot_B1_M1 was collected from a portion of the masonry located in the *praefurnium* area of the *Terme della Rotonda* complex. The mortar belongs to the conglomerate wall structure adjacent to the heating chamber. The sampling point, shown in Figure A.16, was selected to represent the mortars associated with the thermal functional sector of the building, which is among the best-preserved portions of the archaeological complex.

Figure A.16: Sampling point of the Rot_B1_M1 mortar in the *praefurnium* area of the *Terme della Rotonda* complex. The image shows the conglomerate wall structure from which the sample was sampled.

The fragment collected for TL analysis measured approximately 2–3 cm in width and 1–1.5 cm in thickness, providing sufficient material for powder preparation while ensuring the preservation of the masonry integrity at the sampling point.

As described in Section 4.3.1, TL measurements were carried out directly on the unprepared mortar powder, analysing five aliquots of the sample.

A.4.1 Measurement conditions

TL measurements on the unprepared mortar powder were carried out using a Risø TL/DA-15 reader equipped with a BG-39 optical filter. Each sample was subjected to a regenerative measurement protocol, following the sequence reported in Table A.7, which included four regeneration doses after the natural signal measurement.

Table A.7: Measurement sequence applied during the regenerative protocol for the unprepared mortar sample Rot_B1_M1.

Step	Treatment	Observed
1	Thermal stimulation (@430 °C, 5 °C s^{-1})	L_N
2	Give regeneration dose D_i (where i = 6.90, 17.30, 27.60, 38.00 Gy)	–
3	Preheat (@240 °C, 120 s)	–
4	Thermal stimulation (@430 °C, 5 °C s^{-1})	L_i
5	Repeat steps 2–4 for all regeneration doses D_i	–

A.4.2 Analysis and results

The experimental TL glow curves obtained for the unprepared mortar sample Rot_B1_M1 are shown in Figure A.17. The natural TL signal and the regenerated curves corresponding to the applied doses of 6.90, 17.30, 27.60, and 38.00 Gy are reported. As expected, the TL intensity increases progressively with the regeneration dose, maintaining a similar glow-curve shape across all measurements.

For each glow curve shown in Figure A.17, a deconvolution was performed in order to separate the individual TL components contributing to the total signal. The deconvolution procedure was applied to the natural curve and to each regenerated curve corresponding to the selected doses (6.90, 17.30, 27.60, and 38.00 Gy). The fitting was carried out using the general order kinetic (GOK) model, following the same approach described in Chapter 4.

Figures A.18 present, for each regeneration dose, the deconvolution of the corresponding TL glow curve together with the table reporting the kinetic parameters of the individual peaks. For each dose step, the experimental data are fitted by the sum of the single TL components, and the figure also reports the FOM value that quantifies the goodness of each deconvolution.

The corresponding kinetic parameters for all regenerated curves are summarised in Table A.8.

Figures A.19a and A.19b show the variation in TL intensity of the second (P2) and third (P3) deconvolution peaks as a function of the administered

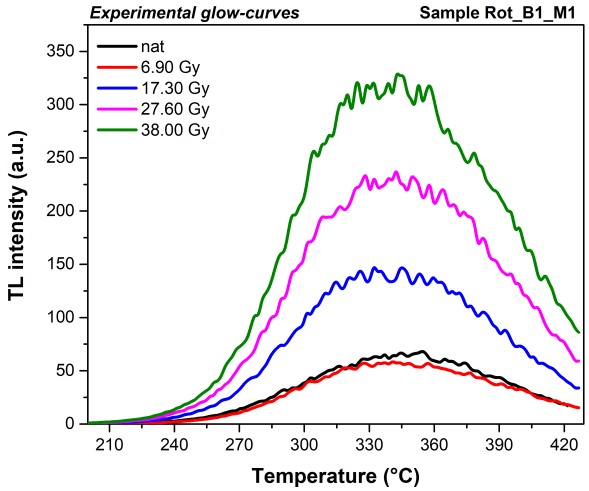

Figure A.17: Experimental TL glow curves obtained for the unprepared mortar sample Rot_B1_M1 under regeneration mode. The natural signal (black) and the regenerated curves corresponding to doses of 6.90, 17.30, 27.60, and 38.00 Gy are shown.

Table A.8: Kinetic parameters derived from the deconvolution of the TL glow curves for sample Rot_B1_M1. The same kinetic structure (P1–P3) was maintained across all regeneration doses.

Peak	T_m (°C)	E (eV)	b
P1	-	-	-
P2	315	1.40	1.90
P3	357	1.51	1.69
P4	397	-	-

dose. The linear growth trend confirms the suitability of these components for constructing the dose–response curve used in the equivalent dose determination.

An integration was performed for the second (P2) and third (P3) deconvolution peaks. The resulting values were used to construct the dose–response curve shown in Figure A.20, where the experimental points represent the integrated TL signals as a function of the administered dose and the red line corresponds to the best-fit linear function used to fit the data.

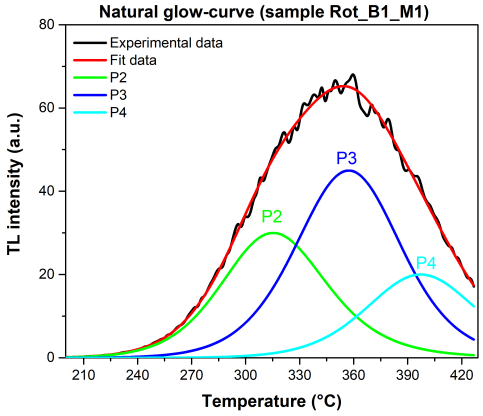

(a) Natural. FOM = 1.5%.

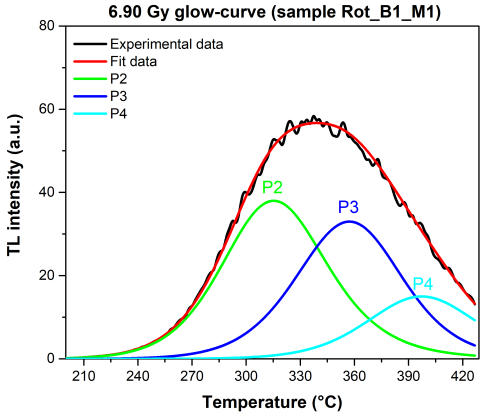

(b) 6.90 Gy. FOM = 1.7%.

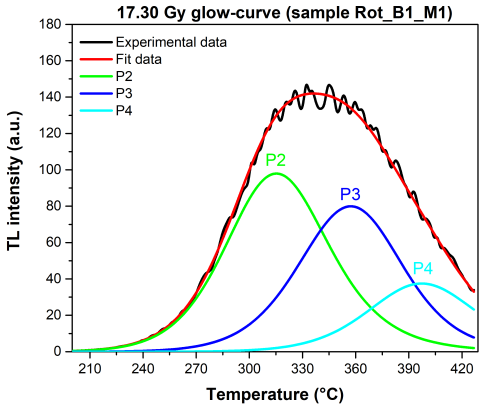

(c) 17.30 Gy. FOM = 1.9%.

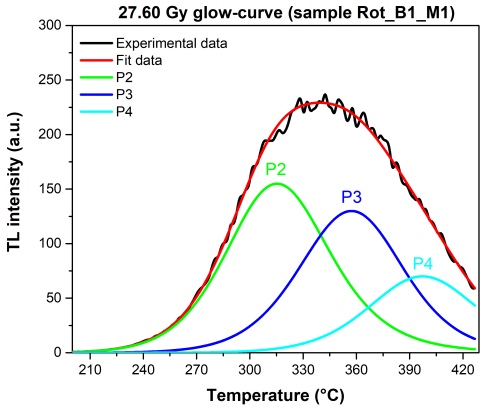

(d) 27.60 Gy. FOM = 2.1%.

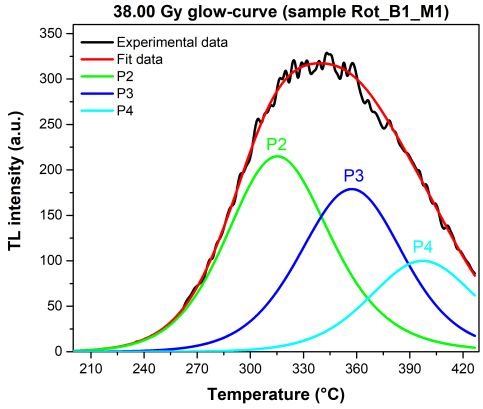

(e) 38.00 Gy. FOM = 1.9%.

Figure A.18: Deconvolution of the TL glow curves for sample Rot_B1_M1 corresponding to the natural signal and to the regeneration doses of 6.90, 17.30, 27.60, and 38.00 Gy. Each plot shows the experimental data (black), the overall fit (red), and the individual TL components (P1–P3) in colour. The FOM values are indicated for each deconvolution, confirming the reliability and consistency of the fitting model.

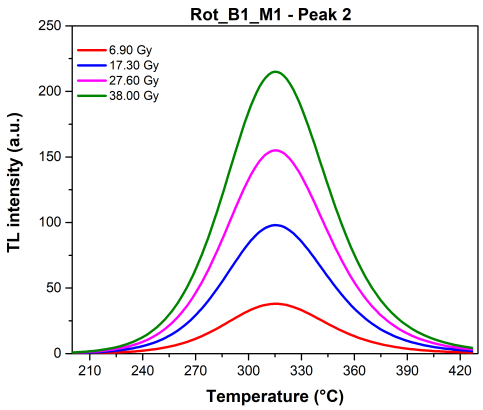

(a) TL intensity variation for Peak 2 (P2) at different regeneration doses.

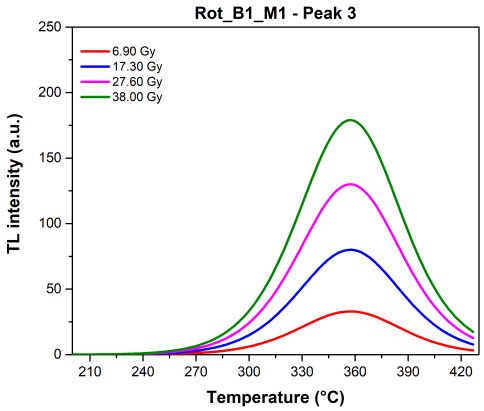

(b) TL intensity variation for Peak 3 (P3) at different regeneration doses.

Figure A.19: Variation in TL intensity of the second (P2) and third (P3) deconvolution peaks for sample Rot_B1_M1 as a function of the administered dose. The progressive increase in luminescence intensity indicates the gradual filling of the traps responsible for these peaks, confirming their suitability for constructing the dose–response curve.

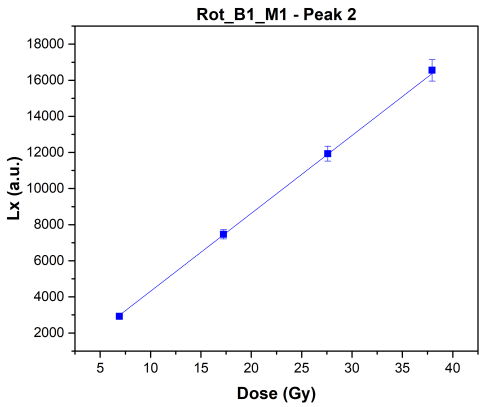

(a) Dose–response curve for Peak 2 (P2).

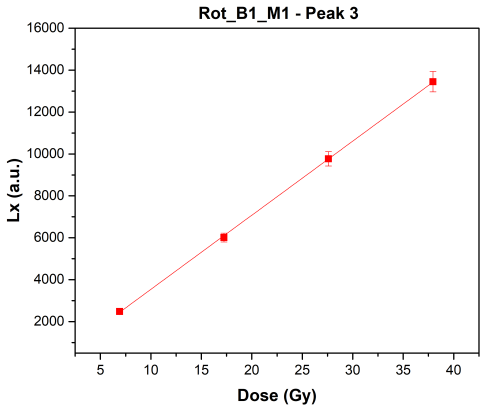

(b) Dose–response curve for Peak 3 (P3).

Figure A.20: Dose–response curves obtained from the integrated intensities of peaks P2 and P3 for sample Rot_B1_M1. The experimental data points represent the integrated TL signal as a function of the administered dose, while the solid lines correspond to the best-fit linear functions used to estimate the equivalent dose.

The integrated data were fitted using linear functions of the form $y = ax$. For sample Rot_B1_M1, the best-fit equations were $y = 431.36x$ for P2 and $y = 353.71x$ for P3, with correlation coefficients of $R^2 = 0.998$ in both cases.

In these dose–response curves, the integral value corresponding to the natural signal was interpolated along the fitted line to determine the equivalent dose (D_e) of the sample.

The equivalent dose (D_e) values obtained from the dose–response curves of peaks P2 and P3 were 5.78 ± 0.25 Gy and 9.56 ± 0.40 Gy, respectively. The uncertainty on the equivalent dose was estimated through standard error propagation, taking into account both the uncertainty of the linear fit parameters and that of the natural signal integral (Poisson counting error and FOM). This approach ensured that the combined effects of fitting and measurement uncertainties were properly reflected in the final D_e values.

The difference between the two estimates, $D_e(P3) - D_e(P2) = 3.78 \pm 0.23$ Gy, represents, according to the approach described in Chapter 4, the equivalent dose (D_e) of the untreated mortar sample. The uncertainty associated with the difference between the two D_e values was calculated by propagating the individual uncertainties of P2 and P3.

A.5 Sample Rot_D_M3

Sample Rot_D_M3 was collected from the inner portion of a pila (brick column) located in the hypocaust system of the hot room, corresponding to the thermal zone D in Figure A.21.

Figure A.21: Sampling point of the Rot_D_M3 mortar, collected from the inner portion of a *pila* (brick column) located in the hypocaust system of the hot room at the Terme della Rotonda. The inner core of the mortar was extracted to minimise exposure to light and surface contamination.

A portion of the unprepared mortar extracted from this pila was subjected to TL measurements.

A.5.1 Measurement conditions

TL measurements on the unprepared mortar powder were carried out using a Risø TL/DA-15 reader equipped with a BG-39 optical filter. Each sample was subjected to a regenerative measurement protocol, following the sequence reported in Table A.9, which included five regeneration doses after the natural signal measurement.

Table A.9: Measurement sequence applied during the regenerative protocol for the unprepared mortar sample Rot_D_M3.

Step	Treatment	Observed
1	Thermal stimulation (@430 °C, 5 °C s^{-1})	L_N
2	Give regeneration dose D_i (where i = 10.40, 20.70, 31.10, 41.40, 51.80 Gy)	–
3	Preheat (@250 °C, 120 s)	–
4	Thermal stimulation (@430 °C, 5 °C s^{-1})	L_i
5	Repeat steps 2–4 for all regeneration doses D_i	–

A.5.2 Analysis and results

The experimental TL glow curves obtained for the unprepared mortar sample Rot_D_M3 are shown in Figure A.22. The natural TL signal and the regenerated curves corresponding to the applied doses of 10.40, 20.70, 31.10, 41.40, 51.80 Gy are reported.

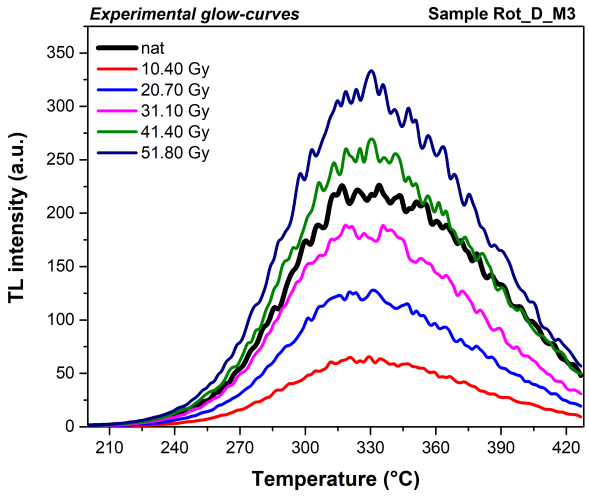

Figure A.22: Experimental TL glow curves obtained for the unprepared mortar sample Rot_D_M3 under regeneration mode. The natural signal (black) and the regenerated curves corresponding to doses of 10.40, 20.70, 31.10, 41.40, 51.80 Gy are shown.

For each glow curve shown in Figure A.22, a deconvolution was performed in order to separate the individual TL components contributing to the total signal. The deconvolution procedure was applied to the natural curve and to each regenerated curve corresponding to the selected doses (10.40, 20.70, 31.10, 41.40, 51.80 Gy). The fitting was carried out using the general order kinetic (GOK) model, following the same approach described in Chapter 4.

Figures A.23 present, for each regeneration dose, the deconvolution of the corresponding TL glow curve together with the table reporting the kinetic parameters of the individual peaks. For each dose step, the experimental data are fitted by the sum of the single TL components, and the figure also reports the FOM value that quantifies the goodness of each deconvolution.

The corresponding kinetic parameters for all regenerated curves are summarised in Table A.10.

Table A.10: Kinetic parameters derived from the deconvolution of the TL glow curves for sample Rot_D_M3.

Peak	T_m (°C)	E (eV)	b
P1	-	-	-
P2	316	1.42	1.91
P3	357	1.50	1.67
P4	398	-	-

Figures A.19a and A.19b show the variation in TL intensity of the second (P2) and third (P3) deconvolution peaks as a function of the administered dose. The linear growth trend confirms the suitability of these components for constructing the dose–response curve used in the equivalent dose determination.

An integration was performed for the second (P2) and third (P3) deconvolution peaks. The resulting values were used to construct the dose–response curve shown in Figure A.25, where the experimental points represent the integrated TL signals as a function of the administered dose and the red line corresponds to the best-fit linear function used to fit the data.

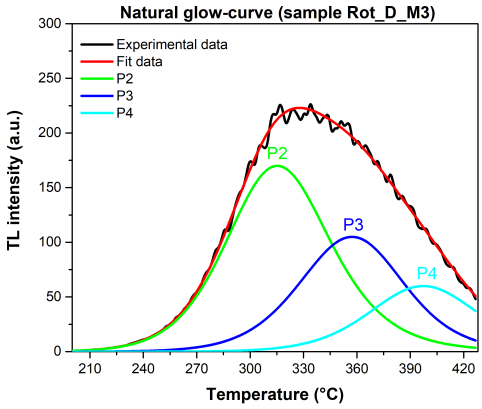

(a) Natural. FOM = 1.7%.

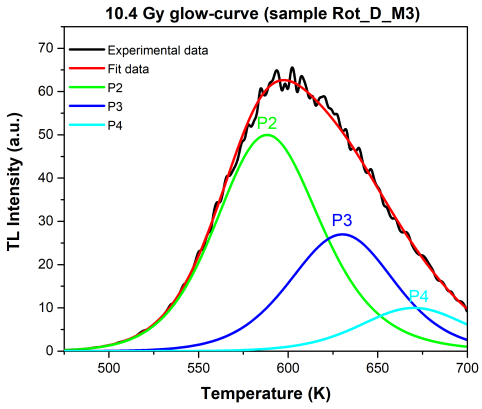

(b) 10.40 Gy. FOM = 2.0%.

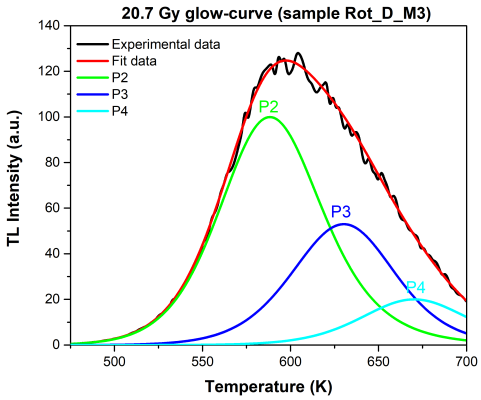

(c) 20.70 Gy. FOM = 2.2%.

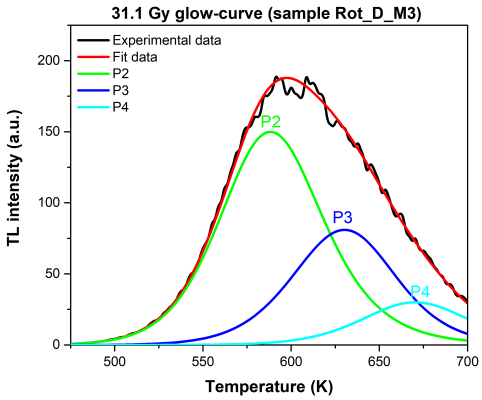

(d) 31.10 Gy. FOM = 2.4%.

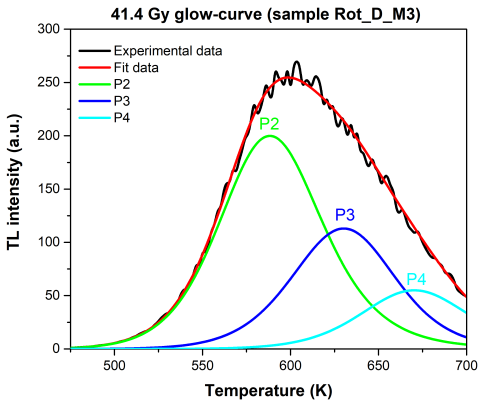

(e) 41.40 Gy. FOM = 2.1%.

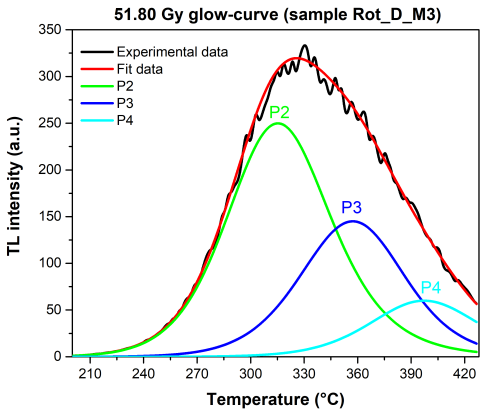

(f) 51.80 Gy. FOM = 2.5%.

Figure A.23: Deconvolution of the TL glow curves for sample Rot_D_M3 corresponding to the natural signal and to the regeneration doses of 10.40, 20.70, 31.10, 41.40, 51.80 Gy. Each plot shows the experimental data (black), the overall fit (red), and the individual TL components (P1–P3) in colour. The FOM values are indicated for each deconvolution, confirming the reliability and consistency of the fitting model.

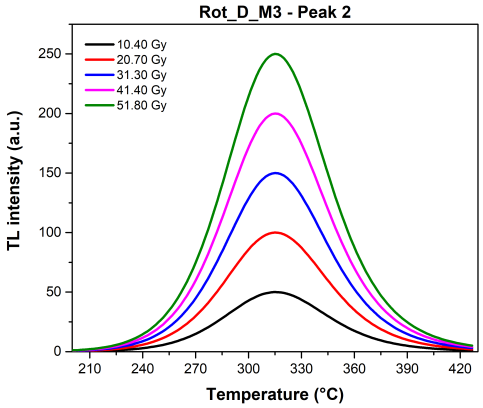

(a) TL intensity variation for Peak 2 (P2) at different regeneration doses.

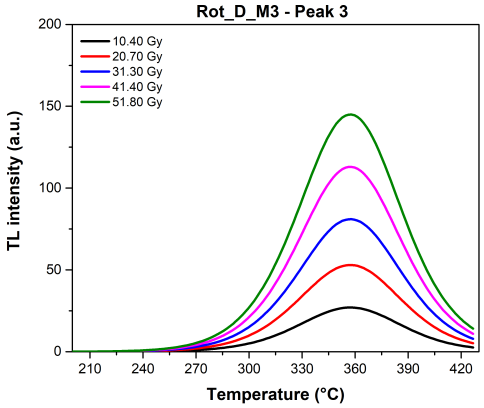

(b) TL intensity variation for Peak 3 (P3) at different regeneration doses.

Figure A.24: Variation in TL intensity of the second (P2) and third (P3) deconvolution peaks for sample Rot_D_M3 as a function of the administered dose. The progressive increase in luminescence intensity indicates the gradual filling of the traps responsible for these peaks, confirming their suitability for constructing the dose–response curve.

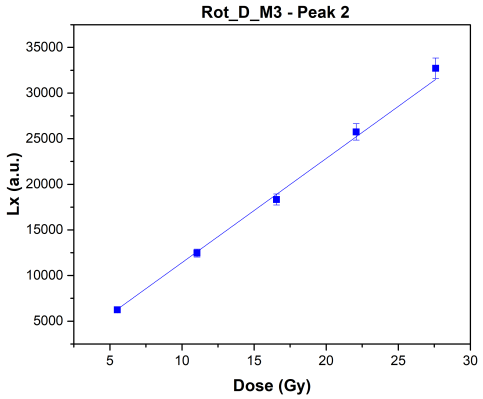

(a) Dose–response curve for Peak 2 (P2).

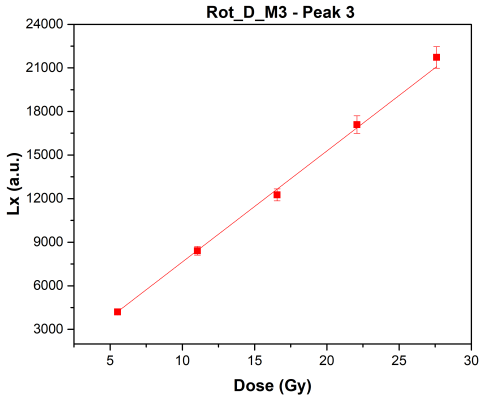

(b) Dose–response curve for Peak 3 (P3).

Figure A.25: Dose–response curves obtained from the integrated intensities of peaks P2 and P3 for sample Rot_D_M3. The experimental data points represent the integrated TL signal as a function of the administered dose, while the solid lines correspond to the best-fit linear functions used to estimate the equivalent dose.

The integrated data were fitted using linear functions of the form $y = ax$. For sample Rot_D_M3, the best-fit equations were $y = (371.92 \pm 5.97)x$ for P2 and $y = 199.50 \pm 3.22x$ for P3, with correlation coefficients of $R^2 = 0.999$ and $R^2 = 0.997$ respectively.

In these dose–response curves, the integral value corresponding to the natural signal was interpolated along the fitted line to determine the equivalent dose (D_e) of the sample.

The equivalent dose (D_e) values obtained from the dose–response curves of peaks P2 and P3 were 35.19 ± 1.42 Gy and 38.64 ± 1.60 Gy, respectively. The uncertainty on the equivalent dose was estimated through standard error propagation, taking into account both the uncertainty of the linear fit parameters and that of the natural signal integral (Poisson counting error and FOM). This approach ensured that the combined effects of fitting and measurement uncertainties were properly reflected in the final D_e values.

The difference between the two estimates, $D_e(P3) - D_e(P2) = 3.45 \pm 0.20$ Gy, represents, according to the approach described in Chapter 4, the equivalent dose (D_e) of the untreated mortar sample. The uncertainty associated with the difference between the two D_e values was calculated by propagating the individual uncertainties of P2 and P3.

A.6 Sample Rot_D_M5

Sample Rot_D_M5 was collected from the inner portion of a second *pila* located in the hypocaust system of the thermal zone D in Figure A.26.

Figure A.26: Sampling point of the Rot_D_M5 mortar, collected from the inner portion of a *pila*. The inner core of the mortar was extracted to minimise exposure to light and surface contamination.

A portion of the unprepared mortar extracted from this *pila* was subjected to TL measurements.

A.6.1 Measurement conditions

TL measurements on the unprepared mortar powder were carried out using a Risø TL/DA-15 reader equipped with a BG-39 optical filter. Each sample was subjected to a regenerative measurement protocol, following the sequence reported in Table A.11, which included five regeneration doses after the natural signal measurement.

Table A.11: Measurement sequence applied during the regenerative protocol for the unprepared mortar sample Rot_B1_M5.

Step	Treatment	Observed
1	Thermal stimulation (@430 °C, 5 °C s^{-1})	L_N
2	Give regeneration dose D_i (where i = 13.80, 27.60, 41.40, 55.20, 69.00 Gy)	–
3	Preheat (@260 °C, 120 s)	–
4	Thermal stimulation (@430 °C, 5 °C s^{-1})	L_i
5	Repeat steps 2–4 for all regeneration doses D_i	–

A.6.2 Analysis and results

The experimental TL glow curves obtained for the unprepared mortar sample Rot_B1_M1 are shown in Figure A.22. The natural TL signal and the regenerated curves corresponding to the applied doses of 13.80, 27.60, 41.40, 55.20, 69.00 Gy are reported.

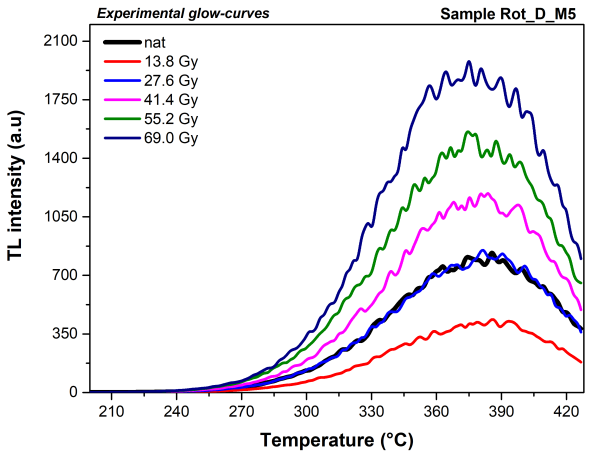

Figure A.27: Experimental TL glow curves obtained for the unprepared mortar sample Rot_D_M5 under regeneration mode. The natural signal (black) and the regenerated curves corresponding to doses of 13.80, 27.60, 41.40, 55.20, 69.00 Gy are shown.

For each glow curve shown in Figure A.22, a deconvolution was performed in order to separate the individual TL components contributing to the total signal. The deconvolution procedure was applied to the natural curve and to each regenerated curve corresponding to the selected doses (13.80, 27.60, 41.40, 55.20, 69.00 Gy). The fitting was carried out using the general order kinetic (GOK) model, following the same approach described in Chapter 4.

Figures A.28 present, for each regeneration dose, the deconvolution of the corresponding TL glow curve together with the table reporting the kinetic

parameters of the individual peaks. For each dose step, the experimental data are fitted by the sum of the single TL components, and the figure also reports the FOM value that quantifies the goodness of each deconvolution.

The corresponding kinetic parameters for all regenerated curves are summarised in Table A.12.

Table A.12: Kinetic parameters derived from the deconvolution of the TL glow curves for sample Rot_D_M5. The same kinetic structure (P1–P3) was maintained across all regeneration doses.

Peak	T_m (°C)	E (eV)	b
P1	-	-	-
P2	317	1.39	1.90
P3	357	1.52	1.65
P4	397	-	-

Figures A.29a and A.29b show the variation in TL intensity of the second (P2) and third (P3) deconvolution peaks as a function of the administered dose. The linear growth trend confirms the suitability of these components for constructing the dose–response curve used in the equivalent dose determination.

An integration was performed for the second (P2) and third (P3) deconvolution peaks. The resulting values were used to construct the dose–response curve shown in Figure A.30, where the experimental points represent the integrated TL signals as a function of the administered dose and the red line corresponds to the best-fit linear function used to fit the data.

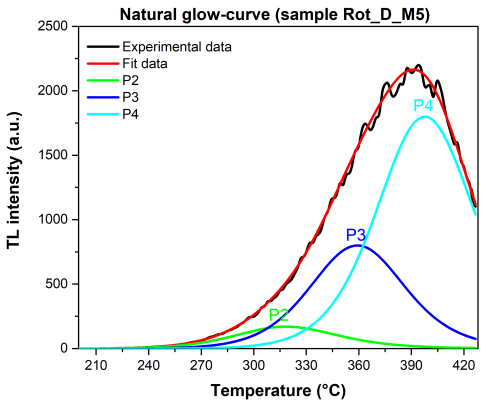

(a) Natural. FOM = 1.6%.

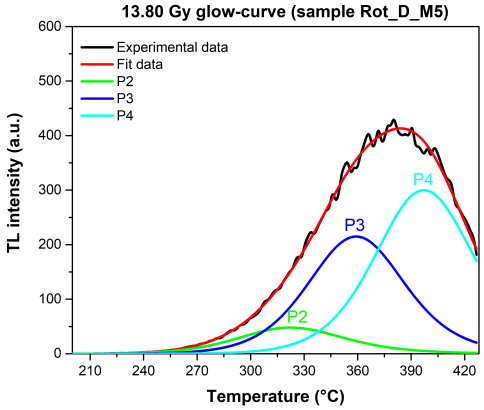

(b) 13.80 Gy. FOM = 1.8%.

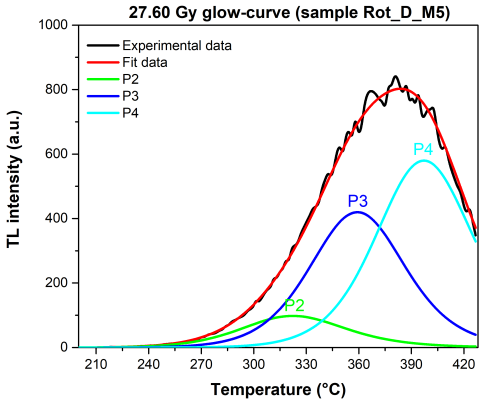

(c) 27.60 Gy. FOM = 1.9%.

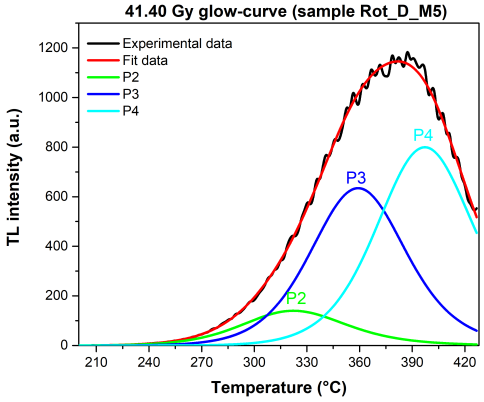

(d) 41.40 Gy. FOM = 2.0%.

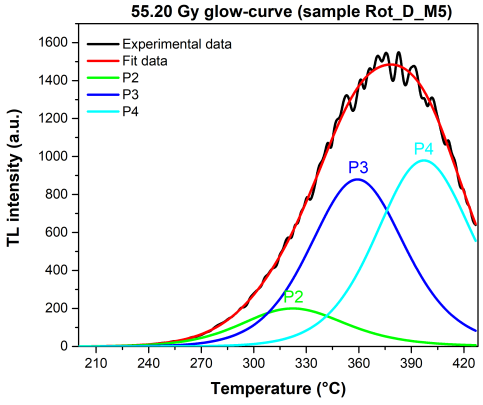

(e) 55.20 Gy. FOM = 2.1%.

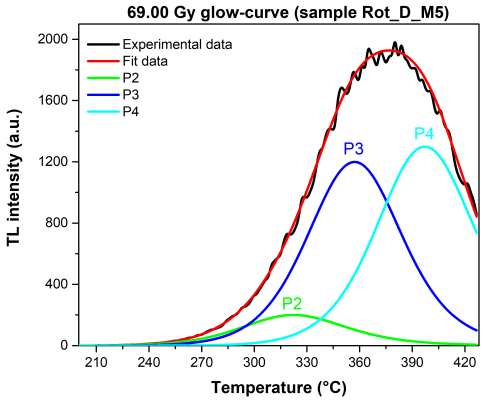

(f) 69.00 Gy. FOM = 2.0%.

Figure A.28: Deconvolution of the TL glow curves for sample Rot_D_M5 corresponding to the natural signal and to the regeneration doses of 13.80, 27.60, 41.40, 55.20, 69.00 Gy. Each plot shows the experimental data (black), the overall fit (red), and the individual TL components (P1–P3) in colour. The FOM values are indicated for each deconvolution, confirming the reliability and consistency of the fitting model.

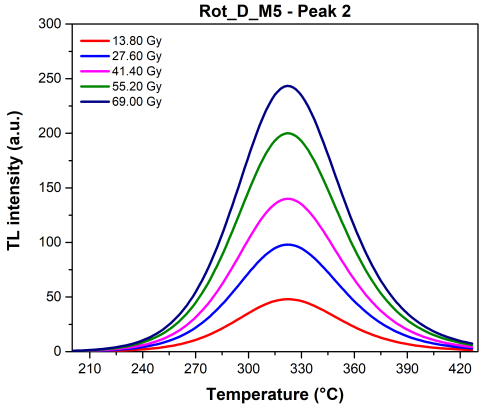

(a) TL intensity variation for Peak 2 (P2) at different regeneration doses.

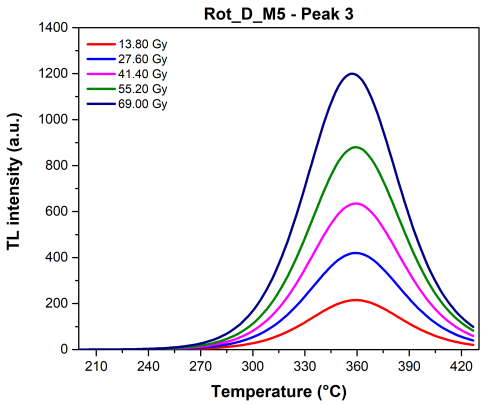

(b) TL intensity variation for Peak 3 (P3) at different regeneration doses.

Figure A.29: Variation in TL intensity of the second (P2) and third (P3) deconvolution peaks for sample Rot_D_M5 as a function of the administered dose.

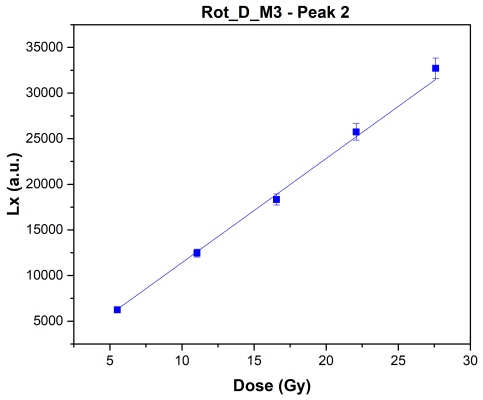

(a) Dose–response curve for Peak 2 (P2).

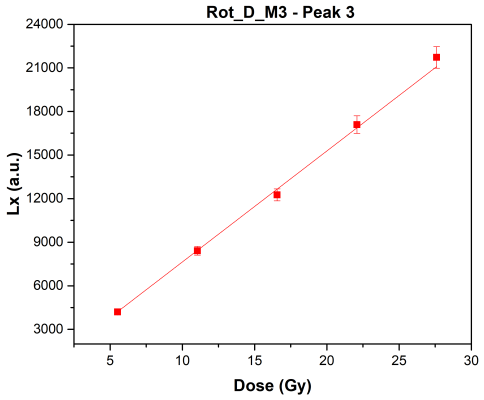

(b) Dose–response curve for Peak 3 (P3).

Figure A.30: Dose–response curves obtained from the integrated intensities of peaks P2 and P3 for sample Rot_D_M5. The experimental data points represent the integrated TL signal as a function of the administered dose, while the solid lines correspond to the best-fit linear functions used to estimate the equivalent dose.

The integrated data were fitted using linear functions of the form $y = ax$. For sample Rot_D_M5, the best-fit equations were $y = (275.15 \pm 5.24)x$ for P2 and $y = (1087.34 \pm 19.94)x$ for P3, with correlation coefficients of $R^2 = 0.999$ and $R^2 = 0.997$ respectively.

In these dose–response curves, the integral value corresponding to the natural signal was interpolated along the fitted line to determine the equivalent dose (D_e) of the sample.

The equivalent dose (D_e) values obtained from the dose–response curves of peaks P2 and P3 were 47.98 ± 2.01 Gy and 51.54 ± 2.10 Gy, respectively. As already specified for the previous samples, the uncertainty on the equivalent dose was estimated through standard error propagation, taking into account both the uncertainty of the linear fit parameters and that of the natural signal integral (Poisson counting error and FOM). This approach ensured that the combined effects of fitting and measurement uncertainties were properly reflected in the final D_e values.

The difference between the two estimates, $D_e(P3) - D_e(P2) = 3.56 \pm 0.21$ Gy, represents, according to the approach described in Chapter 4, the equivalent dose (D_e) of the untreated mortar sample. The uncertainty associated with the difference between the two D_e values was calculated by propagating the individual uncertainties of P2 and P3.

Bibliography

[1] M. J. Aitken. *Thermoluminescence dating*. Academic Press, London, 1985.

[2] P. Guibert, I. K. Bailiff, S. Blain, A. M. Gueli, M. Martini, E. Sibilia, G. Stella, and S. O. Troja. Luminescence dating of architectural ceramics from an early medieval abbey: The st philbert intercomparison (loire atlantique, france). *Radiation Measurements*, 44(5-6):488–493, 2009.

[3] I. K. Bailiff. Methodological developments in the luminescence dating of brick from english late-medieval and post-medieval buildings. *Archaeometry*, 49(4):827–851, 2007.

[4] M. Martini and E. Sibilia. Absolute dating of historical buildings: The contribution of thermoluminescence (tl). *Journal of Neutron Research*, 14(1):69–74, 2006.

[5] J. Sanjurjo-Sánchez and J. L. Montero Fenollós. First test for luminescence dating of ancient mud-brick buildings from northern mesopotamia. In A. Daneels, editor, *Monumental Earthen Architecture in Early Societies*, pages 45–52. Archaeopress, Oxford, 2016.

[6] A. Galli, M. Martini, F. Maspero, L. Panzeri, and E. Sibilia. Surface dating of bricks, an application of luminescence techniques. *The European Physical Journal Plus*, 129(5):101, 2014.

[7] C. Goedicke. Dating mortar by optically stimulated luminescence: A feasibility study. *Geochronometria*, 38(1):42–49, 2011.

[8] C. Groot, R. Veiga, I. Papayianni, R. Van Hees, M. Secco, J. I. Alvarez, P. Faria, and M. Stefanidou. Rilem tc 277-lhs report: Lime-based mortars for restoration – a review on long-term durability aspects and experience from practice. *Materials and Structures*, 55(10):245, 2022.

[9] P. Urbanová, E. Boaretto, and G. Artioli. The state-of-the-art of dating techniques applied to ancient mortars and binders: A review. *Radiocarbon*, 62(3):503–525, 2020.

[10] S.-H. Li. Optical dating: Insufficiently bleached sediments. *Radiation Measurements*, 23(2-3):563–567, 1994.

[11] J. Wallinga. *The Rhine-Meuse system in a new light: Optically stimulated luminescence dating and its application to fluvial deposits*. PhD thesis, Utrecht University, Utrecht, 2001.

[12] K. J. Thomsen. *Optically stimulated luminescence techniques in retrospective dosimetry using single grains of quartz extracted from unheated materials*. PhD thesis, Risø National Laboratory, Denmark, 2004.

[13] P. Urbanová and P. Guibert. Methodological study on single grain osl dating of mortars: Comparison of five reference archaeological sites. *Geochronometria*, 44(1):77–97, 2017.

[14] L. Panzeri, M. Caroselli, A. Galli, S. Lugli, M. Martini, and E. Sibilia. Mortar osl and brick tl dating: The case study of the unesco world heritage site of modena. *Quaternary Geochronology*, 49:236–241, 2019.

[15] V. A. Anupama and M. Santhanam. Morphological evolution of calcium carbonate crystals in dry hydrated lime mortar. In *Historic Mortars International Conference*, volume 204 of *Lecture Notes in Civil Engineering*, pages 469–475, Cham, 2022. Springer.

[16] P.-N. Maravelaki, A. Theologitis, M. Budak Unaler, C. Kapridaki, K. Kapetanaki, and J. Wright. Characterization of ancient mortars from minoan city of kommos in crete. *Heritage*, 4(4):3908–3918, 2021.

[17] G. Ponce-Antón, M. C. Zuluaga, L. Á. Ortega, J. Jiménez Echevarría, and C. Alonso Fernández. Characterization of historic lime mortars from the arch of san martin to identify the construction phases of the city wall of burgos (spain). *Minerals*, 14(2):147, 2024.

[18] R. Galvagno, G. Stella, R. Reitano, and A. M. Gueli. Discrimination of thermoluminescent signals from natural quartz and carbonate crystals mixture. *Crystals*, 15(4):306, 2025.

[19] S. W. S. McKeever. *Thermoluminescence of Solids*. Cambridge Solid State Science Series. Cambridge University Press, Cambridge, 1985.

[20] C. M. Sunta. *Unraveling Thermoluminescence*, volume 1. Springer, Berlin, Heidelberg, 2015.

[21] E. G. Yukihara and S. W. S. McKeever. *Optically stimulated luminescence: Fundamentals and applications*. John Wiley & Sons, Chichester, 2011.

[22] G. F. J. Garlick. Luminescence. *Light and Matter II / Licht und Materie II*, pages 1–128, 1958.

[23] D. Curie. *Champ cristallin et luminescence: Applications de la théorie des groupes à la luminescence cristalline*. FeniXX, Paris, 1968.

[24] J.-F. Zhang, W.-W. Huang, Y. Hu, S.-X. Yang, and L.-P. Zhou. Optical dating of flowstone and silty carbonate-rich sediments from panxian dadong cave, guizhou, southwestern china. *Quaternary Geochronology*, 30:479–486, 2015.

[25] A. C. Lewandowski and S. W. S. McKeever. Generalized description of thermally stimulated processes without the quasiequilibrium approximation. *Physical Review B*, 43(10):8163–8169, 1991.

[26] J. H. Schulman and W. D. Compton. *Color Centers in Solids*. Pergamon Press, Oxford, 1962.

[27] R. Chen and S. W. S. McKeever. *Theory of thermoluminescence and related phenomena*. World Scientific, Singapore, 1997.

[28] A. J. J. Bos. Theory of thermoluminescence. *Radiation Measurements*, 41(S1):S45–S56, 2006.

[29] J. T. Randall and M. H. F. Wilkins. Phosphorescence and electron traps–i. the study of trap distributions. *Proceedings of the Royal Society of London. Series A: Mathematical and Physical Sciences*, 184(999):365–389, 1945.

[30] G. F. J. Garlick and A. F. Gibson. The electron trap mechanism of luminescence in sulphide and silicate phosphors. *Proceedings of the Physical Society*, 60(6):574–590, 1948.

[31] C. E. May and J. A. Partridge. Thermoluminescent kinetics of alpha-irradiated alkali halides. *The Journal of Chemical Physics*, 40(5):1401–1409, 1964.

[32] G. Kitis, J. M. Gomez-Ros, and J. W. N. Tuyn. Thermoluminescence glow-curve deconvolution functions for first, second and general orders of kinetics. *Journal of Physics D: Applied Physics*, 31(19):2636–2641, 1998.

[33] C. M. Sunta, W. E. Feria Ayta, R. N. Kulkarni, R. Chen, and S. Watanabe. Pre-exponential factor in general order kinetics of thermoluminescence and its influence on glow curves. *Radiation Protection Dosimetry*, 71(2):93–97, 1997.

[34] S. W. S. McKeever. Optically stimulated luminescence dosimetry. *Nuclear Instruments and Methods in Physics Research Section B: Beam Interactions with Materials and Atoms*, 184(1-2):29–54, 2001.

[35] L. Bøtter-Jensen. Luminescence techniques: Instrumentation and methods. *Radiation Measurements*, 27(5-6):749–768, 1997.

[36] P. W. Levy. Thermoluminescence kinetics in materials exposed to the low doses applicable to dating and dosimetry. *Nuclear Tracks and Radiation Measurements*, 10(4-6):547–556, 1985.

[37] L.-P. Zhou and N. J. Shackleton. Photon-stimulated luminescence of quartz from loess and effects of sensitivity change on palaeodose determination. *Quaternary Science Reviews*, 20(5-9):853–857, 2001.

[38] F. Preusser, M. L. Chithambo, T. Götte, M. Martini, K. Ramseyer, E. J. Sendezera, G. J. Susino, and A. G. Wintle. Quartz as a natural luminescence dosimeter. *Earth-Science Reviews*, 97(1-4):184–214, 2009.

[39] A. G. Wintle. Fifty years of luminescence dating. *Archaeometry*, 50(2):276–312, 2008.

[40] D. Mebhah, D. Imatoukene, F. Z. Abdelazziz, and Z. Lounis-Mokrani. Evaluation of trap parameters associated with thermoluminescence peaks in fired quartz. *Radiation Measurements*, 41(7-8):813–818, 2006.

[41] M. Jain and L. R. Lindvold. Blue light stimulation and linearly modulated optically stimulated luminescence. *Ancient TL*, 25(2):69–80, 2007.

[42] N. A. Spooner and A. D. Franklin. Effect of the heating rate on the red tl of quartz. *Radiation Measurements*, 35(1):59–66, 2002.

[43] M. R. Krbetschek, J. Götze, A. Dietrich, and T. Trautmann. Spectral information from minerals relevant for luminescence dating. *Radiation Measurements*, 27(5-6):695–748, 1997.

[44] D. J. Huntley, D. I. Godfrey-Smith, and M. L. W. Thewalt. Optical dating of sediments. *Nature*, 313(5998):105–107, 1985.

[45] M. Martini and A. Galli. Ionic mechanisms in the optically stimulated luminescence of quartz. *Physica Status Solidi C*, 4(3):1000–1003, 2007.

[46] L. Bøtter-Jensen, G. A. T. Duller, and N. R. J. Poolton. Excitation and emission spectrometry of stimulated luminescence from quartz and feldspars. *Radiation Measurements*, 23(2-3):613–616, 1994.

[47] D. J. Huntley, M. A. Short, and K. Dunphy. Deep traps in quartz and their use for optical dating. *Canadian Journal of Physics*, 74(3-4):81–91, 1996.

[48] M. Softa, J. Q. G. Spencer, H. Sözbilir, S. Huot, and T. Emre. Luminescence dating of quaternary marine terraces from the coastal part of eastern black sea and their tectonic implications for the eastern pontides, turkey. *Turkish Journal of Earth Sciences*, 30(3):359–378, 2021.

[49] A. G. Wintle. A thermoluminescence dating study of some quaternary calcite: Potential and problems. *Canadian Journal of Earth Sciences*, 15(12):1977–1986, 1978.

[50] J. Zhang and L. Wang. Thermoluminescence dating of calcite: Alpha effectiveness and measurement protocols. *Journal of Luminescence*, 223:117205, 2020.

[51] G. A. T. Duller, D. A. Richards, J. Eikenberg, and K. Dornich. Assessing the potential of optical dating using biogenic calcites. *Radiation Measurements*, 44(5-6):429–433, 2009.

[52] M. B. Toffolo, G. Ricci, L. Caneve, and I. Kaplan-Ashiri. Luminescence reveals variations in local structural order of calcium carbonate polymorphs formed by different mechanisms. *Scientific Reports*, 9(1):16170, 2019.

[53] I. Liritzis, A. K. Singhvi, J. K. Feathers, G. A. Wagner, A. Kadereit, N. Zacharias, and S.-H. Li, editors. *Luminescence Dating in Archaeology, Anthropology, and Geoarchaeology: An Overview*. Springer, Berlin, Heidelberg, 2013.

[54] D. I. Godfrey-Smith, D. J. Huntley, and W.-H. Chen. Optical dating studies of quartz and feldspar sediment extracts. *Quaternary Science Reviews*, 7(3-4):373–380, 1988.

[55] L. Bøtter-Jensen, G. A. T. Duller, A. S. Murray, and D. Banerjee. Blue light emitting diodes for optical stimulation of quartz in retrospective dosimetry and dating. *Radiation Protection Dosimetry*, 84(1-4):335–340, 1999.

[56] N. Zacharias, B. Mauz, and C. T. Michael. Luminescence quartz dating of lime mortars: A first research approach. *Radiation Protection Dosimetry*, 101(1-4):379–382, 2002.

[57] C. Goedicke. Dating historical calcite mortar by blue osl: Results from known age samples. *Radiation Measurements*, 37(4-5):409–415, 2003.

[58] M. Jain, K. J. Thomsen, L. Bøtter-Jensen, and A. S. Murray. Thermal transfer and apparent-dose distributions in poorly bleached mortar samples: Results from single grains and small aliquots of quartz. *Radiation Measurements*, 38(1):101–109, 2004.

[59] A. Gueli, G. Stella, S. Troja, G. Burrafato, D. Fontana, G. Ristuccia, and A. Zuccarello. Historical buildings: Luminescence dating of fine grains from bricks and mortar. *Il Nuovo Cimento B*, 125(5-6):719–729, 2010.

[60] G. Stella, D. Fontana, A. M. Gueli, and S. O. Troja. Historical mortars dating from osl signals of fine grain fraction enriched in quartz. *Geochronometria*, 40(3):153–164, 2013.

[61] G. Stella, L. Almeida, L. Basílio, S. Pasquale, J. Dinis, M. Almeida, and A. M. Gueli. Historical building dating: A multidisciplinary study of the convento de são francisco (coimbra, portugal). *Geochronometria*, 45(1):119–129, 2018.

[62] A. S. Murray, J. M. Olley, and G. G. Caitcheon. Measurement of equivalent doses in quartz from contemporary water-lain sediments using optically stimulated luminescence. *Quaternary Science Reviews*, 14(4):365–371, 1995.

[63] J. Olley, G. Caitcheon, and A. Murray. The distribution of apparent dose as determined by optically stimulated luminescence in small aliquots of fluvial quartz: Implications for dating young sediments. *Quaternary Science Reviews*, 17(11):1033–1040, 1998.

[64] A. S. Murray and A. G. Wintle. Luminescence dating of quartz using an improved single-aliquot regenerative-dose protocol. *Radiation Measurements*, 32(1):57–73, 2000.

[65] G. W. Berger and J. J. Luternauer. Preliminary field work for thermoluminescence dating studies at the fraser river delta, british columbia. Paper 87-1E, Geological Survey of Canada, Ottawa, 1987.

[66] G. W. Berger. Progress in luminescence dating methods for quaternary sediments. In *Dating Methods for Quaternary Deposits*, volume 2, pages 81–104. Geological Association of Canada, Waterloo, Ontario, 1995.

[67] G. A. T. Duller. Luminescence dating of poorly bleached sediments from scotland. *Quaternary Science Reviews*, 13(5-7):521–524, 1994.

[68] G. A. T. Duller. Luminescence dating using single aliquots: Methods and applications. *Radiation Measurements*, 24(3):217–226, 1995.

[69] M. L. Clarke. Irsl dating of sands: Bleaching characteristics at deposition inferred from the use of single aliquots. *Radiation Measurements*, 26(4):611–620, 1996.

[70] M. L. Clarke, H. M. Rendell, and A. G. Wintle. Quality assurance in luminescence dating. *Geomorphology*, 29(1-2):173–185, 1999.

[71] J. M. Olley, G. G. Caitcheon, and R. G. Roberts. The origin of dose distributions in fluvial sediments, and the prospect of dating single grains from fluvial deposits using optically stimulated luminescence. *Radiation Measurements*, 30(2):207–217, 1999.

[72] G. A. T. Duller, L. Bøtter-Jensen, A. S. Murray, and A. J. Truscott. Single grain laser luminescence (sgll) measurements using a novel automated reader. *Nuclear Instruments and Methods in Physics Research Section B: Beam Interactions with Materials and Atoms*, 155(4):506–514, 1999.

[73] L. Bøtter-Jensen, E. Bulur, G. A. T. Duller, and A. S. Murray. Advances in luminescence instrument systems. *Radiation Measurements*, 32(5-6):523–528, 2000.

[74] M. Jain, L. Bøtter-Jensen, A. S. Murray, and H. Jungner. Retrospective dosimetry: Dose evaluation using unheated and heated quartz from a radioactive waste storage building. *Radiation Protection Dosimetry*, 101(1-4):525–530, 2002.

[75] P. Urbanová, D. Hourcade, C. Ney, and P. Guibert. Sources of uncertainties in osl dating of archaeological mortars: The case study of the roman amphitheatre "palais-gallien" in bordeaux. *Radiation Measurements*, 72:100–110, 2015.

[76] P. Urbanová, A. Michel, N. Cantin, P. Guibert, P. Lanos, P. Dufresne, and L. Garnier. A novel interdisciplinary approach for building archaeology: The integration of mortar "single grain" luminescence dating into

archaeological research, the example of saint seurin basilica, bordeaux. *Journal of Archaeological Science: Reports*, 20:307–323, 2018.

[77] R. F. Galbraith, R. G. Roberts, G. M. Laslett, H. Yoshida, and J. M. Olley. Optical dating of single and multiple grains of quartz from jinmium rock shelter, northern australia: Part i, experimental design and statistical models. *Archaeometry*, 41(2):339–364, 1999.

[78] J.-P. Adam and A. Mathews. *Roman Building: Materials and Techniques*. Routledge, London, 2005.

[79] J. Elsen. Microscopy of historic mortars: A review. *Cement and Concrete Research*, 36(8):1416–1424, 2006.

[80] A. S. Murray and R. G. Roberts. Measurement of the equivalent dose in quartz using a regenerative-dose single-aliquot protocol. *Radiation Measurements*, 29(5):503–515, 1998.

[81] A. S. Murray and A. G. Wintle. The single aliquot regenerative dose protocol: Potential for improvements in reliability. *Radiation Measurements*, 37(4-5):377–381, 2003.

[82] D. Banerjee, A. S. Murray, L. Bøtter-Jensen, and A. Lang. Equivalent dose estimation using a single aliquot of polymineral fine grains. *Radiation Measurements*, 33(1):73–94, 2001.

[83] M. Ballarini, J. Wallinga, A. G. Wintle, and A. J. J. Bos. A modified sar protocol for optical dating of individual grains from young quartz samples. *Radiation Measurements*, 42(3):360–369, 2007.

[84] D. G. Hong, M. J. Kim, J. H. Choi, N. A. El-Faramawy, and H. Y. Göksu. Equivalent dose determination of single aliquot regenerative-dose (sar) protocol using thermoluminescence on heated quartz. *Nuclear Instruments and Methods in Physics Research Section B: Beam Interactions with Materials and Atoms*, 243(1):174–178, 2006.

[85] Y. Gu, M. Wang, Q. Zhang, L. Ge, L. Xu, and H. Lu. Accurate-parametric sar-tl dating protocols for older sediments using quartz. *Applied Radiation and Isotopes*, 181:110072, 2022.

[86] A. Chruścińska, B. Jesionowski, H. L. Oczkowski, and K. Przegiętka. Using the tl single-aliquot regenerative-dose protocol for the verification of the chronology of the teutonic order castle in malbork. In *Proceedings of the GADAM Centre Conference on Luminescence and ESR Dating*, Gliwice, Poland, 2008. Institute of Physics, Silesian University of Technology.

[87] S. A. Mahan, T. M. Rittenour, M. S. Nelson, N. Ataee, N. Brown, R. DeWitt, J. Durcan, M. Evans, J. Feathers, M. Frouin, L. A. Gliganic, M. Jain, G. E. King, C. Lahaye, T. Lauer, M. C. Meyer, K. Munyikwa, A. S. Murray, N. Porat, H. M. Roberts, K. J. Thomsen, A. G. Wintle, J.-P. Yue, A. V. Zander, and K. Zenobia. Guide for interpreting and

reporting luminescence dating results. *Geological Society of America Bulletin*, 135(5-6):1480–1502, 2023.

[88] R. F. Galbraith and R. G. Roberts. Statistical aspects of equivalent dose and error calculation and display in osl dating: An overview and some recommendations. *Quaternary Geochronology*, 11:1–27, 2012.

[89] L. J. Arnold, R. G. Roberts, R. F. Galbraith, and S. B. DeLong. A revised burial dose estimation procedure for optical dating of young and modern-age sediments. *Quaternary Geochronology*, 4(4):306–325, 2009.

[90] P. Urbanová. *Recherches sur la datation directe de la construction des édifices: Exploration des potentialités de la datation des mortiers archéologiques par luminescence optiquement stimulée (OSL).* Thèse de doctorat, Université Michel de Montaigne - Bordeaux III, France, 2015. Archéologie et Préhistoire. NNT: 2015BOR30078.

[91] M. J. Aitken. *Introduction to Optical Dating: The Dating of Quaternary Sediments by the Use of Photon-Stimulated Luminescence.* Clarendon Press, Oxford, 1998.

[92] C. Lahaye. *Nouveaux apports de la thermoluminescence à la chronologie du Paléolithique dans le Sud-Ouest de la France: Études en milieu hétérogène et en présence de déséquilibres radioactifs dans les séries de l'uranium.* PhD thesis, Université Bordeaux Montaigne, Bordeaux, 2005.

[93] S. M. Hossain, F. De Corte, and D. Vandenberghe. A comparison of methods for the annual radiation dose determination in the luminescence dating of loess sediment. *Nuclear Instruments and Methods in Physics Research Section A: Accelerators, Spectrometers, Detectors and Associated Equipment*, 490(3):598–613, 2002.

[94] G. Guérin, N. Mercier, and G. Adamiec. Dose-rate conversion factors: Update. *Ancient TL*, 29(1):5–8, 2011.

[95] P. Guibert and M. Schvoerer. Tl dating: Low background gamma spectrometry as a tool for the determination of the annual dose. *International Journal of Radiation Applications and Instrumentation. Part D. Nuclear Tracks and Radiation Measurements*, 18(1-2):231–238, 1991.

[96] K. Siegbahn. *Alpha-, Beta- and Gamma-Ray Spectroscopy.* Elsevier, Amsterdam, 2012.

[97] Y. A. Ellis-Akovali. Nuclear data sheets for a = 226. *Nuclear Data Sheets*, 50(1):229–254, 1987.

[98] E. Browne, R. B. Firestone, and V. S. Shirley. *Table of Radioactive Isotopes.* John Wiley & Sons, New York, 1985.

[99] D. G. Olson. Gamma intensities for ^{226}ra and daughters, and ^{235}u. *Nuclear Instruments and Methods in Physics Research*, 206(1-2):313–316, 1983.

[100] G. A. T. Duller. *Luminescence Dating: Guidelines on Using Luminescence Dating in Archaeology*. English Heritage, Swindon, 2008.

[101] Y. Ichikawa. Dating of ancient ceramics by thermoluminescence (special issue on physical, chemical and biological effects of gamma radiation, vi). *Bulletin of the Institute for Chemical Research, Kyoto University*, 43(1):1–6, 1965.

[102] S. J. Fleming. Thermoluminescent dating: Refinement of the quartz inclusion method. *Archaeometry*, 12(2):133–143, 1970.

[103] S. Stokes. Optical dating of young (modern) sediments using quartz: Results from a selection of depositional environments. *Quaternary Science Reviews*, 11(1-2):153–159, 1992.

[104] K. Munyikwa. Luminescence dating: Applications in earth sciences and archaeology. In *Luminescence: An Outlook on the Phenomena and Their Applications*, pages 259–296. IntechOpen, London, 2016.

[105] A. Murray, L. J. Arnold, J.-P. Buylaert, G. Guérin, J. Qin, A. K. Singhvi, R. Smedley, and K. J. Thomsen. Optically stimulated luminescence dating using quartz. *Nature Reviews Methods Primers*, 1(1):72, 2021.

[106] I. Liritzis, P. Guibert, F. Foti, and M. Schvoerer. Solar bleaching of thermoluminescence of calcites. *Nuclear Instruments and Methods in Physics Research Section B: Beam Interactions with Materials and Atoms*, 117(3):260–268, 1996.

[107] A. D. Franklin, W. F. Hornyak, and A. A. Tschirgi. Thermoluminescence dating of tertiary period calcite. *Quaternary Science Reviews*, 7(3-4):361–365, 1988.

[108] C. Huang, J. Zhang, L. Wang, H. Zhao, and S.-H. Li. Equivalent dose estimation of calcite using isothermal thermoluminescence signals. *Quaternary Geochronology*, 70:101310, 2022.

[109] B. Middendorf, J. J. Hughes, K. Callebaut, G. Baronio, and I. Papayanni. Chemical characterisation of historic mortars. In *Characterisation of Old Mortars with Respect to their Repair. Final Report of RILEM TC 167-COM*, pages 39–56. RILEM Publications SARL, Bagneux, France, 2004.

[110] F. Casadio, G. Chiari, and S. Simon. Evaluation of binder/aggregate ratios in archaeological lime mortars with carbonate aggregate: A comparative assessment of chemical, mechanical and microscopic approaches. *Archaeometry*, 47(4):671–689, 2005.

[111] H. G. Balian and N. W. Eddy. Figure-of-merit (fom), an improved criterion over the normalized chi-squared test for assessing goodness-of-fit of gamma-ray spectral peaks. *Nuclear Instruments and Methods*, 145(2):389–395, 1977.

[112] A. Romero-Salido, F. M. Olmedo, J. Berenguer-Antequera, V. Correcher, and J. F. Benavente. Correlation between figure of merit function and deviation in the assessment of kinetic parameters in realistic tld-100 behavior using fully-connected neural networks. *Radiation Physics and Chemistry*, 213:111259, 2023.

[113] R. K. Gartia, L. Lovedy, and U. Ranita. Analysis of glow curves of quartz and transluminescence dating. *Indian Journal of Pure & Applied Physics*, 47(6):417, 2009.

[114] R. K. Gartia and L. L. Singh. Evaluation of trapping parameter of quartz by deconvolution of the glow curves. *Radiation Measurements*, 46(8):664–668, 2011.

[115] Y. Kirsh, P. D. Townsend, and S. Shoval. Local transitions and charge transport in thermoluminescence of calcite. *International Journal of Radiation Applications and Instrumentation. Part D. Nuclear Tracks and Radiation Measurements*, 13(2-3):115–119, 1987.

[116] V. Pagonis and C. Michael. Annealing effects on the thermoluminescence of synthetic calcite powder. *Radiation Measurements*, 23(1):131–142, 1994.

[117] S. D. Singh and S. Ingotombi. Thermoluminescence glow curve of gamma-irradiated calcite. *Journal of Physics D: Applied Physics*, 28(7):1509, 1995.

[118] M. L. Chithambo, V. Pagonis, and F. O. Ogundare. Spectral and kinetic analysis of thermoluminescence from manganiferous carbonatite. *Journal of Luminescence*, 145:180–187, 2014.

[119] K.-B. Kim and D.-G. Hong. Kinetic parameters, bleaching and radiation response of thermoluminescence glow peaks separated by deconvolution on korean calcite. *Radiation Physics and Chemistry*, 103:16–21, 2014.

[120] C. Tardo, L. Floriano, M. Liuzzo, A. M. Gueli, G. Stella, and G. Margani. Historical, geometrical, and constructive analyses of the rotonda roman baths in catania (sicily). *Buildings*, 15(4):515, 2025.

[121] M. G. Branciforti. Le terme della rotonda. notizie preliminari degli interventi negli anni 2004–2008. In M. G. Branciforti and G. Guastella, editors, *Le Terme della Rotonda di Catania*, pages 15–69. Regione Siciliana, Assessorato dei Beni Culturali e Ambientali e della Pubblica Istruzione, Catania, 2008.

[122] G. A. T. Duller. Single-grain optical dating of quaternary sediments: Why aliquot size matters in luminescence dating. *Boreas*, 37(4):589–612, 2008.

[123] L. Bøtter-Jensen, E. Bulur, A. S. Murray, and N. R. J. Poolton. Enhancements in luminescence measurement techniques. *Radiation Protection Dosimetry*, 101(1-4):119–124, 2002.

[124] D. Rufer and F. Preusser. Potential of autoradiography to detect spatially resolved radiation patterns in the context of trapped charge dating. *Geochronometria*, 34(1):1–13, 2009.

[125] A. S. Murray and J. M. Olley. Precision and accuracy in the optically stimulated luminescence dating of sedimentary quartz: A status review. *Geochronometria*, 21:1–16, 2002.

[126] A. Medialdea, K. J. Thomsen, A. S. Murray, and G. Benito. Reliability of equivalent-dose determination and age-models in the osl dating of historical and modern palaeoflood sediments. *Quaternary Geochronology*, 22:11–24, 2014.

[127] Z. Jacobs, G. A. T. Duller, and A. G. Wintle. Interpretation of single grain de distributions and calculation of de. *Radiation Measurements*, 41(3):264–277, 2006.

[128] Z. Jacobs, E. H. Hayes, R. G. Roberts, R. F. Galbraith, and C. S. Henshilwood. An improved osl chronology for the still bay layers at blombos cave, south africa: Further tests of single-grain dating procedures and a re-evaluation of the timing of the still bay industry across southern africa. *Journal of Archaeological Science*, 40(1):579–594, 2013.

[129] P. Vermeesch. Radialplotter: A java application for fission track, luminescence and other radial plots. *Radiation Measurements*, 44(4):409–410, 2009.

[130] P. Guibert, C. Lahaye, and F. Bechtel. The importance of u-series disequilibrium of sediments in luminescence dating: A case study at the roc de marsal cave (dordogne, france). *Radiation Measurements*, 44(3):223–231, 2009.

[131] C. Lebedinsky. Spectrométrie gamma. Équipement destiné à mesurer la radioactivité naturelle des échantillons de brique soumis à la datation par luminescence, 2008. Photographie.

[132] N. Mercier and C. Falguères. Field gamma dose-rate measurement with a nai(tl) detector: Re-evaluation of the "threshold" technique. *Ancient TL*, 25(1):1–4, 2007.

[133] B. J. Brennan, R. G. Lyons, and S. W. Phillips. Attenuation of alpha particle track dose for spherical grains. *International Journal of Radiation Applications and Instrumentation. Part D. Nuclear Tracks and Radiation Measurements*, 18(1-2):249–253, 1991.

[134] V. Mejdahl. Thermoluminescence dating: Beta-dose attenuation in quartz grains. *Archaeometry*, 21(1):61–72, 1979.

[135] C. Lahaye, P. Guibert, and F. Bechtel. Uranium series disequilibrium detection and annual dose determination: A case study on magdalenian ferruginous heated sandstones (la honteyre, france). *Radiation Measurements*, 47(9):786–789, 2012.

[136] G. Adamiec and M. J. Aitken. Dose-rate conversion factors: Update. *Ancient TL*, 16(2):37–50, 1998.